TECHNISCHE UNIVERSITÄT MÜNCHEN
LEHRSTUHL FÜR LEICHTBAU

Investigation of a shape adaptive aircraft wing leading edge with pneumatic actuation

Johannes Kirn

Vollständiger Abdruck der von der Fakultät für Maschinenwesen der Technischen Universität München zur Erlangung des akademischen Grades eines

Doktor-Ingenieurs

genehmigten Dissertation.

Vorsitzender:	Prof. Dr.-Ing. Mirko Hornung
Prüfer der Dissertation:	1. Prof. Dr.-Ing. Horst Baier
	2. Prof. Dr.-Ing. Klaus Drechsler

Die Dissertation wurde am 21.01.2016 bei der Technischen Universität München eingereicht und durch die Fakultät für Maschinenwesen am 22.12.2016 angenommen.

Abstract

This work describes a feasibility study of a shape adaptive aircraft wing leading edge with a pneumatic actuation system. The motivation to create such a seamless and gapless high lift device (droop nose) at the wing's leading edge is to enable laminar wing flow. Natural laminar wings on an A320 size aircraft promise a 3-4% drag reduction on aircraft level. Using a droop nose instead a conventional slat reduces the airframe's noise significantly. The challenge lies in enabling laminar flow while also having high-lift capabilities. To solve this, one possible option is to create a morphing leading edge. This requires a flexible outer skin and an actuation mechanism. This mechanism has to be able to provide the necessary deformation for high lift and to support the skin to keep a laminar surface.

To meet the surface requirements with a mechanical actuation system the skin has to be supported in many positions (depending on the leading edge size), which can lead to very complex systems. To reduce complexity and still achieve the required surface precision, the idea pursued in this work is to continuously support and actuate the skin with inflatable actuation-tubes. This concept will work pneumatically and use flexible matrix composites (FMC) for the actuators. FMCs are a combination of highly flexible materials and very stiff continuous fibres, as such enabling a high flexibility in one and being very stiff in the other direction. The actuator concept in this work requires customizable fiber-layup and -orientation to tailor the required stiffness. As off the shelf materials did not satisfy all requirements, several production methods and material combinations were reviewed and a suitable material was produced. With this material tensile and three-point bending tests were performed to accumulate mechanical parameters and failure behavior.

Developing and verifying a simulation model of the pneumatically actuated leading edge was an integral part of this work. The model has to be able to accurately reproduce the large deformation of the leading edge for high-lift configuration. A challenge for the development of the simulation model was the large interaction between the actuators and the outer skin, leading to complex contact problems, while also taking into account that the FMC actuator skin can exhibit non-linear material behavior. The simulation model was developed in parallel to the development of the actuators and the design of the overall system by comparing simulation results with the mechanical material tests and deformation behavior of the actuators. The thus verified simulation model was used to evaluate different proposed actuation system concepts. For this different concepts were created in an extruded 2D leading edge segment. Using the deformation behavior at different airloads a down-selection of the concepts was made. A final concept was further refined with a sensitivity study (variation in loads and geometry). In the last section of this work the final concept was compared to a mechanical system developed for the same geometry (in FP7 project SADE) and a standard A320 leading edge system.

Kurzfassung

Diese Arbeit beschreibt die Machbarkeitsstudie einer formvariablen Flugzeugflügelvorderkante mit einem pneumatischen Aktuationssystem. Die Motivation der Arbeit ist es, ein naht- und lückenloses Hochauftriebssystem (Droop-Nose) an der Flügelvorderkante zu entwickeln, um laminare Flügelströmung zu ermöglichen. Laminare Flügel an einem Flugzeug von der Größe eines A320 versprechen eine 3-4% Verringerung des Strömungswiderstandes. Mit Hilfe einer Droop-Nose statt einem herkömmlichen Vorflügel reduziert sich der Lärm des Flugzeugs erheblich. Die Herausforderung liegt darin, laminare Strömung zu ermöglichen und gleichzeitig die Hochauftriebsfunktionen zu erhalten. Eine Möglichkeit hierfür stellt die Entwicklung einer formvariablen Vorderkante dar. Dies erfordert eine flexible Außenhaut und ein dazu passendes Verformungssystem für den Hochauftrieb. Dieses System muss neben der Formgebung in der Lage sein, die Haut zu unterstützen um die laminare Oberfläche zu erhalten.

Um die Oberflächenanforderung mit einem mechanischen System zu erfüllen, muss die Haut (abhängig von der Größe der Vorderkante) an vielen Stellen unterstützt werden, was zu sehr komplexen Systemen führen kann. Diese Arbeit verfolgt die Idee, die Haut mit schlauchförmigen, aufblasbaren Aktuatoren kontinuierlich zu unterstützen und zu verformen, um die Komplexität zu reduzieren und trotzdem die erforderliche Oberflächengenauigkeit einzuhalten. Dieses Konzept arbeitet pneumatisch und nutzt flexible Faserverbundwerkstoffe (FMC) für die Aktuatoren. FMC, als Kombination aus hochflexiblen Materialien und sehr steifen kontinuierliche Fasern, ermöglichen hohe Flexibilität in der einen und hohe Steifigkeit in der anderen Richtung. Das Antriebskonzept in dieser Arbeit erfordert variierbare(n) Faserorientierung und Lagenaufbau, um die erforderliche Steifigkeit zu erreichen. Verfügbare Materialien konnten die Anforderungen nicht komplett erfüllen, was dazu führte, dass verschiedene Herstellungsverfahren und Materialkombinationen getestet und darauf basierend ein geeignetes Material produziert wurde. Um mechanische Parameter und Informationen zum Versagensverhalten zu sammeln, sind mit diesem Material Zug- und Dreipunktbiegetests durchgeführt worden.

Die Entwicklung und Validierung eines Simulationsmodells der pneumatisch angetriebenen Vorderkante war ein integraler Bestandteil dieser Arbeit. Das Modell muss in der Lage sein, die große Verformung der Vorderkante in die Hochauftriebskonfiguration zu reproduzieren. Eine Herausforderung für die Entwicklung des Modells war die große Interaktionsfläche zwischen den Aktuatoren und der Außenhaut, was zu komplexen Kontaktsimulationen führt. Zusätzlich musste berücksichtigt werden, dass die FMC-Haut der Aktuatoren nichtlineares Materialverhalten aufweisen kann. Das Simulationsmodell wurde parallel zur Entwicklung der Aktoren und zur Konstruktion des Gesamtsystems durch den Vergleich der Simulationsergebnisse mit den mechanischen Materialtests sowie dem Deformationsverhalten der Aktuatoren entwickelt. Das auf diese Weise verifizierte Simulationsmodell wurde verwendet, um verschiedene Aktuationskonzepte zu bewerten. Dazu wurden unterschiedliche Konzepte in einem extrudierten 2D Vorderkantensegment simuliert. Unter Verwendung des Deformationsverhaltens unter verschiedenen Luftlasten wurde eine Bewertung durchgeführt. Das endgültige Konzept wurde mit einer Sensitivitätsanalyse (Variation von Luftlast und Geometrie) weiter verfeinert. Im letzten Abschnitt dieser Arbeit wurde das endgültige Konzept mit einer für die gleiche Geometrie (in FP7-Projekt SADE) entwickelten Mechanik und einem Standard-A320 Vorderkante System verglichen.

Content

Abstract .... *II*

Kurzfassung .... *III*

List of Figures .... *VIII*

List of Tables .... *XI*

Abbreviations .... *XII*

1. Introduction 1

1.1 Motivation for shape adaptive applications on aircraft 2

1.2 State of the art: Shape adaptive technologies for aircraft 7

1.2.1 Shape adaptive technologies focus: Pneumatics 9

1.3 Objectives of this thesis 11

1.4 Outline 12

2. System requirements for leading edge devices on laminar aircraft wings 14

2.1 Aerodynamic requirements for laminar wing flow 14

2.2 Certification specification of leading edge devices 15

2.3 Aircraft manufacturer and operator requirements 15

2.4 Overall assessment criteria for leading edge systems 15

3. Design concepts of a shape adaptive leading edge actuation mechanism 17

3.1 Actuation design concepts 24

3.1.1 Stringer hook concept 24

3.1.2 Tensile belt concept 25

3.1.3 Pneumatic stringer concept 26

3.1.4 Single actuator concept 27

3.1.5 Single actuator with rubber support concept 28

3.1.6 Two actuators concept 29

3.2 Assessment criteria and preliminary concept comparison 30

4. Characterization of the leading edge pneumatic actuators 32

4.1 Pneumatic actuator with flexible, non-stretchable skin 35

4.2 Pneumatic actuator with flexible, stretchable skin 36

5. Finite element modelling approach to adaptive structures 37

5.1 Consideration of two different finite element methods 37

5.1.1 Static (non-)linear method 38

5.1.2 Dynamic explicit method 38
5.2 Preparation of the simulation model for the droop nose 39
5.2.1 Discretization of the pneumatic droop nose 39
5.2.2 Selection of simulation method: static vs dynamic 42
6. Material development for pneumatic actuators 47
6.1 Properties of thermoplastic elastomers 49
6.2 Comparison: Elastic and hyperelastic material models 52
6.2.1 Hook’s law 52
6.2.2 Mooney-Rivlin model 55
6.2.3 Ogden model 55
6.2.4 Fung model 56
6.2.5 Holzapfel-Gasser-Ogden model 56
6.3 Fiber composites 57
6.3.1 Application of rule of mixture to flexible matrix composites 58
6.4 Material and production process options and selection 61
6.4.1 Material trials with rubber 62
6.4.2 Material trials with silicone rubber 63
6.4.3 Material trials with thermoplastic elastomers 63
6.5 Mechanical testing of flexible matrix composites 67
6.5.1 Mechanical testing: Preparation and challenges 67
6.5.2 Tensile tests of flexible matrix composites at different fiber angles 67
6.5.3 Theoretical evaluation of the tensile-test results 71
6.5.4 Three-point bending tests 72
6.6 Conclusion material development and testing 73
6.6.1 Numerical representation of (non-linear) material behavior 75
6.6.2 Comparison of simulation model and coupon testing 79
6.7 Flexible matrix composite material models 83
6.7.1 Enhanced Mooney-Rivlin model for flexible matrix composites 84
7. Pneumatic actuator prototypes 86
7.1 Manufacturing of the pneumatic actuators 88
7.1.1 Actuator skin manufacturing 88
7.1.2 End caps manufacturing 89

7.2 Pneumatic actuator testing 91
  7.2.1 Comparison of 3D-deformation simulation and testing 92
8. Pneumatic actuation of a droop nose 94
8.1 Description of the droop nose system simulation model 95
8.2 Simulation results of proposed actuation design concepts 99
  8.2.1 Stringer hook concept with two actuators 99
  8.2.2 Tensile belt concept with two actuators 100
  8.2.3 Pneumatic stringer concept with two actuators 101
  8.2.4 Single actuator concept 102
  8.2.5 Single actuator with rubber support concept 104
  8.2.6 Two actuators concept 106
8.3 Comparison and evaluation of the different actuation concepts 107
  8.3.1 Final design: Stringer hook with two actuators 109
8.4 Sensitivity study based on final design 110
  8.4.1 Influence of angle of contact area on performance 110
  8.4.2 Influence of varying air loads on deformation performance 112
8.5 Generalized design guidelines for a pneumatically actuated droop nose 115
  8.5.1 Influence of geometry 115
  8.5.2 Influence of the number of actuators 116
  8.5.3 Influence of (air)-loads 116
  8.5.4 Modeling methods 116
8.6 True scale demonstration of actuation principle 117
8.7 Comparison between mechanical and pneumatic actuation concept 118
  8.7.1 Weight comparison 118
  8.7.2 Comparison of the deformation performance 119
8.8 Complexity and scale-ability of the pneumatic system concept 120
8.9 Adaptation and impact on A/C-level of the pneumatic concept 122
  8.9.1 From 2D simulation to 3D system design 123
  8.9.2 Actuation pressure distribution on A/C level 124
  8.9.3 Actuator control on aircraft level 125
9. Summary and conclusion 127
9.1 Summary 127

9.2 Conclusion and outlook 127

Bibliography 129

Appendix 138

Appendix A: Material parameters Hexply 913 138

Appendix B: Material parameters Torayca T700S 143

Appendix C: Material parameters Rubber SAA1052/70 145

Appendix D: Material parameters TPE HTF9471/16 147

Appendix E: Material parameters Silicone LR 7665 A/B 148

Appendix F: Introduction to continuums mechanics 150

Appendix G: Classical laminate theory 156

Appendix H: Stacking sequence GFRP of the droop nose 158

Appendix I: Excerpt input-file tube in contact with two plates 159

Appendix J: Excerpt input-file actuation variant: Two actuators 163

Appendix K: Measurement points to evaluate the divergence from the target-shape 166

Appendix L: Results from sensitivity study (Pictures) 167

List of Figures

Figure 1: A proposed pneumatic actuation system 1
Figure 2: Conventional droop nose A380 4
Figure 3: Conventional slats on an A310 4
Figure 4: Cruise shape vs. landing shape (dotted line) of a leading edge (based on F15 wing by DLR) 5
Figure 5: SADE Kinematic Cruise (top) and deployed position (bottom) 5
Figure 6: Different implementations of the kinematic actuation system 6
Figure 7: Adaptive pneumatic wing for fixed wing 9
Figure 8: Bellow Actuator 10
Figure 9: Flat Tube Actuator (Prototype, natural rubber skin) 10
Figure 10: Festo pneumatic muscle 10
Figure 11: FNG-Planform SADE profile position 17
Figure 12: 2D FNG section for SADE 17
Figure 13: Design space static structure of the droop nose 18
Figure 14: Cruise shape in comparison to unsupported skin under airloads 18
Figure 15: Airloads on the leading edge during cruise and on the deflected leading edge 19
Figure 16: Pressure Distribution Nose Section, cruise (green) and deployed (red) 19
Figure 17: Kinematic actuation system 20
Figure 18: Counter-pressure system 21
Figure 19: Design space for the static structure 22
Figure 20: Schematic of a pneumatically actuated droop nose 23
Figure 21: Stringer hook concept 24
Figure 22: Tensile Belt concept 25
Figure 23: Pneumatic stringer concept 26
Figure 24: Single actuator concept 27
Figure 25: Large actuator with rubber support concept 28
Figure 26: Two actuator concept 29
Figure 27: Work-principle of pneumatic actuators 32
Figure 28: Skin-loading dependencies 33
Figure 29: General Motion of a Deformable body 35
Figure 30: Exemplary deformation of a flexible, non-stretchable actuator (without external load) 35
Figure 31: Exemplary deformation of a flexible, stretchable actuator (without external load) 36
Figure 32: Simplified CAD-model of a droop nose actuation system 39
Figure 33: Generic model of large scale contact problem with an actuator (green) 42
Figure 34: Comparison of energies during simulation of a single actuator in contact with plates 43
Figure 35: Comparison of energies during simulation of a single actuator in contact with plates 44
Figure 36: Comparison of energies during simulation of a single actuator in contact with plates 46
Figure 37: Deformation and stress response of generic tube simulation 46
Figure 38: Flexible Matrix Composite 47
Figure 39: Woven glass-fibers in a TPE matrix 48
Figure 40: Overview Polymer 49

Figure 41: Macromolecular structure of thermoplast, thermoset and elastomer 50
Figure 42: Qualitative comparison of elastic vs. plastic vs. hyperelastic behavior 52
Figure 43: Comparison of hyperelastic models 57
Figure 44: Single composite ply with general directions 59
Figure 45: Rubber-fiber composite; pressure molded at 250-400bar at KRAIBURG Gummiwerke 62
Figure 46: Change in viscosity in TPE under shear forces at 180°C 64
Figure 47a/b: Thermoplastic elastomer injected in carbon-fiber preform at 190°C 65
Figure 48: 2 layers of biax-6k-carbon fiber infused with TPE at 2.5bar at 180°C 65
Figure 49: Carbon-fibers with a TPE matrix, after VAP (for 3h) and as a comparison dry fibers 66
Figure 50: FMC-UD-prepreg 66
Figure 51: Schematic of test sample with coordinate systems 67
Figure 52: Test-specimen under load - S-shaped 68
Figure 53a/b/c: Force-strain curve of tensile tests (0°/90°/±45°) 69
Figure 54: Comparison of stress-strain curves 15°-90° 70
Figure 55: Three point bending experimental setup (0°-test sample) 72
Figure 56: Three-Point-Bending test results (mean curve from all tests) 73
Figure 57: Tensile test simulation model 75
Figure 58: Comparison of static and dynamic tensile simulation 76
Figure 59: Comparison of Rebar reinforced material with orthotropic material 77
Figure 60: Comparison Rebar tensile simulation and test at 45° 78
Figure 61: Comparison rebar simulation 90° and TPE 78
Figure 62: Comparison of 0° tensile test with simulation 79
Figure 63: Comparison of ±45° tensile test with simulation 80
Figure 64: Comparison of 90° tensile test with simulation 81
Figure 65: Comparison of 3-point bending test with simulation 82
Figure 66: Stress-Strain curve of a TPE tensile test with an Ogden-curve-fit (3rd order) 83
Figure 67: Comparison between Experimental Data 90° & mod. Mooney-Rivlin Model 85
Figure 68: Comparison between Experimental Data 0° & mod. Mooney-Rivlin Model 85
Figure 69: Expected max. internal pressure of the actuators wrt fiber angle and skin thickness (1) 87
Figure 70: Expected max. internal pressure of the actuators wrt fiber angle and skin thickness (2) 87
Figure 71: Mandrel for actuation tube manufacturing 88
Figure 72: Prototype during manufacturing in a vacuum bag (during cool-down period) 88
Figure 73a/b: Prototype before testing with round and elliptic metallic end caps 89
Figure 74: Elliptical TPE End cap 90
Figure 75: Minimum space TPE End-cap 90
Figure 76: Single walled TPE End cap 91
Figure 77: Flat triangular TPE End Cap 91
Figure 78: Actuator with partial simulation overlay 93
Figure 79: Actuator with simulation overlay (seen from "top") 93
Figure 80: Simulation model, general setup 95
Figure 81: Stringer Hook Design with Cruise Forces and BC 96
Figure 82: Stringer Hook Design with landing forces and BC 96

Figure 83: Smooth step function 97
Figure 84: Comparison of viscous, kinetic and internal energy 97
Figure 85: Design variant: Stringer Hook 99
Figure 86: Stringer Hook in cruise configuration, actuators at 0,004 N/mm² 99
Figure 87: Design variant: Tensile Belt 100
Figure 88: Tensile Belt Tensile Belt in cruise configuration, actuators at 0,004 N/mm² 100
Figure 89: Design variant: Pneumatic Stringer 101
Figure 90: Pneumatic Stringer in cruise configuration, actuators at 0,004 N/mm² 101
Figure 91: Design Variant: Single Actuator 102
Figure 92: Single Actuator with 0,22 N/mm² internal pressure under landing loads 103
Figure 93: Single Actuator with 0,4 N/mm² internal pressure under landing loads 103
Figure 94: Design variant: Single Actuator with rubber support 104
Figure 95: Single Actuator with rubber support at 0,22 N/mm² under landing loads 105
Figure 96: Single Actuator with rubber support at 0,4 N/mm² under landing loads 105
Figure 97: Design variant: Two Actuators 106
Figure 98: Two Actuators at 0,22 N/mm² under landing loads 106
Figure 99: Comparison of different "tensile" concepts 108
Figure 100: Comparison of actuation concepts 108
Figure 101: Stringer Hook with deployed actuators at 0,22 N/mm² under landing loads 109
Figure 102: Setup of actuation system sensitivity study: Angle of contact area 110
Figure 103: Rotation of contact area of 1° (left) and 2° (right) 111
Figure 104a/b: Rotation of contact area of 5° and different internal pressure 111
Figure 105: Results of sensitivity study angle of contact area 112
Figure 106: Comparison of airload changes in the sensitivity study 113
Figure 107: Droop nose with Aluminum skin (2mm constant) with actuation pressure 0,22 N/mm² 114
Figure 108: Design of the rigid structure 115
Figure 109: Completed demonstrator without actuators 117
Figure 110: Demonstrator with actuators at 0,03 N/mm² 117
Figure 111: SADE Kinematic system (DMU with mass) 119
Figure 112: Comparison of kinematic vs pneumatic actuation simulation under air loads 119
Figure 113: Deformation in meters in cruise configuration with limit stop position 120
Figure 114: From 2D to 3D simulation process 123
Figure 115: Source of pneumatic pressure on A/C (with redundancy) 125
Figure 116: Actuator control logic (pneumatic black, electric blue) 126
Figure 117: General Motion of a Deformable body 150
Figure 118: Full body with external forces and cut body with area-segment dA_0 153
Figure 119: Stress vectors S_k and all components of the stress tensor σ_{ij} exemplary on a body 155
Figure 120: Stacking sequence of the GFRP droop nose 158
Figure 121: Measurement points along the skin 166
Figure 122: Cruise and actuation loads increased by 50% 167
Figure 123: Landing and actuation loads increased by 50% 167
Figure 124: Cruise loads increased by 5% 168

List of Tables

Table 1: Design requirements for a leading edge pneumatic actuation system 2
Table 2: Materials used in shape adaptive applications (selection) 7
Table 3: Overall requirements for (adaptive) leading edge devices 16
Table 4: Unit-definition for the FE-model 39
Table 5: List of relevant simulation parts and their impact on deformation 40
Table 6: Overall model setup of sub-simulation "actuator tube in contact with plates" 42
Table 7: Finalized simulation parameters 45
Table 8: Hyperelastic material models (phenomenological approach) 54
Table 9: Tested Material combinations (Overview) 61
Table 10: Material and production methods (+ means tested configuration; - means not tested) 61
Table 11: Number of specimens per test and angle 68
Table 12: Material properties of the TPE-C-FMC at ϕ_f=0,2 70
Table 13: Failure behavior depending on fiber direction 70
Table 14: Material properties of the TPE-C-FMC at ϕf=0.20 (analytical calculation) 71
Table 15: Tested materials (X+: tested and success, X-: tested failure, blank: not tested) 74
Table 16: Comparison of static vs dynamic tensile test simulations 76
Table 17: Possible approaches to FMC-material simulation 77
Table 18: Material parameters in the simulation model (in N/mm²) 79
Table 19: Constants for the mod. Mooney-Rivlin-Model [N/mm²] 84
Table 20: Types of prototype actuators manufactured 89
Table 21: Pneumatic tests of the prototype actuators (* maximum pressure reached) 91
Table 22: Material parameters for the actuator simulation (in N/mm²) 92
Table 23: Mechanical properties if UD GFRP prepreg (Hexply 913 UD S2GL) 95
Table 24: Summary of simulation model setup 98
Table 25: Mechanical properties: Rubber in the Simulation 104
Table 26: Summary of concept performance 107
Table 27: Design guideline criteria: Pneumatic droop nose 116
Table 28: Weight comparison of different leading edge actuation systems (scaled to 1m span) 118
Table 29: Comparison of part counts (scaled to 1m span) 121

Abbreviations

A/C	Aircraft
ACARE	Advisory Council for Aviation Research and Innovation in Europe
ALLIE	Internal energy of the whole model
AoA	Angle of Attack
APU	Auxiliary Power Unit
BC	Boundary Condition
CFD	Computational Fluid Dynamics
CLT	Classical Laminate Theory
CRFP	Carbon Fiber Reinforced Plastics
CS	Coordinate System
CuAlNi	Copper Aluminum Nickel
DLR	Deutsches Zentrum für Luft- und Raumfahrt (German Aerospace Center)
DMU	Digital Mock Up
DoF	Degree of Freedom
EU	European Union
FCS	Flight Control System
FEM	Finite Element Method
FMC	Flexible Matrix Composites
FNG	Flügel nächster Generationen (Wing of next generation Aircraft)
FP7	Seventh Framework Program of the European Commission
GFRP	Glass Fiber Reinforced Plastics
L/E	Leading Edge
MBB	Messerschmitt-Bölkow-Blom
MFC	Macro Fiber Composite
NASA	National Aeronautic and Space Administration
NiTi	Nickel Titanium
NLF	Natural Laminar Flow
PEEK	Polyetheretherketon
PEO-PET	Polyethyleneoxide-Polyethylenterephthalat
RF	Reference Point

ROM	Rule of mixture
SADE	Smart High Lift Devices for Next Generation Wings
SMA	Shape Memory Alloys
SmartLED	Smart Leading Edge
SMP	Shape Memory Polymers
TPA	Thermoplastic Polyamids
TPC	Thermoplastic Copolyester
TPE	Thermoplastic Elastomer
TPO	Polyolefin Blends
TPS	Styrenic block Copolymers
TPV	Elastomeric alloys
TRL	Technology Readiness Level
UAV	Unmanned Aerial Vehicle
UD	Unidirectional
VAP	Vacuum Assisted Process
WT	Wind Tunnel

Note: Delimiter for decimals is , in this work.

1. Introduction

With regard to the ACARE Vision 2020 and Flightpath 2050, which are outlines for European aeronautics research targets, work has been ongoing to reduce the CO_2, NOx emissions as well as the noise footprint of commercial aircraft. Based on these goals one attractive option is to develop technologies to realize natural laminar wings, which promise a 3-4% drag reduction on aircraft level for an A320 sized airplane *[Braslow, 1999].* This directly impacts the fuel consumption and has the potential effect of decreasing the airframe generated noise by a significant amount *[Chow et al, 2002; Pott-Pollenske et al, 2007].*

For a natural laminar wing several hurdles have to be taken, especially with regard to skin-smoothness, as any unevenness can lead to a laminar-turbulent transition. Looking at a state-of-the art-wing today, most dominantly in the area of the leading edge, several clear gaps and steps related to parts of the high-lift system, the slats, can be seen. One possibility to overcome this issue is to create an adaptive droop nose, which is a fully integrated part of the wing and not a separate structure as today. To make this possible the skin in the leading edge has to be flexible enough to allow for large deformation to enable a deployment of a high-lift device. In this work the design of a pneumatically actuated shape adaptive leading edge will be discussed and compared to a mechanical actuation solutions. The proposed system has the potential benefit of creating a gap- and slat-less leading edge for a fixed wing aircraft. In additional a reduction of complexity in comparison to a classical mechanical system is possible. For this new materials and new actuation systems have to be considered and evaluated. As the proposed system can no longer be considered a classical mechanical system, the scope of this work has to include shape-adaptive/morphing technologies.

A possible pneumatic actuation system can consist of several separate and independent "tubes" and "tension belts or tensile load carrying structures", see Figure 1. To use tubes as actuation devices the wall-material has to be flexible enough to allow a certain degree of deformation (depending on the intended use), but if used as a structure, as in this case, also needs a certain stiffness (secondary use, to carry loads). At first glance these two requirements stand in conflict with each other, but there are several materials or special geometries that can fulfil them. Some examples are corrugated sheets *[Yokozeki et al., 2005]*, flexible matrix composites (FMC) *[Peel, 1998; Shan et al, 2004, laboratory setting]* or adaptive selectively-deformable structures *[Amiryants, 1998]*. Corrugated sheets and adaptive selectively-deformable structures are very limited in their design given by their selected geometry and also their need of some sort of flexible cover material to work properly. Flexible matrix composites on the other hand are a material with a wide field of application as they are not as restrained by their inherent

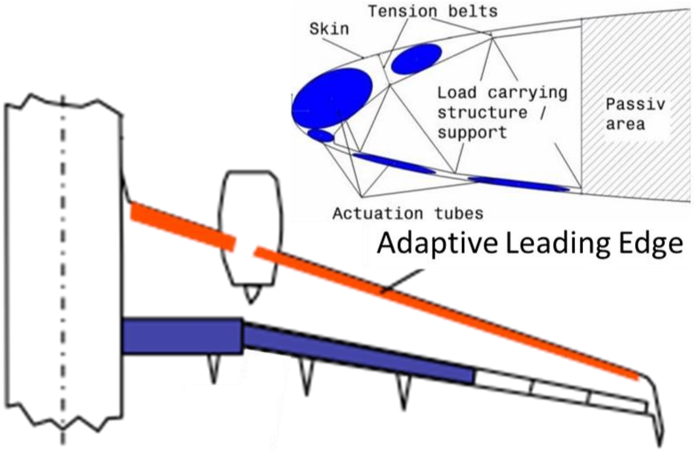

Figure 1: A proposed pneumatic actuation system [A/C-wing drawing - Source: DLR]

structure. In the widest sense flexible matrix composites can be found in quite a few places in everyday life, e.g. car-tires, inflatable boats, escalator hand rails *[Keun et al., 2006]* etc. In the above mentioned FMCs the fiber-volume-fraction is rather low (hand-rail, rubber-tire) or the fibers are in weave form (inflatable boats). However the actuator concept envisioned in this study requires also a dependable and customizable fiber-layup and -orientation, to be able to tailor the required stiffness for each direction. Through this control of stiffness the laminate is only easily deflected in the wanted direction and offers a certain degree of resistance in the other directions. As existing off the shelf materials cannot comply with these requirements, a development of production capability and evaluation of the produced material was necessary, a list of overall design requirements for the actuation system and with it the used material can be seen in Table 1.

Table 1: Design requirements for a leading edge pneumatic actuation system

Design requirements	Rationale
Flexible skin material	Large deformation
Stiff-skin material	Support of structure
Lightweight	Aerospace application
High-deformation capability	Inherent in the application
Small space requirement	Large deformation leave little static space
Air-tight	Stable and constant actuation

1.1 Motivation for shape adaptive applications on aircraft

Most aircrafts today have a specific flight profile and are most efficient when flown inside that profile *[Perkins et al., 2004]*. To reduce this strict dependency on one flight profile, aircraft need to be able to change their wing-shape to adapt to a new routine. To enable this change in structure shape-adaptive technologies have been and are being developed. Shape adaptability or morphing in general means to change from one configuration to another, be it structure, virtual models or pictures. In this thesis the mention of morphing always pertains to a structural or system change from one configuration to another. This can be a gradual change or a direct transition between distinct configurations (two or more). The technologies discussed in the following paragraph are mostly focused on aerospace applications. Almost all aircraft-platforms today are able to change certain parts of their geometry to adapt to different points of their mission-profile (e.g. deployment of slats and flaps for take-off or landing). This distinct change of shape is commonly not considered morphing, but it must still be included when drawing a complete picture. More accepted as morphing are technologies which allow for a drastic change in shape (e.g. significant change of wing-span or sweep-angle), but a clear line between what is morphing and what is not cannot be drawn. For aerospace applications morphing is usually equivalent with adaptation. More importantly it is necessary to have the ability to change the geometry of an aircraft to perform relevant mission requirements. The change of wing-camber during lift-off and landing of a fixed wing aircraft is crucial for the overall performance of the aircraft (A/C). If the wing-camber would remain constant, a much higher lift-off and landing speed would be necessary. As mentioned commercial passenger A/C today are optimized for a single flight point (cruise) and are less efficient if flown outside that design-point *[Voit-Nitschmann, 2006],* making the fixed wing a compromise to all other flight phases. Morphing technologies can enable gradual change to the A/C structure to adapt the efficiency for a wider range of flight phases. For military applications a much higher degree of flexibility in aircraft systems would be preferable (see Tornado or F14 sweep wings). Here a mission profile has a much greater diversity than for a commercial passenger A/C. These profiles can include a drastic change between a loiter phase (low velocity, long airtime) vs. a dash phase (high velocity). The geometrical changes of an aircraft can be separated in three groups: planform alteration (span, sweep, and chord), out of plane transformation (twist, dihedral/gull, and span-wise bending) and airfoil adjustment (camber and thickness). In recent years many in-depth-studies were performed describing the required shape change for different mission scenarios and the aerodynamic effects of morphing (e.g. the control stability etc.). Full-scale evaluations of the impact of morphing technologies on aircraft-level were performed. So there is a lot of data available on morphing benefits and drawbacks for aircraft applications. For example: *[Barbarino et al., 2011; Bowman et al., 2002; DeBreuker et al., 2011; Kudva, 2004; Olympio et al., 2010, 2010; Wlezien et al., 1998; Vocke et al., 2011].* A lot of these technologies aim to afflict large shape changes on an A/C during flight. To achieve this, different topics have to be evaluated and the corresponding technologies developed. As morphing in aerospace applications is almost always a shape-change, three core topics have to be regarded:

- Actuators
- System
- (Skin) material

In some cases two of these points (e.g. actuator and skin) can be seen as symbiotic. The skin can act as an actuator based on the used material. Additionally it should be mentioned that a traditional separation between actuator, system and material is in most cases no longer applicable. This leads to a much greater complexity for the design. A clear separation between structural and system design is no longer possible, demanding a multi-disciplinary approach from an early stage in the development. Morphing of aircraft structures is in a lot of cases inspired by nature. Birds have high degrees of freedom for changing the shape of their wing. Birds can loiter with high-aspect ratio configurations and moments later dash to catch their prey, transforming their wings very quickly and efficiently. The idea to change the wing geometry is as old as powered, heavier-than-air flight. The Wright Flyer (1903), the first airplane, used wing twist (controlled by the pilot through cables) to enable roll control. The development of the common aircraft of today with the need for higher cruise speeds and pay-loads led to stiffer aircraft structures, mainly due to a limitation in materials and actuators that could withstand the higher loading while still enabling the required deformation (fixed wing, conventional flaps, slats etc.) *[Wagg et al, 2007]*.

The renewed interest in the possibilities and benefits of morphing technologies is related to a multitude of factors. The development of new and smart materials and new actuation devices make seemingly radical morphing concepts look possible. The demand for versatile unmanned aerial vehicles (UAV) has increased the possibility to research and test morphing technologies on flight platforms with less cost and certification requirements than traditional A/C. Another very important aspect is the demand for greener and more efficient aircraft (e.g. Vision 2020) for commercial applications. This demand has shown the limits of optimization of standard A/C systems, which have been improved to near perfection over the past decades.

To increase the overall efficiency (e.g. drag reduction) and to make aircraft more flexible in their flight profiles possibilities have to be found which enable adaptive aircrafts (and also to evaluate these changes upon their impact on the overall performance) *[Wittman et al., 2009]*. Literature presents a lot of ideas, e.g. wing-morphing in camber, span-wise or cord-wise direction and the benefits therefrom *[Bae et al., 2004; Cesnik et al., 2004; Thill et al., 2008]*, but the actual technology to achieve the described morphing is in most cases still missing or under development *[Philen et al., 2006, 2007; Murray et al., 2007; Lan et al., 2009]*. The motivation for this research stems from the EU FP7-project SADE[1] and the national project SmartLED *[Monner et al., 2009]*. The aim of both projects is to create a seamless and gapless high lift device (Droop Nose) at the wing's leading edge with the goal to reduce the airframe's noise and drag and to enable laminar wing flow. Laminarisation (natural laminar flow) is one of the technologies which can significantly reduce drag and is also within the scope of today's capabilities *[Holmes et al., 1992 and Saeed et al., 2009]*. On today's passenger-aircraft the gaps between the wing's main box and slat as well as flap (see Figure 2 or Figure 3) and also the rivets would lead to a laminar-turbulent transition of the flow *[Holmes et al., 1992],* if today's technologies would simply be transferred to a laminar wing profile. Therefore among others a way has to be found to eliminate the gap between the static wing part and the active parts. That leads to a recombination of the two previously separate structures and requires a new skin and a new set of actuation methods for this new "morphing" structure. The skin in the region of the leading and trailing edge has to be flexible enough to enable the required deflection and the actuation system has to, apart from moving the structure, stabilize the skin enough to fulfill the requirements for a laminar wing (e.g. surface quality, skin waviness).

Figure 2: Conventional slats on an A310 (Source: Adrian Pingstone)

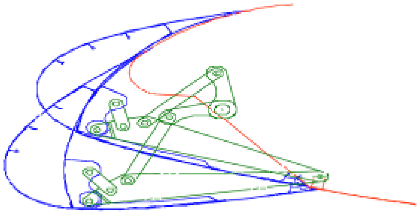

Figure 3: Conventional droop nose A380 (Source: Airbus)

On today's conventional passenger turbojet aircraft the leading edge has two main aerodynamic positions/functions, during cruise to create a continuous airfoil and for landing and take-off to drastically alter the shape of the airfoil (from low to high camber). This change is needed firstly to enable a higher angle of attack without flow separation, secondly to increase the camber of the wing to provide the same lift (as undeformed) at lower airspeed and thirdly to increase the drag during landing. On conventional aircraft the leading edge separates from the center wing box to reach its "drooped" position. A difference has to be made between a conventional slat and a conventional droop nose, compare Figure 2 and Figure 3. Both of these have the same basic function but a conventional slat has a

---

[1] http://www.sade-project.eu (see Newsletter 1 and 2)

better drag (more drag) performance in the deployed position. Multiple studies have been performed on the impact of high-lift devices on aircraft with regard to performance *[Rudolph, 1996; Sanders, 1996]*, noise *[Andreou et al., 2007; Chow et al., 2002]* and laminar flow *[Carmichael, 1979; Croom, 1988; Collier, 2010]*, which show the benefits and draw-backs of a droop nose leading edge and also challenges for laminar wing flow. In this work the deformation is achieved without the separation present in the conventional solutions. The target-shapes can be seen in Figure 4.

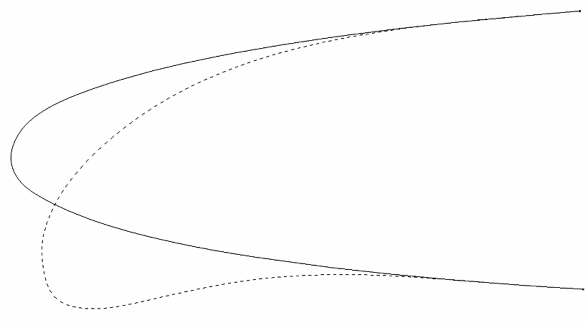

Figure 4: Cruise shape vs. landing shape (dotted line) of a leading edge (based on F15 wing by DLR)

To develop such a morphing system certain technological challenges have to be mastered. As mentioned above the surface quality of the skin is of paramount importance and therefore one major requirement. The skin smoothness is important not only in flight direction but also in span-wise direction, as the wing will most likely have a sweep angle, inducing cross-flow over the airfoil. Additionally the system has to be able to withstand all forces acting on the wing (e.g. aerodynamic, gravitational (constant, maneuver), landing shock, etc.). If the wing did not have to change shape, these points while still challenging could be solved with existing technologies (already in use on gliders/sailplane). To deform the skin some sort of actuation system is needed. Optimally this system adds the required stiffness to the skin, as the skin is most likely not able to provide sufficient stiffness while maintaining its flexibility.

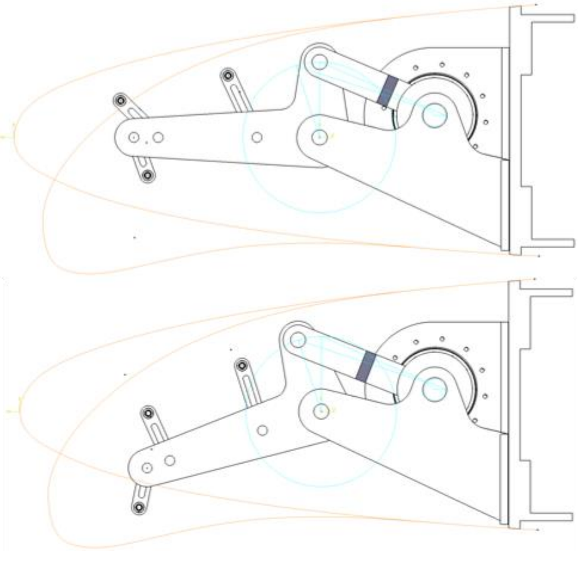

Figure 5: SADE Kinematic Cruise (top) and deployed position (bottom) (missing the fourth skin connection lever)

In the EU-FP7 project SADE a mechanical solution was developed to deform the wing nose. The so called droop nose required a relatively heavy kinematic system, see Figure 5. Additionally this system introduced a high complexity, which is relatively common to mechanical morphing solutions. Based on this work a more unusual idea was proposed. The new concept aims to create a pneumatically actuated droop nose. Under the words “pneumatically actuated droop nose” lie a multitude of different possible solutions. Parts of the levers and struts used in the mechanical solution could be replaced by pneumatic muscles, or the kinematic could have been redesigned to use pneumatic cylinders as actuators. One aim was to reduce the complexity of the actuation system. Therefore the basic idea was to eliminate the need for kinematics and to use pneumatic bladders and the inflation-deformation of these bladders to act as actuators, see Figure 1. These bladders have a two-fold requirement, on the one hand they have to facilitate the deformation, while on the other hand provide stiffness to the system. From a material point of view large deformation and stiffening are contradictory demands and require a thorough look at potential materials and material behavior for these actuators and additionally the interaction of the various components. The idea to use pneumatics as actuation devices on aircraft is not new, compare: *[Gomis-Bellmunt et al., 2010; Jenkins, 2001; RameshGupta et al., 2007; Ruggerio et al., 2002; Salama et al., 2000; To et al., 2002; Vos et al., 2011; Wernicke, 1996, Woods et al., 2013]*. Based on this research pneumatic actuation for the leading edge was judged to be feasible and beneficial in terms of weight and complexity.

The kinematical solution is based on the Patent DE 2907912 A1 of the Dornier Company (today Airbus Group). The research for these particular kinematics started with the project HID-SmartLED, 2007 and was continued in the SADE project, see also e.g. *[Kintscher et al., 2013; Pecora et al., 2011]*. As can be seen in Figure 5 the concept is based on a flexible skin (yellow line) supported by an internal framework of discrete struts and force transmission points between the skin and the framework. A centralized main lever is connected to the skin via (in this case) four discrete levers. The main lever rotates around a pivot point and transmits the actuation moment to the skin and thereby deforms the skin. During cruise (undeformed position) the internal framework transports the loads from the skin into the structure and holds the skin in position. For the loads transmission between skin and levers omega-stringers were introduced in this concept in span wise direction (not shown in Figure 5). The stringers help to spread the load from a discrete point to an area, avoiding localized deformation peaks, and also act as a stiffening support for the nose in span wise direction. Extending this design to a whole wing could be done in two ways. Either all kinematic stations (36 per wing) in one wing are connected and driven by one torque shaft (Option A) or each station is individually actuated by an (electromechanical) actuator (Option B), see Figure 6.

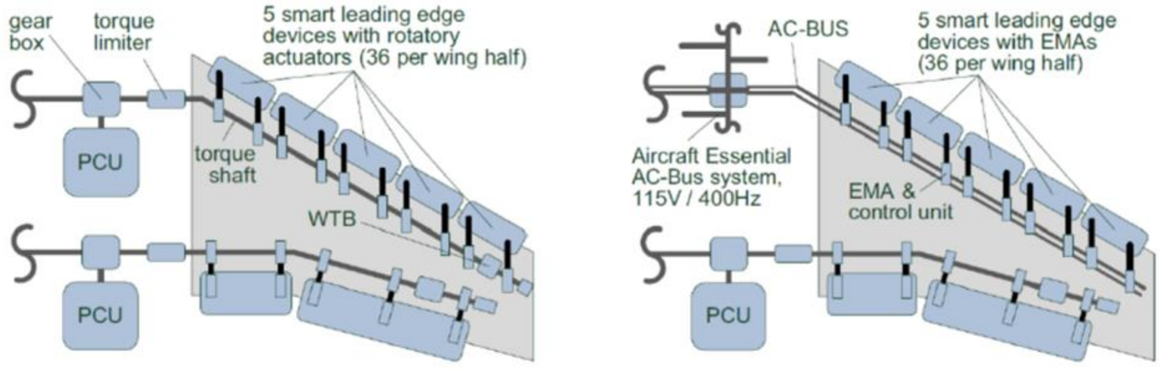

Option A – conventional drive

Option B – electrical drive

Figure 6: Different implementations of the kinematic actuation system *[Lammering et al., 2010]*

1.2 State of the art: Shape adaptive technologies for aircraft

In this paragraph an overview is given about shape adaptive technologies with a strong focus on aerospace concepts. Even if e.g. classical slats or flaps movement can be considered as shape adaptation the concepts discussed here focused on larger shape-change or deliver a more integrated approach to the classical flaps. The aim of most shape adaptive aerospace technologies on the wing is to enable a big geometrical change while keeping an aerodynamic profile.

Today shape-change is achieved usually by moving discrete bodies in relation to each other with the use of separate actuators and connected kinematic solutions. In shape-adaptive technologies this discrete separation between structure and system is becoming blurry. Shape-memory alloys for example have the ability to act as a load carrying structure while at the same time provide movement actuation. Research in the field of shape adaptability is very divers and not easily summarized. Most notably is the use of a multitude of different materials which are used and researched, the following Table 2 is an exemplary list of possible materials. Table 2 is by no means a complete list of all possible materials, it is to be understood as a selection to demonstrate the wide range of the topic. Descriptions and examples on the use of most of the presented materials are given in the following paragraphs (with focus on the use in this work).

Table 2: Materials used in shape adaptive applications (selection)

Shape adaptive materials	Details	Use
Piezo materials	Polymers, Ceramics, Crystals, Organic materials) (Stacks, fibers (MFC), etc.); electrical	Low stroke, high frequency applications (e.g. active vibration damping); active variable stiffness
Shape-memory alloys (SMA)	CuAlNi or NiTi alloys; temperature	Valves, several medical applications; reaction time usually below 1s
Shape-memory polymers (SMP)	Polyurethanes, polynorbornene, PEO-PET, PEEK; Temperature, magnetic or electrical, light, chemical	Sealing, self-repair plastics; very slow actuation (up to minutes)
Magnetorestrictive materials	Cobalt, Terfenol-D; magnetic	Similar to piezos; (higher stresses)
(Carbo-nanotube) Aerogel	Silica, Carbon, Alumina; passive ultralight structure	Insulation, passive structure, heating elements
Solid foams	Can be adaptive by using SMPs as basis; externally actuated	Lightweight filler material, in most cases passive structure
Composites	Fiber or particle reinforced materials (e.g. CFRP, GFRP); mostly passive structure	Lightweight structure, bistable composites need external stimuli
Microstructures	Structurally determined surface of (almost any) material; passive	Influences mechanical as well as chemical properties (e.g. corrosion resistance)

The materials can be roughly divided into two groups: active and passive. This classification is not consistent as it depends on the combination or intended use of the materials. For example composites are usually understood to be passive (and in general stiff) materials, but in the case of piezo-fibers (MFC) they become active. The two last entries in Table 2 are not materials in the classical sense but e.g. in case of composites a combination of different ones. And it is this combination that decides whether the material can be used as shape adaptive or not.

Piezo materials generate an electrical charge in response to applied mechanical stress/force and vice versa. This effect makes it possible to use piezo materials as actuators. Regrettably piezos have only a relatively small stroke and are usually not applicable for large scale deformation application without movement amplifier mechanisms (such as e.g. levers) *[Gautschi, 2001]*. Piezos as actuators for active helicopter rotor blades have been heavily researched over the last years *[Grohmann et al., 2009; Grohmann et al., 2011 and Airbus Helicopter Blue Pulse^{TM}]*.

Shape-memory alloys (SMA) are alloys that in a way “remember” their original form and return to it after deformation through heating. This effect can be used as an actuation mechanism. But the temperature-range for most materials is too close to the operating temperature of the A/C leading edge to be of use for this application. A recent use-case of SMAs was the variable-geometry-chevrons on an engine nozzle fan by Boeing in 2007 (Dreamliner 787 prototype) based on the Boeing patent 6718752, 2002.

Shape memory polymers (SMP) are comparable in their functionality to SMA, such as that they return to their permanent (original) shape through external trigger. This trigger can be a temperature change, as for the SMAs, or electric/magnetic field, light or a (chemical) solution.

Foam is a structure that is formed by trapping pockets of gas in liquid or solid materials. Foams are divided in open- and closed-cell foams. Solid foams are typically made from plastics but metal foams exist as well. Solid foams are commonly used as a filler or insulation material. In aerospace applications foams are mostly used for sandwich-structure. Foams can be made from shape memory polymers and become active structures or actuators. Research on foam as an actuator was e.g. performed by *[Larsen et al, 2009].*

Magnetorestrictive materials are able to transform magnetic energy into kinetic energy (or vice versa) and can as such be used as actuators or sensors. Similar to piezo materials the achievable stroke is very small but very precise.

Composite materials are a combination of two or more distinctively, different materials. The purpose is to create a material with different properties than the base materials. The mechanics of composite materials are discussed in more detail in chapter 6.3 and appendix G. Use of composites as a morphing material (bistable states) was looked at e.g. by *Daynes et al., 2011.*

Microstructures are not a particular material themselves, but they can have large influences on the physical properties of the material-substrate they are applied on. Microstructure is e.g. the prepared surface or thin foil of/on the substrate material.

Active materials are researched for morphing applications as they have a dual-functionality; they behave as load-carrying structure and as actuators. Thereby reducing the need for a separate actuation and therefore in most cases leading to a reduction in weight and complexity. Good examples of this duality can be seen in e.g. *[Chen et al., 2014; Fink et al., 2007; Olympio et al., 2010].*

Very often in morphing the actuation mechanism appears as a secondary system, whereas it makes more sense to combine both structure and actuation system and see it as a unit. In this work the actuation system is highly integrated with the structure and creates such a unit, as well as having structural properties. The actuation system is developed based on the structural behavior and response of the deformed structure. Stabilizing the structure in the required positions and also enabling the necessary deformation.

A good overview and further information about state of the art morphing structures and materials with regards to aerospace applications is given for example in “Morphing Skins by Thill *et al., 2008*”, “ *’Classic’* and Emerging Smart Materials and their Applications by Monner, 2006” and “A Review of Morphing Aircraft by Barbarino *et al., 2011”.*

1.2.1 Shape adaptive technologies focus: Pneumatics

Pneumatic in a general sense is the overhead word used to describe any and all technical applications were pressured gas (commonly air) is used to perform mechanical work. It can be compared to hydraulics with the difference, that hydraulics use fluids (non-compressible) as a working medium instead of gas (compressible). Pneumatic driven actuators are used in a wide variety of technical applications and are often used as a clean alternative to hydraulics (leakage leaves no residue). Background information on hydraulics and pneumatics can be found in *[Parr, 2006].*

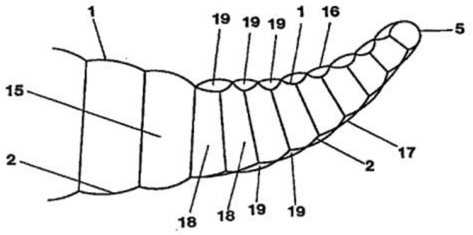

Figure 7: Adaptive pneumatic wing for fixed wing *[Reinhard et al., 2001]*

In the field of industrial processes and controls an actuator is a device that turns a signal from the control loop into a mechanical or temperature change. The actuator enables e.g. movement, change in pressure, change in temperature, etc. Actuators are available in a wide variety of working principles:

- Electrical
- Hydraulic
- Pneumatic
- Electrochemical
- Electromechanical
- Piezo
- Shape-memory alloys
- Magnetostrictive
- Rheological

A good general overview on actuators is given by *Zupan et al., 2002*. Pneumatic actuators can be regarded as mechanical actuators, which turn a (positive) pressure difference (compressed air) into a mechanical motion or force. Traditionally a pneumatic actuator consists of a piston, cylindrical housing and valves or ports. Common pneumatic actuators are, for example:

- Tie rod cylinders
- Rotary actuators
- Pneumatic artificial muscles / Fluidic *muscle [Yerkes et al., 2008; Wereley et al., 2009; Philen et al., 2007]* (see Figure 10)
- Vacuum gripper
- rodless actuator (with or without guide)
- bellow and diaphragm drives (see Figure 8)
- clamping cylinders

Figure 8, Figure 9 and Figure 10 show some existing pneumatic actuators that could be of use to this study. Especially pneumatic artificial muscles, bellow and diaphragm drives or a combination have the potential to be beneficial; for example in the form of the in Figure 9 shown flat tube actuator. Figure 7 shows a patented idea of how pneumatic systems could be used on shape adaptable aircraft structures. Several studies over the years have discussed the potential benefit of a pneumatic leading edge *[Jiang et al., 2009],* pneumatic trailing edge *[Gramüller, 2015]* or whole wings comprised entirely of an adaptive, pneumatic structure *[Cadogan et al., 2004 or Harris et al., 1984]*. Pneumatic structures show the potential of being a lightweight, reliable actuation systems, see *[Suhey et al., 2005].*

Figure 8: Bellow Actuator (Source: Norgren)

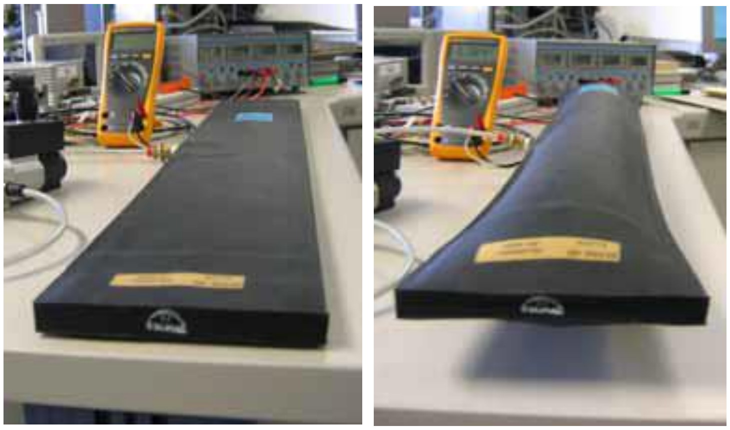

Figure 9: Flat Tube Actuator (Prototype, natural rubber skin)

Figure 10: Festo pneumatic muscle

1.3 Objectives of this thesis

In this thesis a pneumatic actuation mechanism for highly adaptive aircraft structures is researched. This thesis will answer if and where such a system is feasibly used and which benefits can be reached in comparison to a mechanical (kinematic) solution.

Pneumatic actuation is used in multiple different applications, mostly to power linear actuators such as pistons. The system developed here will also be a linear actuator as such as it will provide deformation/force in one main direction. Different from a piston actuator is the area of effect. Instead of a single load introduction point, here the force is introduced over a wide area. Additionally the actuator can become an important structural component and partly adopt the role of a stringer. So the distinct differentiation of structure and system becomes obsolete and an integrated solution has to be considered during the design. This thesis aims to provide a thorough understanding of the involved material, the developed actuators and the overall system as well as the challenges involved in designing an adaptive structure-system hybrid. Additionally a background on the involved theory and tools is included. Due to the special nature of the actuators a study on possible materials and manufacturing processes was performed. To properly describe the behavior of the actuators, material testing was done to create and validate a simulation model of first the material, then the actuators and finally the complete system. The development of a simulation model of the overall system can become very challenging for adaptive structures as a separation of system and structures is usually not possible. Therefore the selection and evaluation of an appropriate simulation model is an integral part of this work and has to find the right balance between detailed material representation and overall system behavior; as these two requirements can be contradictory. Additional focus was placed on preparing and performing large deformation simulation. In the final section of this work the difference of 2D to 3D simulation is discussed and the issue of scale-ability of such a system is evaluated. As a last step the final design for the adaptive droop nose was compared to an adaptive mechanical system, which was developed in correlation to this work in the publicly funded FP7-project SADE - Smart High Lift Devices for Next Generation Wings.

1.4 Outline

Over the course of this thesis the tools to design and evaluate a functional actuation system of a droop nose using pneumatic actuation are identified and developed. This new design has to fulfill the criteria for a NFL – leading edge device, as listed in chapter 2. The outer skin of the in parallel developed mechanically actuated system (see FP7 SADE project) can be used as a baseline design for the pneumatic system. The pneumatic actuators have to be able to provide sufficient deformation under air loads and add to the stiffness of the skin, as the mechanical support structure is completely removed. Additionally the available space for the actuators in the neutral/cruise position of the droop nose is limited.

Based on these general requirements the development of the pneumatic actuators is one focus. In addition to designing the actuators, reliable methods for the evaluation of the performance of the actuation and the whole system are defined and selected.

The design of the actuators can be differentiated into the following points:

- Material study
- Production method of actuator skin material
- Production method of actuators (if separate from production of material)
- System requirements
- Actuator evaluation
    - Inflation tests
    - Comparison of test and simulation
    - Complex simulation model

In and following the third chapter the challenge of developing a pneumatic actuation system is highlighted and several different concepts for such a system are presented. Based on the various concepts, the necessary behavior of the actuators is identified and further described. This description is used to start the development of a finite element model for the described structures, which is further tuned and validated in chapter 6.6 and chapter 7.2. Chapter 6 starts with an overview on different types of materials (with potential to fulfill the requirements) and describes them analytically. Then the development process of the flexible matrix composites is described. Here different material combinations are tested with various production methods. After a suitable material is identified it is mechanically tested and its properties are documented. The data collected in the material tests is used to create an analytical material model using the previously described analytic models. Additionally the behavior of the developed material is reproduced with the finite element model and compared to the different mechanical tests.

The successfully produced material is used to produce several different pneumatic actuator prototypes, see chapter 7. For this a production process is developed and various end-caps for the actuators are looked at. The produced actuators are then mechanically tested and the tests are compared to simulation results. The simulation model is further validated by replicating the deformation behavior of the pneumatic actuators.

After this the validated finite element model is used to simulate the proposed actuation concepts introduced in chapter 3. The different results from these simulations are discussed and a finalized actuation concept for the droop nose is presented at the end of chapter 8.3. Based on the finalized system a sensitivity study is performed. With the knowledge gained during the simulation a design guideline for such kind of a system is presented.

As a last point the up- and down-scaling of a 2D-pneumatic system to a 3D-geometry is discussed and a weight comparison with the in parallel (not as part of this work) developed mechanical system is performed. As a reference values for an A320 leading edge system are included in the weight comparison. Additionally the comparison includes also a rough estimate on system complexity, scale-ability and overall requirements.

2. System requirements for leading edge devices on laminar aircraft wings

As written in chapter 1.3 the aim of this work is to develop a pneumatically actuated droop nose. To be able to properly define the requirements of and also to be able to evaluate such kind of system the following paragraphs will describe the overall system requirements. At this point it has to be mentioned that a droop nose is inferior to a conventional leading edge system (slat) in terms of maximum lift coefficient. The reason for this difference is the missing gap between center wing box and slat on a droop nose configuration *[Raymer, 2006].* During cruise this draw-back can be neglected, only during take-off and landing this is of interest, as the maximum lift coefficient directly impacts the maximum take-off weight of an aircraft. This issue will be further discussed during the evaluation of the different concepts in subchapter 8.6 and following. The following paragraphs establish an overall basis for the system requirements for the leading edge.

2.1 Aerodynamic requirements for laminar wing flow

Natural laminar wing flow requires a very precise surface to remain laminar. A list of requirements for NLF can be seen in Table 4.

Table 4: Estimates for surface quality of NLF wing application *[Kintscher, et al, 2011]*

	Upper Side	**Lower Side**
Forward Facing step [mm]	0,26-0,27	0,28-0,30
Backward Facing step [mm]	0,13-0,14	
b/a chord wise for a > 30mm	0,001	
b/a span wise for a > 30mm	0,001	

The data derives mostly from theoretical investigations and flight test done by NASA in the 1980s. The maximum height of a forward facing step is 0,26-0,27mm. Backward facing steps cannot exceed a height of more than 0,13-0,14mm. These limits were found to be the critical values at which the flow did not transition from laminar into turbulent directly at the disturbance. Nonetheless even these small disturbances can lead to an earlier transition than without these kind of gaps or steps. This was shown by flight tests performed by MBB in 1988 *[Dreßler et al, 1988]*. With just 0,05mm "thick" tapes they showed that the transition point could shift forward by 25% chord. In their study it also became apparent that disturbances in the area between 5-20% chord have the highest influence on the transition behavior of the flow. One important fact to be kept in mind is that the susceptibility of the flow to surface irregularities is extremely dependent on the airfoil shape. The study performed by MBB also mentions that 3D disturbances (such as insects or rivets) have an even higher negative impact than steps or gaps (can be considered 2D disturbances). However it can be concluded that these overall requirements have to be investigated for each airfoil individually. The stated requirements do not guarantee a laminar flow over sufficient length of the airfoil. The quality of the skin surface has to be as perfect as possible to provide a margin for contamination, which can be expected during operation. In row 3 and 4 of Table 4 a maximum for the ratio of *b* to *a* is defined, where a is the length of a "bump" and b the height. This ratio is mostly called skin waviness. Criteria and requirements with regard to skin quality can also be found in *Holmes et al, 1986* and *Pennycuick, 2008*.

2.2 Certification specification of leading edge devices

The baseline aircraft for the SADE project is a single aisle passenger aircraft with short to medium range, therefore the EASA CS25 certification specification can be used to evaluate the system. The CS25 defines the structural and system safety factors and specifies failure behavior for individual systems and the whole aircraft. In CS25.675, for example, is stated that each control surfaces shall be limited in their range by stops. This means the droop nose has to have a system in place to limit the range of motion. Also related to leading edge systems is CS25.701, which states the high-lift devices of both wings have to be mechanically coupled. The aim of this is to avoid unsymmetrical setting of the high-lift devices, as this would lead to unsafe flight conditions. CS25.697 and CS25.699 specify the safe control and indication of flight-systems. Inadvertent operation must be avoided and the status of the system has to be indicated at any time. Any leading edge on an aircraft also has to fulfill the requirements for ice protection system (CS25.1419), bird impact protection (CS25.631) and lightning strike protection (CS25.581).

2.3 Aircraft manufacturer and operator requirements

Additionally to the official safety requirements the A/C manufacturer and the operator have the competitiveness of the product in mind. This leads to the manufacturing and operational cost of an A/C. The cost is directly related to the weight and complexity of the overall and also particular systems. Complexity is obviously always relative; in this case complexity is to be understood as a multitude of different parts or systems. If a new system is to be introduced it is important that the overall complexity of the A/C is not increased disproportionally to the benefit. Therefore a reduction in weight with an increase in complexity has to be carefully evaluated. Introducing new systems, new features or new material to the aircraft often includes an inherent danger of increasing the complexity in terms of validation and integration. In the end the benefits of the new system have to outweigh the drawbacks to be considered for an aircraft. In this work the pneumatic system will be compared to the equivalently new kinematic system and partially to an existing one on the A320.

Maintenance is an important criterion for all aircraft systems. As both the kinematic and the pneumatic system are still very new, any assessment with regard to maintenance can only be engineering judgment *[Scholz, 1998].*

2.4 Overall assessment criteria for leading edge systems

In Table 3 the requirements from the three paragraphs above for an adaptive leading edge for laminar wing flow are summarized and sorted based on their most likely system/structure impact. This list shows the diversity of the tasks that have to be “performed” by the leading edge. As can be seen this list is separated into three rough blocks and the points from this list can be roughly associated with one of the three “separate” system-components: skin, actuation system and passive structure. Which item is directly linked to the pneumatic actuation system and which is rather part of a different system will be one result of this thesis.

Table 3: Overall requirements for (adaptive) leading edge devices

Requirement	Impacted component
Aerodynamic performance	
- high-lift performance	Skin, actuation system
- surface quality (NLF)	Skin, actuation system
- deformation-precision	Skin, actuation system
Safety	
- bird strike protection	Actuation system, passive structure
- lightning strike protection	Skin
- Anti-Erosion	Skin
- Anti-Ice	Skin
- Monitoring capabilities	Actuation system, skin
- Defined range of motion	Actuation system, skin, passive structure
Low Complexity	Actuation system, skin
Reliability	Skin, actuation system
Low Maintenance	Skin, actuation system, passive structure
- Maintenance possible	
Low cost	all

3. Design concepts of a shape adaptive leading edge actuation mechanism

As mentioned in the introduction the baseline geometry for this work is based on the EU-FP7 project SADE and the work performed therein. This chapter describes the geometrical boundaries, the relevant load cases and several general requirements for the shape adaptive leading edge. The requirements include surface quality (see above), deformation shape and design space. The reference wing for this work is the FNG (F15) ("Flugzeug nächster Generation (airplanes of the next generations)")-wing developed during a LuFo project in 2001. A main focus is on a 2D cut just outboard of the engine pylon; see Figure 11 and Figure 12. The section is roughly 4m chord (flaps and slats retracted) and has a maximum thickness of 45cm. To create an actuation system for the droop nose, the design-space, the range of motion and the force distribution on the structure have to be evaluated.

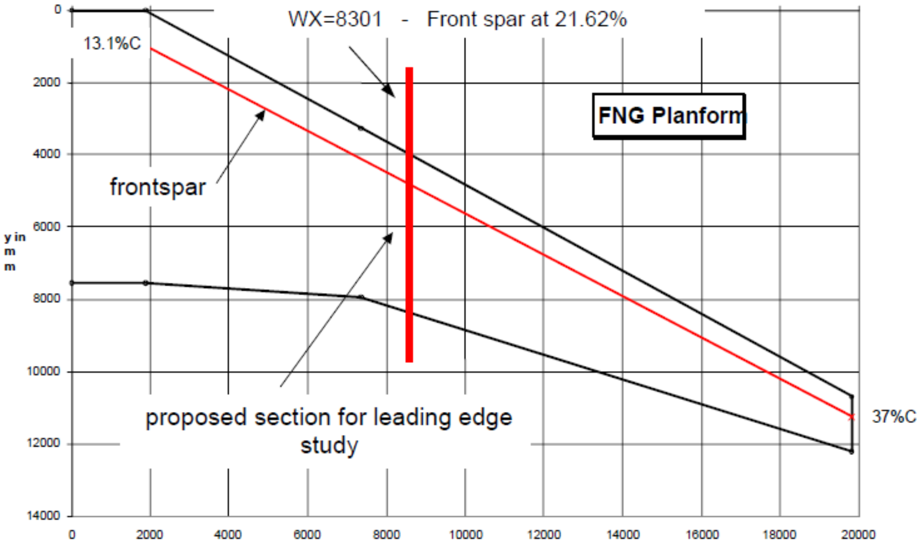

Figure 11: FNG-Planform SADE profile position (Source: SADE-project)

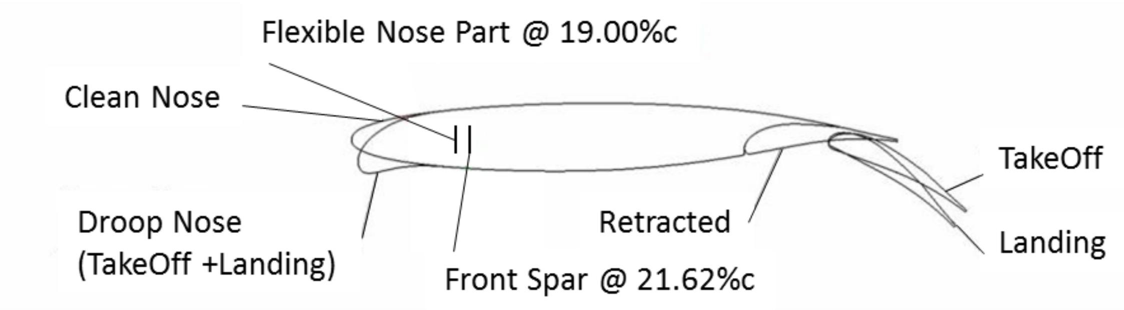

Figure 12: 2D FNG section for SADE (Source: SADE project)

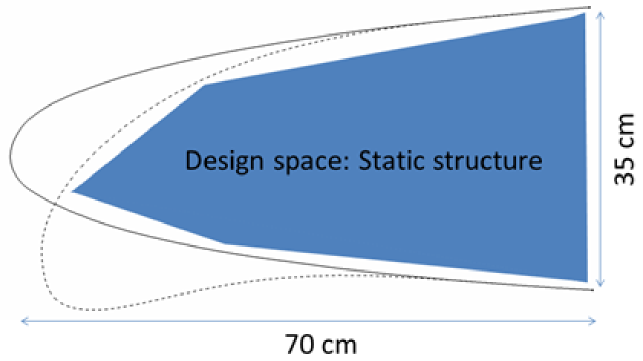

Figure 13: Design space static structure of the droop nose

The relevant nose section is about 70cm x 35cm, dimensioning the available design space. The front spar is the limiting factor in the rear. For any static structure the design-space is further limited due to the droop of the nose, reducing the available space by roughly 10%. Figure 13 shows the dimensions of the complete droop nose and the relevant design space. For a full-wing design these dimensions obviously change based on span wise position. The droop nose has two primary functions. During cruise it has to ensure the optimized airfoil shape for cruise-flight. For take-off and landing the droop nose becomes a high-lift. The deployment of the droop nose changes the camber of the wing, allowing higher angles of attack (AoA) and slower airspeeds. These two requirements translate into two distinct geometrical positions for the droop nose; retracted or deployed. These two distinct positions are the target-shapes for any actuation-system device (studies performed by the DLR during the SADE project showed the same droop shape could be used for take-off and landing). Traditionally the droop nose is a discrete part of the wing, mounted e.g. with a hinge kinematic to the center wing box. Here, as mentioned above, the droop nose is an integral part of the wing, and the whole wing-tip is elastically deformed. For this the skin is very flexible and supported by an actuation system. This actuation system does not only provide the necessary deformation/movement of the skin but also supports the skin against unwanted deformation (see Figure 14). The actuation system is therefore a hybrid between structure and system. For an actuation system this means that it has to be able to carry all loads seen by the skin and transport them to the underlining (static) structure. For this the different loads and load cases have to be identified and described. Also the structural change between retracted and deployed position needs to be understood and analyzed. The loads on the structure and therefore on the actuators come predominantly from the aerodynamic pressure distribution. Smaller but equally important is the inherent stiffness of the skin (through geometrical or material stiffness), which adds a force to be overcome by the actuators during deployment. In the retracted position the skin-stiffness helps to achieve the target shape during cruise. As shown in Figure 13 the static design space for the actuation system is limited by the deformation of the nose.

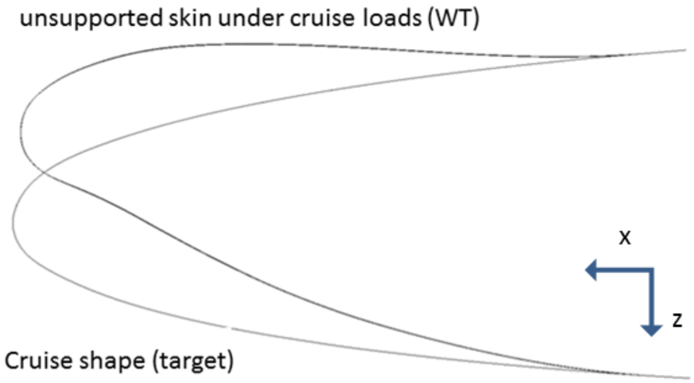

Figure 14: Cruise shape in comparison to unsupported skin under airloads

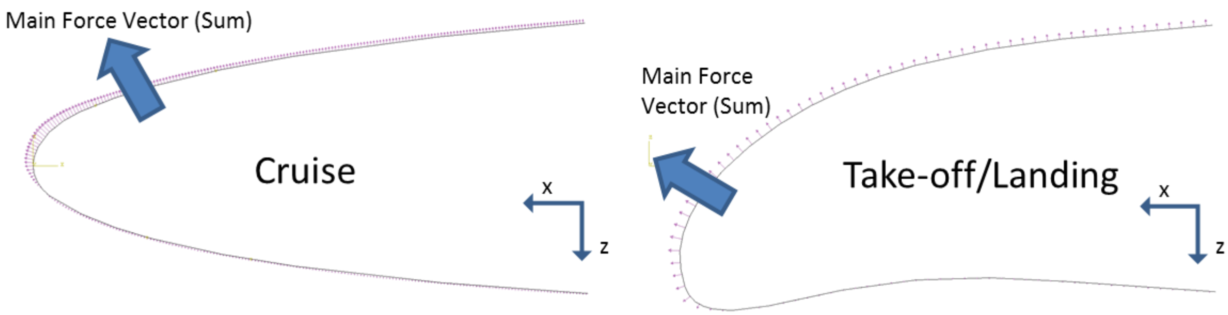

Figure 15: Airloads on the leading edge during cruise (WT) 0°-AoA (left) and airloads on the deflected leading edge during landing 15°-AoA (right) (Airloads were provided by DLR within SADE consortium)

This means, that any support structure for the actuators has to be situated in the designated space. The actuators have to bridge the gap between neutral and deployed configuration and fit mostly into the design-space for static structure. Obviously if the actuators are deformable pneumatic bladders or tubes they can encroach in the space "reserved" for the deflected skin. Figure 14 shows the deformation of the skin, if no support structure exists. The shown deflection is a result of the cruise pressure distribution (an aerodynamic adaptation of the pressure-distribution to accommodate the deformation has not been performed). As shown a proper support of the skin is necessary at all stages as the skin stiffness (in the regarded section) is not sufficient to bear the aerodynamic forces. When looking at the pressure distribution during cruise in Figure 15 (left), it quickly becomes clear that the main force acting on the skin is directed in –z and slightly x direction from the skin; pulling on the skin, creating lift. This pulling force has to be directed from the skin to the underlying structure without deformation of the skin during cruise. To calculate the air load as a single force, special care has to be taken to account for the change of the geometry. The pressure-values are always perpendicular to the surface.

This fact changes their influence on the geometry in terms of moments and force continuously. Dividing the force into F_x and F_z shows, that the load in x-direction is higher than in z-direction.

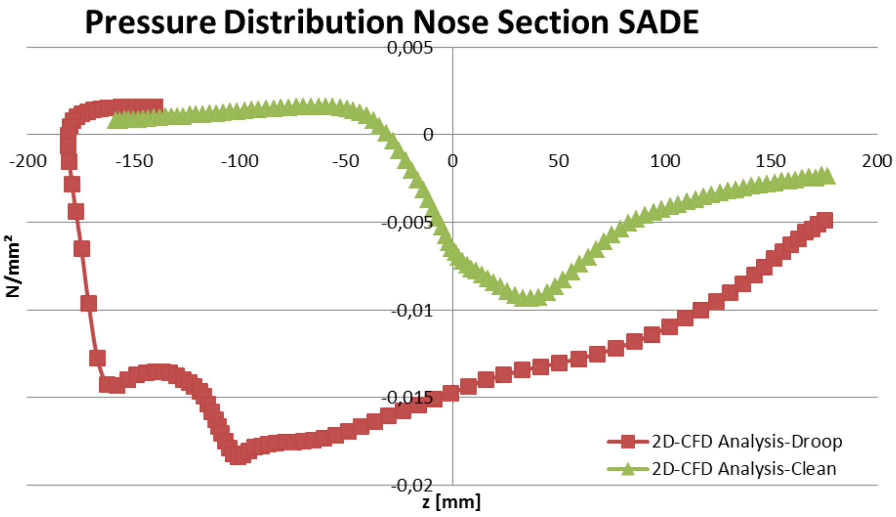

Figure 16: Pressure Distribution Nose Section, cruise (green) and deployed (red) from 2D CFD simulation (Airloads were provided by DLR within SADE consortium)

Most of the x-load is transferred through the skin to the two constraints on top and bottom of the nose, however thinking of the skin as a rope, the force would also pinch the nose together, this effect has to be counteracted with the actuation system. The design of the actuation system therefore has to consider these forces. The force vectors in Figure 15 (left and right) are only rough representations of the overall force direction for the depicted section of geometry. The overall force on the wing is obviously different. Figure 16 shows the pressure distribution over the height of the droop nose, the graph shows the difference between clean and drooped configuration *[Airloads were provided by DLR within SADE consortium]*. Important to note for the actuation system design is the overall increase in force on the system from clean to droop.

The actuation solution in the SADE project for the deformation and stiffness requirements was to develop a complex mechanical kinematic. For this four load-introduction points were identified and used to connect the skin to the kinematic system, see Figure 17. The skin stiffness was optimized for this kinematic system and for these specific load introduction points, with regard to the two operational use cases. The skin is made from (Hexply 913, see Appendix A) GFRP and (therefore) the stiffness-tailoring was achieved through fiber-angle and thickness adaptation. The aim was to create a layup which was as stiff as possible but also allowed the large deformation; especially controlled by the high strains in the skin *[Kintscher, et al.; 2011]*.

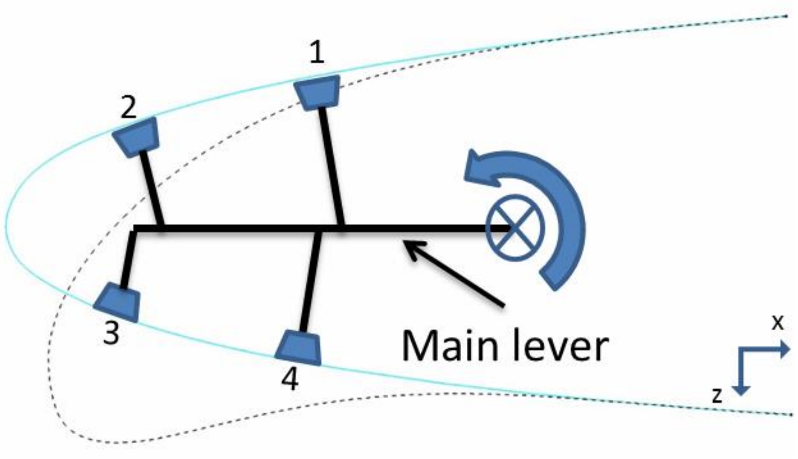

Figure 17: Kinematic actuation system (SADE project)

The first step when trying to recreate the function of the kinematic system with a pneumatic system, is to determine how a pneumatic actuation system could achieve that. In the above paragraph the space-allocation of static and moving parts was already indicated. Furthermore the basic system requirements were described. To use pneumatic piston to drive a mechanical system would create a “pneumatic actuation” system, but remain similar in design to the already established one. With this in mind, the development of the alternative pneumatic actuation concept started by removing all the mechanical parts from the skin as well as the stringers. The tailored stiffness distribution was kept, as it was also optimized with regard to strength and strain for the target-shape.

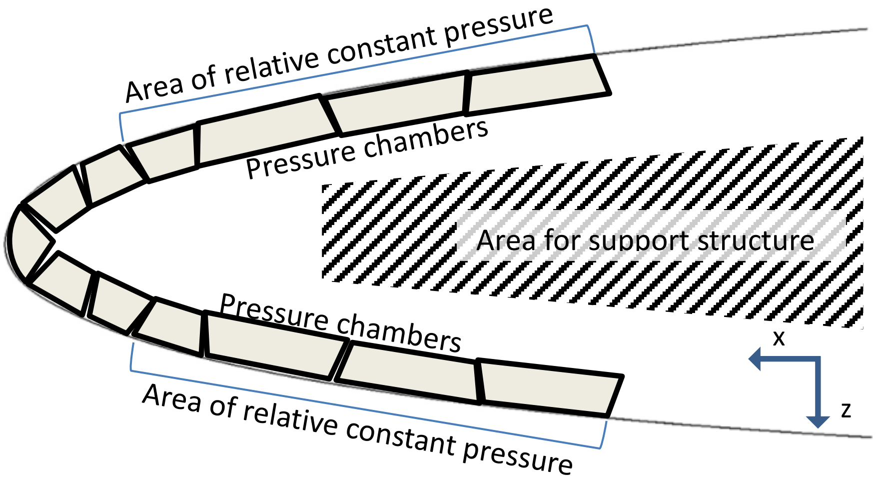

Figure 18: Counter-pressure system

The task to solve is to create a way to generate counter-pressure to the air loads acting on the skin and transfer these loads to the front spar. This could be achieved by placing differently pressurized segments on the inside of the skin. These segments could then be individually controlled to the correct pressure, for the various flight phases. Pressure works always omnidirectional therefore to counteract the forces on the skin, the pressure chambers need to be directly connected to some kind of support structure, see Figure 18. This kind of connection has to be designed such that the connection is flexible to allow movement of the skin to reach the target shape. One possible solution for this could be to make the walls of the pressure chambers flexible, which are then able to adapt to different geometrical conditions; in this case mainly between retracted and deployed droop nose. Following that line of thought means that for such a type of actuation system two general parts are necessary. One is a geometrically flexible pressure chamber (or more than one) and the second is a geometrically fixed support structure. To design both structures the design space has to be properly segmented based on function. During the cruise phase part of the static structure needs to handle tensile loads. The same part has no real function during deployment of the droop nose. For this the other "side" of the structure becomes crucial, where it has to support the large deformation of the skin against the pull of the air loads, through pressure forces, see Figure 19. With these design criteria in mind the design space for the flexible pressure chambers becomes clear. During cruise they need to be in the small area between skin and static structure, for deployment they have to provide the deformation and the actuation forces. As they are simply put inflatable tubes, the positioning of these tubes is an important factor for the deployment shape.

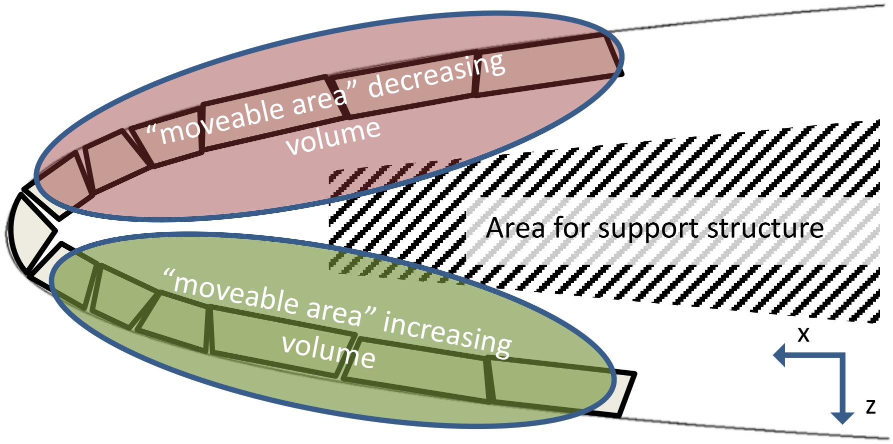

Figure 19: Design space for the static structure

Air as a working medium is used in multiple applications. Air pads, air bearings, pneumatic cushions and pneumatic cylinders are of the shelf products that use air as a low cost, nontoxic and easily available medium. Air pads, pneumatic cushions and pneumatic cylinders can move very high loads at comparably small internal pressures (e.g. multiple tons with less than 10 bar). Pneumatic cushions are used to lift very heavy unregularly formed parts; the pneumatic tubes researched in this work move this principle in reach of use on an aircraft. Even though air pads and pneumatic cushions rely on a big enough area to create their force (lifting capability), their influence on the "movable piece" can be rated as locally. The pneumatic tubes on the other hand have to influence and shape the airfoil over its whole span, the influence is no longer locally. This challenge shows the complexity of designing such a system. To design this system for a 2D case requires to take a multitude of parameters into account. Especially the two primary target-shapes for cruise and landing, as well as the related pressure distributions require special care. The pressure distribution for the two main cases is drastically different, see Figure 15. This means, that the actuator(s) used, has (have) to be able to handle each pressure-distribution and provide the right amount of support to the skin. Without a proper support the skin would be deflected upwards which would most likely destroy lift over the whole wing, see Figure 14. The first goal was therefore to develop a support-structure which would support the skin with and without (in case of failure) the help of one or more actuators. This support structure would also have to provide the necessary support for the actuator, in such a way, that the actuator(s) would be able to work only in the intended direction. The deformation direction in this case is at a slight angle to the horizontal, requiring the actuator to push downward and forward in flight direction. The required functions can be fulfilled through various different designs, some of which are described in the following paragraphs.

To start out with the geometrical design space in neutral position is divided into sections based on functionality, see Figure 20. From this segmentation different actuation concepts were derived. To fulfill the different functions at point 2 and 4 different solutions are presented that can be combined almost arbitrarily. It can be said, that the functional design of the upper side (point 4; to carry tensile forces during cruise/neutral position) can be almost completely separated from the functional design of the lower side (point 2; support and deformation of the skin with pressure loads). Obviously for a detailed design or optimization the two "separate" areas have to be combined into one system.

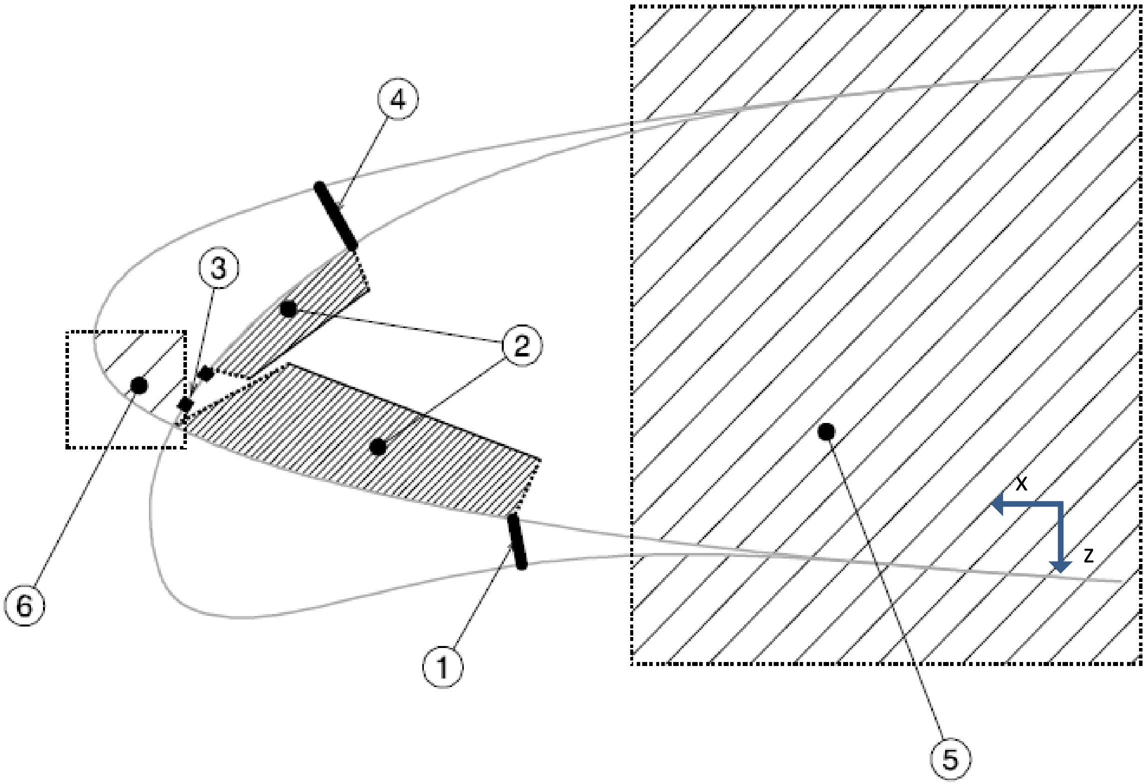

Figure 20: Schematic of a pneumatically actuated droop nose

1: Structure to carry tensile loads to influence the shape (optional)
2: Area for actuator mounting and deployment (mounting surface perpendicular to direction of actuator "force")
3: Contact area for skin support in cruise shape
4: Structure to carry tensile loads (e.g. "tensile belt", "pneumatic stringer" or "stringer hook")
5: Area of increased skin stiffness: Mounting point of support structure (can be designed as Bird-Strike-protection structure)
6: Stowage space of actuators in cruise shape

To fulfill the function at *"point 4"* three different concepts were chosen and described in more detail:

- Stringer Hook Concept
- Tensile Belt
- Pneumatic Stringer.

For the function at *"point 2"* also three different concepts were described and evaluated in more detail:

- One large actuator
- Large Actuator with rubber support
- Two actuators

Each of the three concepts of *"point 4"* should be interchangeable with each of the three concepts of *"point 2"*.

3.1 Actuation design concepts

3.1.1 Stringer hook concept

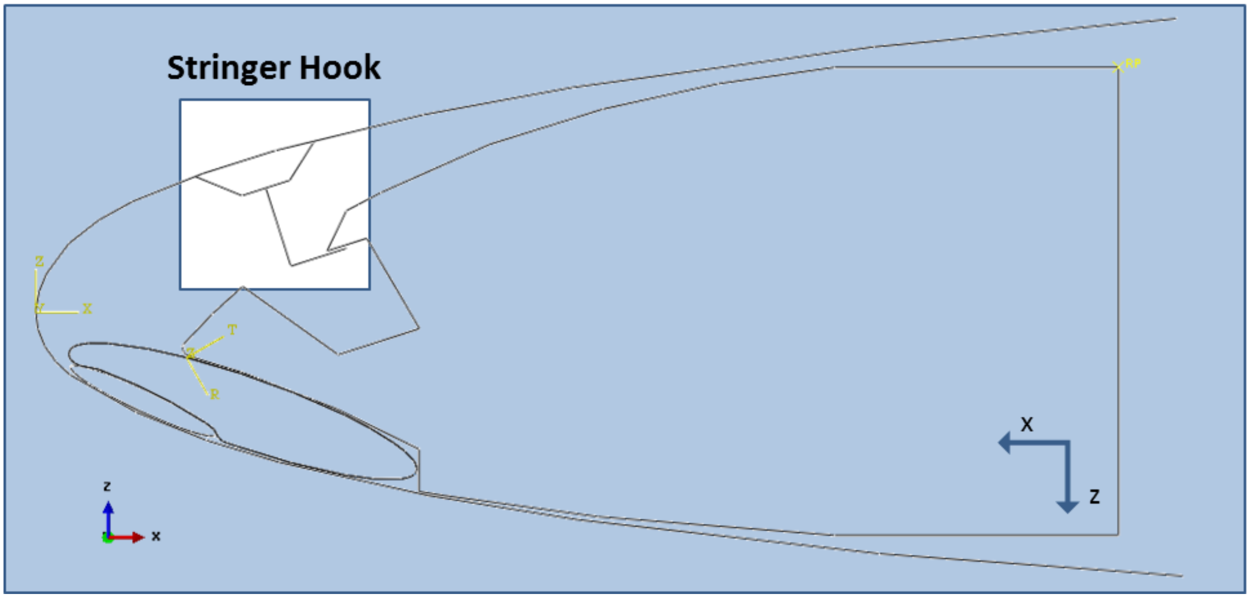

Figure 21: Stringer hook concept

As can be seen in Figure 21 for this concept a hook-like structure is attached to an omega-stringer. The stringer is connected to the skin and positioned in the forward upper part of the nose section (the original SADE concept had two omega stringers in this section). The hook reaches into the support structure and in the cruise position has contact with it. The support structure has a specified cutout, to allow (only) downward movement of the stringer hook for the droop position. The contact in cruise can be passive like a floating bearing or active with a lock. The passive variant has the drawback, that it cannot completely suppress vibrations of the skin. The active lock requires an additional system, making the overall system more complex and prone to failure. The contact between the Hook and the support structure ensures that the upward loads acting on the skin in this section are transferred into the support-structure without an upwards deformation of the skin. For this the elastic deformation of these two parts has to be appropriately small. As the stringer runs the full length of the nose, it reinforces the skin against span-wise bending, this effect is increased by the hook itself. The hook has the effect of a C-spar on top the omega-stringer against bending. The size of this effect depends on whether the hook runs the whole length (span) of the wing or if it is locally placed where needed. It might suffice to only have a discrete number of hooks, to reduce overall system weight and complexity.

As the purpose of the hook is to prevent unwanted deformation of the skin (upward) the stringer is positioned as far in the front as possible, as the deformation in this area is expected to be at a maximum (for comparison see Figure 15 (left)) The limiting factors for the forward position are the maximum deformation vs. the thickness of the support structure at this location. As the support structure has to carry the loads from the hook on the one side as well as the loads from the actuator on the other side, the structure cannot be reduced past a certain minimal thickness.

3.1.2 Tensile belt concept

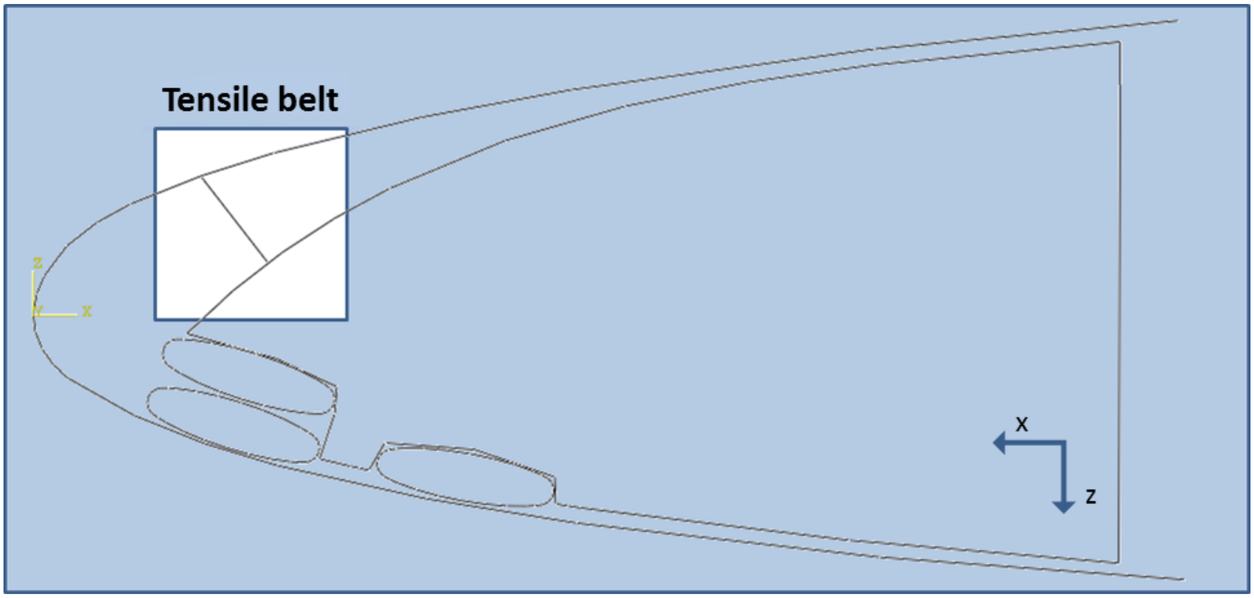

Figure 22: Tensile Belt concept

This concept replaces the hook of the previous concept with a flexible (but not elastic) belt like structure, see Figure 22. This belt is unmovably attached to the support structure as well as the skin. The attachment to the skin can be either indirectly with a stringer or directly to the skin. Important to note here is that the belt structure is only able to carry tensile loads, hence the name *"tensile belt"*. This means, that this structure is not able to either actively or passively negate any positive z deformation. This behavior is obviously important for the secondary function: to not be in the way of the wanted droop deformation of the skin. Nonetheless this lack off stiffness in positive z-direction means the tensile belt is only able to dampen e.g. vibrational induced deformation unidirectional. As already described for the stringer hook, the tensile belt can either be implemented only locally or along the whole span of the wing. If the tensile belt is attached directly to the skin, a continuous belt would be preferably, as the bending-stiffness of the skin is greatly reduced without the stringer. Attaching the belt directly to the skin requires special care with regard to the deformation behavior of the skin, as the belt creates a singular load introduction point (or rather line in 3D). Using a stringer like structure might be preferable. The solution to this particular issue lies greatly in the stiffness-distribution/tailoring of the skin and not as much in the precise design of the tensile belt. It is stated above, that the belt has to be flexible but not elastic. This means the bending stiffness of the belt has to be very low, whereas its tensile strength needs to be several orders of magnitude higher; a good example for this kind of behavior is a rope or a chain.

3.1.3 Pneumatic stringer concept

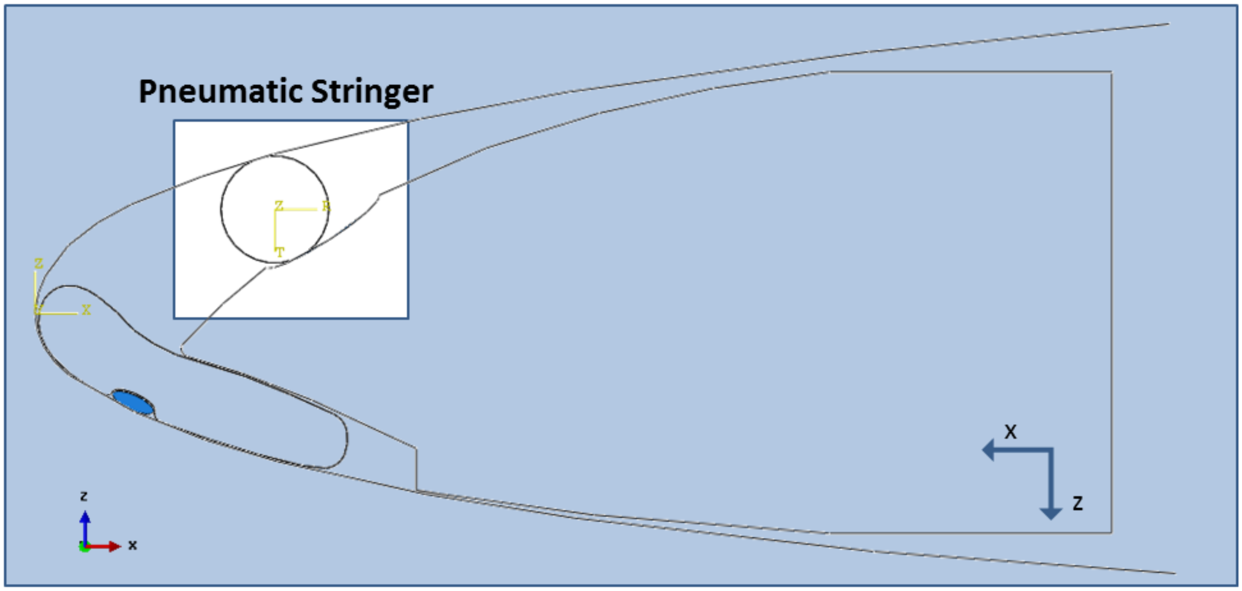

Figure 23: Pneumatic stringer concept

For the *"Pneumatic Stringer"* concept, see Figure 23, the function of keeping the skin in the correct position for the cruise flight is performed by a so called "pneumatic stringer". One idea to enable a "pulling" pressure device is to overcome the air loads with a high enough internal pressure of a *"Pneumatic Stringer"*. If the internal pressure is higher than the locally introduced pulling-force a lifting of the airfoil-skin can be prevented. Depending on the position of the front actuator and the position of this pulling actuator the force carried by the pulling actuator is determined by the free upper airfoil of the leading edge.

As stated above pressure works omnidirectional. This effect is used here by inflating the pneumatic stringer with a pressure several magnitudes above the air loads acting in this area of the skin. As the "pneumatic stringer" is unmovably attached to the skin and the support structure and as the pressure wants to keep the stringer in a circular shape a force is created countering the air loads. Important for the function of this pneumatic stringer is a flexible but inelastic skin-material of the stringer. The pneumatic stringer can only keep the nose-skin in the correct position if it does not inflate and increase in size due to the high internal pressure. At the same time the wall of the pneumatic stringer has to be very flexible to not impede the deformation of the nose-skin for the droop deployment.

By actively controlling the pressure inside the *"Pneumatic Stringer"* it could be even possible to have an active dampening effect on skin vibrations. Constantly keeping the pressure controlled means that this system is active over the whole of the flight, whereas the two previously proposed concepts can be completely passively designed and used.

3.1.4 Single actuator concept

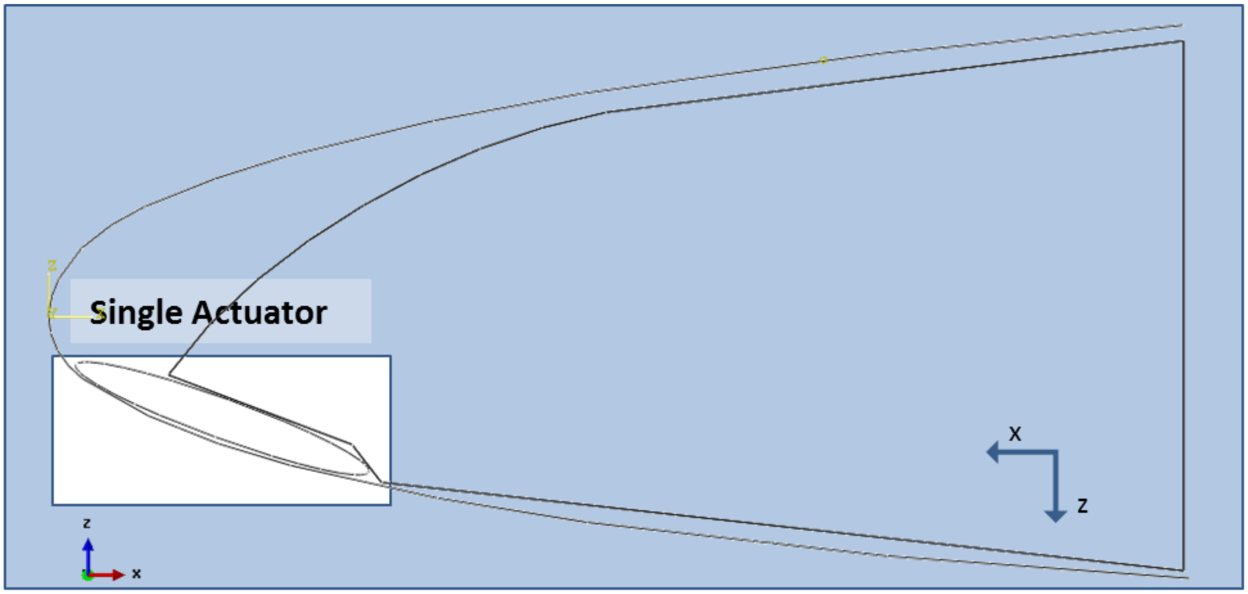

Figure 24: Single actuator concept

To deform the nose skin according to the target shape, different options are possible. One such option is to use one single large actuator, see Figure 24. This actuator lies partly underneath the support structure on the lower side of the nose skin. The actuator is inflated with air (or gas) to provide deformation to the nose-skin. For this the material of the actuator skin needs to be flexible to allow the unhindered expansion of the actuator but at the same time stiff enough for the required internal loads. Additionally two possible traits can be useful for the actuator. As already mentioned the skin needs to be flexible, but it can also be elastic. This would enable the actuator to be smaller during the retracted phase, as it would "grow" in volume during inflation. The contact area with the skin is in direct relation to the pressure inside the actuator and the contact area with the base-structure. As the load the actuator transmits is directly related to this area, this could be beneficial.

$$F = p_i * A_{contact} \tag{1}$$

with: F: the overall force acting on the skin and the support structure from the actuator; $[F] = N$

p_i: internal pressure of the Actuator; $[p_i] = Pa$

$A_{contact}$: Area of contact between Actuator and nose skin; $[A_{contact}] = mm^2$

Important for this concept is not only the size or the pressure of the actuator but the location as well. The angle of the support structure plays a critical role for the deployment direction. During inflation such a pneumatic actuator aims to achieve a circular shape. The support structure has to therefore position and direct this circle into the right position. This holds true for all such concepts, whether only one or multiple actuators are used. The circular shape is also the drawback of this concept, as the radius of the inflated actuator directly relates to the deformation shape of the nose skin. If a varying curvature over a short portion of skin is needed, a single actuator is most likely not able to achieve the target shape.

3.1.5 Single actuator with rubber support concept

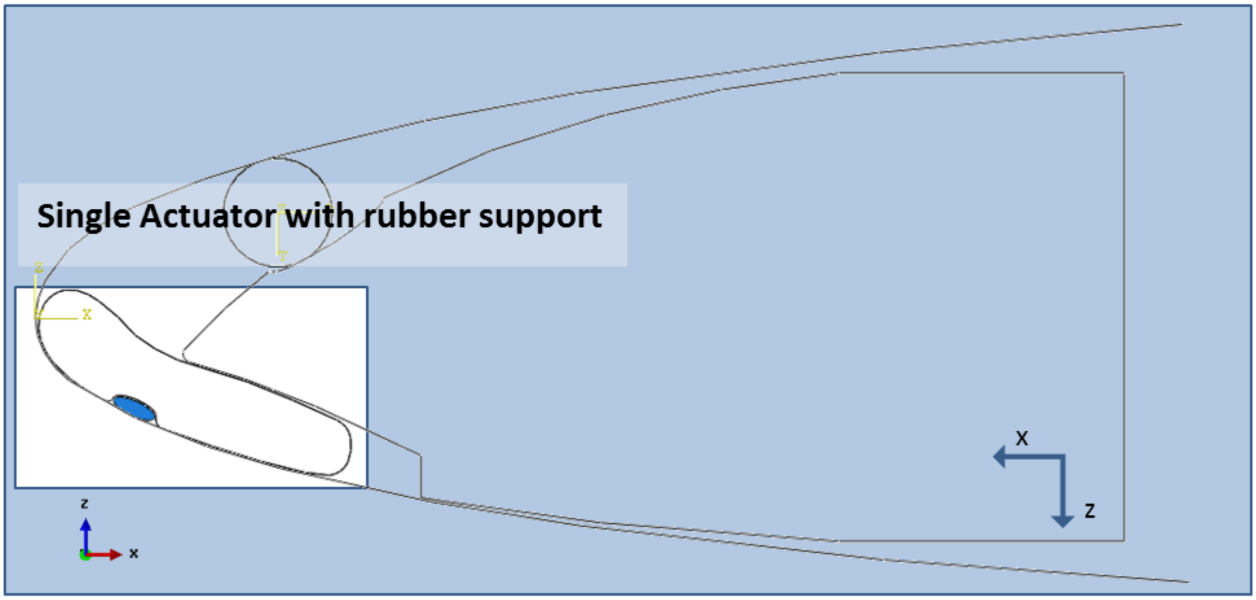

Figure 25: Large actuator with rubber support concept

For this concept a piece of rubber (elastomer of any kind) is added between the actuator and the skin, while the basic setup of position of the actuator and static structure stays the same, see Figure 25 and compare to Figure 24. As mentioned earlier the actuator strives to achieve a circular shape, but as the bending-radius of the target-shape of the nose cannot always be assumed to be constant, the rubber helps to extend the “reach” of the actuator a bit. It also changes the overall actuation-shape to a more elliptical form. At the same time, rubber is very flexible and does not impede the deformation of the skin. Overall this concept is very similar to the previous one, with the difference of an additional option to influence the deformation of the skin. Size and position of the rubber piece can be modified to enable the desired target shape up to a certain point. An extension of this concept could be to use multiple rubber pieces. The rubber can also be formed to the desired target shape on the one side while being circular on the other side, with this it would further increase the accuracy of the target-shape. Increasing the number or the size of the rubber strip to much could have a negative impact on the bending behavior of the skin and on the overall weight of the system.

3.1.6 Two actuators concept

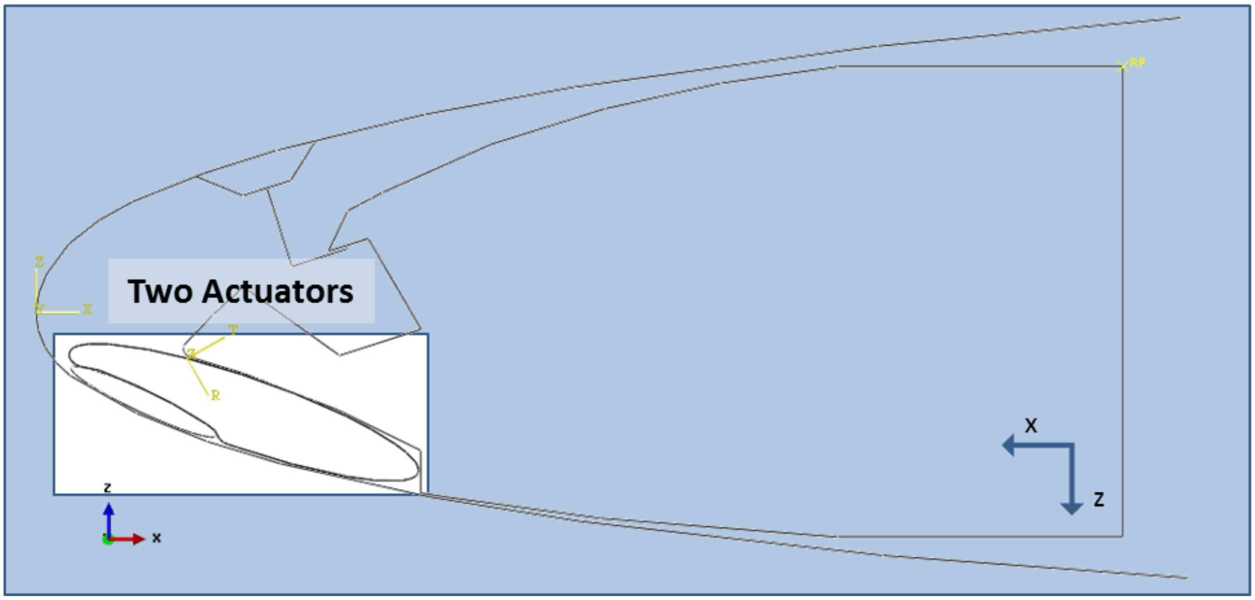

Figure 26: Two actuator concept

This concept is more or less a combination of the two already presented, see Figure 26. The two actuators are differently sized, where the larger one is responsible for the stroke of the actuation and the smaller one to achieve the correct target shape of the skin. In a sense the smaller actuator is an active replacement for the passive rubber piece of the previous concept. Here it is important, that the bigger “upper” actuator begins inflation slightly before the smaller one, otherwise the smaller one will push the larger one out of position and the system cannot reach the target-shape. This concept also only works if the actuator skin material is flexible but inelastic, or at least the smaller actuator has to stay as small as it is. If the smaller one were to inflate past its defined size, it could no longer achieve the right curvature for the target shape.

3.2 Assessment criteria and preliminary concept comparison

Without a detailed design of the different concepts a precise evaluation is difficult, nonetheless it is possible to compare the concepts with each other. Several general aspects like expected (system) complexity can also be evaluated. For most aircraft systems safety is a paramount design criteria *[CS25]*. The less complex a system is, the less likely it is to develop a fault. One criterion therefore has to be system complexity, for this comparison more parts mean a higher complexity. It is also possible to compare the design effort, as more parts, or moving parts require usually a higher degree of design-work. Additional criteria were presented in chapter 2.4, Table 3; these were included in this preliminary assessment as far as reasonable at this point. In Table 5 the different actuation concepts are rated based on these criteria.

Table 5: Comparison of actuation concepts

Evaluation Criteria / Concept	Active System	System Complexity	Design Complexity	Adaptive	Wing bending	Monitoring	Active Shape control	Material properties	3D capability
Stringer Hook	No	Low	Low	No	support	No	No	Stiff, non flexible, e.g. CFRP/GFRP	Yes, space allocation potential issue
Tensile Belt	No	Medium	High	No	Support, one-direction only	Yes	No	Flexible, non elastic	Yes, space allocation potential issue
Pneumatic Stringer	Yes	High	High	Yes	Support	Yes	Some	Flexible, non elastic	Yes, space allocation potential issue
Single Actuator	Yes	Low	Low	Yes	Support	Yes	Yes	Flexible, elastic or non-elastic	Yes
Actuator with Rubber	Yes	Medium	Medium	Yes	Support	Yes	Yes	Flexible, elastic or non-elastic	Yes
Two Actuators	Yes	Medium	High	Yes	Support	Yes	Yes	Flexible, non elastic	Yes

Included is a criterion called *“Monitoring”*, this column tries to answer whether or not active monitoring of the pneumatic system is necessary or not. Even though it reads as if certain concepts are more preferable to others, a final assessment is not yet possible and will not be performed at this stage. For this system the two operation points (cruise and drooped position) are the design-driver and most important benchmark. How good each of the concepts performs in this regard cannot be said without at least a detailed simulation of each concept. In chapter 8 a more in depth analyses of each concept was performed and a final selection is presented.

4. Characterization of the leading edge pneumatic actuators

As shown in the previous chapter the required pneumatic actuator for this application differs from more traditional actuators and can be best described as an inflatable tube or bladder. Using (pressurized) air as a working medium more or less enforces a circular active cross-section of the actuator. Obviously external additions can be made to the actuator to achieve other shapes. Nonetheless the pressurized shape of a flexible-walled actuator will always be very close to a circle, as the pressure in any contained space will always be the same everywhere (as long as the space is small enough, otherwise it will equalize depending on the speed of sound and shape of the container). Such a pneumatic actuator could ideally be folded together and have a very small deflated pack-size, while inflating to the required dimension. Pneumatic actuators transform a pressure difference into a mechanical displacement usually through a single point of contact. This motion can be linear or rotary.

The pneumatic actuators developed in this thesis work differently. Instead of being simply an actuator free of the influence of the surrounding structure, these rely heavily on the interaction with the structure and the deformation response thereof. Also these actuators do not have “single/1-dimenional” force/displacement attachment points but require a 2-dimensional contact to work. Instead of comparing them to pneumatic actuators a more accurate comparison would be to inflatable seals. Inflatable seals are usually used where:

- a seal of two surfaces, that move in relation to another or
- an uneven/changing (due to e.g. temperature) gap exists.

Based on the proposed actuation system, see Figure 1 and chapter 3, the basic design of the actuators was determined. The actuators should be cylindrically shaped and deliver their force/deformation perpendicular to their longitudinal axis. Additionally they needed to be collapsible or foldable to increase their deformation range, and also account for the tight design space. Two basic possibilities combine these characteristics. The difference between these two is in the end the deformation capability of the actuator skin. One design incorporates a bending-flexible, non-stretchable actuator skin. The other possible solution has a flexible and stretchable skin. Both variants have benefits and drawbacks, which will be explained in the following paragraphs.

The work principle of the actuators is, as stated, similar to inflatable seals. This means the force F_A of the actuator is directly related to the contact area A_c between the actuator and the actuated surface and the support surface. Additionally the contact area is also influenced by external forces F_E acting on it (e.g. airloads, weight, structural stiffness). This behavior can be summarized with the following expressions:

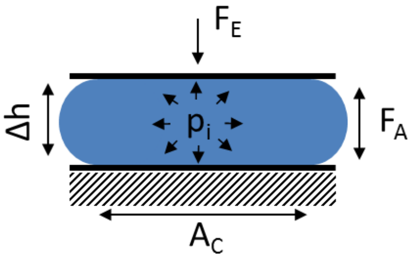

Figure 27: Work-principle of pneumatic actuators

$$\Delta h = \frac{C_u - 2A_c}{\pi} \tag{2}$$

$$A_C = \frac{F_E}{p_i} \tag{3}$$

with: Δh: stroke of the actuator; $[\Delta h] = m$

C_u: circumference of the actuator; depends on behavior of actuator-material; $[C_u] = m$

A_c: contact-area between structure and actuator; $[A_c] = m^2$

F_E: external forces; $[F_E] = N$

p_i: internal pressure of the actuator (accurately this is a pressure difference against p_o: surrounding pressure); $[p_i] = Pa$

Several assumptions have been made for these equations. The most important one is that the free segments (left and right, see Figure 27) are perfectly circular in such a way that Δh is the diameter of the half-circles. Additionally special note has to be made of C_u in these calculations. If the circumference of the actuator is constant C_u is a known quantity, but if the circumference changes under load, it becomes more complicated. If the skin material is stretchable, meaning a noticeable increase in diameter of more than 1%, than follows:

$$C_u = f(\Delta h, p_i, F_E, E_{skin}, t, l) \tag{4}$$

with: E_{skin}: stiffness of the skin in circumferential direction, not constant; $[E_{skin}] = \frac{N}{mm^2}$

t: thickness of the skin; $[t] = m$

l: length of the actuator; $[l] = m$

In detail this means the skin at the free sides of the actuator will stretch until an equilibrium between the internal pressure and the stiffness of the skin is achieved. This equilibrium has a direct impact on Δh because as the size of the actuator increases the contact area A_c increases as well. The force F_t acting on the skin is a tensile force (this formula is valid for stretchable or non-stretchable skin).

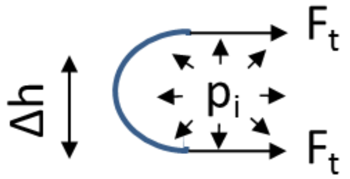

Figure 28: Skin-loading dependencies

$$F_t = p_i * \frac{\Delta h}{2} * l \tag{5}$$

Looking at the formula it becomes apparent that an increase in Δh leads to a linear increase in F_t. If as stated above a diameter increase of more than 1% is observed the behavior of the skin-material plays a crucial part in describing the deformation of such an actuator. To analytically describe the inflation of such an actuator it is therefore necessary to create a mathematical description of this kind of behavior. This description has not only to be able to describe large deformations but also include material specific behavior (in some cases non-constant material behavior). One such model that focuses on the deformation of similar actuators can be found in *[Müller et al., 2002].* In this the material is modeled by using a so called Mooney-Rivlin material model, see chapter 6.2.2, but for this thesis a description of the deformation behavior of only the actuators is not enough.

Most shape adaptive technologies aim for large deformations of a structure, while also creating a difficult to separate bond between system and structure, or actuator and structure. Traditionally the structure, system and the actuator would be mostly independent from each other. Adaptive technologies create highly integrated structure-systems symbiosis, demanding different in most cases more complex design rules. For most classical structures linear analytics or simulation would be completely sufficient e.g. a static stress analysis. Large deformations make the use of linear mechanics inaccurate, to the point of uselessness. Additionally a separate evaluation of different structural parts, which in classical systems could be performed as standalone solutions, might still be possible but would most likely lead to inaccurate solutions, as the interaction of different structures has a much higher influence here.

To be able to describe the proposed actuators and the system from a mechanical and material point of view the following paragraph and chapter will try to provide a background of the necessary tools. A very powerful and commonly used tool to describe the behavior of a material or structure under external load is the linear elasticity theory. To be able to use linear elasticity several criteria have to be met:

- infinitesimal strain or
- “small” deformations
- linear relation between components of stress and strain

Looking at the described actuation concepts in chapter 3 or the more detailed description of the actuators in this chapter it becomes clear that theses condition will not be met by some of the described components. Simply looking at the proposed actuator concept mentioned above already clearly demonstrates that large deformations and finite strain material models need to be used sometimes. As linear elasticity is a simplification of the more general nonlinear theory of elasticity, the general theory will most likely be more suitable to describe the expected behavior. Nonlinear theory elasticity is also called finite strain theory and forms a branch of continuum mechanics. Continuum mechanics are used to analyze kinematics and mechanical behavior of materials (regarded as continuous mass).

An in depth description of continuum mechanics will not be part of this work, only concepts relevant to understand the mathematical difference between linear and non-linear material definitions will be discussed in chapter 6. A complete explanation of continuum mechanics can be found in e.g. *Batra, 2006*; *Betten, 1993* and with a focus on material characteristics in *Westphal-Kay, 2005*. A short introduction with focus on description of deformation is also included in Appendix F.

It is important to understand that in mechanics displacements are divided in rigid body motion and deformation, see Figure 29. A rigid body motion describes the displacement (translation and/or rotation) of a body without changing its shape or size (in Figure 29 the vector from Q to q). Deformations describe the change of a body from its original shape/size to a new/current shape or size (in Figure 29 compare shape at Time=0 with Time=t). While the non-linear elasticity theory allows plastic deformations (permanent deformation), elasticity is generally understood to describe a non-permanent deformation. Specifically that the original shape is regained after the external influence is removed.

It is essential to note that it is possible to have a geometrically non-linear deformation without having finite strain in the material. It is therefore possible to use non-linear deformation theory with linear material models. So it is important to differentiate between linear or non-linear deformation theory and infinitesimal strain or finite strain theory and to understand for which type of problem which kind of models/theories have to be used. This differentiation will be picked up repeatedly over the course of this work and plays a significant part in the development of a simulation model of the actuators and the overall system.

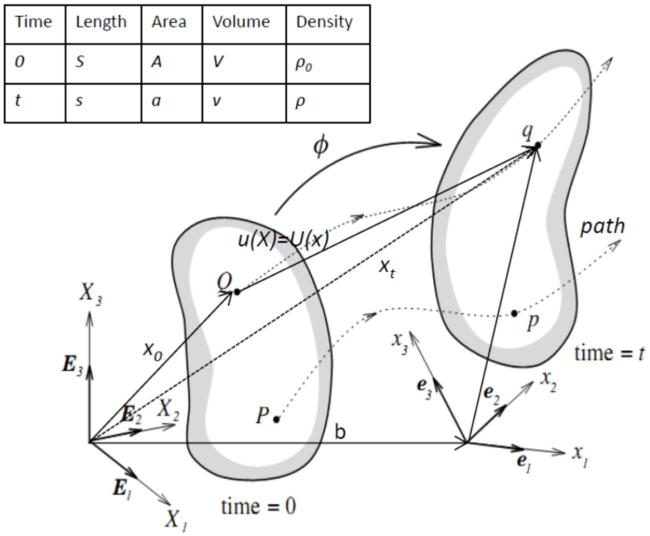

Time	Length	Area	Volume	Density
0	S	A	V	ρ_0
t	s	a	v	ρ

Figure 29: General Motion of a Deformable body
[Bonet et al., 1997]

4.1 Pneumatic actuator with flexible, non-stretchable skin

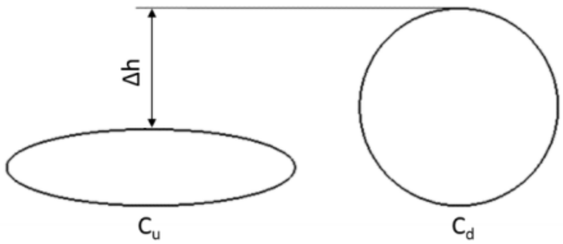

Figure 30: Exemplary deformation of a flexible, non-stretchable actuator (without external load)

This actuator design is simply put a cylinder with a constant circumference ($c_u = c_d$) but changing shape, due to pressure/force change (inside or outside), see Figure 30. The pliable skin enables this actuator to adapt to big changes in external geometry, as long as the inside pressure of the actuator is a lot smaller than the outside pressure. The benefit of such a design is that the maximum deflection remains constant, even if the pressure ratio changes. A very high inside pressure ensures a very stable actuation stroke. Additionally this ensures a predetermined actuation stroke regardless of external influences (as long as the outside forces are distinctly smaller than the inside pressure). This type of skin also enables the creation of a 3-dimensional actuator. This means that a controlled change in diameter is possible, as the inside pressure has no influence on the diameter of the actuator. This ability makes this kind of actuator ideal for applications which have a location-specific deflection requirement, with for example a span-wise change in geometry like a wing. One drawback of this type of actuator is that the support of the deformed structure from the actuator is minimal, as the actuator skin does not expand. This can result in local bulging or buckling of the deformed structure, if the structural stiffness is to low or too high.

4.2 Pneumatic actuator with flexible, stretchable skin

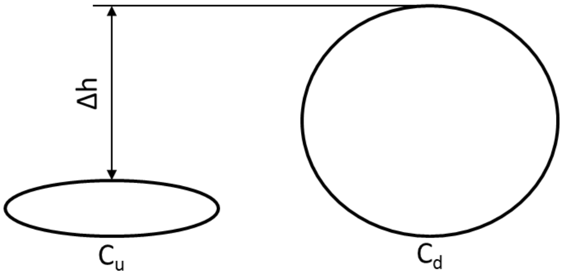

Figure 31: Exemplary deformation of a flexible, stretchable actuator (without external load)

For this actuator the basic design is also a cylindrical shape, but the circumference of the actuator depends on the pressure difference between inside and outside of the actuator and also the contact with the surrounding structure. In comparison to the previously described actuator the stretchable skin has the benefit to allow large changes in size of the actuator. Making this kind of actuator ideal for applications with very small (undeformed) design space but requiring large shape changes. In Figure 31 an example of such an actuator-cross-section is shown, Δh represents the stroke of the actuator; $c_u < c_d$. To be able to create such kind of an actuator materials and descriptions thereof have to be found which are capable of very large elastic deformations e.g. elastomers; see chapter 6.

5. Finite element modelling approach to adaptive structures

Finite Element Method (FEM) was originally developed for numerical calculations of structural problems that could not be solved using analytical methods *[Mathiak, 2010]*. FEM offers a wide variety of different approaches to simulate a certain problem. Therefore the creation of a representative simulation model of a structural problem is not always very straight forward and depends strongly on what type of answer is wanted. For this work a simulation of the multifunctional adaptive systems proposed in chapter 3 and the needed materials is essential to better evaluate the different concepts. Therefore the overall concept was analyzed and several simulations approaches were selected for detailed study. This included an analysis of the possible discretization of the structure with regard to different modelling techniques. Through this the scope out of the multitude of possible modeling approaches was reduced. Based on this preselection the model was fine-tuned and verified over the course of four steps. The first step was to numerically recreate the tensile and bending tests described in chapters 6.5. This recreation should ensure an accurate numerical representation of the developed flexible matrix composite (FMC)-material in the tested/simulated range. Secondly the inflation behavior of stand-alone actuators was simulated (using the results from the numerical tensile tests) and compared. With these two steps taken, the behavior of the selected material model and the selected simulation model was verified and could be adapted for the simulation of the complete system. Due to the complexity of the complete system these two steps were repeated using different approaches (always having the overall system in mind). The next paragraph gives a very rough outline of two distinct simulation methods used for numerical simulation of structural problems.

5.1 Consideration of two different finite element methods

FEM is an approximation method. For this method the structure in question is divided into a finite amount of elements (meshing). Each of these elements is similar in shape and size. Each element is described with nodes. The movement of these nodes builds the basis for the calculation. Based on the movement of the nodes, the deformation of the element can be interpolated. With this the strain for each element and therefore the whole structure can be calculated. The level of discretization of the structure decides on the level of accuracy of the solution. Areas of the structure with e.g. a rapid change in geometry may need a high level of discretization (fine mesh) to deliver a realistic local strain representation. Based on constituent models the stress-strain response of each element and the whole structure is calculated. The numerical solution of the closed equation-system, which describes the relationship between forces and displacement of each node, is the deformation response of the structure (based on known external stimuli).

FEM can be divided in static and dynamic modelling. The difference between dynamic and static modelling is the used equation for solving the problem. Static FEM solve a virtual displacement problem whereas dynamic FEM uses equations of motion to calculate the solution. Static modelling is further divided into linear and nonlinear problems. Dynamic models are typically either implicit or explicit models. Static models that try to capture and simulate non-linear material behavior (e.g. hyperelastic materials), large deformations or both have to use non-linear modelling. Deformations can be strain, rotation displacement or a combination. For strains larger than 3% linear simulations are usually no longer suitable *[Bathe, 2002].*

5.1.1 Static (non-)linear method

There are various ways to approach a linear static problem using FEM but in general the problem is first discretized and for the solution function different ansatz-functions are defined. If these functions and the boundary conditions are linear, the problem is overall linear and can be solved directly (as long as the number of decrees of freedom is not too large) by using e.g. a Gauss elimination principle (Galerkin method-differential equation). If the problem is nonlinear a different approach has to be taken e.g. like the Newton Raphson method, which uses linearization of the problem to find an approximation of the solution by iteratively trying to converge.

5.1.2 Dynamic explicit method

All dynamic methods use an equation of motion to calculate the system response. For nonlinear dynamic methods such as implicit or explicit methods this equation is used:

$$R = M\ddot{u} + I - P = 0 \tag{6}$$

with: $R =$ Residual-vector

$M =$ mass matrix

$\ddot{u} =$ acceleration vector

$I =$ Vector inner loads (contribution of stress, assumption: $I = I(u, \ddot{u})$)

$P =$ vector external loads (assumption: $P = P(u, \dot{u})$)

Dynamic explicit methods solve the problem by calculating the state of the system at a later time based on the state of the system at the starting time (implicit methods uses both states in one equation to solve the problem). In contrast to implicit methods the explicit methods do not need a stiffness-matrix or a conventional (equation) solver, as there are no iterations necessary. That means e.g. no Newton-Raphson- method has to be used. Dynamic explicit simulation methods are able to handle large deformation, non-linear material behavior as well as complex contact problems for quasi-static simulations *[Nasdala, 2010]* and can be used for:

- simulations of short duration dynamics like crash-simulation of stability problems with local buckling (no or small (local) mass-scaling)
- quasi-static problems like forming-processes and large contacts with friction (mass-scaling)

To simulate quasi-static problems the right time-scale with regard to density has to be found, additionally dynamic effects like oscillations of the whole model or parts thereof have to be suppressed. To suppress oscillations, the external energy has to be either introduced very slowly, the mass has to be very high or some sort of dampening has to be used. If the external energy is introduced very slowly, the overall simulation-time increases. Increasing the mass (so called mass-scaling) has to be performed carefully as it increases the inertia. A high inertia means that it takes time to get a part moving, but also time and energy to slow it down again. Therefore a high inertia can lead to unresponsive systems oscillations later in the simulation, as the high inertia stores energy once it is moving. To use damping to stabilize a simulation has always to be done with caution. Artificial damping suppresses energy, which otherwise would have let to “different” system response. So when dampening is used, the effect has to be carefully watched.

5.2 Preparation of the simulation model for the droop nose

As mentioned above to begin with it was necessary to analyze the overall simulation goal. With a clear simulation target in mind it is possible to divide a model into sub-components and sub-simulations that in the end would help the creation of the complex system-simulation. As a first step a conclusive discretization of the complete model is performed to set some boundaries for the sub-simulations. This also helps to identify potential challenges that need to be addressed in the sub-simulations.

The following paragraphs describe the preparation and segmentation of a complete model based on the actuation design concepts shown in chapter 3.1. Included are explanations of various approaches that did or did not work and why. In previous chapters nonlinear behavior of the material and the actuators was mentioned, this has a clear impact on the modeling approach. Therefore it can be said that the goal has to be a reliable simulation of the deformation behavior and the interaction of different subcomponents of the complete leading edge actuation mechanism. SI-units were used for all simulations, unless otherwise stated, see Table 4. For this work Abaqus was used as simulation software.

Table 4: Unit-definition for the FE-model

Length	Force	Mass	Time	Stress	Energy	Density
mm	N	tonne (10^3kg)	s	MPa (N/mm^2)	mJ (10^{-3}J)	tonne/mm^3

5.2.1 Discretization of the pneumatic droop nose

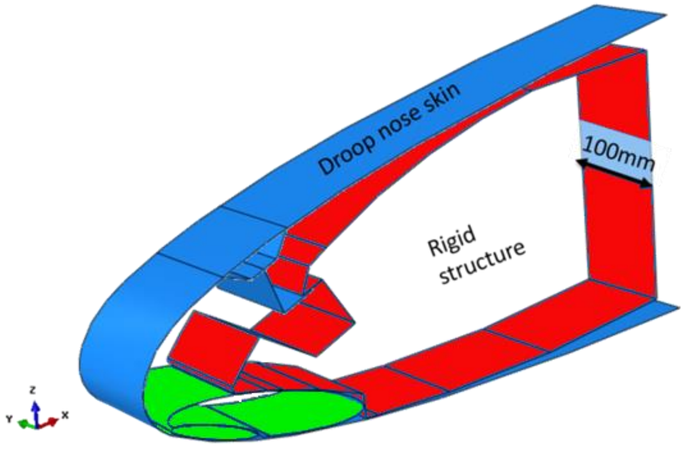

Figure 32: Simplified CAD-model of a droop nose actuation system

Looking at the overall system, compare Figure 32, the first step has to be to define what simulation outcome is desired. The setup of the simulation varies whether the focus is e.g. on overall deformation or on the stress-strain response of the rigid structure (red parts). Just comparing these two examples shows quickly that the basic setup can be quite different. To investigate the stress-strain response of the rigid structure the simulation of the actuators (green) and the skin (blue) is not absolutely necessary and could be replaced by proper boundary conditions. On the other hand to simulate the overall deformation response of the system, the deformation of the rigid structure should be negligible and can therefore be excluded from the simulation. If the rigid structure is excluded from the simulation the degrees of freedom of the overall system are drastically reduced and in parallel the simulation time.

An accurate simulation of the deformation behavior of the droop nose is the target result for the simulations performed in this work. Additionally the interaction of the different parts is a relevant result. It has to be mentioned, that the stress-strain response of the different components was not the focus here. In Table 5 the different components for the simulation are listed and rated based on their expected impact on the deformation behavior.

Table 5: List of relevant simulation parts and their impact on deformation

Part Name	Element	Impact deformation behavior
Actuators	Shell-elements (S4R)	High
Skin	Shell-elements (S4R)	High
Rigid Structure	Shell-elements (Rigid)	low
Front Spar	Represented with BC	none

To achieve the above defined simulation target the skin and the actuators have to be correctly represented in terms of deformation behavior, e.g. stiffness in the model. The rigid structure and the front spar will have only a very limited impact on the overall deformation behavior and will therefore be assumed to be rigid and simulated as such. With the target and the possible simplification in mind it is now possible to start a discretization of the different parts.

The droop nose skin is in relation to its length and width very thin and can therefore be model using shell-elements. The same logic applies to the actuators. Shell elements can be used as long as two dimensions are much greater than the third one and when the change of the analyzed feature (like stress) across this third direction can be neglected. For shell elements two different laws can be used Kirchoff or Mindlin-Reißer, whereas the first one is the more commonly used and the second is usually used for “thick” shells. An alternative to shell elements would be to use continuum-shells which are very good for large deformation simulation but cannot be used with hyperelastic material models (in Abaqus) *[Abaqus User Manual, 2015]*. Additionally the geometrical model generation for continuum-shells can be more complex and time consuming, very similar to solid elements. Generally the mesh-generation is usually easier for shell-elements than for solids, reducing the overall time needed to setup the simulation model. This does not have a big impact on singular modeling efforts but as for this study multiple geometrically different setups needed to be analyzed, it became relevant. As such this was another reason to use shells instead of solids. Abaqus offers a large variety of different shell elements to choose from; however two types stand out for the problem described herein. S4R (square)- and S3R(triangle)-shell elements are both appropriate for large-strain problems. However because the S3R-element has three nodes instead of 4 as the S4R element it is not very accurate for curved applications. Due to the “missing” node S3R reacts stiffer for bending applications than the S4R element (compare *Laulusa et al., 2005*). As booth the skin and the actuators are both inherently curved, the S4R element seems to be the likely candidate for the overall model.

In general S4R elements are not the best choice for problems with predominant bending strain, better would be S4 elements. As the dominant deformation of the skin and the actuators is bending, this has to be mentioned. However while the actuator-skin will experience bending strain during the deployment, the membrane strains are significantly higher and of more relevance for the modelling approach. As such S4R elements remain a good choice for the problem herein. A direct comparison between S4 and S4R elements showed almost a 50% increase in simulation-time with no change in results for this problem. This is further pointing towards S4R elements (see next paragraph for details).

Simulating simple tensile tests with a static nonlinear approach, works very well, as long as the deformations are not extremely large. The simulation of an actuator inflating and coming in contact with a wall or another actuator is another story. While it is possible to perform static nonlinear simulation of such a problem, the setup of these models is a lot more complicated (and becomes more so, the higher the part count). Especially problematic proved to be a stress-controlled deformation rather than a strain-controlled deformation. In direct comparison strain-controlled contact problems are a lot more robust as they eliminate the potential of rigid-body motion, which is not solvable using static simulation. This can be stabilized by adding artificial dampening modes to the model, which can falsify the results and have to be treated very carefully. Another option is to add a simulation-step which forces the contact to close and eliminates the initial separation of the two bodies. Unfortunately this process does not always work, and does not guarantee a stable simulation.

Besides selecting the element type it is important to understand the different challenges posed by the overall problem. For this the overall system is divided into separate parts to understand and prepare the simulation model accordingly. The following different effects have to be adequately represented:

- bending behavior of the skin (and the actuators)
- interaction between skin, actuators (with themselves) and rigid structure

This translates into four different sub-simulations that need to be completed and understood before the overall simulation can be performed:

- simulation/recreation of the tensile tests described in chapter 6.5.2/6.6.
- simulation/recreation of the 3-point bending test described in chapter 6.5.3/6.6
- simulation of single actuators and compared to inflation tests described in chapter 7.2
- simulation of the interaction of a deforming actuator and another structure

These four different simulations are in part depended on each other and the outcome of one can change the parameters of another. The biggest overall impact on any simulation is the selection of the solver. For structural simulations the solver is either a static solver or a dynamic solver. The most likely sub-simulation to address this issue is the simulation of the interaction of a deforming actuator with another structure. Herein large deformations, potential non-linear material behavior and large and changing contact problems come into play. Almost all full-scale models simulated in this work exhibit usually large deformations, contact problems and in some cases also non-linear material behavior, compare concepts presented in chapter 3.1. The deformation of the droop nose from cruise to landing configuration is not a dynamic process (> 1s); the geometrical change is allowed to take up to 30s. In terms of simulation this is a static or quasi-static deformation, as such a static solver should be able to handle the problem. Regrettably static solvers as mentioned above can become unstable when solving large stress-controlled (force-controlled) contact problems. As such is the case during the deployment of the leading edge the next paragraph addresses these issues and presents one possible solution for this particular case.

5.2.2 Selection of simulation method: static vs dynamic

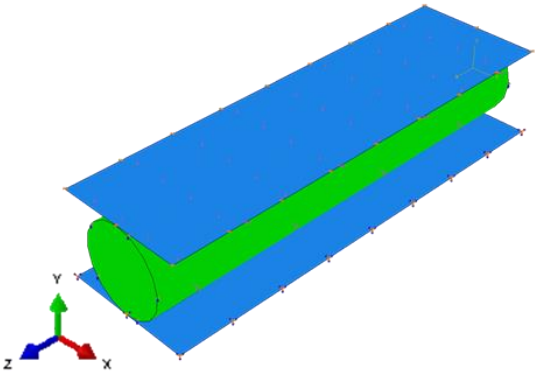

Figure 33: Generic model of large scale contact problem with an actuator (green)

To be able to select either one of the two possible methods (static or dynamic) a sub-simulation was performed. The model for this consists of a generic tube-segment and plates. The tube-segment represents the actuators and the plates can be either seen as the leading edge skin, another actuator or the rigid structure, see Figure 33. The general setup of the model can be seen in Table 6. Even if a finalized material model (representing the tensile tests) was not available at this point a linear orthotropic material formulation was used here, closely based on the linearized results from the tensile test. This general setup was used for both static and dynamic simulations.

Table 6: Overall model setup of sub-simulation "actuator tube in contact with plates"

	Actuator tube	Top plate (bottom plate is rigid)
Element Type	S4R Shell elements	S4R Shell elements
Element Size	5mm (side length)	10mm (side length)
Overall Dimensions	Radius of 40mm x 400mm	120mm x 400mm x 1mm
Material	Orthotropic (see Table 16)	Isotropic
Loading	0,03 N/mm² (internal pressure)	0,01 N/mm² (on top plate only)
Boundary Condition	Movement only x/y-direction/ Y-Rotation locked	Movement only y-direction / Rotation locked
Contact Parameters	Hard contact with allowed separation after impact / Coefficient of friction of 0,5	

The pressure difference in the plate and in the tube should result in a compression of the plate and a contact area between the plates and the tubes of 40mm x 400 m. At a width of 40mm the internal pressure of the tube equals the external pressure of the plates.

As a first simulation a simple single step static non-linear simulation was performed (non-linear due to expected large deformations). For this simulation the solver was unable to converge. Therefore a second step was introduced to “close” the contact and stabilize the simulation. This proved to be slightly better but did not result in a converged solution either. Only by introducing artificial dampening to the model, was the simulation able to converge to a solution. The overall process to find a workable simulation-model for this problem (tube in contact with a plate) using a static solver was extremely time-consuming and not very robust. As possible alternative a dynamic quasi-static simulation model was created based on the same parameters as shown in Table 6.

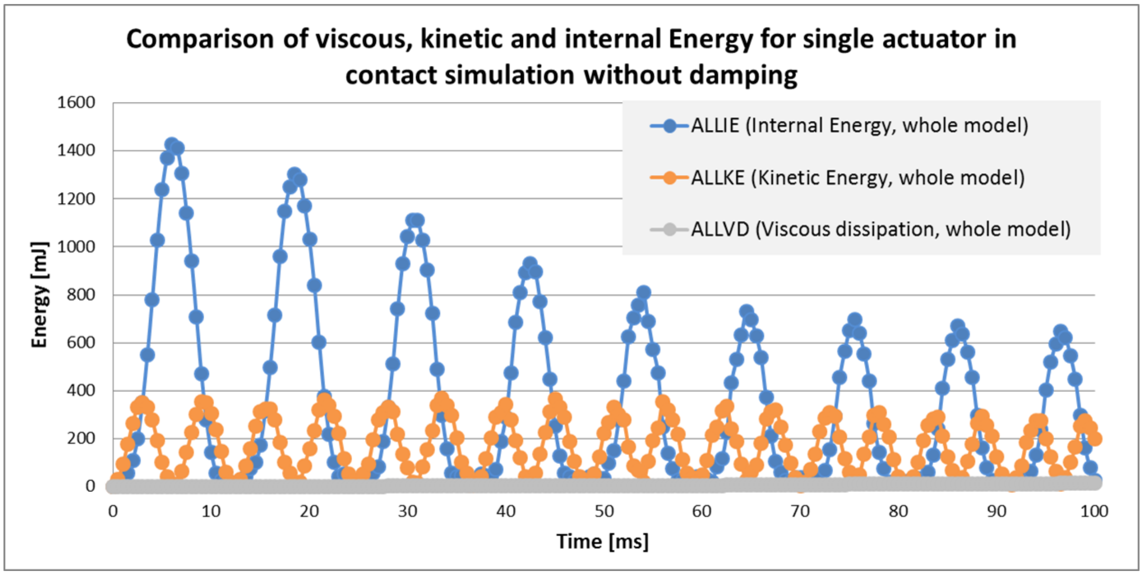

Figure 34: Comparison of energies during simulation of a single actuator in contact with plates (Step time: 100ms; no damping; instant application of force)

Quasi-static simulation is a dynamic explicit modelling variant that can be used to model static behavior using a dynamic solver as a baseline. This option offers certain benefits as dynamic simulations are more robust with regard to contact problems and large deformations. Rigid body motion in stress-based simulations is possible (this is due to the use of equations of motion). To ensure quasi-static behavior and with it the correct system-response certain precautions have to be taken. As the governing formula is based on acceleration the system can easily start to oscillate if the force/deformation is applied to quickly (see Figure 34) (as simulation models lack natural forms of damping like air friction) or will not move at all if the applied force is too small and too fast to overcome the inertia of the system. It is therefore critical to achieve the correct balance between inertia of the system, applied force and time to result in a quasi-static behavior. If one of the three elements does not fit with the rest the resulting deformation cannot be assumed to be a quasi-static response of the system. Finding the right balance of the three aspects is explained in the following for the generic model shown in Figure 33 and detailed in Table 6.

Usually the setup of a quasi-static analysis with a dynamic-explicit solver starts by looking at the first structural mode of the part that is being deformed. With this the loading speed for an accurate static response can be estimated (additionally the speed of sound of the deformed structure has to be known, as a rule of thumb the deformation speed should not exceed 1% of that speed) *[Abaqus User Manual, 2015]*. The loading speed directly influences the step time.

Here an actuator interacts with two plates. The deformation of both plates is completely blocked, the top plate can only move in y-direction. Therefore the structural modes of the plates are completely suppressed and have no relevance for this simulation. With this the modes of the actuator are the only relevant ones. The first two modes of the actuator are at 82,7Hz and 114,9Hz. As the interaction with the plates, the boundary-conditions and the loading suppress almost all modes, a baseline step-time of 100ms was chosen. This is additionally based on the fact, that a typical quasi-static simulation does usually not run longer than 1s and if there is no large kinetic energy to be expected even shorter step times are usual. (As is the case for this model (hardly any rigid body motion)).

As mentioned the external loading has to be applied over a certain period of time if a quasi-static response is the target. If the loading is applied instantaneously the deformation response is not a static response but rather a localized deformation in the contact area, additionally due to a lack of damping the complete model is excited and starts oscillating, see the relevant energy-response in Figure 34. The oscillation can be correlated with the behavior of the kinetic energy (the almost constant peak value is the result of missing damping effects). Important to understand is that the graphs in Figure 34, Figure 35 and Figure 36 do not show the complete energy (ETOTAL) of the model, here only the for this comparison relevant energies are shown. As an instantaneous loading does not qualify for quasi-static behavior a smooth step loading (see Figure 83) was introduced in the model, leading to the system response as shown in Figure 35.

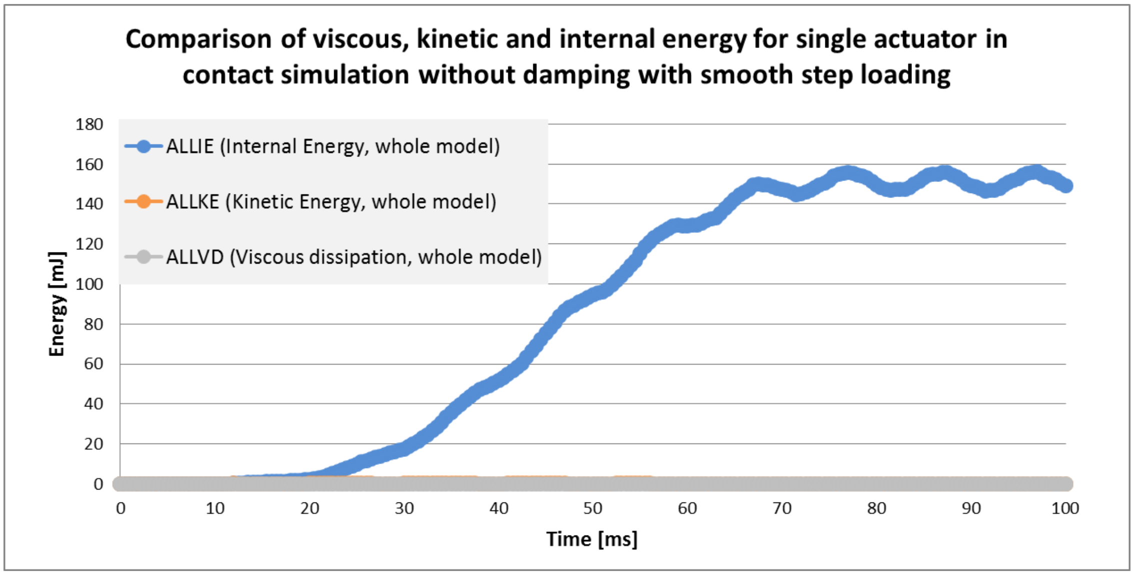

Figure 35: Comparison of energies during simulation of a single actuator in contact with plates (Step time: 100ms; no damping; smooth step loading) (ALLVD covers ALLKE curve, almost identical)

Here the proportions between internal energy (total strain energy) (ALLIE), kinetic energy (ALLKE) and viscous dissipation (ALLVD) are in the correct range for a quasi-static system response (ALLKE << ALLIE *[Abaqus User Manual, 2015]*). Unfortunately oscillation of the internal energy is still occurring. The effect of this oscillation is not all of the available energy is going into deformation or strain energy, falsifying the deformation response of the overall system. An option to control the oscillation behavior is to introduce artificial damping into the system very carefully, as too much damping would “absorb” too much energy and possibly falsify the results. Abaqus offers viscous pressure as a damping mechanism.

In Abaqus viscous pressure can only be applied to surfaces. It is able to locally and dynamically absorb pressure waves on free surfaces of the model, with a maximum set value. If no pressure wave is detected the damping effect is zero. The damping is adjusted automatically up to the maximum set value. Viscous pressure only applies damping on the surface of bodies. The value for viscous pressure is case depended and has to be calculated individually for each problem

$$c_v \leq 0{,}02 * \rho * c_d \tag{7}$$

with: c_v: viscous pressure coefficient; $[c_v] = \frac{N}{mm^2} * \frac{s}{mm}$

ρ: density of the surface/relevant material; $[\rho] = \frac{tonne}{mm^3}$

c_d: dilatational wave speed of the material; $[c_d] = \frac{mm}{s}$

For isotropic materials:
$$c_d = \sqrt{\frac{\lambda + 2\mu}{\rho}} = \sqrt{\frac{E\,(1+\nu)}{\rho(1+\nu)(1-2\nu)}} \tag{8}$$

with: λ, μ: Lamé constant; $[\lambda, \mu] = \frac{N}{mm^2}$

E: E-Modulus of the material; $[E] = \frac{N}{mm^2}$

ν: Poisson ratio; $[\nu] = 1$

As the material used for these simulations is not isotropic c_d is not constant, but rather depended on the directionality of the material. As such various calculations were performed to determine the viscous pressure coefficient using the directional E-moduli (see Table 12 for the actuators and Table 23 for the skin). These calculations showed that the viscous pressure coefficient should not be larger than 7e-05 N/mm² s/mm. For this particular model the viscous pressure was set to 1e-6 N/mm² s/mm on the tube and the plates (always in the opposite direction of the expected motion). This introduction of damping resulted in a stable and accurate deformation of the model (therefore no further simulations were performed with a different viscous pressure coefficient). Figure 36 shows the corresponding energies. Important to make note of is that the viscous dissipation does increase in comparison to the previous simulation without damping (see Figure 35) but is still only a fraction of ALLIE. The contact area between the plates and the tube is with 41,3mm x 400mm slightly larger than the expected (40mm x 400mm) but still within expectable tolerances, as the element size of the tube is 5mm degrading the overall resolution, see Figure 37. A refined mesh (2,5mm element length) increased the accuracy of the result (contact area 40.8mm x 400mm) but also increased the simulation time more than 5 times (5mm elements = 831s CPU time / 2,5mm elements = 5235s CPU time). Despite the increase in runtime, deformation accuracy is a key issue for the overall simulations. Therefore the element size for the actuators in the overall simulation will be set to 2mm. Table 7 summarizes the resulting loading parameters for the in model shown in Figure 33 and described in Table 6.

Table 7: Finalized simulation parameters

Part	Step Time	Loading	Viscous Pressure
Actuator	100ms	Smooth step (80ms)	1e-06
Plate		Smooth step (80ms)	1e-06

To ensure that the simulation represented a static response of the model a final simulation was performed with a step time of 120ms without any other changes. The deformation response of the structure remained exactly the same. Additional this model was also used to investigate the difference (if any) for this kind of problem of S4 and S4R. As such the simulation was rerun with S4 elements, which showed the identical behavior as the simulation using S4R elements. The only notable difference was the computational time which more than doubled (S4R = 831s / S4 = 1786s). A representative input-file for the different models presented in this paragraph can be found in appendix I.

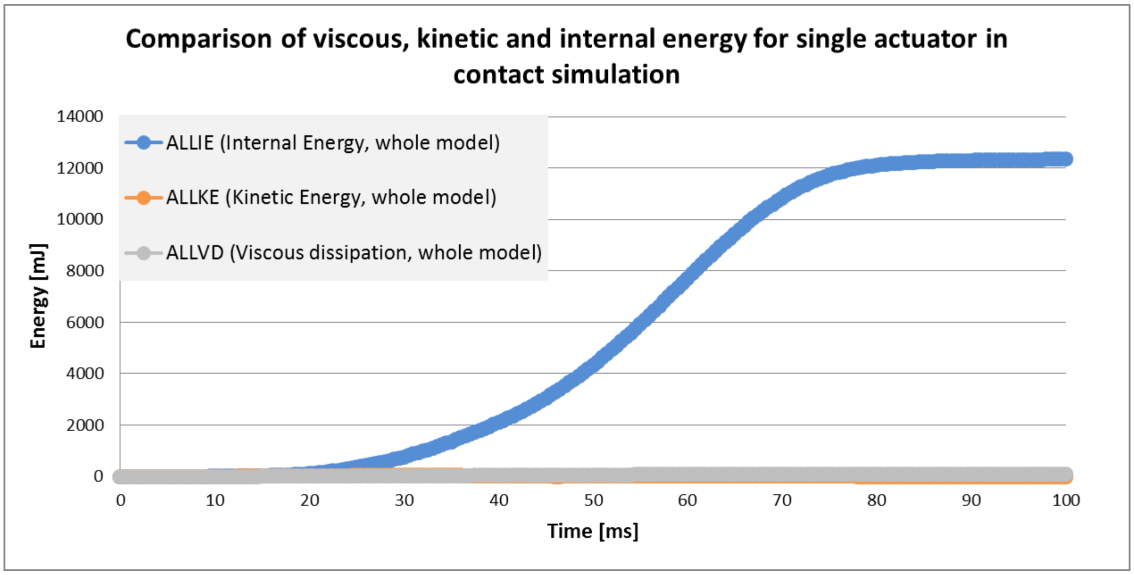

Figure 36: Comparison of energies during simulation of a single actuator in contact with plates (Step time: 100ms; Viscous pressure: 1e-6) (ALLVD covers ALLKE curve, almost identical)

The simulations performed show a clear benefit of using a quasi-static dynamic solver for a problem as shown in Figure 33, while also highlighting how such a model has to be set up.

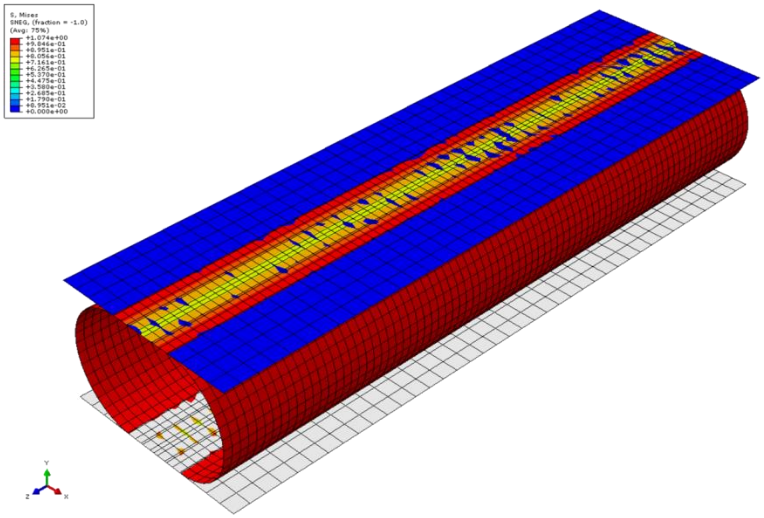

Figure 37: Deformation and stress response of generic tube simulation at 100ms step time, smooth step and damping

6. Material development for pneumatic actuators[2]

As mentioned repeatedly, see chapter 3 and 4, for the different actuation concepts certain material behavior is required. The actuator material e.g. has to be flexible, meaning very low bending stiffness. For some concepts a highly elastic-stretchable skin material might be beneficial. Additionally all concepts call for very large elastic (meaning non-plastic) deformation of the actuators (and the tensile-belts). For pneumatic actuators the skin material has to be airtight. Also large deformations have to repeatedly be performed without (fatigue-) failure. Also as for almost all concepts any structural support was removed from the skin, the actuation system has to additionally provide this “support” function, or at least enable the support structure to it. This means the actuators have to be able to provide a certain “stiffness”, at least directionally.

Most standard aerospace materials are designed to be very stiff, especially composites used for primary structures. When looking at the requirement list, see Table 1, things like e.g. tires and inflatable boats come to mind. While tires are made mostly of rubber, they are not very stretchable (and should not be), which is due to a steel-wire and/or fabric reinforcement. Rubber-tires are very robust and heavy, but in general steel and fabric reinforced rubber fulfills a lot of the stated requirements. Missing is a potential stretch-ability as well as a more light-weight solution. Over the years research has been performed on this, see: *[Murray et al., 2007; McKnight et al., 2010; Shan et al., 2005, Coffey et al., 2007; Peel, 1998]*.

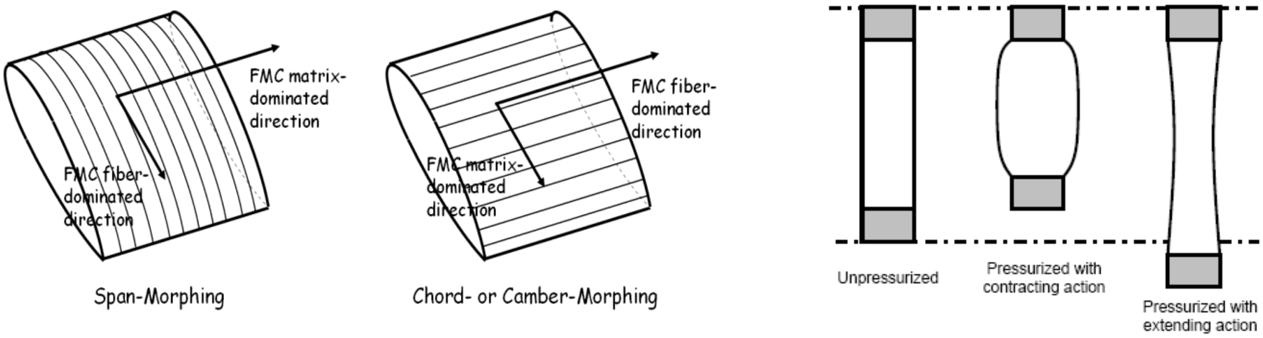

Figure 38: Flexible Matrix Composite (left figure: *[Murray et al., 2007]* / right figure: *[Shan et al., 2005]*)

Composites with a rubber-like matrix are called flexible matrix composites (FMC). As known from classical fiber reinforced plastics a variation in the fiber-layup (ply-angle) has an influence on the deformation under load (mechanical or thermal). An example of this in use for FMCs can be seen schematically e.g. in Figure 38, demonstrating the actuation potential of this type of material. On the right hand side of the figure a so called pneumatic muscle is shown, herein the fiber angle determines whether a contracting or extending action is performed under pressure.

---

[2] Some content of this chapter has been published by the author previously in *[Kirn et al, 2011 Journal of Structural Integrity; SAMPE-SETEC 11 Conference]*

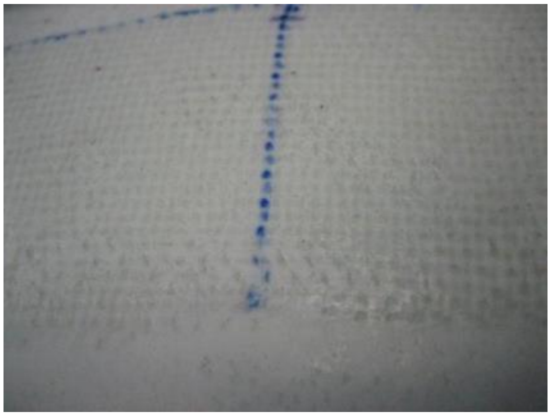

Figure 39: Woven glass-fibers in a TPE matrix

In this chapter a focus is first placed on creating an understanding of the manufacturing of such kind of material, looking at several different matrix and fiber materials and combinations with different production processes. As such in the next paragraph a short introduction on elastomers and on composites is given, included is also a short analytical description of composite materials. In the above stated references a multitude of possible material combinations and several possible production techniques were described. Unfortunately all remained in a laboratory setting or are not easily adaptable to large scale manufacturing. As the actuators are meant for use on passenger aircraft a more industrialized production method was to be preferred. With this condition in mind the focus during this material and production study was on proven and used production processes already in use by the (aircraft) industry. Also a material with good handling qualities similar to e.g. carbon-fiber prepreg would be preferable. Based on these preliminary constrains several possible materials for matrix and fibers as well as several production processes were preselected. As matrix material several types of material came into consideration all of them elastomers, such as natural rubber, silicone rubber and thermoplastic elastomers (TPE), see Figure 39 Each matrix material comes with wide variety of properties, but the foremost requirement for this study was that the matrix material could be liquefied enough to impregnate the fiber material thoroughly. Based on experience a viscosity of 100mPa*s or less is needed to successfully impregnate dry fiber material using the standard infusion techniques (e.g. vacuum infusion process). At the same time different materials had to be evaluated and a material combination for the actuator had to be found. The following two paragraphs provide some in depths information on the proposed materials (elastomers and composites) and information on the classical analytical description of composites. This is done to set a reference for the tests and create an understanding of the observed behavior.

6.1 Properties of thermoplastic elastomers

In this paragraph a very rough overview of different elastomers mainly thermoplastic elastomers will be given. Elastomers as well as thermoplastics are polymer materials. They are therefore macromolecular materials, whose molecules are created from chaining of base-units (monomers). Figure 40 gives an overview on the different families of polymers. The focus in this work is on polymers with elastomeric as well as thermoplastic behavior.

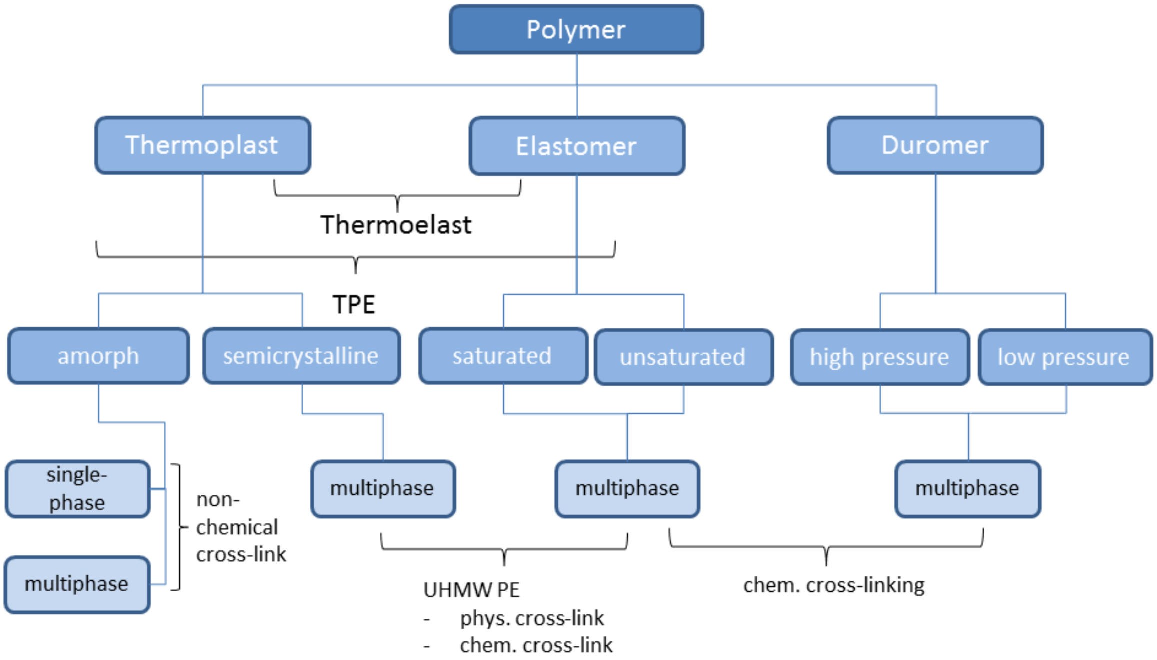

Figure 40: Overview Polymer *[Dominighaus, 2008]*

The difference between elastomers and thermoplast can be seen in Figure 41, a special case of elastomers are so called thermoplastic elastomers. Thermoplastic elastomers are plastics, which behave like conventional elastomers under room temperature but become plastic (almost liquid) at elevated temperature and return to an elastic behavior after cooling. This behavior is made possible by the lack of chemical cross-linking between the molecules, and enables e.g. welding after manufacturing. TPEs are two- or multi-phase polymers. Instead of cross-linking some TPEs have crystalline domains where one kind of block co-crystallizes with another block in adjacent chains.

Natural rubber or silicone based elastomers on the other hand are both thermoset elastomers, see Figure 41, right hand side. The raw material undergoes plastic deformation (final shape) and the application of heat locks the material into shape. Detailed information on rubber and silicone can be found in e.g. *Nagdi, 1981 or Dominighaus, 2008.*

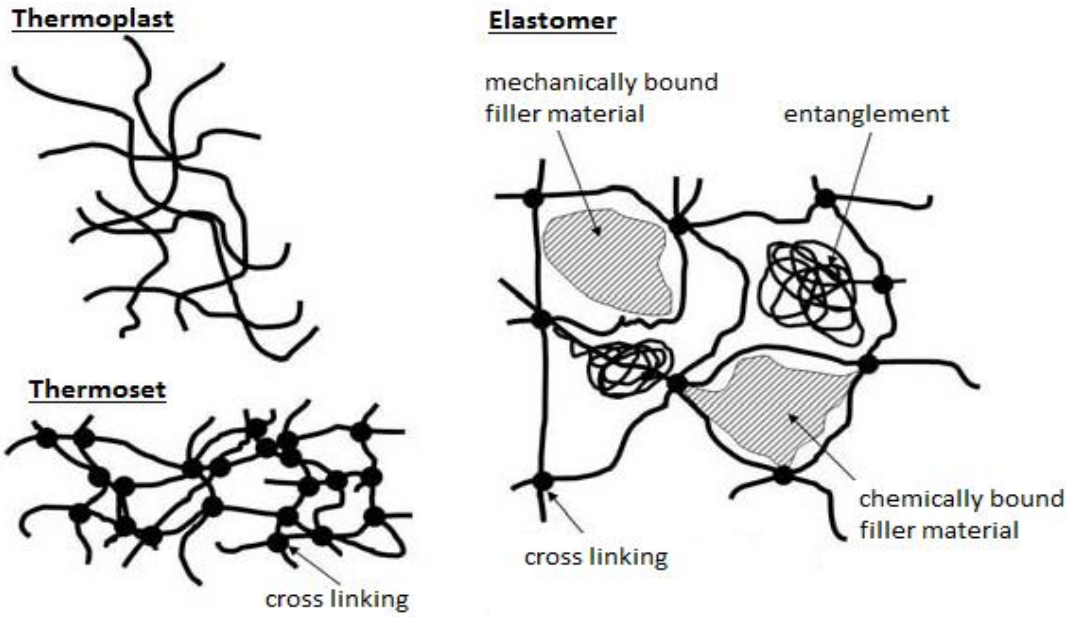

Figure 41: Macromolecular structure of thermoplast, thermoset and elastomer *[Westphal-Kay, 2005]*

TPEs are so called Polyblends, a mixture of different finished polymers. There are six different classes of commercial TPEs:

- Thermoplastic copolyester (TPE-E or TPC)
- Thermoplastic polyamids (TPE-A or TPA)
- Thermoplastic polyurethanes (TPE-U or TPU)
- Elastomeric alloys (TPE-v or TPV)
- Polyolefin blends (TPE-O or TPO)
- Styrenic block copolymers (TPE-S or TPS)

All TPE's in the list are block-copolymer except the two underlined ones, they are elastomeric alloys.

The limiting factors of the free movement of chain-segments of an elastomer are the covalent and intermolecular forces. It is still possible that chain-segments can move and slide in relation to another. External forces on an elastomer move the molecule-chains into "orderly" positions. With relaxing of the external force, the molecular-chains try to return to their original position. This behavior is called entropy[3] elasticity *[Benedix, 2003* and *Tobolsky, 1967]*.

---

[3] Entropy can be taken as a measure of disorder of a system. In statistical mechanics entropy S is described as:

$$S = k_b \, ln \, \Omega \qquad (9)$$

with: k_b : Boltzmann constant; $k_b = 1{,}38066x10^{-23} \frac{1}{K}$
Ω: describes the number of microstates of a macro-state
Based on the second law of thermodynamics the entropy of an isolated system never decreases, it rather strives for a state of equilibrium which is the state of maximum entropy

Due to their special molecular-structure TPEs have a rubber-like behavior, but reheating and reapplication of shear-forces makes a reshaping/deformation of the material possible. This also leads to a high recyclability of the material. TPE has very fast cycle-times during production and can be processed with almost any polymer-usual production process, e.g.: Injection moulding, extrusion, thermoforming, heat-welding or blow-moulding.
The main properties of a TPE are defined by the matrix, a coherent soft-phase; the dispersed hard-phase achieves the modification.

TPE act like rubber at temperatures between -20° and +120°C, and like thermoplasts at the melting range of 160°-180°C. They are available in a wide range of hardness, between A4-A95 shore. Important to note is the relation between stiffness and temperature. In general the increase of temperature leads to a decrease in stiffness of the TPE *[Domininghaus, 2008]*. More information on TPE can also be found in *[Babu et al., 2011].*

6.2 Comparison: Elastic and hyperelastic material models

The relationship between stress and strain can be mathematically described using material laws. Material laws usually assume perfect material behavior. One of the most well-known (elastic) material laws is Hooke's law. As a material law describing elastic behavior the Hooke's law, as all elastic laws, only describes time-independent material behavior. Elastic material laws are not able to take things like hysteresis into account. Therefore the load-history is not represented in calculated stress-strain plots. It is assumed that if the external forces are taken away the elastic material will always return to its original configuration. The absorbed work/energy during the deformation is completely released upon load removal.

6.2.1 Hook's law

The Hook's law was first published in 1660 in Latin, stating that "the extension is proportional to the force" and was originally describing the deformation behavior of springs. For continuous media this can be expressed mathematically as:

$$\boldsymbol{\sigma} = E * \boldsymbol{\varepsilon} \qquad (10)$$

with: $\boldsymbol{\sigma}$: stress-tensor; $[\boldsymbol{\sigma}] = \frac{N}{mm^2}$

E: modulus of elasticity; $[E] = \frac{N}{mm^2}$

$\boldsymbol{\varepsilon}$: strain-tensor; (see Appendix F: technical strain)

As can be seen in equation 5 Hook's law assumes perfect linear relation between (external) loading and response of a body and is therefore unable to reproduce plastic or any other type of non-linear stress-strain behavior.

A special case of elasticity is hyper elasticity. Hyperelastic material models are needed to mathematically describe the behavior of materials such as elastomers (e.g. rubber, silicone), biological soft tissue etc. To be able to describe hyperelastic behavior an elastic potential has to be introduced. The stress is the result of a partial differentiation of the potential function with respect to the strain. This potential describes the strain energy density W.

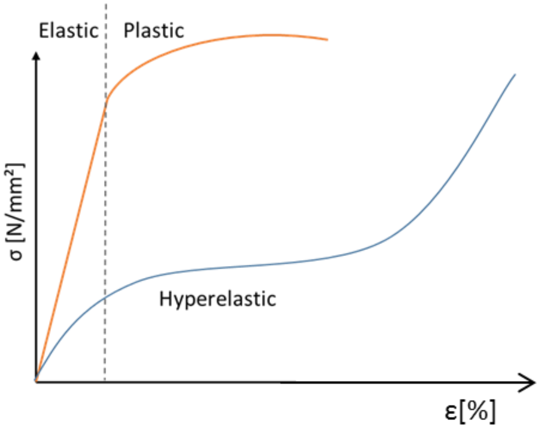

Figure 42: Qualitative comparison of elastic vs. plastic vs. hyperelastic behavior

The strain energy density is the volume based energy, which is stored in a material due to deformation.

$$\boldsymbol{S}_{ij} = \frac{\delta W}{\delta G_{ij}} \tag{11}$$

with: $\boldsymbol{S}_{ij}$: 2nd Piola-Kirchhoff stress tensor; $[\boldsymbol{S}_{ij}] = \frac{N}{m^2}$

W: strain energy density; $[W] = \frac{N}{m^2}$

$\boldsymbol{G}_{ij}$: Green-Lagrange deformation tensor; $[\boldsymbol{G}_{ij}] = 1$

For the calculation of the strain energy density W different material models exist, some of them will be discussed in the following paragraphs.

All hyperelastic material models are based on a change of the strain energy density W. Usually the strain energy density is shown as function of the three invariants I_i of the Green deformation tensor (also called right Cauchy-Green deformation tensor), see Appendix F, or as function of the elongation along the principal axis λ_i (principal stretches). The use of invariants makes the results independent of the used coordinate system.

$$W = W(I_1, I_2, I_3) \tag{12}$$

with: $I_1 = \lambda_1^2 + \lambda_2^2 + \lambda_3^2$ (13)

$I_2 = \lambda_1^2\lambda_2^2 + \lambda_2^2\lambda_3^2 + \lambda_3^2\lambda_1^2$ (14)

$I_3 = \lambda_1^2\lambda_2^2\lambda_3^2$ (15)

λ_i ; $i = 1,2,3$ aspect ratio in principal coordinates; main strain of the Chauchy-Green Deformation Tensor; $[\lambda_i] = 1$

I_i ; $i = 1,2,3$: Invariants of the Cauchy-Green deformation tensor; $[I_i] = 1$

Looking at a cutout cube of material (as e.g. Appendix F Figure 118):

- I_1 represents the change in length along the body diagonal
- I_2 represents the change of the surfaces of the cube and
- I_3 represents the change of volume of the cube.

From the partial derivative of the strain energy density function W with regard to the aspect ratio in principal coordinates λ_i, result the true main stresses t_i along the direction i.

$$t_i = \lambda_i \frac{\delta W}{\delta \lambda_i} = \lambda_i \left(\frac{\delta W}{\delta I_1} \frac{\delta I_1}{\delta \lambda_i} + \frac{\delta W}{\delta I_2} \frac{\delta I_2}{\delta \lambda_i} + \frac{\delta W}{\delta I_3} \frac{\delta I_3}{\delta \lambda_i} \right) \quad (16)$$

with: $t_i, i = 1,2,3$: true main stresses; $[t_i] = \frac{N}{m^2}$

(for λ_i, W and I_i see above)

The strain energy density W describes ideal-elastic material behavior, assuming homogeneous, isotropic, incompressible and purely elastic materials. If an incompressible behavior is assumed the third invariant turns into 1, ($I_3 = 1$ as the volume stays constant).

These assumptions for the formulation of a constitutive law disregard viscoelastic effects such as hysteresis and stress relaxation. It is therefore necessary to regard certain boundary conditions:

- Under cyclic loading there can be no difference between first loading and subsequent ones
- The stress-strain curve is independent of the maximum experienced stress
    - W is independent of the "stress-history" of the material
- The stress-strain-curve is reversible disregarding the direction of loading
- Plastic behavior cannot be represented
- Temperature and humidity effects cannot be represented

To remedy this shortcoming of the purely analytical material description two groups of models are used. One option to create such a model is to choose a phenomenological approach. Here a mathematical formulation is chosen to fit existing data (from e.g. coupon testing). This approach has the inherent danger, that the resulting formulation may not be able to represent new test data. The second option is the statistical approach, which takes the molecular structure of the considered material into account. The phenomenological approach is a completely mathematical approach, having no direct connection to the physics involved. As the material parameters for the statistical approach are usually very difficult to obtain, the phenomenological approach is used more commonly, despite its drawbacks. In Table 8 several different phenomenological hyperelastic material models are presented and information on their application is summarized.

Table 8: Hyperelastic material models (phenomenological approach)

Model Name	Details
Mooney-Rivlin	- not good for pressure - disregards re-stiffening of material at high strains - good results up to 100% strain
Ogden	- uses a variable shear-modulus - allows compressible material behavior - up to 700% strain
James-Green-Simpson	- uses a variable shear-modulus - can become unstable
Fung	- allows anisotropic materials
Holzapfel	- assigns separate strain energy functions to different layers

6.2.2 Mooney-Rivlin model

Mooney developed a general approach for the stress-strain relationship of a hyperelastic material under the assumption, that the material is isotropic, incompressible and hysteresis effects can be neglected. Monney's approach is one of the most often used to calculate the strain energy density W. Rivlin later expressed the model in terms of invariants.

$$W = C_{10}(\lambda_1^2 + \lambda_2^2 + \lambda_3^2 - 3) + C_{01}(\lambda_1^2\lambda_2^2 + \lambda_2^2\lambda_3^2 + \lambda_3^2\lambda_1^2 - 3) = C_{10}(I_1 - 3) + C_{01}(I_2 - 3) \qquad (17)$$

with: C_{10}/C_{01} : material constants; $[C_{10}] = [C_{01}] = \frac{N}{m^2}$

λ_i : aspect ratio in principal directions; $[\lambda_i] = 1$

$I_{1,2}$: first and second invariants of the Chauchy-Green deformation tensor; $[I_{1,2}] = 1$

Based on the above mentioned boundary conditions W has to be symmetrical with regard to the aspect ratio λ_i. As a result of the above written formulation the following stress-strain-relationship can be formulated:

$$t_i - t_j = 2(\lambda_i^2 - \lambda_j^2)(C_{10} + \lambda_k^2 C_{01}) \qquad (18)$$

with: t_i / t_j : true principal stresses; $[t_i] = [t_j] = \frac{N}{m^2}$

For uniaxial tensile-/compression load which results in a strain of -50% - 100% the Mooney approach yields a good agreement between test results and calculated data. Problematic is the point of contraflexure of the stress-strain curve, which this approach cannot represent.

6.2.3 Ogden model

The depicted form is able to account for compressibility, in case of incompressibility $\lambda_3^{\alpha_p}$ is replaced by $\lambda_1^{-\alpha_p}\lambda_2^{-\alpha_p}$ [Odgen, 1972].

$$W(\lambda_1, \lambda_2, \lambda_3) = \sum_{p=1}^{N} \frac{\mu_p}{\alpha_p}(\lambda_1^{\alpha_p} + \lambda_2^{\alpha_p} + \lambda_3^{\alpha_p} - 3) \qquad (19)$$

with: λ_i : aspect ratio in principal directions; $[\lambda_i] = 1$

α_p, N: material constants; $[\alpha_p] = [N]$=1

μ_p: material constant; $[\mu_p] = \frac{N}{m^2}$

As mentioned above, all of these models assume isotropic material behavior. As the material behavior described for the actuators is at least orthotropic this assumption is no longer valid. There are a few models that try to compensate such kind of behavior, e.g.: Fung *[Fung, 1993]* and Holzapfel-Gasser-Ogden *[Gasser et al., 2006; Holzapfel, 2006, Holzapfel, et al., 2005; Holzapfel et al.; 2009]*.

6.2.4 Fung model

The Fung model was developed to describe the deformation-behavior of biological tissues. These tissues can be described as a fiber-matrix composite. Collagen, elastin and ground substance are surrounded by extracellular matrix. The behavior of biological tissues can be approximated with hyperelastic models (after preconditioning to a load pattern). Therefore the Fung model can be called a hyperelastic material model, even so it wasn't developed as such. It can be used for full anisotropic as well as orthotropic behavior. It is completely phenomenological based.

$$W = \frac{1}{2}\left[a_{ijkl}E_{ij}E_{kl} + c\left(e^{b_{ijkl}E_{ij}E_{kl}} - 1\right)\right] \tag{20}$$

with: E_{ij}: components of quadratic forms of Green-Langrange strain tensors; $\left[E_{ij}\right] = 1$

a_{ijkl}: material constants; $[a_{ijkl}] = \frac{N}{m^2}$

c: material constant; $[c] = \frac{N}{m^2}$

b_{ijkl}: material constant; $[b_{ijkl}] = \frac{N}{m^2}$

6.2.5 Holzapfel-Gasser-Ogden model

The HGO-model is built on the idea of the Fung model but additionally takes into account two different orientations and types of fiber. The model is split into two parts; isotropic and anisotropic behavior and depends on the fiber dispersion factor κ .

$$W = \frac{c}{2}\left(\hat{I}_1 - 3\right) + \frac{k_1}{k_2}\left\{exp\left[k_2\left(\kappa\hat{I}_1 + (1-3\kappa)\hat{I}_4 - 1\right)^2\right] - 1\right\} \tag{21}$$

with: $I_{1,4}$: invariants of the right Cauchy-Green strain tensor; $\left[I_{1,4,6}\right] = 1$

k_1; c: material parameter; $k_1 > 0, c > 0$; $[k_1;\ \mu] = \frac{N}{m^2}$

k_2: material parameter; $k_2 > 0$; $[k_2] = 1$

κ: fiber dispersion factor, $[\kappa] = 1$

$\kappa = 0$ for perfectly aligned fibers,

$\kappa = 0{,}226$ for full anisotropy,

$\kappa = \frac{1}{3}$ for isotropic behavior

It is assumed that the fibers are not able to support compressive stresses; therefore the anisotropic term contributes only when the fibers experience tensile stress.

In Figure 43 some of the previously presented models are compared to test-data from a tensile test. It shows the different responses of the models and gives a rough overview which material behavior they can reproduce.

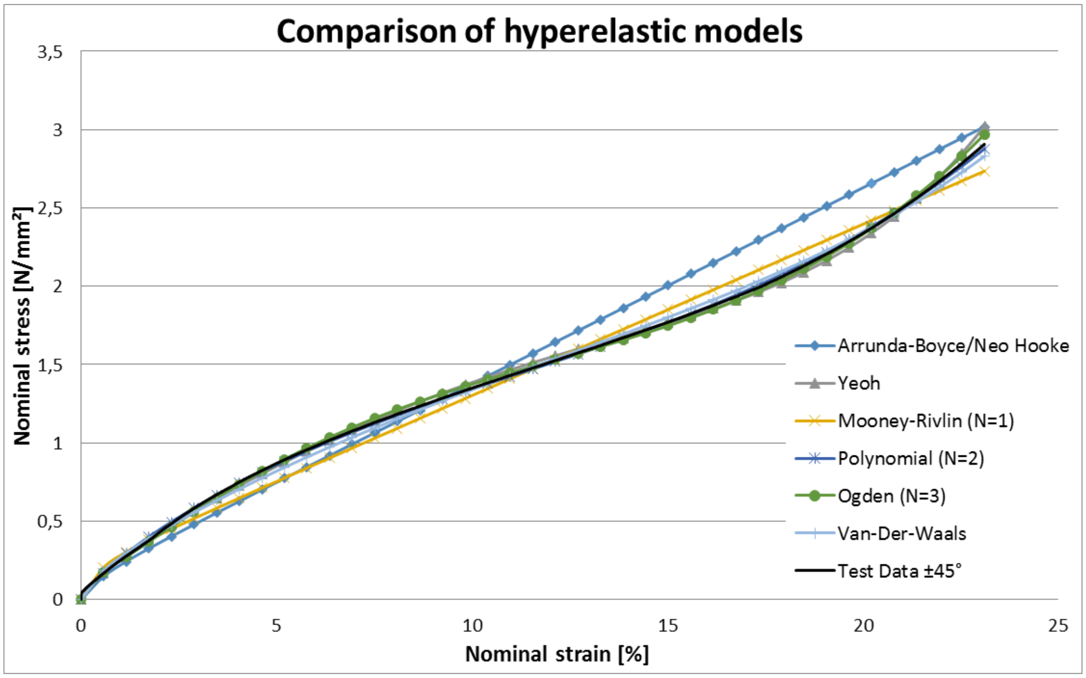

Figure 43: Comparison of hyperelastic models (based on uniaxial test data from ±45° TPE-CFRP test specimen)

6.3 Fiber composites

Fiber composite are part of the family of composite materials, which consist of two or more discrete materials. The most commonly known representatives of fiber composites are fiber-reinforced plastics e.g. glass-fiber reinforced plastic (GFRP) or carbon-fiber reinforced plastic (CFRP). Carbon, glass and aramid are the most frequently used fibers *[Drechsler, 2007].* More exotic fibers like boron fiber (while having better mechanical properties) are mostly used only for military air- or spacecraft (e.g. Eurofighter Typhoon).

The most notable property of fiber composites is the anisotropy or direction dependency of the material. This behavior can be influenced by varying the fiber direction and the numbers of layers. The main difference to metallic or plastic materials is that the material is not made and then formed but rather it comes into existence at the same time as the part is produced. The main advantage in comparison to traditional metallic materials is the high specific stiffness and stability (when looking at standard CFRP composites). *[Drechsler, 2007]* Most fiber-reinforced plastics show good damping qualities, low fatigue behavior, good corrosion resistance and in part neutral thermal expansion (depending on specific fiber-matrix combination).

Due to their light weight CRFP and GFRP structures have gained more and more importance in the aerospace-sector. The development of CFRP parts for the aircraft industry has increased substantially over the last decades.

6.3.1 Application of rule of mixture to flexible matrix composites

As fiber-composites consist of two or more materials, the mechanical properties of the composite depend on the properties and the volume fraction of the base materials. Additionally the directions, the ratio of length to thickness of the fibers and the boundary surface between fiber and matrix have an impact on the overall properties.

Calculating the mechanical properties of fiber composites can be very challenging, as the overall properties depend on various factors, e.g. material properties of the different source materials, the volume fraction of each in the final part, the interaction between the different materials and the fiber directions.

For classical composites (rigid) as a baseline calculation method the classical laminate theory is usually used. For its use, several assumptions have to be made:

- Unidirectional (parallel) and equidistant fibers embedded as slender bodies in a matrix
- Material properties of the fibers are constant over their whole length
- Sliding between fibers and matrix under load cannot happen
- Fibers have no contact with other fibers

As a start the material parameters of one unidirectional layer of fiber composite are calculated. This results in a so called stiffness matrix [Q] of the material. To generate the stiffness-matrix of the whole laminate, the single stiffness matrices of all layers are transformed to the global coordinate system and then combined to the overall stiffness-matrix [ABD]. This matrix contains the membrane-stiffness-matrix [A], the coupling-stiffness-matrix [B] and the bending-stiffness-matrix [D]. It represents the connection between the line loads N and M and the strain ε and the curve κ (see Appendix G for a short summary of classical laminate theory). With this relationship it is possible to calculate a stress response of the complete laminate in the global coordinate system. However in most cases, the stress response of the single layer is of more relevance and therefore the global stress response has to be transformed back into the local coordinates of each ply. Only with this information is it possible to compare and evaluate the strength (or residual strength) of each ply.

To analytically describe a laminate and its behavior the following parameters are necessary:

- the stacking sequence, describing the angles of all plies in the global coordinate system
- mechanical elasticity: $E_{11}, E_{22}, G_{12}\ and\ \nu_{12}$ of each ply
- Environmental elasticity: $\alpha_{11}, \alpha_{22}, \beta_{11}\ and\ \beta_{22}$, which represent the thermal and moisture expansion, respectively and have direct influence on the plies strain through e.g. $\varepsilon_x^T = \Delta T * \alpha_{11}$
- Normal forces: N_x, N_y, N_{xy}
- Moment (twisting) forces: M_x, M_y, M_{xy}
- Environmental boundary conditions: ΔT [°C] and ΔM [% Moisture]

While the whole laminate is defined according to the global x,y,z – coordinate system, in an individual ply “11” defines the direction of the fiber, “22” denotes the direction orthogonal to the fiber, etc. as can be seen in Figure 44.

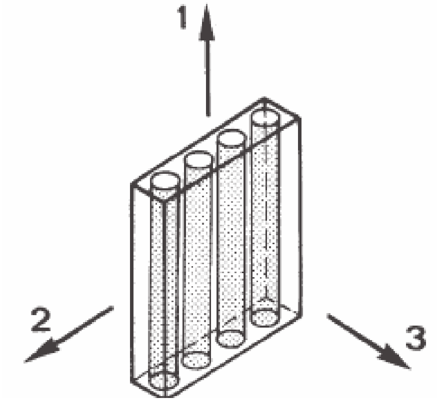

Figure 44: Single composite ply with general directions *[Drechsler, 2007]*

The mechanical elasticity $E_{11}, E_{22}\ and\ G_{12}$ can be calculated by using the so called rules of mixture (ROM):

$$E_{11} = E_{F1}\varphi_F + E_M(1-\varphi_F), \tag{22}$$

$$E_{22} = \frac{E_{F2} * E_M}{E_M\varphi_F + E_{F2}(1-\varphi_F)}, \tag{23}$$

$$G_{12} = \frac{G_F(1+\varphi_F) + G_M(1-\varphi_F)}{G_F(1-\varphi_F) + G_M(1+\varphi_F)}, \tag{24}$$

$$\nu_{12} = \nu_F\varphi_F + \nu_M(1-\varphi_F) \text{ and} \tag{25}$$

$$\nu_{21} = \nu_{12}\frac{E_{11}}{E_{22}}. \tag{26}$$

with: E_F= Module of elasticity of the fiber

E_M= Module of elasticity of the matrix

φ_F= volume-ratio of the fibers (based on whole volume)

G_F= Module of shear of the fiber

G_M= Module of shear of the matrix

ν_F= Possion ratio of the fiber

ν_M= Possion ratio of the matrix

Looking at the formulas written above (No. 19-23) with the stated material behavior in mind (chapter 3, 4 and 6) quickly shows that they are most likely unable to describe the behavior accurately. Therefore as a first step the following equations are modified versions (of No. 19-23) based on the assumption that the material properties of the matrix material have no large impact on the mechanical properties of the laminate ($E_F, G_F > E_M, G_M;\ \nu_M = 0$) :

$$E_{11\_FMC} = E_F \varphi_F, \tag{27}$$

$$E_{22\_FMC} = \frac{E_F * E_M}{E_F(1-\varphi_F)}, \tag{28}$$

$$G_{12\_FMC} = \frac{1+\varphi_F}{1-\varphi_F}, \tag{29}$$

$$\nu_{12\_FMC} = \nu_F \varphi_F \text{ and} \tag{30}$$

$$\nu_{21\_FMC} = \nu_{12} \frac{E_{11}}{E_{22}}. \tag{31}$$

Obviously this still does not include any non-linear material behavior and can therefore be only an approximation of the behavior for small strain values.

The rules of mixture written above are very idealistic, as they require for E_{22} and G_{12} a square cross section of the fibers and a quadratic distribution of the fibers in the matrix. In literature modified versions of the ROM exist, which allow a more realistic fiber geometry and distribution for example Förster/Knappe, Puck, Schneider, Halpin-Tsai, HSB and Hopkins-Camis *[Long, 2005]*. Recalling the requirements for the use of the ROM (as stated above) and comparing them with the expected behavior of the actuators and their material the validity of using the CLT to describe the material is highly doubtful. Even though idealistically most of the assumption still hold true the low stiffness of the matrix-material in comparison to the fiber-stiffness will probably lead to a “sliding” between the fiber and the matrix. The low stiffness can also not prevent localized fiber-failure such as buckling. Additionally the non-linear behavior of the matrix has to be taken into account. All these factors will have to be considered when evaluating the results of the material tests.

6.4 Material and production process options and selection

As mentioned above, a preselecting of materials and production processes was performed based on state of the art fiber-composite manufacturing processes and traditionally used materials in the aviation industries. This selection process was based primarily on a literature research as well accompanied by first small scale lab tests. Different materials in the case of this study mean not only different chemical composition but also different fiber preforms, so different material can also mean to be a difference between for example single roving and multiaxial-weave carbon fiber. An overview over the tested material combinations is given in Table 9. In the column matrix material the different “materials” stand for the different classes of elastomers researched in this study. A detailed description of the matrix materials tested can be found in the following paragraphs.

Table 9: Tested Material combinations (Overview)

Fiber Material		**Matrix Material**		
		TPE	Rubber	Silicone
Carbon fibers	Single rovings	X	X	
	UD-Tape	X	X	
	UD-non crimp fabric	X		
	Mutiaxial-weave	X		X
Glass fibers	Multiaxial-weave	X		X

As can be seen in Table 9 carbon as well as glass fibers were initially tested, however the more or less repetitive tests with the glass fibers were quickly abandoned as the results proved to be very similar (almost identical) to the tests with the carbon fibers. As the handling of glass fibers is comparable to carbon fibers any results gained in terms of production-processes with carbon fibers can be applied to glass fibers as well. Another reason for abandoning is the higher stiffness of carbon fibers in comparison to glass fibers. Also not all matrix materials were tested with every fiber material as after a first or second test the results would allow a prediction which grammage would deliver best results and therefore making further tests unnecessary.

One goal of this work was to find a production process which can reliably and repeatedly produce large quantities of flexible matrix composites (FMC). Therefore several different production methods were researched; the processes were selected based on their use in the composite industry.

Table 10: Material and production methods (+ means tested configuration; - means not tested)

Production method / Material	**Hand lamination**	**Vacuum assisted process (VAP)**	**Injection moulding**	**Pressure moulding**	**Pultrusion**
Rubber	-	-	-	+	-
Silicone	+	-	-	-	-
TPE	-	+	+	+	+

In Table 10 can be seen, that not all materials were tested with each process, the simple reason for that is, that some materials are just not suited for every process. For example the viscosity of rubber is so high, that it cannot be used with VAP or classical hand lamination. Also silicone and rubber are usually cured at elevated temperature and are after that no longer mouldable or formable. The temperature needed to achieve a low enough viscosity in rubber and silicone speeds up the solidification and therefore time-consuming or long-duration processes are not an option, neither is producing a semi-finished part (wrought material) possible with these materials.

During the experiments with the different materials special regard was paid to the grammage and weave of the fiber material. These two factors can be a deciding factor for a material-combination with a certain production process. The first experiments in this work were conducted with 12k-carbon fiber rovings. These quickly proved much too thick for the tested production process, all following experiments were carried out with a much lower grammage.

6.4.1 Material trials with rubber

The rubber used in these tests was exclusively natural rubber sheets (Kraiburg Gummiwerke SAA1052/70, Appendix C). These rubber sheets are available in different thicknesses. As a first test single-fiber-rovings (Torayca FT 300B 6000 50B) were pressed into a rubber sheet. This first test showed that the viscosity of the rubber is much too low to impregnate the fiber, therefore the fibers have to be spread very thin to achieve a good saturation. Based on this first trial, further tests were conducted with Dynanotex HS 15/50SL carbon fiber-tape and again SAA1052/70 rubber sheets. The fiber-tape and the rubber were repeatedly pressed at 90°C. It was necessary to repeatedly press the compound to achieve a good saturation and distribution of the fibers in the rubber. The rubber sheets were only available with a 0.5mm thickness. To maximize the effect, the specimen was doubled and repressed multiple times.

Figure 45: Rubber-fiber composite; pressure molded at 250-400bar at KRAIBURG Gummiwerke

Experiment description

To produce a composite the carbon fiber UD-tape and the rubber sheet were stacked and pressed at 90°C and a starting pressure of 250bar for 5 minutes. As mentioned above, the result from this first molding was cut in two equal pieces. These pieces were than stacked on top of each other and pressed again. This cutting and stacking procedure was repeated until an eight-layer strong “laminate” was produced. During the cutting and stacking the pressure was progressively increased from 250bar to 400bar. After eight layers were achieved the final sample was cured at 140°C for ten minutes. In total two eight layered and one twelve layered laminate were produced. The eight-layered laminates had a thickness of 0.4mm.

Conclusion rubber testing

Pressing the carbon fibers into the rubber at pressures between 250-400bar worked very well with regard to the distribution of fibers in the rubber. The repeated folding and repressing of the rubber-fiber composite distorted the fibers a lot; see Figure 45 , thereby making it almost impossible to create a predetermined lay-up (fiber-direction wise). Concluding it can be said, that this technique can be used to create a highly anisotropic rubber-fiber composite but does not offer the possibility to create a preplanned lay-up. Additionally it has to be mentioned, that even so the tests were only conducted with the natural rubber sheets SAA1052/70, very similar or inferior results can be expected when a different rubber composition is used. The used composition has a very low viscosity for a rubber.

6.4.2 Material trials with silicone rubber

Tests with various silicone materials were conducted in previous in-house studies (which were not part of this work) with varying results. Due to these results and the information available in literature on this topic, the investigation of silicone as a matrix material for this work was conducted mostly as a literature research and only some very small experiments were performed. Tests for this work were conducted using a two component silicone (LR 7665 A/B, Appendix E) and a bi-axial carbon fiber. It quickly became apparent through the literature research, that most silicone materials have a too high viscosity to properly infuse the fiber materials. The above mentioned experiment led to the same outcome. No further experiments were conducted with different fibers, as the results did not promise more success with a thinner fiber material. There are only some very specialized silicone materials (e.g. Wacker Elastosil S 690 or S 692) which (theoretically) have a low enough viscosity, but these silicones are very expensive and therefore not preferred for producing a large quantity of material. Information on tests, proven production processes and performance of Wacker Elastosil S690/S692 infused carbon fibers can be found in the work of Datashvili *et al, 2005, 2007* and Baier *et al, 2005*.

6.4.3 Material trials with thermoplastic elastomers

The third matrix-material to be investigated was thermoplastic elastomer (TPE). In other studies TPE has proven to be viable as matrix materials for dynamically loaded flexible matrix composites *[Keun et al., 2006]*. TPEs are available in a wide variety regarding hardness, temperature range and mechanical properties.

Preliminary tests were performed at KRAIBURG TPE and Airbus Group Innovations in parallel to the two other matrix materials described above. These promising preliminary tests resulted in a much more intensive investigation of the TPE in combination with carbon fibers. TPE was the only matrix material to be tested with all four production techniques mentioned in Table 10.

One important property for these tests of molten TPE is the reduction in viscosity through temperature and shear forces. Shear-forces reduce the viscosity dramatically, as can be seen in Figure 46.

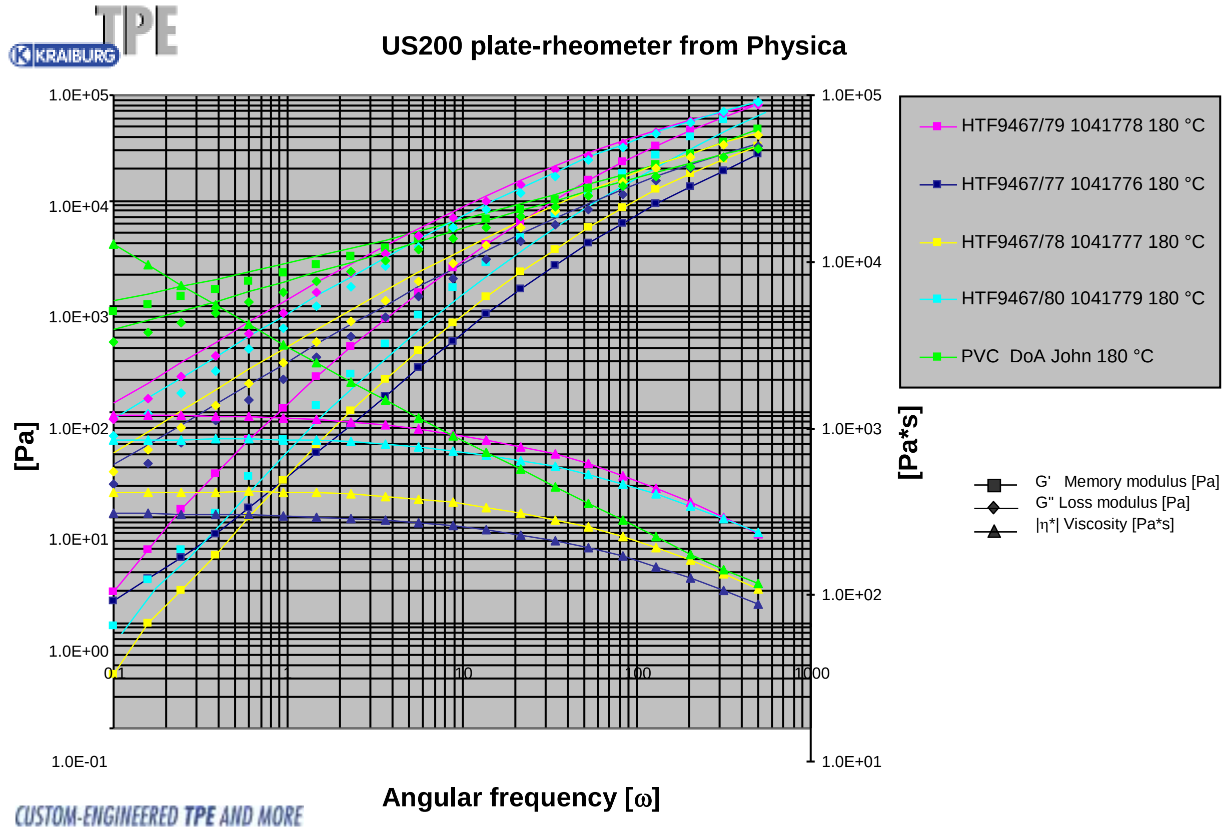

Figure 46: Change in viscosity in TPE under shear forces at 180°C (Source: KRAIBURG TPE)

Preliminary tests with TPE

The preliminary testing using a pressure mould was conducted at Kraiburg TPE with poor results. In these tests one 2,5mm thick plate of TPE was placed on top and on bottom of a unidirectional 12k carbon-fiber fabric. This assembly was heated to 190°C and pressed at 4bar.

As can be seen in Figure 43a, the TPE did not infuse the carbon fibers properly, but stayed on the surface of the carbon-fiber-fabric. Also probably due to the heat, resulting in outgassing, the TPE is infused with gas-pockets, further reducing the quality.

Further production trials using injection moulding produced slightly better results but also made clear, that the fibers have to be restraint during the process, as they moved with the matrix material which resulted in a highly distorted fiber orientation. Due to the speed of the TPE and the resulting flow the fibers at the injection-point were pushed away, see Figure 47b. Also the TPE did not infuse the fibers completely which was likely caused by the rapid cooling of the TPE due to the “cold” cast.

Figure 47a: TPE and carbon fibers processed in a pressure mould at 190°C at 4bar

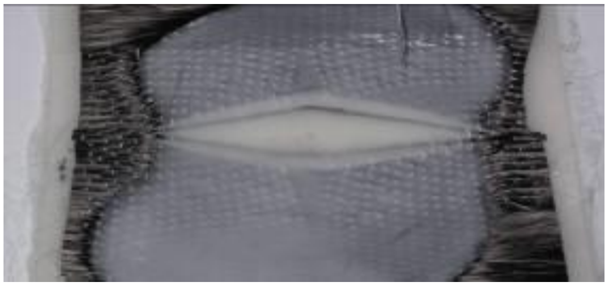

Figure 47b: Thermoplastic elastomer injected in a unidirectional 12k carbon-fiber preform at 190°C in a cast at room-temperature

Based on the first tests using injection moulding further tests using pressure moulding were performed to find ways to improve the production process to the point of being able to produce full impregnated flexible matrix composites materials with a TPE matrix.

The tests were performed on a fully automatic pressure mould with heat-able plates. These plates were heated to 180°C, the pressure was set to 2.5bar and the processing time was 30s-60s depending on the fiber-layer’s thickness. This process produced good results but also quickly showed some draw-backs and a limit for the thickness of the dry fibers to be used.

Figure 48: 2 layers of biax-6k-carbon fiber infused with TPE at 2.5bar at 180°C

One draw-back is the amount of movement the liquefied TPE performs, as through this movement the fibers are shifted from their position and fiber-ondulations are created, similar to pressure moulding. In contrast to classic fiber-composites some change in fiber-angle has a very large impact on the mechanical properties of the resulting FMC-composite, see *[Peel, 1998]*. As can be seen in Figure 48, the TPE successfully infused the fibers and created a good surface. Again the problem of the flowing of the TPE during the infusion-process becomes apparent. The fluid TPE carried fibers at the edge of the fiber material with it, disturbing the orthotropic properties. The problem becomes even more pronounced when using unidirectional fiber material.

TPE with vacuum assisted process

To investigate if VAP would be a viable production method for FMCs with a TPE matrix a classical VAP built-up was used. The preform and the matrix were heated to 180°C and then the TPE was sucked into the preform at a pressure difference of 0.8bar. The idea to reduce the viscosity of the molten TPE through the suction worked not as well as expected. The pressure difference in the VA-process proved to be too low for the relatively high viscosity (in comparison to a standard resin, e.g. RTM6) and due to the slowing of the TPE as it contacts the fibers the viscosity reduction through shear forces is greatly reduced. Therefore the molten TPE could not flow very far into the fiber layer. The process was very slow (<5mm/hour) and therefore the total amount of matrix infused into the fibers was very small. It could also be observed that the TPE did not bond with the fibers. The positive effect of the vacuum was, that the fibers stayed in place and therefore no ondulations occurred and also no gas-pockets remained. The results from this trial can be seen in Figure 49, important to note is that the area of the fibers that were successfully infused had a rather high fiber-volume-fraction (of about 70%) and showed good handling quality.

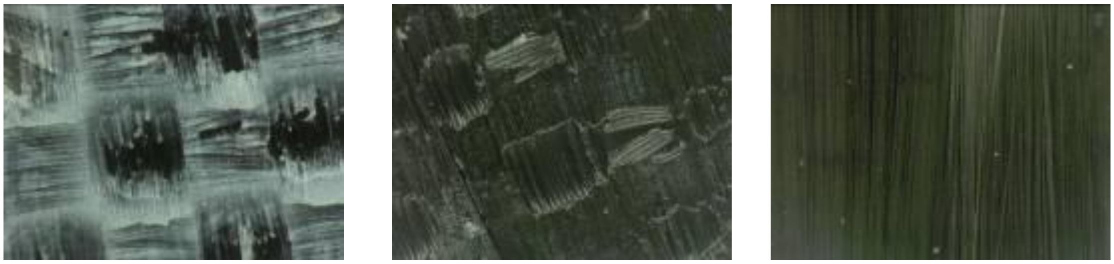

Figure 49: Carbon-fibers with a TPE matrix, after VAP (for 3h) (left and middle) and as a comparison dry fibers (right)

TPE pressure moulding

Pressure moulding as described above in the preliminary tests proved to be a viable production method if the movement of the fibers could be prevented. In order to achieve this, a special cast was constructed. This cast was a metal frame into which the fibers were clamped. The tests were again performed at 180°C with a variable pressure range from 1-2.5bar and 30s-120s. The cast was preheated to the required 180°C.

Pressure moulding in general produced very good results with the above defined settings in terms of impregnation of the fibers. The tests showed that the cast could also not constrain the fibers completely. The results were better than without but still the fiber angle could not be set to a predefined orientation.

Pultrusion Process

In cooperation with Jonam Composites Ltd. it was possible to produce a prepreg-like FMC through the use of a pultrusion process. A pultrusion process offers the advantage that the fibers are all oriented in the same direction and are kept under tension at all times, therefore the above repeatedly mentioned ondulations cannot or only minimally appear with this production process. With the pultrusion process the FMCs were produced at a speed of 2m/min at 180°C with a fiber-volume fraction of 50%. The produced FMC is a material-combination of Torays T700S carbon fiber (Appendix B) and the TPE-SEBS patch HTF 9471/16 from KRAIBURG TPE (Appendix D). The tape is 0,16mm thick and has a width of 75mm. The pultrusion process was used to create roughly 20kg of TPE/carbon-fiber FMC for further material testing.

Figure 50: FMC-UD-prepreg

The material produced during the pultrusion process showed a very high fiber volume fraction of roughly 50%. To decrease this value the pultruded material was combined with pure TPE foil using the above described pressure moulding process to create a material with a roughly 20% fiber-volume fraction, without disturbing the fiber orientation.

6.5 Mechanical testing of flexible matrix composites

To determine the mechanical properties and to create a comparable FE-model of the developed material tensile and three-point-bending tests were performed. The tests also help to evaluate the behavior of these composites under load, as the use of highly elastic / hyperelastic matrix material and large strains makes an application of classical laminate theory mostly inaccurate. Additionally the test can offer information on possible failure modes (beside max. stress/strain).

6.5.1 Mechanical testing: Preparation and challenges

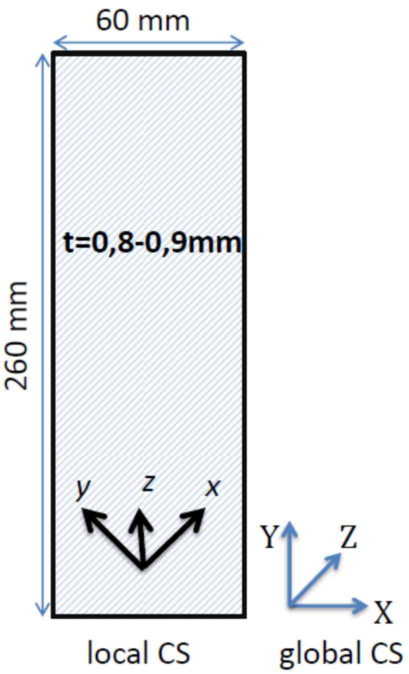

Figure 51: Schematic of test sample with coordinate systems

In preparation for the material test the above described prepreg material was used to produce test-samples. The tape produced in the pultrusion process had a too high fiber volume fraction to create test specimens for the planned tensile tests. Therefore the tape was cut into a desired shape and a 0.25mm TPE foil was layered on top and on bottom of the “prepreg”. This stack was than combined using pressure moulding at 100°C and 3bar for 120s. As no suitable test norm exists, the test-specimens were designed based on CFRP and rubber test norms, literature research *[*e.g. *Peel, 1998]* and FE-simulations to determine the required shape. The final test-specimens were 60mm wide, 260mm long and between 0.8mm and 0.9mm thick. The specimens were 4-layers “prepreg” material (UD-same direction) with a layer TPE on top and on bottom, resulting in a fiber-volume fraction of roughly 20%. In Figure 51 a schematic test sample with a local and a global coordinate system (CS) can be seen, the local coordinate system is oriented so that the *x*-axis is always the fiber direction, *y*-axis along the “surface” and the *z*-axis is always through thickness. The global coordinate system is oriented as shown in Figure 51 for all test samples, X-axis denotes the width, Y-axis parallel to the length and the Z-axis is through thickness oriented. Tests results are expected to be extremely different depending on the tested fiber angle. Additionally deformations larger than 1% are likely to occur. As such strain gauges were not an option and an optical measurement system was chosen instead. The application of strain gauges could also have led to a local stiffening of the structure, falsifying the measurement.

6.5.2 Tensile tests of flexible matrix composites at different fiber angles

The above described test-specimens were tested on an Instron 5566 10kN test-machine with an optical strain measurement (Laser) (continuous measurement). The test specimen were prior to the tests stored at 22°C and 40% humidity for at least 24 hours and the tests were performed under the same environmental conditions. The optical strain gauge was only able to capture strain in one dimension, so the tests were also video- and photo-recorded. For this purpose a grid was applied to the specimens to be able to measure the distortion at every point during the test and calculate the strain in a second direction; see Figure 52. The tests were conducted at low enough speeds to be considered as semi-static. The 0°- and ±45°-specimens were tested at 2mm/min, whereas for the 90°-specimens the speed was increased to 10mm/min, after a load of 10N had been reached. The force was applied in the Y-direction of the global coordinate system. The fiber angle describing the specimens is therefore between the Y-axis of the global coordinate system and the *x*-axis of the local coordinate system.

Two sets of tensile tests were performed, the second test incorporated lessons learned from the first one. In total 40 specimens were tested, ranging from 0° to 90° in 15° steps and ±45° fiber angle direction, for a complete list see Table 11. All performed tests were one-direction tensile tests. The strain measurements were done using only optical measurement systems, as any application of sensors onto the specimens would have falsified their stiffness. In Figure 52 the typical s-shape deformation for off-axis fiber-placement in tensile tests with composite materials can be seen.

Figure 52: Test-specimen under load - S-shaped

Table 11: Number of specimens per test and angle

	0°	15°	30°	45°	±45°	60°	75°	90°
1st test series	8	0	0	0	8	0	0	8
2nd test series	2	2	2	2	0	2	2	4

As expected the results for these tests differ largely depending on the fiber-direction. Testing in 0°-direction proved to be the most difficult, because the specimens started to slip from the clamps which led to inaccurate measurements. Thus material failure could not be achieved and therefore no maximum strength was found. The tests for any other fiber-angle were stopped when the force no longer increased (or started to decrease, see Figure 53b) or the marker for the optical measurement left the maximum possible range. In only one case did the test-specimen fail completely (90°-rent of the matrix material). For a summary of the failure behavior see Table 13.

For an example of the slippage of the 0°-specimen, see Figure 53a. The force-strain graph is roughly linear but shows certain unevenness. These “bumps” are due to the slippage, observed during testing.

Comparing the graphs from 0° tests with 90° or ±45° test the non-linear material behavior of the matrix material becomes apparent; see Figure 53a/b and c. Interesting to note is also the difference in maximum force the samples could carry.

A comparison between the stress-strain curves of the 15°-90° test-specimen can be seen in Figure 54, the stress-strain curves for the 0°-specimens were left out of the diagram for clarity (would appear as a line on the y-axis).

The test results from the 0°, 90° and ±45° specimens were used to approximate linear material properties, see Figure 53a, Figure 53b and Figure 53c, results only valid up to 10% strain as the curves are to nonlinear after that. The fiber volume ratio ϕ_f was determined using the density of the samples, the fibers and the matrix and calculated to be roughly at 20% (depending on the test-series). The tensile tests resulted in the mechanical properties of the material as can be seen in Table 12. It can be noted that the poisson ration is (approximately) zero, an at first glance unusual result, which is probably caused by the large difference in the elasticity modulus of matrix and fiber. The matrix deforms under such small loads, that there is no measurable deformation response of the fibers.

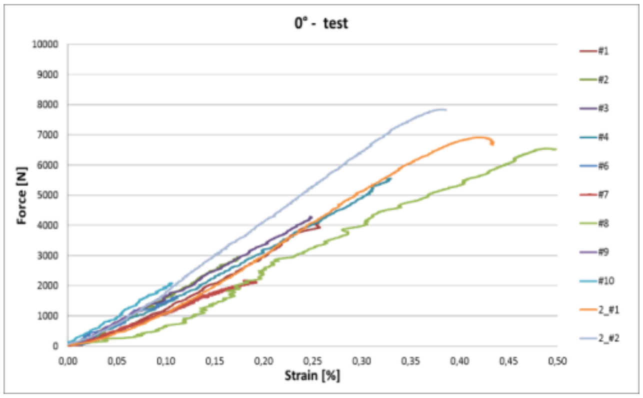

Figure 53a: Force-strain curve 0° tests

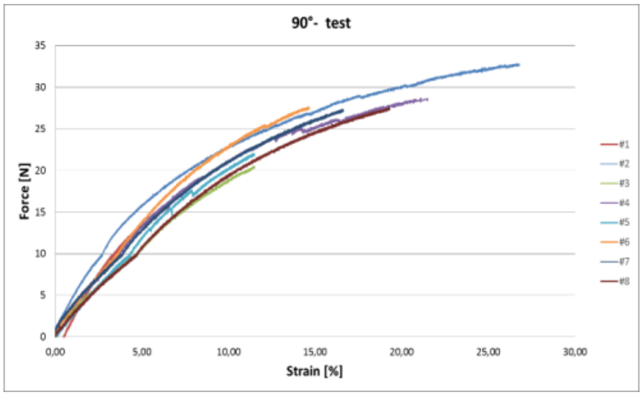

Figure 53b: Force-strain curve specimen 90°

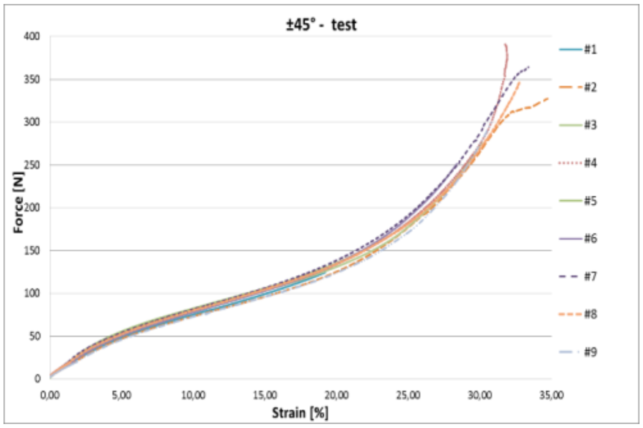

Figure 53c: Force-strain curve specimen ±45°

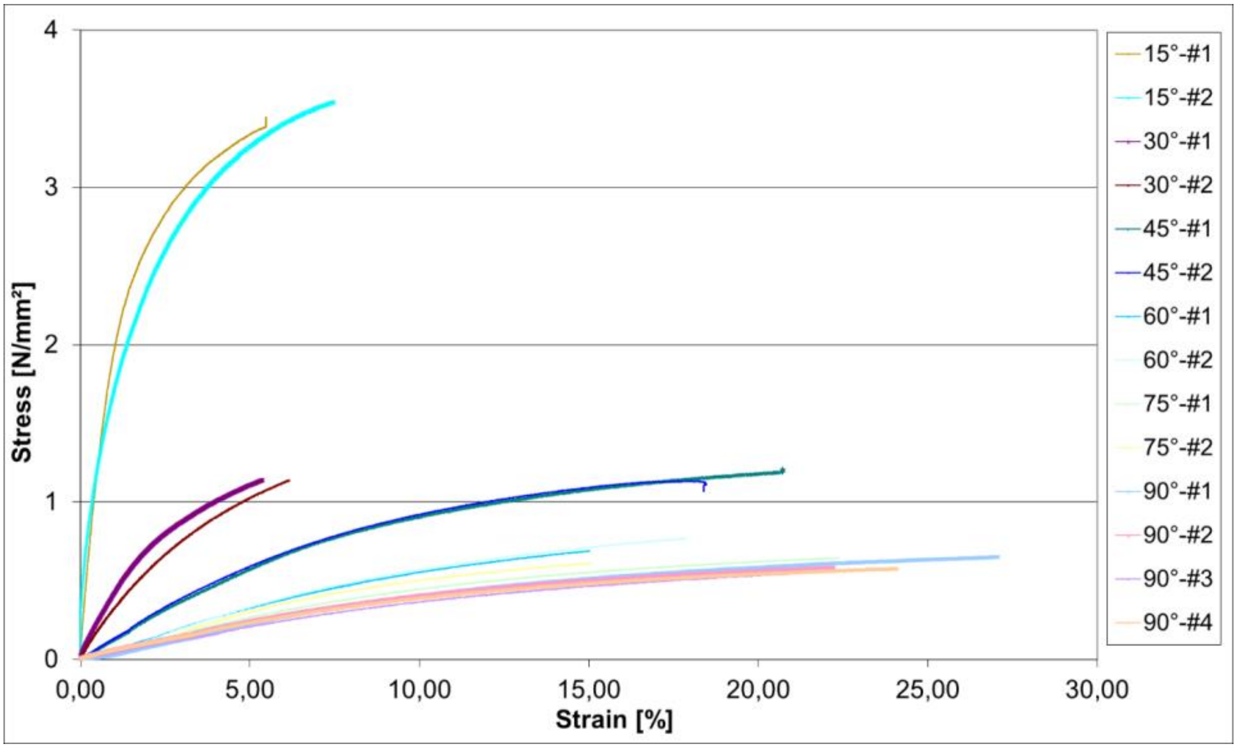

Figure 54: Comparison of stress-strain curves 15°-90°

Table 12: Material properties of the TPE-C-FMC at ϕ_f=0,2

Material properties (calculated using the test-data, only valid up to 10% strain)			
E_1=47081 N/mm²	E_2=4,24 N/mm²	$\nu_{12}\approx 0$/ ν_{21}=0	G_{12}=3,49 N/mm² *

* 1-in fiber direction; 2- orthogonal to 1

Table 13: Failure behavior depending on fiber direction

Fiber direction	**0° and 15°**	**30°, 45°, 60°, 75°**	**90°**	**±45°**
Failure behavior	Delamination of the upper layer of TPE at the clamps/ clamping problem not material failure	Matrix failure, inter-fiber failure	Crack/rent of the matrix material	Delamination on the edges of the specimen

6.5.3 Theoretical evaluation of the tensile-test results

In order to calculate the material properties analytically the classical rule of mixture (ROM) (Formula No. 18-23) and the adapted ROM (Formula No. 24-28) were used simply to verify if they would result in an approximation of the test data, even though the ROM-boundary condition make this very unlikely. Used for these calculations were the material-properties of the carbon-fiber (see Appendix B) and TPE-matrix (see Appendix D). Table 14 shows the analytically results from these calculations, for the first row the standard rules of mixture and for the second row the adapted version was used. These results have to be compared with the test results shown in Table 12.

Comparing the analytical data with the test data shows a very good agreement parallel to the fiber direction (1-direction). But the analytical data is not able to capture the behavior orthogonal to the fibers (2-direction) Here the analytical solutions are off by a factor of 4. The same can be said for the shear-modulus (by a factor of 2,3).

When comparing the results of the classical ROM with the results from the adapted ROM shows almost all values are practically identical. Mathematically the adaptation was therefore correct, except in case of ν_{12} (Formula 22). The values for the poisson-ratio are radically different.

Interesting is the comparison for the poisson ratio ν_{12}. The test data suggests a ν_{12} of 0, following the trend of the adapted ROM, which is most likely a coincidence. The analytical value is the result of the low fiber-volume fraction (ϕ_f=0,2), but the decoupled behavior observed in the tests is unlikely to change with a higher ϕ_f. As measurements in 3-direction are missing no data is available, but due to the observed deformation behavior ν_{12} calculated with the classical ROM could be a good approximation for ν_{13}.

This proves the previous stated expectation that neither the classical ROM nor the adapted ROM can be applied for FMC materials. This is on the one hand caused by the huge difference in stiffness between the fiber (carbon fiber) and the matrix (TPE-rubber) and also because of the large "deformation-freedom" the matrix has in comparison to the fiber. The definition of the ROM states, that there can be no sliding between matrix and fiber, which happens in 2-direction in a way. Not necessarily as result of missing adhesion between fiber and matrix but because of the large deformation of the matrix, this basically constitutes of flowing over the fibers.

Table 14: Material properties of the TPE-C-FMC at ϕf=0.20 (analytical calculation)

Material properties (calculated using the rule of mixture)*				
Classical ROM	E_1=46000,7 N/mm²	E_2=1,125 N/mm²	ν_{12}=0,438 / $\nu_{21}\approx$0	G_{12}=1,5 N/mm²
Adapted ROM	E_1=46000 N/mm²	E_2=1,125 N/mm²	ν_{12}=0,046 / $\nu_{21}\approx$0	G_{12}=1,5 N/mm²

* 1-in fiber direction; 2- orthogonal to 1

6.5.4 Three-point bending tests

To create a more complete picture of the behavior of the developed material a three-point bending test was performed with the 0° specimens, see introduction chapter 6.5. As the specimens consist of a lay-up with varying stiffness through the thickness these tests are used to create a more complete picture of the material and are also a good reference for the FE-simulations. The distance between the longitudinal rotating support roller was 100mm, see Figure 55. The specimen was shaped as described above for the tensile tests (260x60x0,8mm). The tests were performed as closely as applicable based on testing requirements described in ASTM D790-10.

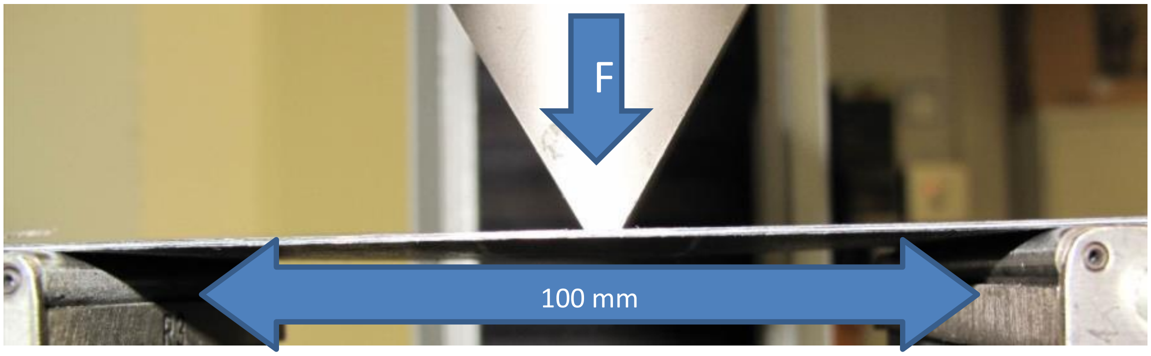

Figure 55: Three point bending experimental setup (0°-test sample)

The deformation during the test was expected, bending with a local maximum at the loading nose but towards the end (flattening of the curve in Figure 56) local buckling could be observed. No permanent damage to the test specimen could be detected after the test.

Based on the results shown in Figure 56 a bending modulus for the tested specimen can be calculated. It is important to note, that this modulus is only valid for bending under load in z-direction (see Figure 51), also in comparison with other test-samples the fiber angle always has to be taken into account.

$$E_{bend} = \frac{L^3 F}{4wh^3 d} \tag{32}$$

with: L: is the distance between the two outer supports; $[L] = mm$

F: the force acting on the specimen; $[F] = N$

d: the correlating displacement; $[d] = mm$

h: the thickness; $[h] = mm$ and

w: the width; $[w] = mm$.

As the force-displacement curve is approximately linear until a plateau is reached the linear bending modulus can be calculated to

$$E_{bend} = 19753 \frac{N}{mm^2}.$$

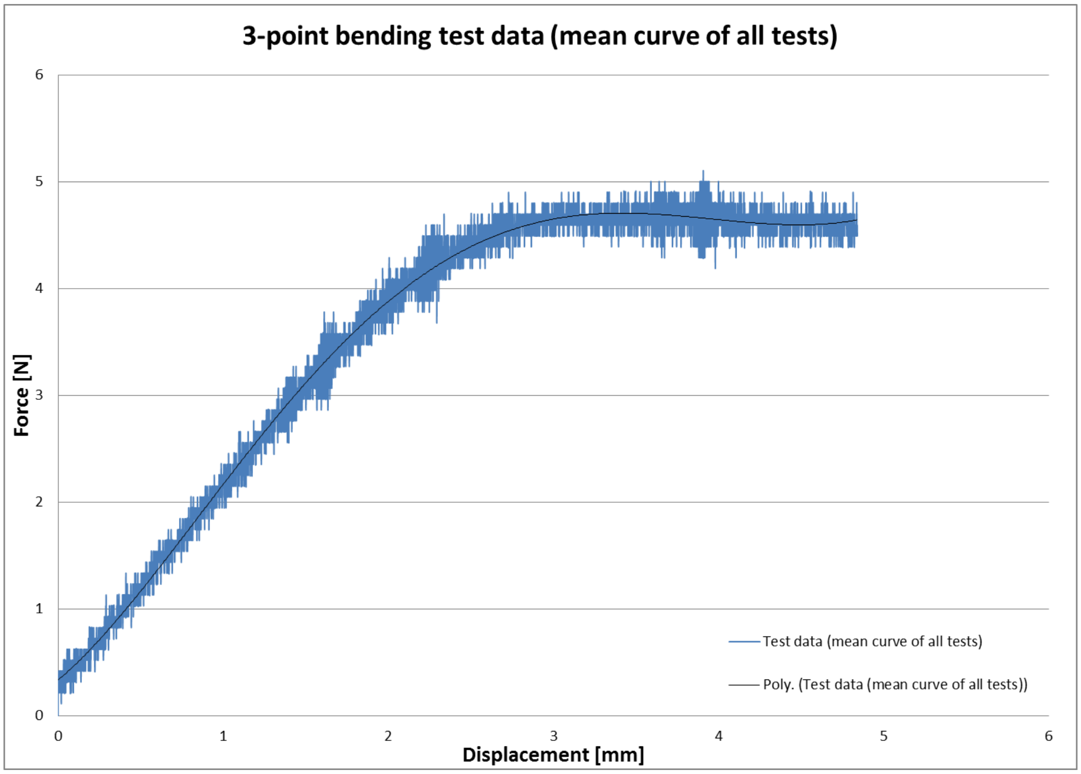

Figure 56: Three-Point-Bending test results (mean curve from all tests)

6.6 Conclusion material development and testing

The need to develop a flexible matrix composite was identified and described. The requirements ask for a stiff/flexible material depending on the regarded direction with dependable fiber direction and similar handling qualities to "classic" composite pre-preg. Also a production method had to be developed, that could produce this type of material reliable in large quantities as well as time and cost efficient. In this work different production trials with different types of material are described.
In Table 15 all tested material-combinations are listed as described in chapter 6.4, not every matrix material was tested with each type of fiber material. Often the first experiment delivered enough results to eliminate certain combinations.

The experiments with the various production processes and materials proved pultrusion and pressure moulding as the leading technologies to create flexible matrix composites. Especially pultrusion enables the production of a constant quality of pre-preg like FMCs.

For pressure moulding to become a viable production technique a way has to be found to properly restrain the fibers to avoid ondulations. Even if fiber-placement could be ensured it would most likely still be necessary to first create a wrought material with which the final lay-up is realized, negating one of the traditional benefits of pressure moulding. The test with pressure moulding showed, that a too thick (above 6k filament number) laminate could not be properly and reliably infused. Further research with the pultrusion process has to be conducted considering fiber-volume-fraction and different mixtures of TPE in order to achieve better mechanical properties. Thermoplastic elastomers in combination with carbon fibers have so far proven to be able to create FMC through the use of pultrusion and pressure moulding.

The tensile tests described were performed to understand the behavior of the composite under load, to discover possible failure modes (beside max. strain/stress) and acquire data to simulate the material. The FE-models will be used to evaluate the different fiber-layups for the actuation tubes and help to decide the final geometry of the actuation system. The tests showed that 10% strain (for ±45° and 90°) is easily achieved and sustained without failure. As long as the design of the actuation system is not finalized no answer can be given on the loads and strains seen by the actuation tubes and whether or not this specific material (values in Table 12) can successfully fulfill all requirements envisioned for the actuation mechanism.

Table 15: Tested materials (X+: tested and success, X-: tested failure, blank: not tested)

Continuous Fibers				Matrix Material		
Base Material	Fiber type	Fabric type	Area weight	TPE*	Rubber**	Silicone***
Carbon Fibers	Torayca T300B-6000	6k-Roving	396 tex	X+	X-	
	Dynanotex HS 15/50SL	UD-tape	50 g/m²		X+	
	Torayca T700S	UD-tape	100 g/m²	X+		
	Torayca FT 300B 6k 50B	6k-UD-fabric	120 g/m²	X+		
	Toho Tenax IMS65 E13 24k 830tex	24k UD-fabric	208g/m²	X-		
	Torayca T300B-6000	6k Biax-fabric	317 g/m²	X+		X-
	Torayca T700S-12000	12k biax-NCF	578 g/m²	X-		X-
Glass Fibers	Interglas technologies	Biax fabric	288g/m²	X-		X(+)
*TPE-SEBS Patch HTF 9471/16 Kraiburg TPE **Rubber SAA1052/70 Kraiburg Gummiwerke ***Silicone: MVQ-silicone (FSU-50-83 by MG Silikon)/ Wacker Elastosil LR 7665						

6.6.1 Numerical representation of (non-linear) material behavior

As written above shell elements have been selected as a preferred representation of the actuators (and the skin). While only using shell elements limits the possible means of modeling the material behavior, it still leaves different options to consider. It is important to analyze beforehand what scope and aim the simulation should encompass. How accurate has the representation of the material to be to give an accurate overall deformation behavior of the model and how important is the stress-strain result? For this it is necessary to keep in mind the overall simulation goal. A very accurate simulation of the tensile tests could become too specialized and therefore not transferable to the global simulation model. Here the modeling effort and the simulation run-time are again key components to consider. Additionally the range of representation has to be considered. If 5% strain are enough for the global model linear material models can be used. If higher strains need to be represented nonlinear material models, which are usually more complex have to be used, see chapter 6.2 and *[Grambow, 2001; Kyriacou et al., 1996; Luo et al., 1990; Stojek et al., 1998]*.

Irrelevant of the material simulation details as a first step a virtual model of the test was created. The model has the same dimension as the test specimens had. The test samples had different thicknesses depending on the fiber angle (0°-specimens were thinner than the rest, due to the required clamping during testing), which were appropriately adopted for the simulation.

The basic model can be seen in Figure 57. The lower boundary condition (BC) is restraining every degree of freedom (DoF) of the shaded area. A similar BC exists on the top of the model, with the exception of movement in y-direction. To monitor the loads and deformation during the simulation so called reference points (RF) were included in the model; RF1 at the “top” and RF2 at the “bottom”. All nodes from the BC on top and bottom are directly tied to the closest RF. The free deformation length of the sample is 200mm.The thickness was adapted based on the fiber angle, see above. To show the validity of the simulation model comparisons were made between 0°, ±45° and 90° fiber angle - test data and simulation. The large deformations observed during the different tests make non-linear simulations for an accurate representation necessary. As an outcome of the results from chapter 5.2.2 the simulations were performed static as well as dynamic explicit, even if the tensile and 3-point-bending tests are static or quasi-static tests (and static simulations should suffice).

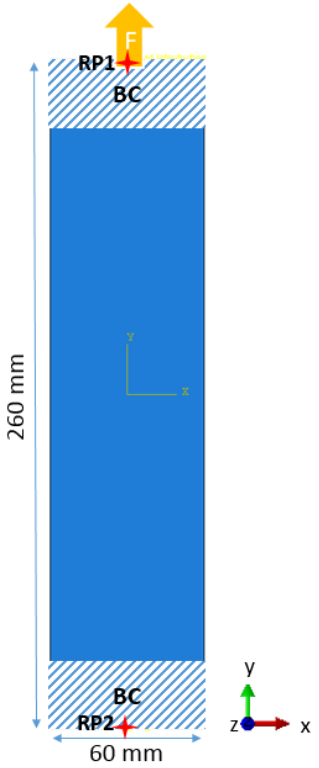

Figure 57: Tensile test simulation model

As described in the previous paragraph a dynamic explicit simulation is beneficial for large/complex contact simulations. Based on this different simulations of tensile tests were performed using either a static or a dynamic solver and compared. This was done to determine the correct setup of the dynamic model and later to ensure an accurate representation of the material behavior with dynamic simulation. The comparison between the two approaches can be seen in Figure 58 and Table 16.

As a first step force- and deformation-controlled simulations of a linear material were compared with each other. The dynamic-force controlled simulation shows a slightly higher stiffness than the rest, but in a range that is deemed acceptable for this application.

Table 16: Comparison of static vs dynamic tensile test simulations

Name	Solver	Material	Loading Type	Deformation [mm]	Force [N]
Tensile Test - Disp	Static	Linear	Deformation	2	21044,7
Tensile Test – Force	Static	Linear	Force	2,01	21044,7
Tensile Test – D – Disp	Dynamic	Linear	Deformation	2	21044,7
Tensile Test – D – Force	Dynamic	Linear	Force	1,99	21044,7

The four simulations described in Figure 58 and Table 16 only show that a dynamic solver can accurately (or at least as accurate as a static solver) represent the behavior of a material during a tensile test. With this the material behavior described in chapter 6.5 is not yet represented.

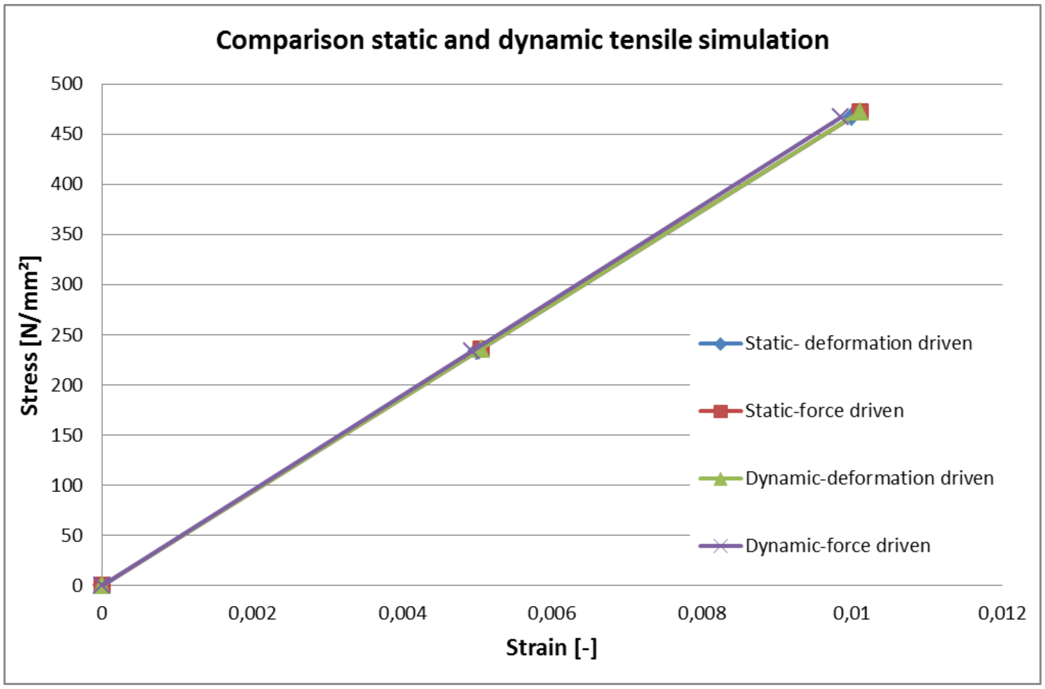

Figure 58: Comparison of static and dynamic tensile simulation

For this different possible material simulation methods and accuracy have to be taken into account. As the developed material is a composite material and shows a clear directional (orthotropic) behavior the simulation has to incorporate this directionality. Additionally the material also exhibits non-linear behavior for all fiber-angles except 0° and an angle-dependent strain level. The best case solution for the system simulation would be to have one material model, which is able to represent the developed material and at the same time easily adaptable for different geometries or load-directions. In Table 17 several different options of how this could be achieved are listed. This selection is limited by the use of shell elements. If continuum-shells or full 3D elements would be used, this list would be longer.

Table 17: Possible approaches to FMC-material simulation

Approach	Description	Limitations
Linear orthotropic material formulation (composite)	Smeared material parameters	5% strain (linear material)
Non-linear orthotropic material formulation (Fung, Ogden, enhanced Mooney-Rivlin))	Model specific parameters, difficult to obtain for the whole range (tensile, compression, etc.)	Fung or Ogden not capable of handling linear fibers / Enhanced Mooney-Rivlin model not fully formed
Rebar reinforced non-linear (matrix-) material	Rebar elements reinforcing the matrix material	Perpendicular to rebar no effect

The two most relevant options are rebar reinforced matrix simulations and/or orthotropic material formulation. Rebar in rubber as cord-reinforced materials were already discussed in e.g. *[Meschke et al., 1994]* and shown to be feasible for certain applications. To understand the limitation of rebar elements simulations with varying “fiber”-degrees were made. For this the same tensile-model as shown in Figure 57 and Figure 58 was used. As matrix material a 3rd order Ogden model (see chapter 6.2.3) based on TPE test data was used. As a first step the 0° behavior is reproduced, see Figure 59.

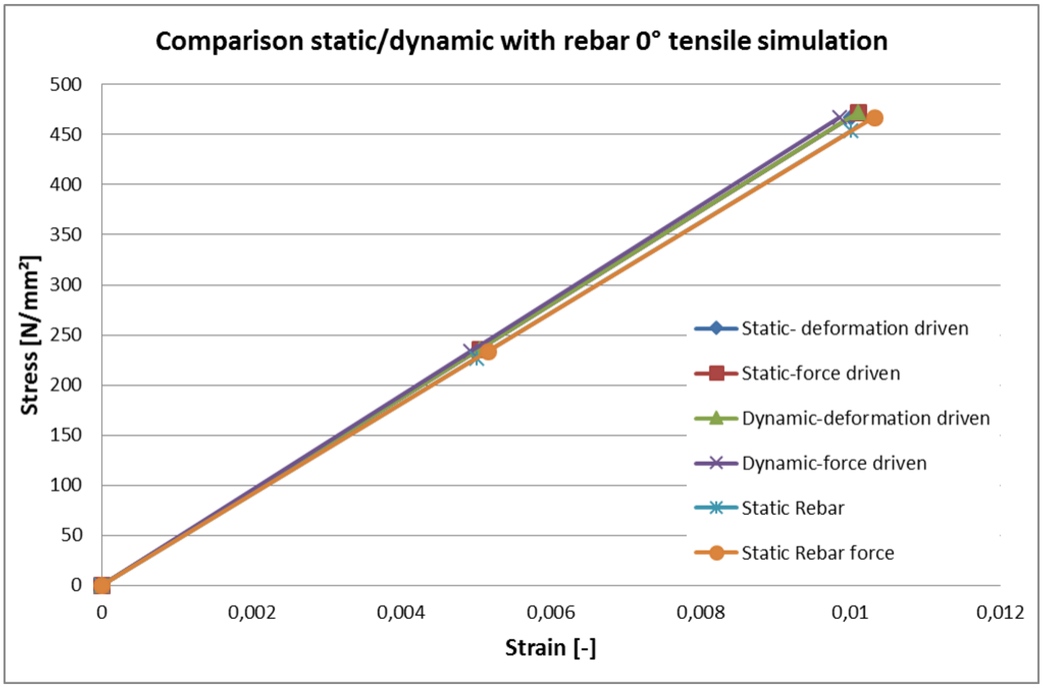

Figure 59: Comparison of Rebar reinforced material with orthotropic material

For 0° rebar reinforced matrix the behavior is equally good as isotropic material with a representative E-modulus (E = 47000 N/mm² compare Table 12 E_{11}). Using the same model and simply rotating the rebar elements by 45° shows a completely different result, see Figure 60. Here the one-dimensional behavior of rebars becomes apparent. As they can only carry load along their axis the overall behavior of the simulation is too soft. This becomes obviously worse at 90°, see Figure 61.

This shows rebars are not able to represent the material behavior of the developed material in all directions.

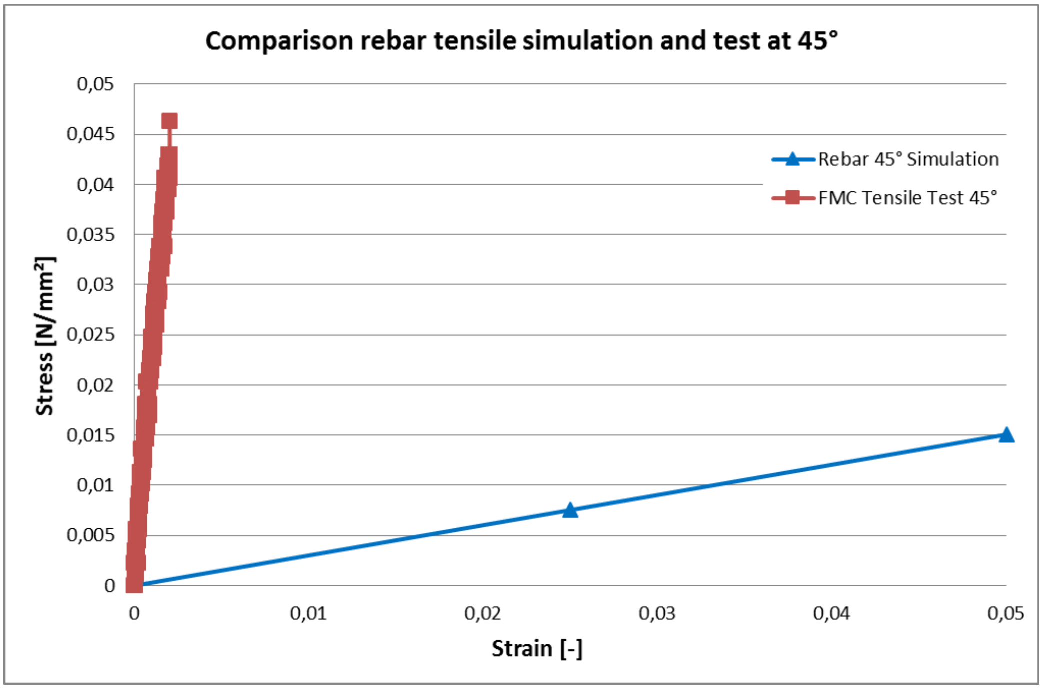

Figure 60: Comparison Rebar tensile simulation and test at 45°

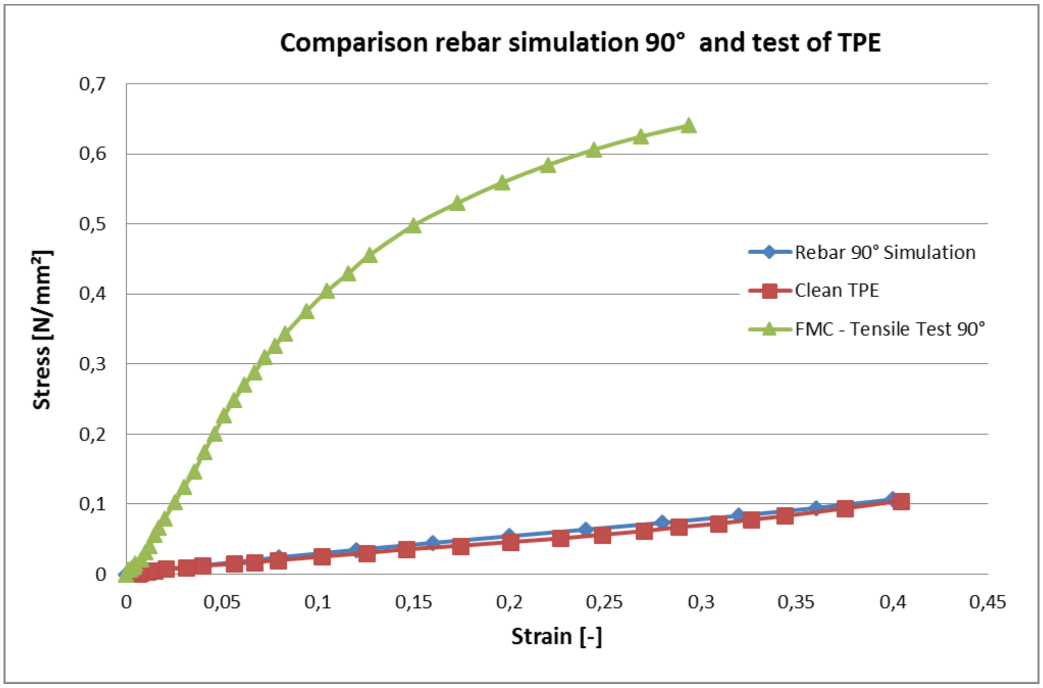

Figure 61: Comparison rebar simulation 90° and TPE

6.6.2 Comparison of simulation model and coupon testing

As the above shown models were not correctly representing the material behavior for all fiber directions, a standard composite material model (linear orthotropic material formulation) was adopted to match the data from the tensile tests and compared to the test results from chapter 6.5. See Table 18 for the orthotropic material parameters used in the simulation model (compare Table 12):

Table 18: Material parameters in the simulation model (in N/mm²)

E_{11}	E_{22}	E_{33}	v_{12}	v_{13}	v_{23}	G_{12}	G_{13}	G_{23}
47000	4,5	4,5	0	0	0	3,5	3,5	3,5

Important to note is that a linear material model was used. Therefore the simulations were limited to a maximum of 5% strain (limit stability of linear material models in Abaqus FEA). The test-specimen was modeled with shell-elements (S4R; 4-node general-purpose shell, reduced integration with hourglass control, finite membrane strains, 6 degrees of freedom) as a two layered laminate, so that different fiber angles could be modeled.

In a direct comparison of the results at 0° the simulation does not seem to fit the test results very well, compare Figure 62, but certain observations during the test have to be taken into account. In the beginning of the test almost every 0°-sample was observed to slide slightly in the brackets holding the sample. This of course produces a misleading plotting of the displacement-force curve. This effect is probably a result of the surface and general architecture of the specimen. The high TPE content makes the specimen very soft in the thickness (z-) direction, making it very difficult to fixate in the tensile-test machine (without breaking the fibers).

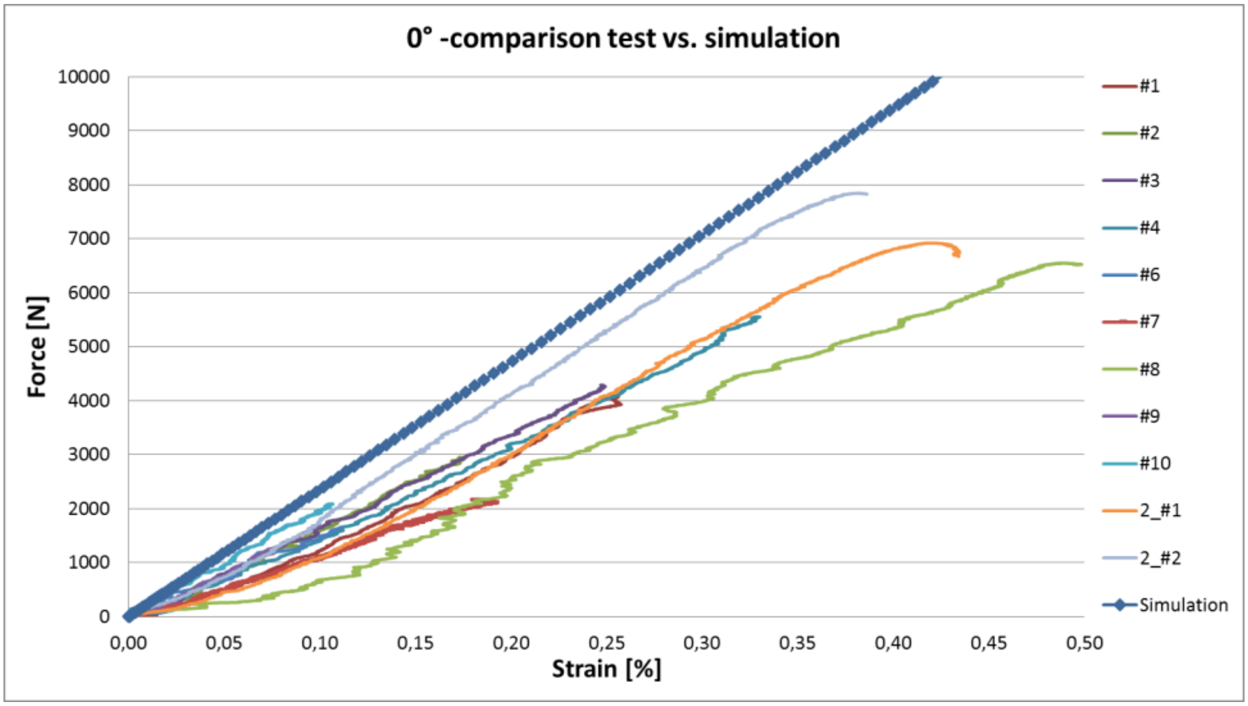

Figure 62: Comparison of 0° tensile test with simulation

The setup of the FE-model does not allow such phenomena to occur, resulting in an idealistic force-strain curve. If approximately the first 0,1% of strain are left-out of the comparison the test curves show an almost parallel behavior with the simulation curve. Based on this observation it can be said, that the simulation is able to accurately predict the behavior of the material in 0°-direction under idealistic conditions.

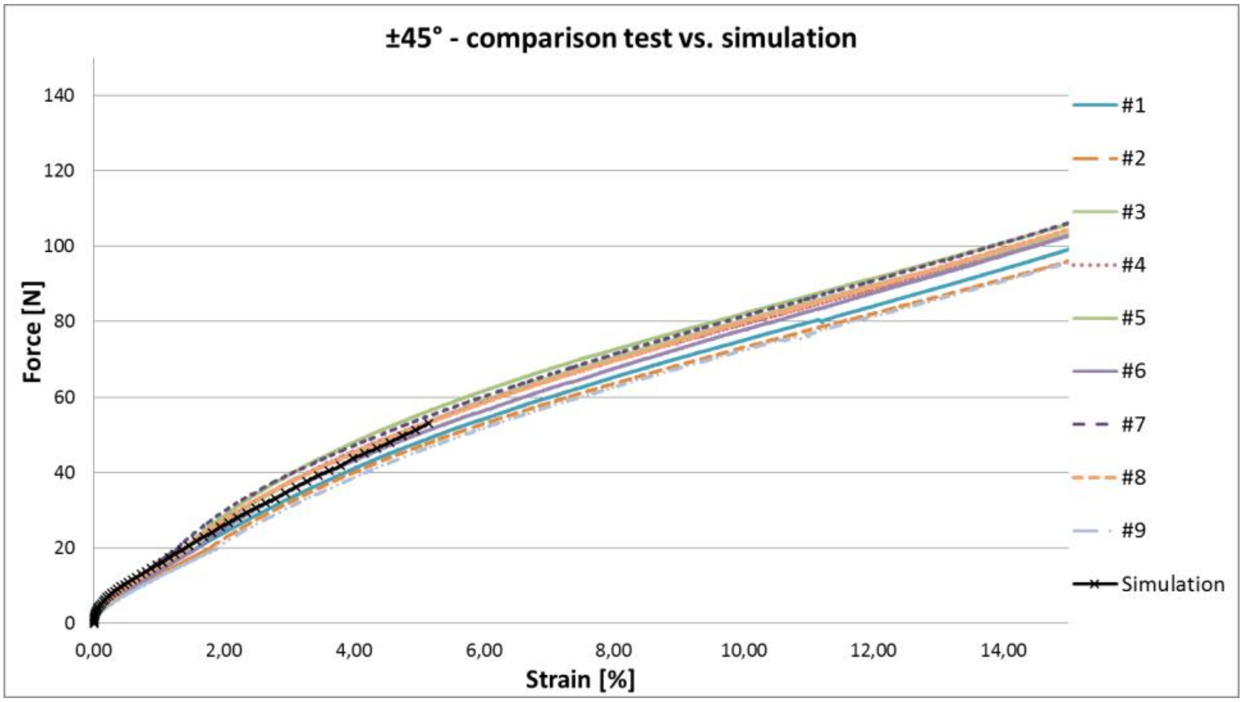

Figure 63: Comparison of ±45° tensile test with simulation

For further validation of the model, a comparison between ±45° test results and simulation was performed. The basic setup for the simulation was identical to the 0° setup except of course a change in fiber angle. In Figure 63 the result of this comparison can be seen. It can be observed that the simulation and the test show the same behavior until 5% strain, after which the simulation was stopped due to the limitation of the simulation model. Due to the “early” stop in the simulation a full comparison is not possible, but the simulation again shows a tendency to be too stiff. Obviously the simulation is not able to represent the non-linear material behavior of the TPE-matrix, which is a likely reason for the observed discrepancy between the two. In addition to the 0° and the ±45° comparison a comparison was made between the 90°- test results and a 90° simulation. As stated above the simulation model remains unchanged, simply the fiber-angle was changed.

In Figure 64 the simulation results can be seen in relation to the test-results. The test results of the 90° specimens are not as closely distributed as the ±45° results, therefore a mean curve of all 90°-tests is included. Compared against this curve the simulation shows an acceptable behavior, nonetheless it has to be noted that the simulation behaves not stiff enough up to roughly 3,5% strain, after this point the simulation behavior becomes stiffer than the material. This overall mismatch is again a result of the highly non-linear material characteristic of the TPE matrix.

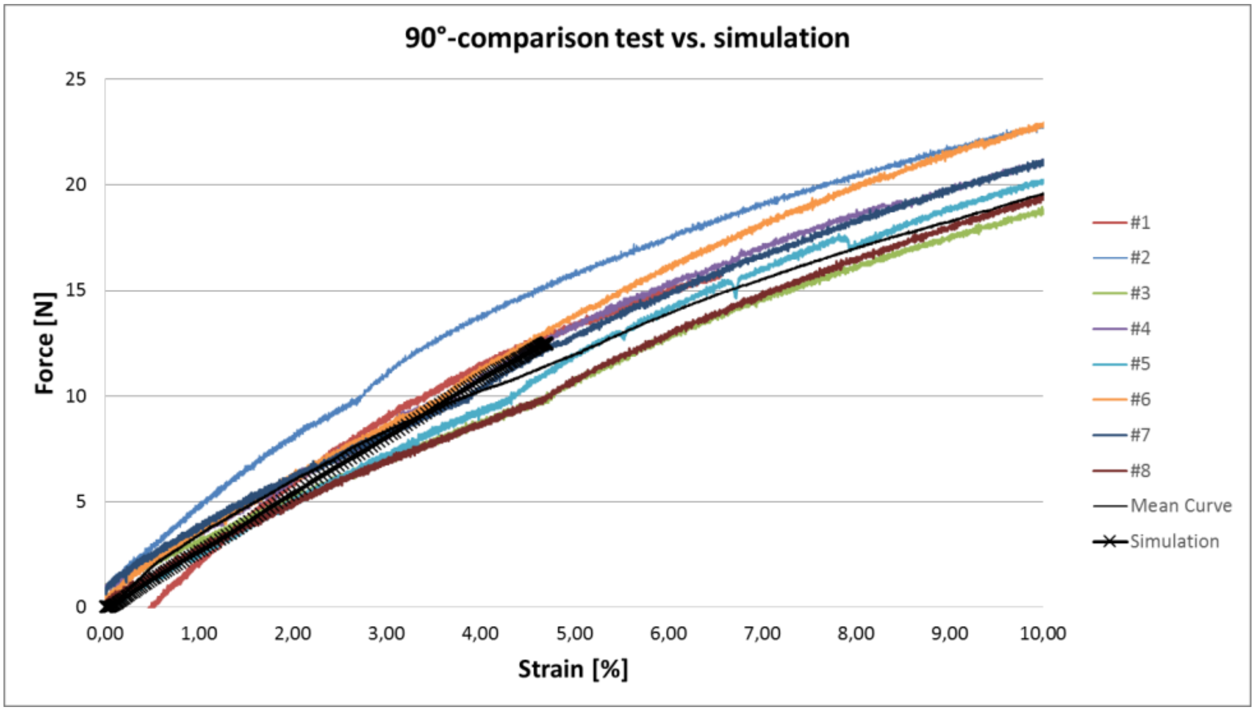

Figure 64: Comparison of 90° tensile test with simulation

To complete the picture a comparison was also made between a simulation model and 3-point bending tests. The simulation model was a geometrical replica of the 3 point bending tests described above in chapter 6.5.4, the material model was the same as for the tensile simulation. In Figure 65 the result of this comparison can be seen. To understand this comparison it is important to highlight that while non-linear modelling was used for the simulation, this model was not capable to represent mathematical instabilities like buckling. Additionally the material model used for this simulation was a standard linear material model, without consideration for localized failure modes in the material. During the test localized fiber-buckling could be observed; starting around 2mm displacement. This localized fiber-failure leads to a decrease in stiffness, which the FE-model cannot duplicate. Therefore after a certain deformation is reached the stiffness of the simulation is too high. Despite this discrepancy the simulation is able to reproduce the bending behavior of the material quiet well (in the linear range).

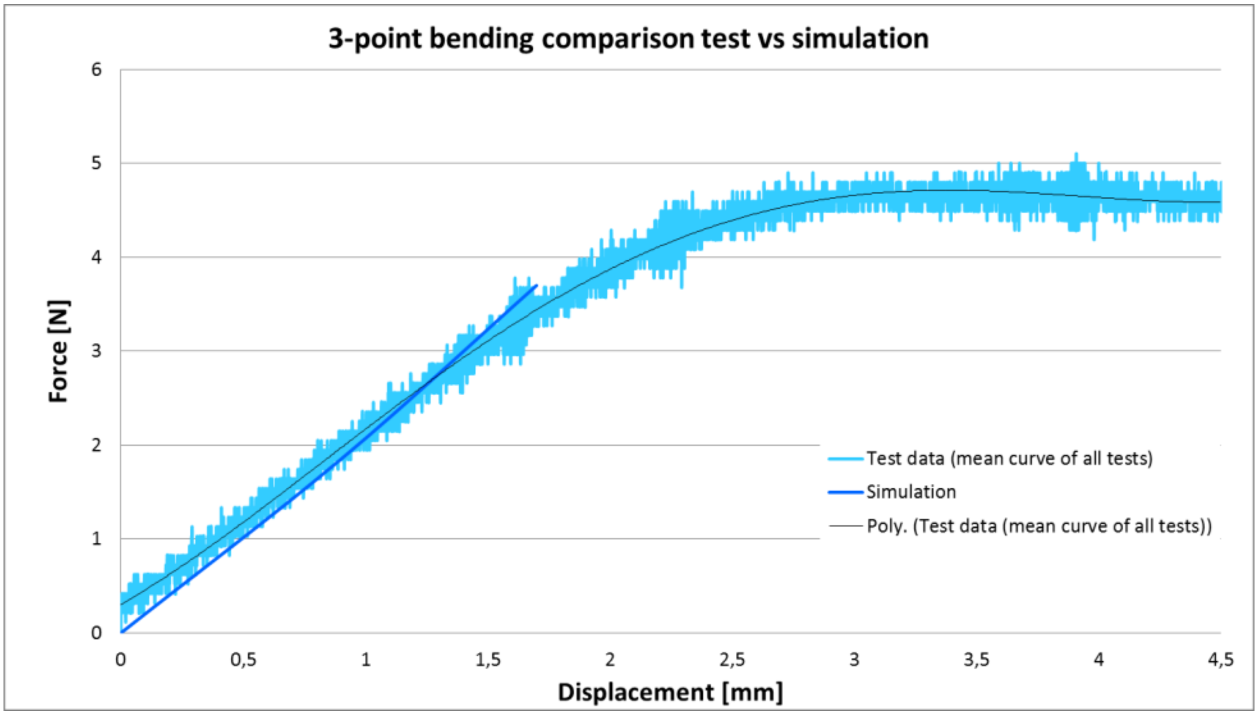

Figure 65: Comparison of 3-point bending test with simulation

In Table 17 three possible material simulation methods are listed. Of these two were discussed in the previous paragraph and the orthotropic material formulation proved to be able to simulate the material behavior satisfactorily up to 5% strain. The third approach to describe the material behavior is discussed in chapter 6.7. It shows that while the enhanced Mooney-Rivlin model is able to represent the behavior at 0° and 90° the angles in between are not so easily represented as the fiber-stretch ratio was not captured during the tensile tests. Additional testing and modeling effort is needed to complete the model and verify its accuracy (both were outside the scope of this work), especially with regard the interaction of the fibers and the matrix.

An additional possibility, not listed in the table as it would make the use of 3D elements necessary, is the idea to simulate the matrix and the fiber as separate entities in the same model. Creating such a simulation is while very accurate (when all relevant data is available, especially data on interaction between fiber and matrix) is also very complex (resolution of the mesh has to resolve individual fibers) and not easily adapted to a new geometry. While it is possible to use e.g. superelements[4] to reduce the modelling complexity slightly the overall increase in simulation effort spoke against this approach.

---

[4] "*The behavior of various component [called superelements] is captured with lesser number of degrees of freedom [called master nodes]. The characteristics of the full system model are achieved by enforcing equilibrium and compatibility along the interfaces of these superelements. This reduction in model provides an efficient solution for large assemblies without losing accuracy"; Rajiv Rath in Ansys-Blog: Analysis of Large Assemblies using Superelements in ANSYS Workbench, 2013.*

6.7 Flexible matrix composite material models

As described in a previous section the composite material developed during this study, cannot be properly described using classical laminate theory (CLT). Therefore different material models were investigated to accurately describe the hyperelastic and anisotropic behavior of the material under load. As the fibers in the material, regarding a single ply, are all oriented in one direction, it is an accurate conclusion to describe the material as transversely isotropic *[Kress et al., 2006]*.

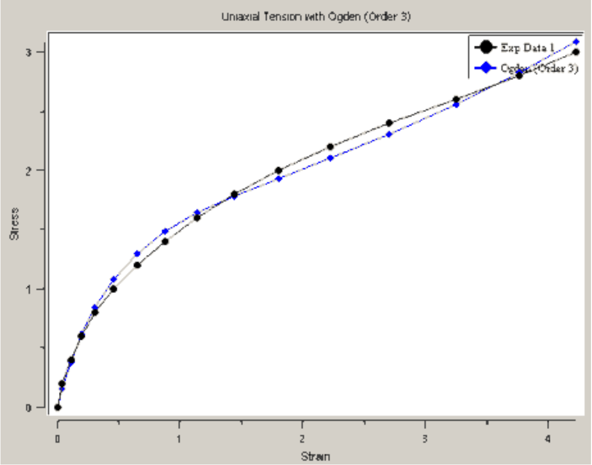

Figure 66: Stress-Strain curve of a TPE tensile test with an Ogden-curve-fit (3rd order)

It is important to understand that at large deformation (higher than 3-5% strain) the elasticity and shear modulus of materials are no longer constant, therefore Hook's (simplified) law is no longer applicable. For the correct description of these materials several different models exist, e.g. Mooney-Rivlin, James-Green-Simpson and Ogden, see chapter 6. These models use the data from stress-strain-curves to calculate certain material dependent parameters. With these parameters the stress-strain-curve is approximated. In comparison with the mentioned models the Ogden model shows the best fit with the test data, see Figure 66 and Figure 43. It incorporates a non-constant shear modulus and allows for compressible material-behavior. Also it is accurate up to a strain of 700%. The other two mentioned models are easier to calculate but do not have the accuracy or the range of the Ogden-model. Mooney-Rivlin is only applicable up to 100% strain and delivers bad results when calculating pressure forces. It also does not include the stiffening of the material for large strains. The James-Green-Simpson-model can become instable. As explained in in chapter 6 these models call for an isotropic material behavior. This is clearly not true for the FMC material. The Ogden model (or any other) can be used to describe the behavior in one direction quiet well, but cannot describe an orthotropic or even transversely isotropic material. For each test case (fiber angle) a new strain-energy potential has to be calculated, which is of course very impractical for any type of characterization or simulation of the material; mostly because the simulation has to be able to handle large deformations and very likely large distortions of the material.

For characterization of anisotropic materials two models were introduced in chapter 6.2, which can originally be found in biomechanics; namely the generalized Fung model *[Fung, 1993]* and the Holzapfel-Gasser-Ogden *[Gasser et al., 2006]* model. These models allow anisotropic material-behavior in connection with hyperelastic characteristic. The difficulty with these two models is that they were developed to describe biological tissue and not engineering materials. Both models were not able to handle the large difference in stiffness between the matrix material and the fibers. Additionally the models base the impact of the fibers on the strain energy on exponential functions, which does not fit the behavior of the fibers used in this study. Carbon and Glass have a linear stress-strain behavior in the relevant strain-range. As such a third model was found by *[Brown et al., 2011]*, which had been developed just for this kind of application. It is an extension of the standard Mooney-Rivlin model with an extra term to describe the anisotropic behavior. Also relevant to this development is *[Ishikawa et al., 2008]*.

6.7.1 Enhanced Mooney-Rivlin model for flexible matrix composites

An alternative approach to anisotropic behavior of hyperelastic material was chosen by *Brown et al, 2011.* In comparison to the previously presented models by Fung and Holzapfel et al. the enhanced standard model looks to combine hyperelastic behavior with linear-elastic elements. With this the model is able to describe fiber-reinforced elastomers. As a baseline the model uses the above described Mooney-Rivlin model. This is enhanced with an invariant based element for the reinforcing fibers. This model is able to accurately predict the behavior of the material for strains up to 10-30%.

The standard Mooney-Rivlin model, written in terms of invariants I_1 and I_2:

$$W^M = C_{10}(\lambda_1^2 + \lambda_2^2 + \lambda_3^2 - 3) + C_{01}(\lambda_1^2\lambda_2^2 + \lambda_2^2\lambda_3^2 + \lambda_3^2\lambda_1^2 - 3) = C_{10}(I_1 - 3) + C_{01}(I_2 - 3) \qquad (33)$$

In terms of stress (simplified for uniaxial loading), the model can be written as

$$\sigma_{11} = (2C_{10} + \frac{2C_{01}}{\lambda_1})(\lambda_1^2 - \frac{1}{\lambda_1}) \qquad (34)$$

To accommodate the transverse isotropy of the material in the model a strain-energy function was calculated based on the work of *[Brown et al. 2011]* to add to the standard Mooney-Rivlin model, here to the three Invariants from the Chauchy-Green tensor one (or two) Invariant has to be added:

$$W^F = C_4(\sqrt{I_4} - 1)^2 \qquad (35)$$

with: $\mathrm{I}_4 = \boldsymbol{a}_0\,\mathbf{C}\,\boldsymbol{a}_0 = \mathbf{C}{:}\,(\boldsymbol{a}_0 \otimes \boldsymbol{a}_0) = \lambda_\mathrm{f}^2$

λ_f: stretch ratio in fiber direction

$\boldsymbol{a}_o$: orientation of the fibers in the material (undeformed)

Resulting in a combined equation for the orthotropic material:

$$W = W^F + W^M = C_{10}(I_1 - 3) + C_{01}(I_2 - 3) + C_4(\sqrt{I_4} - 1)^2 \qquad (36)$$

The test results presented in chapter 6.5 were used to calculate the constants C_{10}, C_{01} and C_4, see Table 19.

Table 19: Constants for the mod. Mooney-Rivlin-Model [N/mm²]

C_{10}	C_{01}	C_4
-0,62	1,42	22500

Figure 67 and Figure 68 show a comparison between tensile test results and the analytical model. The model is able to replicate the behavior of the material for 0° and 90° very well. For intermediate angles the model is a lot more difficult to use, as the stretch of the fibers is an important input parameter, which based on the test data, can only be extrapolated. Additionally it still has the same limitations the standard Mooney-Rivlin model has. As only tensile test data is available, this model is not complete and cannot calculate compression behavior (e.g. pure compression or bending), and as such will not be further used in this work.

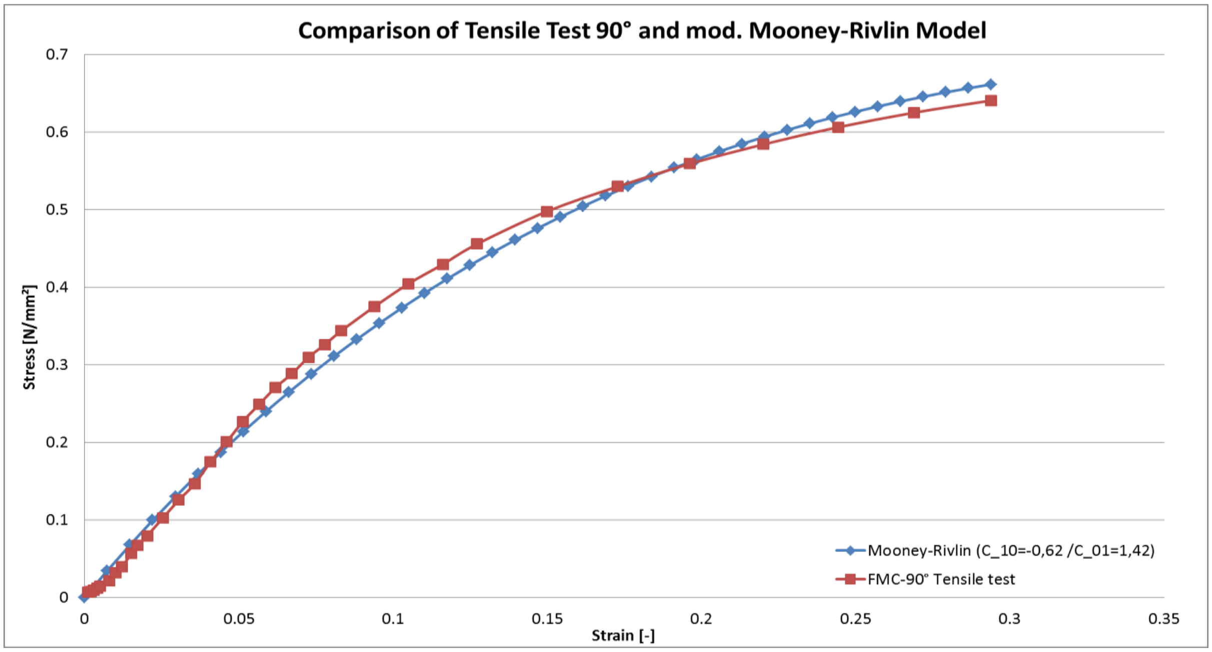

Figure 67: Comparison between Experimental Data 90° & mod. Mooney-Rivlin Model

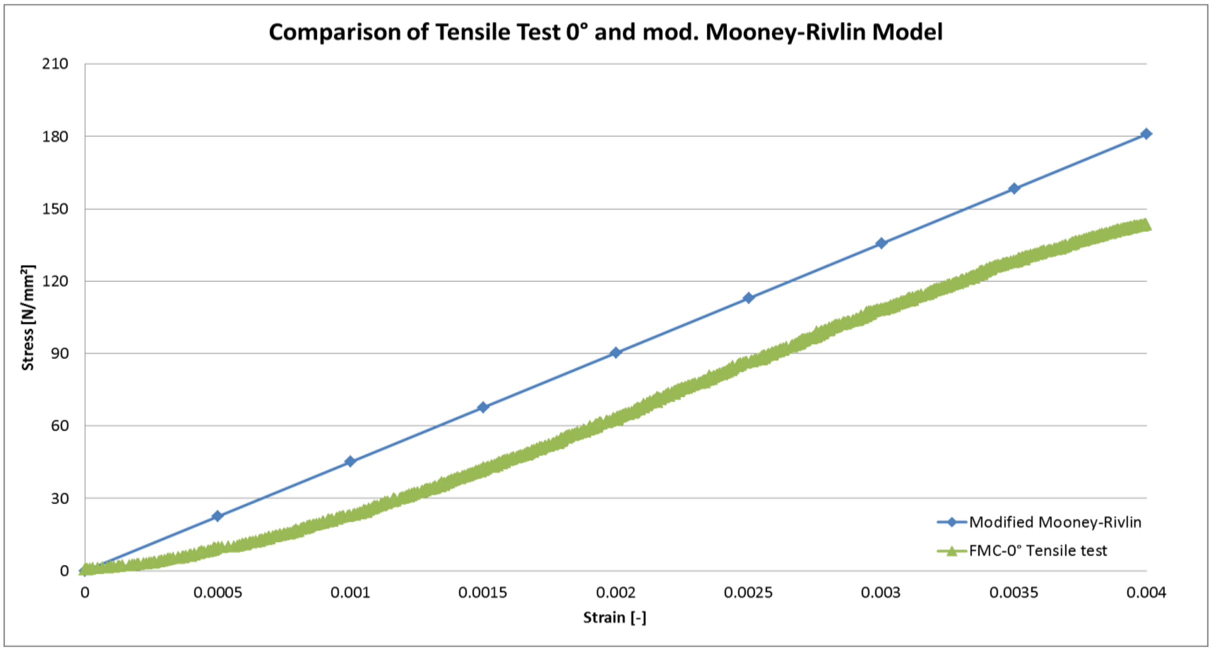

Figure 68: Comparison between Experimental Data 0° & mod. Mooney-Rivlin Model

7. Pneumatic actuator prototypes

With the two possible actuator principles (chapter 4.1 and 4.2) in mind several prototypes were manufactured and tested. To outline the boundary conditions for these tests the tube's pressure range was determined from the pressure distribution on the nose at maximum deflection, which is the worst case (load-wise) for the nose *[DLR, Kühn et al, 2010]*. The highest Δp is 0,0184 N/mm² at the stagnation point, this is therefore one of the dimensioning loads for the actuation-system. Additionally to deform the nose the actuation system also has to overcome the stiffness of the nose-skin. As the desired deflection is predominantly perpendicular to the force on the stagnation-point the structural stiffness and the maximum pressure can be handled mostly separately when designing the actuator.

The first prototypes are circular and have different fiber layups. Several actuators were manufactured with a balanced 0°/90° fiber layup to achieve a flexible but non-stretchable skin. Some prototypes have only 0°-fibers running the length or only a TPE skin, to achieve a flexible, stretchable skin. Additionally actuators were manufactured with a 0°-baseline with the patches of 90°-fibers running the whole length. The patches are 30°-wide and on the outside of the specimen, which will locally create a non-symmetric laminate.

All prototypes have a diameter of 80mm and are 400mm long. Based on these dimensions and the data collected during the tensile tests, it was possible to calculate the expected internal non-failure (minimum) pressure for different skin-thicknesses. For this the strain in axial and tangential direction was considered separately, as the maximum strain allowable in the two principal directions depended on the fiber angle. For the calculation the wall thickness ranges from 0,5mm to 3 mm; additionally the calculation for the tangential results took the inflation of the tubes into account. For this the data from the tensile test was used as such that always a stress/strain pair was used to calculate the corresponding internal pressure based on the related expanded diameter. Based on the results of these calculation it is now possible to predict a certain failure pressure for the prototypes. Figure 69 and Figure 70 show the complete results of these calculations. The appendage "*tangential*" means results based on maximum tangential allowable stress, the appendage "*axial*" is to be understood equally. Only for some fiber angles tangential and axial results are shown, this was done, because in all other cases the results in the other direction were a lot higher than the ones shown, and therefore not relevant as failure cases.

It was not possible to calculate a final failure pressure as no clear failure occurred during tensile testing.

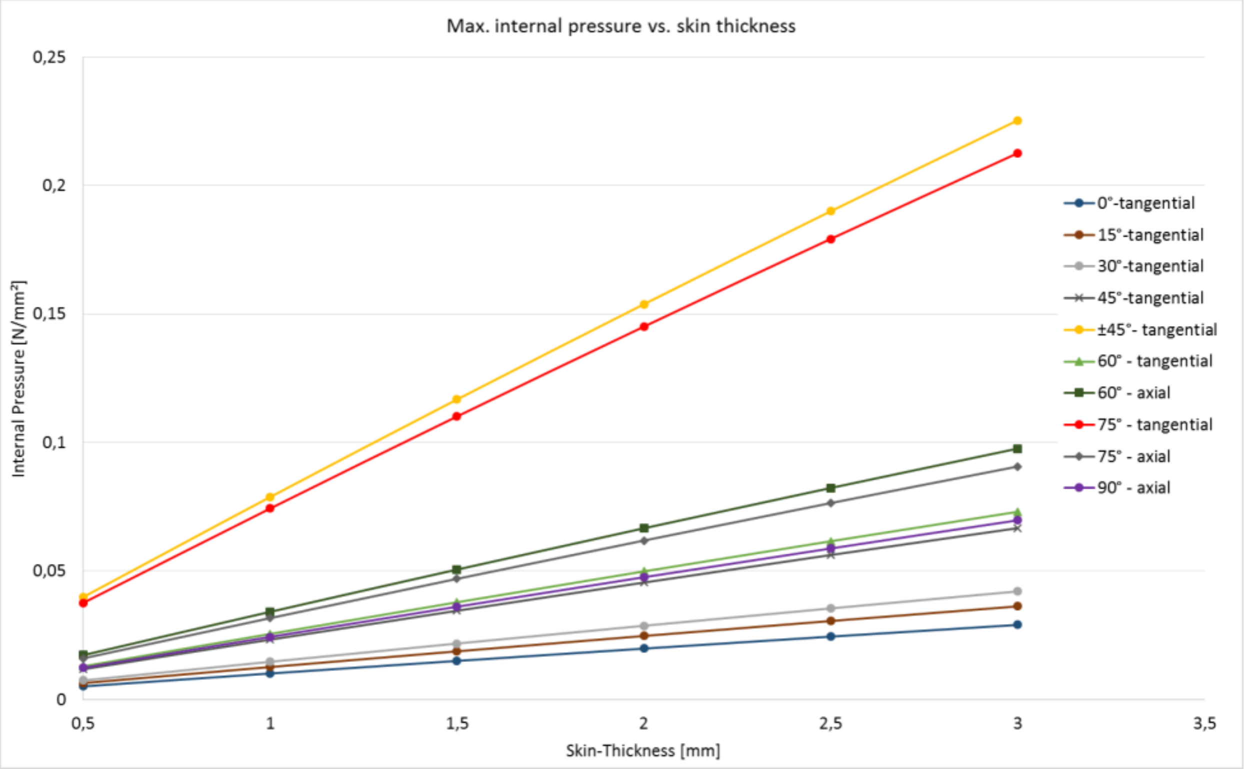

Figure 69: Expected maximum internal pressure of the actuators with regard to fiber angle and skin thickness (1)

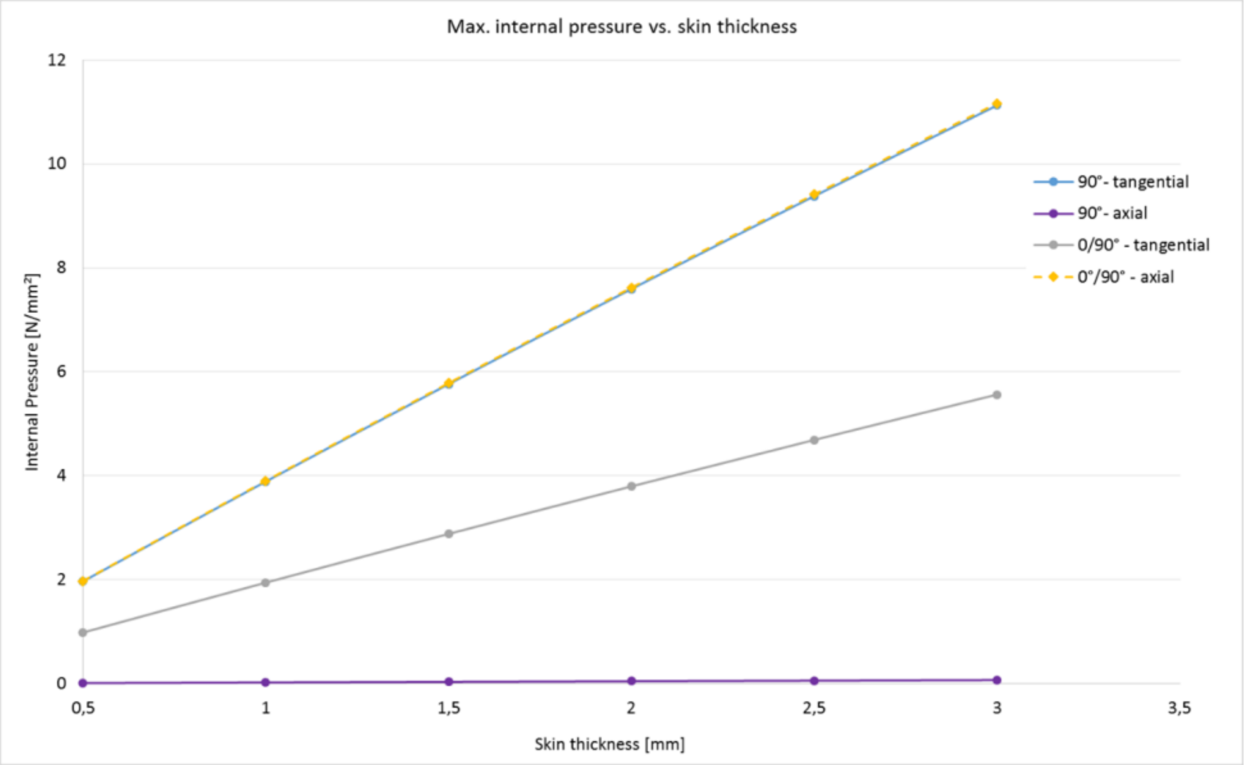

Figure 70: Expected maximum internal pressure of the actuators with regard to fiber angle and skin thickness (2)

7.1 Manufacturing of the pneumatic actuators

The manufacturing of the actuators has to be separated into two sections. First the actuator skin manufacturing and secondly the end-cap manufacturing is described.

7.1.1 Actuator skin manufacturing

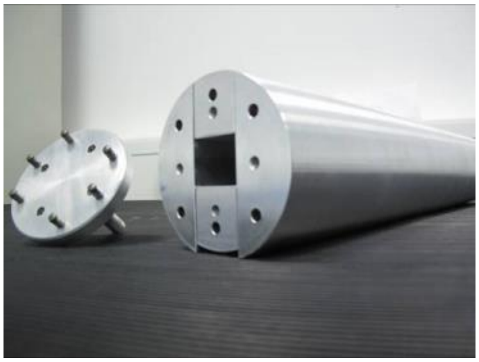

Figure 71: Mandrel for actuation tube manufacturing

The actuators are created similar to composite preforms (layer by layer) on a hot core insert. The mandrel was designed so that it can be removed from the circular tube without damaging it. It consists of 4 main parts, as can be seen in Figure 71. At the moment the actuators are created with open ends and fitted with metal-caps after the mandrel was removed. Using this mandrel a number of prototypes have been produced to develop a suitable production process. The manufactured prototypes were also tested to verify the calculated load carrying capability (based on the tensile test results).

The manufacturing follows the basic principles as any construction using prepreg-(like)-material. The material is prepared and cut to the right size. After that as a first draping step a TPE foil is draped over the mandrel then follow several layers of FMC-plies, depending on the planned stacking sequence and the targeted fiber-volume-fraction (FMC-plies are intermixed with TPE-foil to regulate the fiber-volume fraction). The outer skin is also a TPE-foil, depending on the final wall-thickness. It is in some cases advisable to pre-compact the lay-up to avoid crimping. Crimping of the TPE foil is usually smoothed during the heating and compacting. Crimping of the FMC-plies has to be avoided. As a final step the whole setup is heated to 130°C and compacted onto the mandrel using a vacuum bag for one hour. During this time the temperature has to remain constant. In Figure 72 a prototype is shown shortly after the heating phase, cooling down to approx. 20°C room-temperature. For the cool-down period the vacuum remains intact, to avoid unwanted deformation of the laminate.

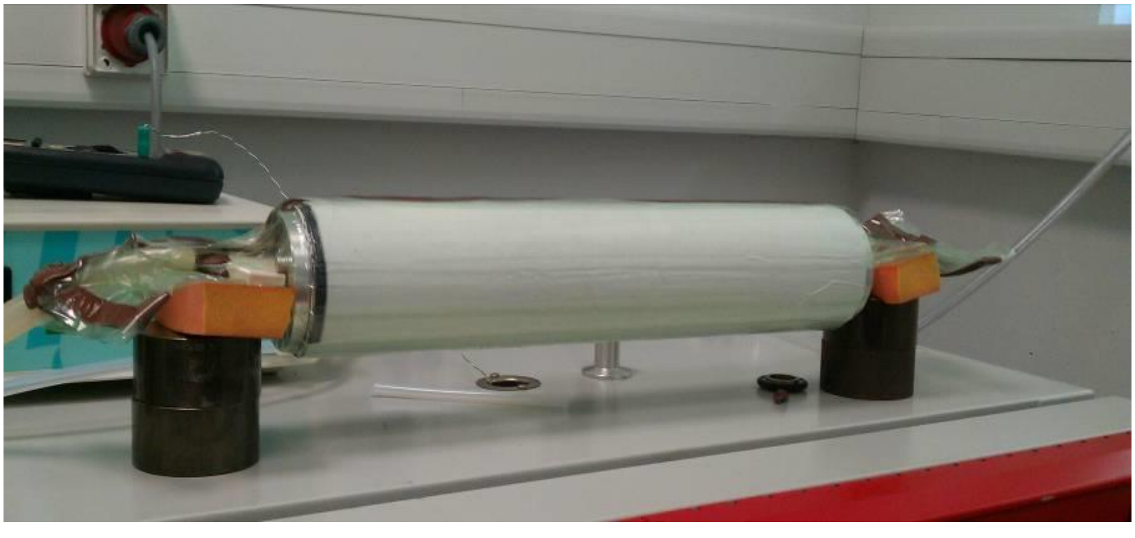

Figure 72: Prototype during manufacturing in a vacuum bag (during cool-down period)

Table 20: Types of prototype actuators manufactured

Prototype Name	Quantity	Pressure Tested	Comments
Pure TPE	2	1	First was just a manufacturing trial, second was tested
0° (with and w/o fiber patches)	4	3	Manufacturing trials and baseline for further tests
0°/90°	3	2	All three were later used for the demonstrator
0° with rubbber	1	-	Manufacturing trial with a 0,5mm natural rubber skin

As the TPE matrix material has a very low stiffness manufacturing trials were performed to combine FMCs with rubber. The adhesion between the two materials proved to be very good, the production process on the other hand was not suited for rubber. It was impossible to remove the mandrel after the vulcanizing of the rubber without destroying the actuator. Therefore this prototype could not be pressure tested. The various prototypes are summarized in Table 20.

7.1.2 End caps manufacturing

As the actuators were manufactured with open ends, end-caps were needed to make the actuators airtight. For the testing of the prototype and with regard to the planned use of the actuator several possibilities were looked at.

An easy solution was metal end-caps. They are durable and have a higher stiffness than the actuators, and are therefore guaranteed to be not the point of failure. And as such perfect for testing with regard to failure cases and behavior of the skin material. Regrettably the high stiffness reduces and interferes with the deformation of the actuator. Two different types of metal end-caps were used for the testing of the actuator, depending in part on the fiber layup. As explained previously two different actuator concepts were regarded. For a skin that allowed large skin-strain the shape of the end-cap was not as relevant as for non-stretchable skin. Therefore for stretchable skin a round end-cap was used. This was done not so much with regard to the actuator but with regard to the testing. A round end-cap was a lot easier to manufacture and to seal airtight, than e.g. an elliptical end-cap. After the first successful tests with the round end-caps, see Figure 73a, tests for non-stretchable skin actuators were performed with elliptical, metallic end-caps, see Figure 73b. This switch was done as elliptical end-caps are closer in shape to the proposed uninflated shape of the actuators for the droop nose.

Figure 73a: Prototype before testing with round, metallic end caps

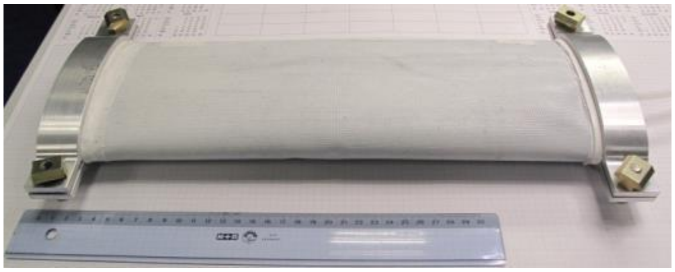

Figure 73b: Prototype before testing with elliptic, metallic end

For testing of the prototypes metal end-caps worked very well, but they possess several drawbacks. It was already mentioned that metallic end-caps are a lot stiffer than the skin material of the actuators. This fact results in an abrupt change in stiffness at the transition between the actuator and the end-cap. This transition leads on the one hand to a high stress concentration in the skin material and can result in failure of such (fatigue hot-spot) or on the other hand this sudden jump in stiffness may cause a sharp change in deformation gradient (very small bending radius) which in this particular case can lead to a breaking of the fibers in the FMC-material. Both cases can result in a failure of the actuator.

To try to mitigate these failure cases different types of end-caps were looked at. One additional design condition was that the end-caps should also not hinder the deformation of the actuators. As such end-caps made out of TPE were tested. For this different shapes of end-caps were built and tested. At this point it is important to note, that flexible end-caps have to perform quit complex deformations depending on their "starting"-shape.


Figure 74: Elliptical TPE End cap

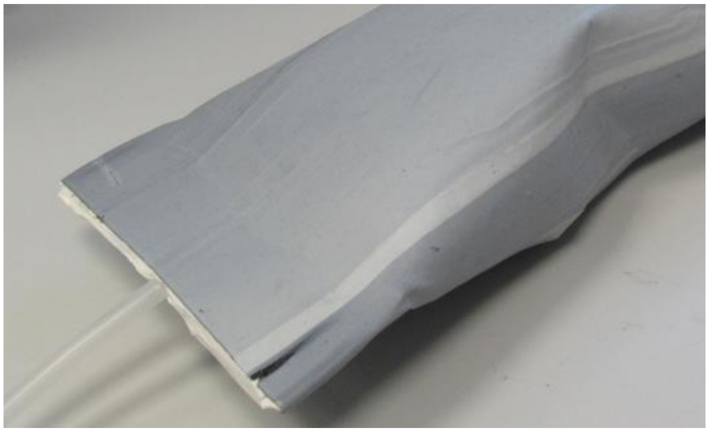
Figure 75: Minimum space TPE End-cap

As a first test the elliptical metal end-cap was "replaced" by a TPE-end-cap of similar shape, see Figure 74. One benefit of a full TPE end-cap is, that is can be attached to the actuator by heating both parts to liquefy the surface of both parts. Additional to the elliptical TPE end-cap several other types of TPE end-caps were tested, with varying results. The elliptical TPE end-cap and the minimum space TPE end-cap (see Figure 75) were successfully tested at 0,03 N/mm²; meaning no failure occurred. The minimum space end-cap resulted in "buckling" of the fibers, which can be seen in Figure 75 (right side). Further tests with a single walled TPE end cap, Figure 76, and a flat triangular end cap, Figure 77, were performed with varying success. Due to the small contact area the single wall end cap lacked the connection to the tube to withstand pressure. Leakage occurred almost instantly. The triangular end cap proved to be a more successful concept. But it showed a similar deformation behavior as the minimum space end cap. The buckling occurred later in the inflation process but it appeared. Buckling does not lead to immediate failure of the actuator but it can weaken the structure over time and is an undesired deformation. At this point no final solution for this application was found, but the metallic endcaps worked sufficiently for the scope of this work (and proved to be the best alternative despite their drawbacks and limitations).

Figure 76: Single walled TPE End cap

Figure 77: Flat triangular TPE End Cap

7.2 Pneumatic actuator testing

Several actuators with different fiber-layups were manufactured and then tested. In Table 21 the different tested prototypes are listed. For the tests metallic (round and elliptic) end caps were used, see Figure 73a and Figure 73b. The air supply was attached via one of the end-caps. The pressure measurements were performed with a precision compensated pressure sensor from PRO (HDOB002GY8P) with a measurement range of 0-0,2 N/mm². With regard to the 0°/90° actuators this maximum testing limit seems a bit low, but due to safety concerns it was decided to limit the maximum pressure to this value.

Table 21: Pneumatic tests of the prototype actuators (* maximum overall pressure reached)

Test #	Fiber Layup	Thickness [mm]	Minimum pressure [N/mm²]	Max. pressure [N/mm²]	Failure behavior
1	0° with 90° patch	1,9	0,02	0,035	Rent of matrix
2	0° with 90° patch	2,4	0,025	0,05	Rent of matrix, delamination
3	0° with 90° patch	1,7	0,015	0,04	Rent of matrix
4	TPE	1,5	-	0,015	Rent of material
5	0°	2,5	0,025	0,03	Rent of matrix
6	0°/90°	2,2	0,38	0,2*	-
7	0°/90°	2,2	0,38	0,18	Sealing failure between actuator and endcap

All prototypes performed successfully past the expected minimal pressure, except test #7 where a failure in the sealing between end-cap and actuator occurred. The test specimens with the 90° patches show a slightly higher failure pressure than the test specimen with just 0° fibers. This is in line with expectations as the 90° fibers reduce the possible maximum strain of the actuator. The diameter is therefore reduced, which in turn reduces the strain in the material (compare formula 3). But the 90° patch also introduces a discontinuity in stiffness, creating a “stress concentration line”. The stress concentration was expected and observed to be at its highest in the middle of the actuator (axially). The reason for this is the maximum deformation occurs in the middle of the actuator, as the metallic end caps create a relative large boundary effect (meaning they hinder the deformation over a rather large area). All specimens with a 90° patch failed at the transition. The patches were tested to simulate an area-attachment of the actuators to e.g. solid structure or another actuator.

During the test of the TPE only actuator it could be observed that there was a variance in stiffness of the TPE matrix material. Additional tensile tests of very thin TPE strips came to the same results. This phenomenon can be explained with the distribution of the molecular “fibers” of the TPE material. Depending on the manufacturing method the molecules align in more or less uncoordinated directions. As the TPE foils for these tests were produced with a pressure mould the stiffness distribution observed could be explained. Looking at such a foil the stiffness was more or less isotropic in the center of the sheet, and more or less orthotropic away from the center, with the main axis of the orthotropy pointing at the center of the sheet. The molecules align with the direction of the flow. This behavior has to be kept in mind for the design/manufacturing of actuators with stretchable skin.

Concluding can be said, that the actuators performed as expected based on the material tests and the skin thickness calculations. The tests with the end caps showed sufficient performance of the metal end-caps for the scope of this work. Further development and tests to increase the performance of the non-metal end-caps is necessary and suggested to be included in future work.

7.2.1 Comparison of 3D-deformation simulation and testing

For further validation of the simulation model the developed actuators (see chapter 7.1) were simulated and compared to test cases. This simulation should conclude if the model is capable of reproducing the observed inflation behavior. For comparison the result of the simulation were projected onto a picture of inflation testing, to verify the simulation and document any differences. In Table 22 the material parameters used for this simulation are shown, here a 0°/90° orientation of fibers was used to limit the deformation to be flexible but non-stretchable. The skin thickness was as for the real demonstrator 2,5mm. For the modeling of the actuators the knowledge gained in the previous two chapters was used. The actuators were modeled using the orthotropic material model discussed in chapter 6.6.2 and the simulation parameters were taken from the results in chapter 5.2.2 (see the actuator columns in Table 6 and Table 7 for the details), with the exception of the element size which was reduced to 2mm to increase the accuracy.

Table 22: Material parameters for the actuator simulation (in N/mm²)

E_{11}	E_{22}	E_{33}	ν_{12}	ν_{13}	ν_{23}	G_{12}	G_{13}	G_{23}
47000	47000	4,5	0	0	0	3,5	3,5	3,5

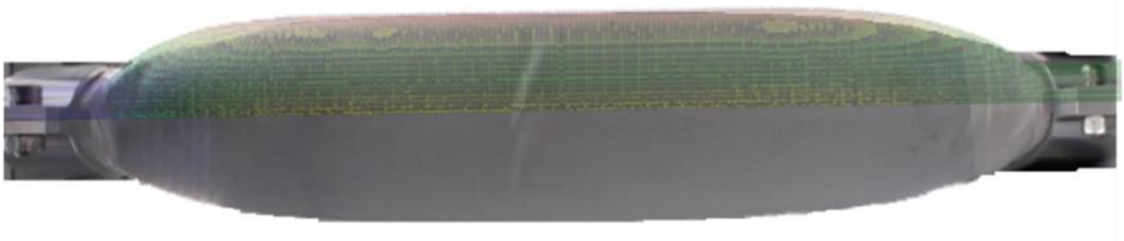

Figure 78: Actuator with partial simulation overlay

Figure 79: Actuator with simulation overlay (seen from "top")

In Figure 78 an inflated actuator can be seen. The internal pressure is at $\Delta p = 0{,}022\ \frac{N}{mm^2}$. As an overlay half of a simulated actuator is shown as a comparison. In Figure 79 the same actuator with a simulation overlay can be seen, only from a different perspective (90° rotated around the central axis). It can be observed that the maximum inflation in the middle of the actuator is a very good match between simulation and test, the boundary effect of the metal end caps in the test appears to be stronger than in the simulation. The simulation shows a “faster” expansion. One reason for this could be an increase in stiffness in this area on the real actuator due to sealing material, which was not included in the simulation.

Concluding it can be said that the chosen material and simulation model is capable of accurately simulating the material behavior within certain limits. As described above the model is not able to simulate the behavior above 5% strain or take failure-modes into account. This means that any complex simulation have to be checked for any of the limitations discussed and observed above. It was shown that the simulation is able to correctly reproduce the deformation behavior of complex structures. The developed model should therefore be able to correctly predict the behavior of the proposed actuation systems.

To represent higher strain behavior of the actuators different material models would have to be used, several possible options were presented in chapter 6.2. For purely tensile-like behavior the data available (test-data) is sufficient. A 2D inflation simulation of an actuator is possible with these models, however if the simulation should represent a fully 3D behavior the available data is not sufficient.

8. Pneumatic actuation of a droop nose

In chapter 3.1 different concepts for possible pneumatic actuation systems were introduced and a preliminary assessment was performed. With a verified simulation model it was now possible to perform FE simulation of the different concepts. As a baseline the simulation results were always compared to the required target shape. After the comparison with each other a sensitivity study of the most promising concept was performed. This included different position of the actuators, different geometry of the support structure, different loads and a difference in skin stiffness of the droop nose.

A list of requirements for the pneumatic actuation tubes was created based on the mechanical system developed in SADE. The foremost parameter for the design of the actuator or actuation-system for the droop nose is the maximum required droop and force. For the SADE geometry the maximum movement in a downward direction is 18 cm and the maximum force is reached at the maximum droop during landing maneuver. As the actuators do not act just locally but two-dimensional no “maximum” force can be named. The maximum pressure depends on the interaction area between the actuator(s) and the nose-skin. As an orientation a pressure-range between $0{,}002\frac{N}{mm^2} \leq \Delta p \leq 0{,}5\ \frac{N}{mm^2}$ can be expected, based on the known air-loads in the two different flight cases, the stiffness of the skin and the size of the actuator. The calculation is based on the known and measured forces of the mechanical SADE actuation system, scaled to the simulation model. One station of the mechanical system was designed to provide actuation for a 0,5m long section of leading edge. The here used simulation model is only 0,1m long, see Figure 80.

Multiple factors influence the setup of the pneumatic system.

- Cruise shape
- Drooped shape
- Skin stiffness distribution
- Available space
- Pressure distribution

All these points will be taken into account during the presentation of the simulation of the different concepts; afterwards these points will be used to assess the concepts.

8.1 Description of the droop nose system simulation model

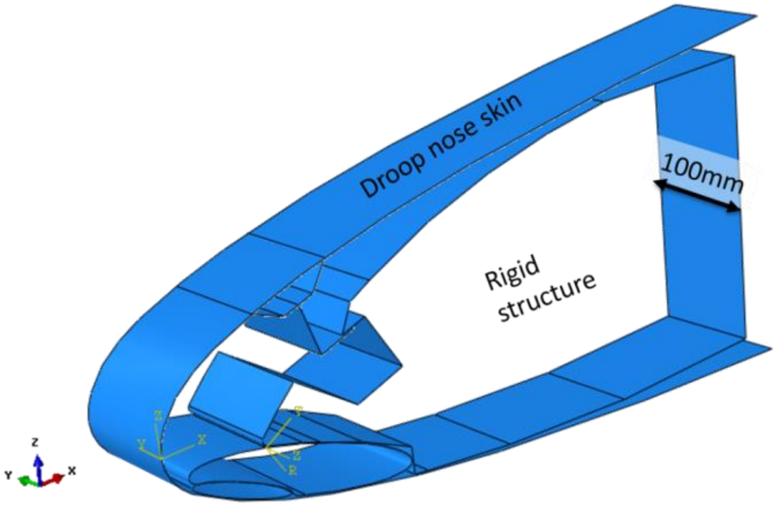

Figure 80: Simulation model, general setup

In Figure 80 the general setup for all simulation models of the pneumatic droop nose actuation system can be seen, on the basis of the stringer hook design with two actuators. The model is a 100mm wide stretched 2D cut of the droop nose skin. The droop nose skin in all simulations is represented by a laminate with a variable ply count and fiber direction, unless otherwise stated. The exact distribution was optimized for the mechanical actuations system by the DLR. For the skin material a GFRP is used with the in Table 23 shown mechanical properties. The skin is modelled with S4R shell elements with an element length of 4mm, the small element size was necessary to represent the stiffness-distribution. For the detailed skin-layup see Appendix H.

Table 23: Mechanical properties if UD GFRP prepreg (Hexply 913 UD S2GL)(in [N/mm²] were appropriate)

E_{11}	E_{22}	E_{33}	ν_{12}	ν_{13}	ν_{23}	G_{12}	G_{13}	G_{23}	ρ [g/cm³]
42000	15000	15000	0,26	0,26	0,26	5600	5600	5600	1,8

The actuators will be simulated with the above verified simulation model (chapter 6.6.2/7.2.1). This means the actuators are modeled with S4R shell-elements (2mm long, due to accuracy) and the material parameters used can be seen in Table 17. As the pressure is expected to be no higher than $\Delta p = 0{,}5\ \frac{N}{mm^2}$ the actuators are simulated with a skin thickness of 1mm (see chapter 7, Figure 69).

On the basis of the "*stringer hook with two actuators concept*" the boundary conditions and load distributions on the structure will be explained. This overview is valid for all design variants and any changes will be remarked upon if necessary. In Figure 81 the boundary conditions and load distribution for the cruise load case are shown. The orange and blue colored symbols depict the boundary conditions. Blue stands for rotational degrees of freedom, orange for translational degrees of freedom.

In Figure 82 the same BC are applied and the cruise load distribution was replaced by the landing load distribution. It is important to note, that the landing load is applied to the undeformed skin. This is of course aerodynamically not correct (or possible). For these simulations it was done regardless, as no load distributions were available for intermediate positions. Also the intermediate positions for the landing case were not relevant (no target shapes available) therefore the precise loading during the deformation process was not important. As pressure is always orthogonal to the surface the pressure distribution in the end-position is correct (if the target shape was achieved). The strain of the skin is also negligible (in comparison to global deformation) and has therefore no relevance to the load distribution.

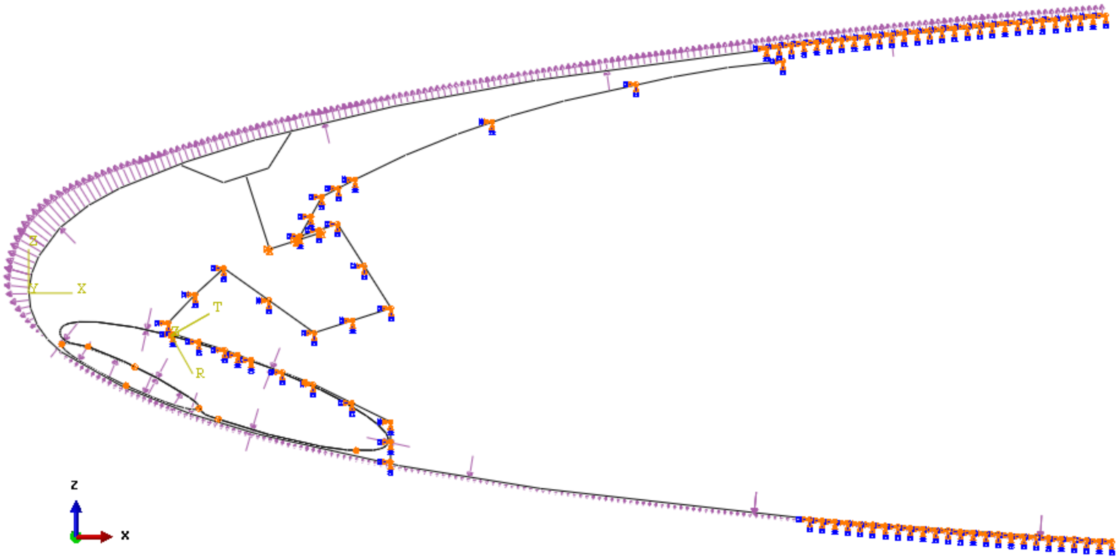

Figure 81: Stringer Hook Design with Cruise Forces and BC

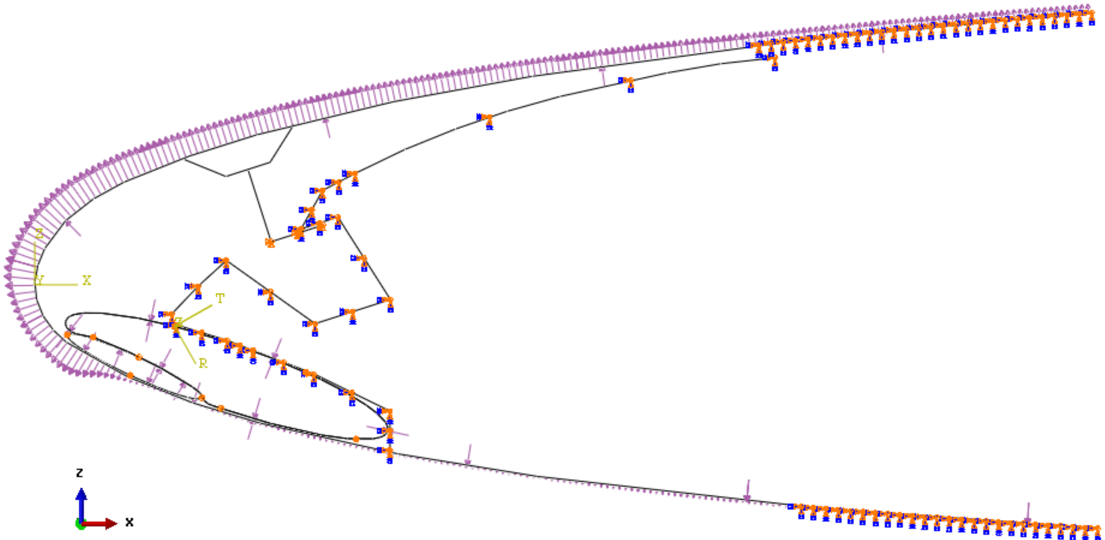

Figure 82: Stringer Hook Design with landing forces and BC

Having chosen shell elements as the preferred discretization for the skin and the actuators it is important to consider which boundary conditions need to be applied and how the different parts interact with each other. As the model is just a representation of a cut-out segment of a complete wing, the boundary conditions have to represent this "infinite" continuation of the model. As such rigid body motion in span-wise direction of the actuators had to be constrained. The boundary condition in the simulation on the skin represent the area in which no deformation is necessary and which is used to attach the skin to the center wing box/front spar. As the deformation response of the static/rigid structure is of no relevance for these comparisons it was modeled as a non-deformable rigid. This reduces the simulation complexity and time.

All simulations were run as quasi-static, dynamic, explicit models based on the results shown in chapter 5, 6.6 and 7.2.1. All forces are applied with a smooth step over a time period of 80ms (unless otherwise mentioned) and the complete runtime of the simulation is 100ms. A smooth step amplitude curve for the loads generate a gradual ramping up in loading in the beginning and a gradual ramping down in the end, see an exemplary curve in Figure 83. If the forces are applied instantaneous on the structure, the overall behavior would rather represent an impact scenario than a quasi-static one, compare Figure 34, Figure 35 and Figure 36.

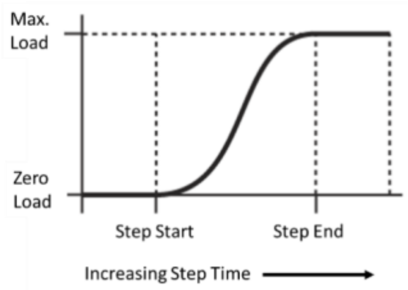

Figure 83: Smooth step function

In Figure 81 and Figure 82 solitary arrows can be seen evenly spaced along the inside of the droop nose skin and the actuators. These arrows symbolize so called "viscous pressure". This pressure has a dampening effect on dynamic effects of all parts. Viscous pressure is one possibility to stabilize a quasi-static dynamic explicit simulation. It is important that the viscous pressure is kept very small, otherwise it would have a too large influence on the overall deformation of the structure. The viscous pressure for the skin is at no times larger than 1e-5. For the actuators it was limited to 1e-6, see explanation and

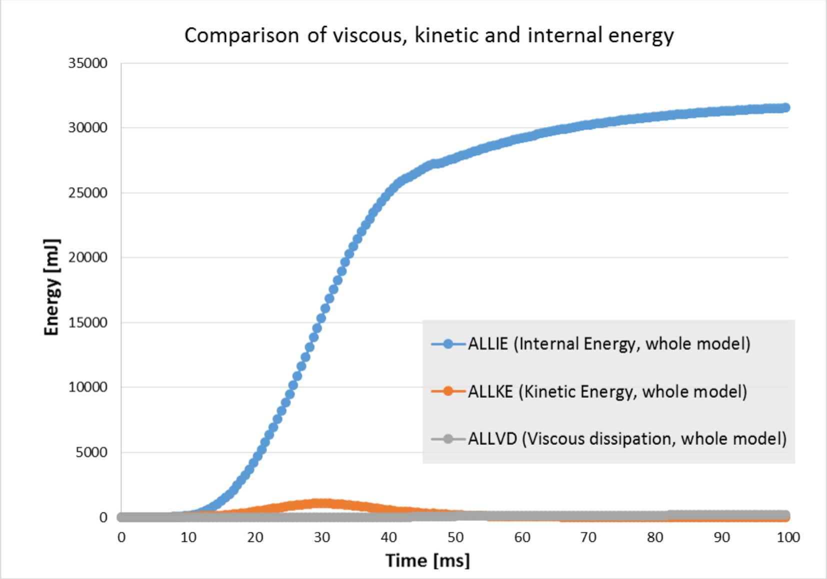

Figure 84: Comparison of viscous, kinetic and internal energy (taken from simulation of design variant: *"single Actuator with rubber support"*)

calculations performed in chapter 5. As the deformation for these simulations is very large mass scaling showed to be a problem with regard to inertia. In Figure 84 a comparison is made of the internal energy with the kinetic and viscous energy of a droop nose simulation. Both the kinetic and the viscous energy stay at a very low fraction of ALLIE, proving this simulation to be quasi static *[Nasdala, 2010; Abaqus User Manual, 2015]*.

To determine the step time the structural modes of the model have to be determined. In this simulation various different parts are deformed while interacting with each other; the structural mode of the different parts depends largely on this interaction. However as the skin is the structure in this model, that is most likely to oscillate first, the modal analysis was performed as a first step only for the skin. The first to modes of the skin are 17,7Hz and 39,1Hz with maximum displacement in the area of the actuators, if it is only supported/connected to the front spar. The frequencies will increase if interactions with different parts are included. A step time of 100ms with a loading time of 80ms is an acceptable loading step for these structural modes. As this simulation involves complex contacts between different parts of the system, criteria for all contacts had to be defined. It proved to be suitable to use a hard contact definition with possible separation after contact for the normal direction and a rough contact behavior for the tangential direction (with a friction coefficient of 0,5). It has to be mentioned that simulations with different coefficients of friction (between 0,2-1) have been performed for comparison and no difference in the deformation results have been seen. Due to the large size of the models and the resulting high number of increments (>500000) all simulations for the system simulations were performed with double precision. Even if this meant an increase of 50% simulation time, a precise deformation response was important. The difference in deformation between single precision and double precision was in the test case *(Actuation Variant: Two Actuators)* between 0,1mm and 0,2mm. This is not a very large divergence in comparison to the overall deformation of the system, but with regard to the target shape (drooped shape) this could locally result in an increase of up to 20% of offset. Table 24 acts as a quick overview of the simulation model, an exemplary excerpt of an input file can be seen in Appendix J.

Table 24: Summary of simulation model setup

	Actuator tubes	**Skin**
Element Type	S4R Shell elements	S4R Shell elements
Element Size	2mm (side length)	4mm (side length)
Overall Dimensions	Design dependent	700mm x 350mm x 100mm
Material	FMC - Orthotropic (see Table 22)	GFRP see Table 23 (Layup see Appendix H)
Loading	0,004 – 0,2 N/mm² (smooth step)	Cruise or Landing loads (smooth step)
	Smooth step loading with maximum after 80ms	
Boundary Condition	Movement only z/x-direction/ z-rotation locked	Movement only z/x-direction / z/x - rotation locked
Damping	Viscous Pressure 1e-6	Viscous Pressure 1e-5
Contact Parameters	Hard contact with allowed separation after impact / Coefficient of friction of 0.5	
Simulation Time	100ms	
Precision	Double Precision	
Rigid structure	All DOF locked, simulated with rigid elements	

8.2 Simulation results of proposed actuation design concepts

In the following paragraphs the simulation results of the three concepts addressing the tensile forces are presented. To be able to compare these variants correctly the static structure, the position, type and inside pressure of actuators was kept the same for all three variants. For this the two actuator concept was chosen. The pressure in the actuators was $\Delta p = 0{,}004\ \frac{N}{mm^2}$[5]. Following the three tensile concepts the simulation results for the different pneumatic actuation concepts are shown (for these simulations no tensile concept was included). For the actuation concepts the rigid structure is changed slightly, depending on the concept.

8.2.1 Stringer hook concept with two actuators

This design variant has a rigid stringer hook in place to carry the lifting forces on the upper side of the droop nose. This stringer hook requires a stringer integrated into the skin over the whole span of the wing, which is already implemented in the design for the mechanical actuation system (see SADE project). Attached to this stringer is a hook like lever, which is in contact with the static support structure during cruise.

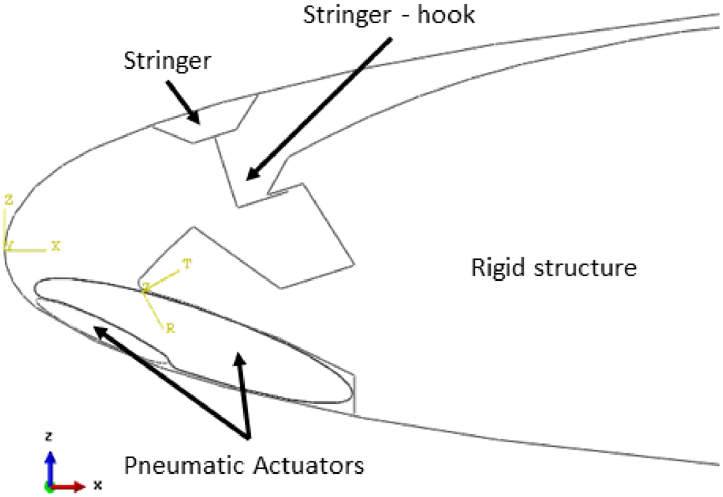

Figure 85: Design variant: Stringer Hook

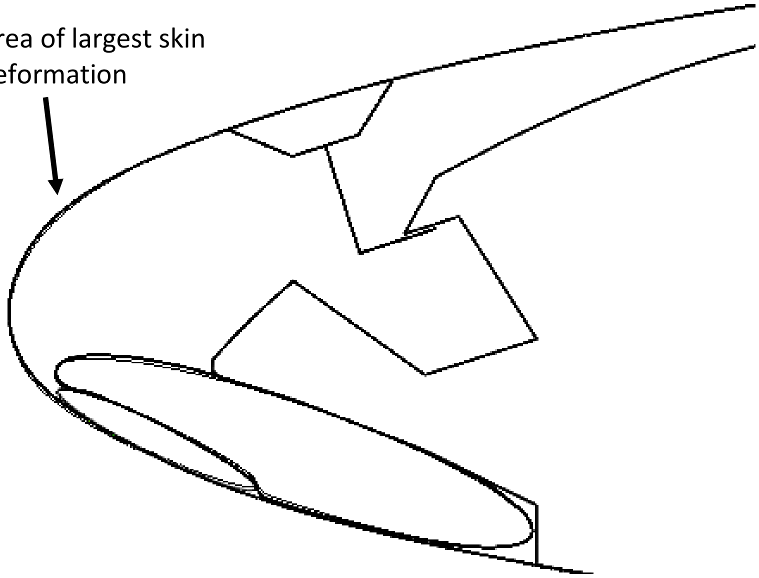

Figure 86: Stringer Hook in cruise configuration, actuators at 0,004 N/mm²

In Figure 85 the detailed setup of the stringer hook simulation is shown. The stringer and stringer hook are both simulated with the same material as the droop nose skin (see Table 18) but with a quasi-isotropic fiber layup and a thickness of 2mm. Figure 86 shows the result of the simulation. The left-hand side has been cut off to show the resulting deformation at the tip of the nose in more detail. The figure shows both the initial position (thin lines) and the deformed position (thick lines). This is best observed

---

[5] Based on known forces of the mechanical actuation system, scaled to the dimension of the simulation/ contact area.

with the deformation of the actuators. The deformation of the skin can only be guessed at from this figure. A detailed analyses showed that the maximum divergence from the target shape for this setup was 1,4mm at the tip of the nose. The complete circumferential divergence can be seen in Figure 99.

8.2.2 Tensile belt concept with two actuators

For this variant the lifting forces are carried by a, so called, tensile belt. The simulations were again performed with two actuators. For the simulation the tensile belt was modelled with the same material properties as the pneumatic actuators and a thickness of 1mm. The tensile belt is rigidly connected to the droop nose skin and the rigid structure, with rotational degrees of freedom locked directly at the connection. In Figure 88 the result of the simulation can be seen. The area of the largest deformation is rearward of the tensile belt with 4,5mm, whereas the front of the nose shows a very good alignment with the target shape (compared to the stringer hook variant). Forward of the tensile belt the deformation is only in the range of 0,3mm.

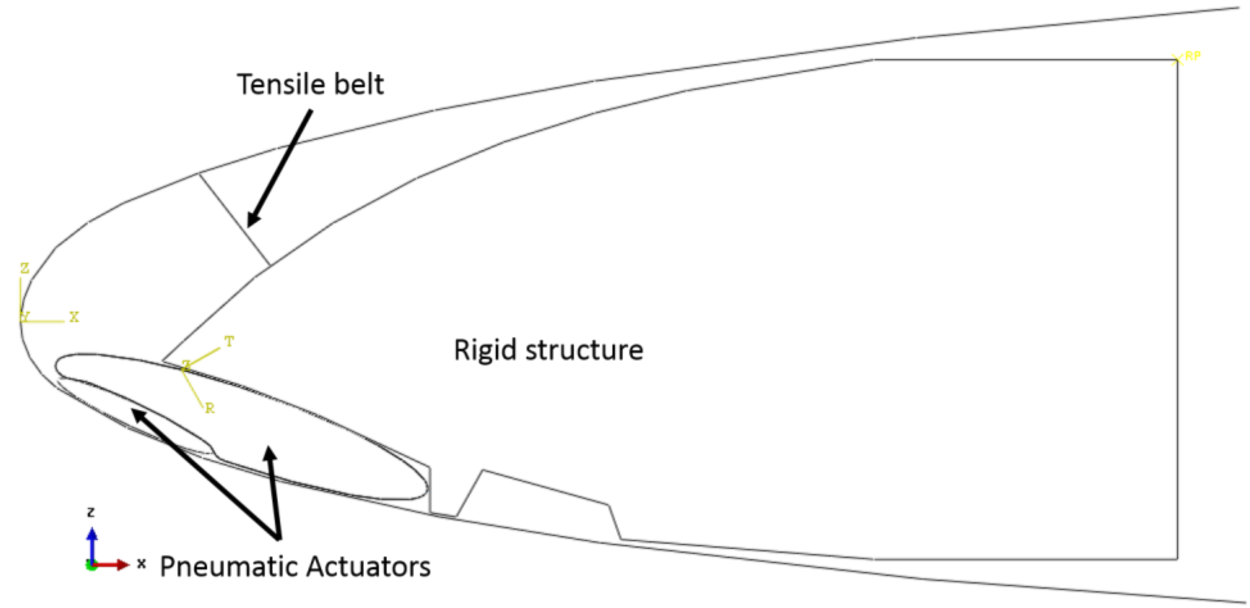

Figure 87: Design variant: Tensile Belt

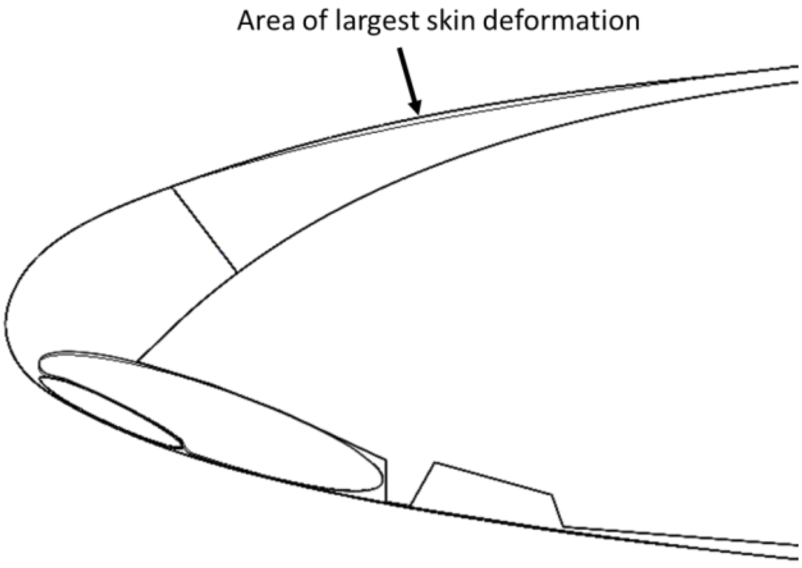

Figure 88: Tensile Belt Tensile Belt in cruise configuration, actuators at 0,004 N/mm²

8.2.3 Pneumatic stringer concept with two actuators

For this concept a pneumatic stringer is used to carry the tensile loads. Again the simulation was performed with two actuators for comparison. The pneumatic stringer is modeled identical to the pneumatic actuators, in terms of material, material orientation and skin thickness.

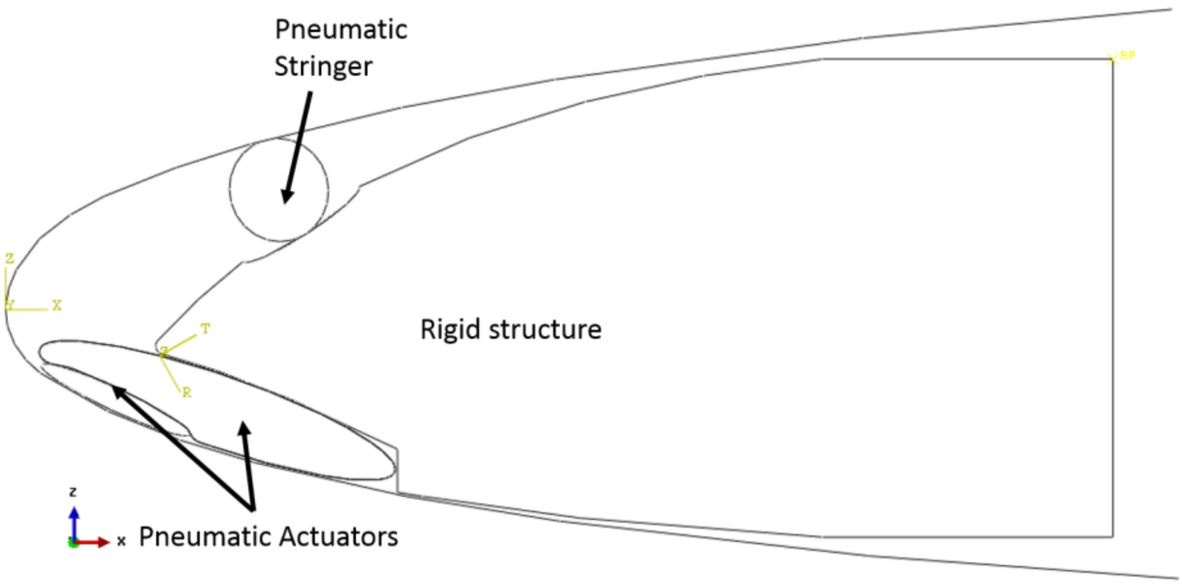

Figure 89: Design variant: Pneumatic Stringer

The pneumatic stringer is inflated with a $\Delta p = 0{,}2\,\frac{N}{mm^2}$ to ensure geometrical stability. In this simulation the "external" loads were introduced over a separated timescale. The maximum pressure in the pneumatic actuator is reached twice as fast (after 40ms) as the cruise loads and the air-loads. All loads are still applied by a smooth step function. The pneumatic stringer is rigidly connected to the skin and the rigid structure. At the point of contact all DoF of the pneumatic stringer are slaved to the relative structure.

Figure 90 shows the simulation results. The deformation observed here is relatively large. The tip of the nose moves collectively upwards by 4,5 mm.

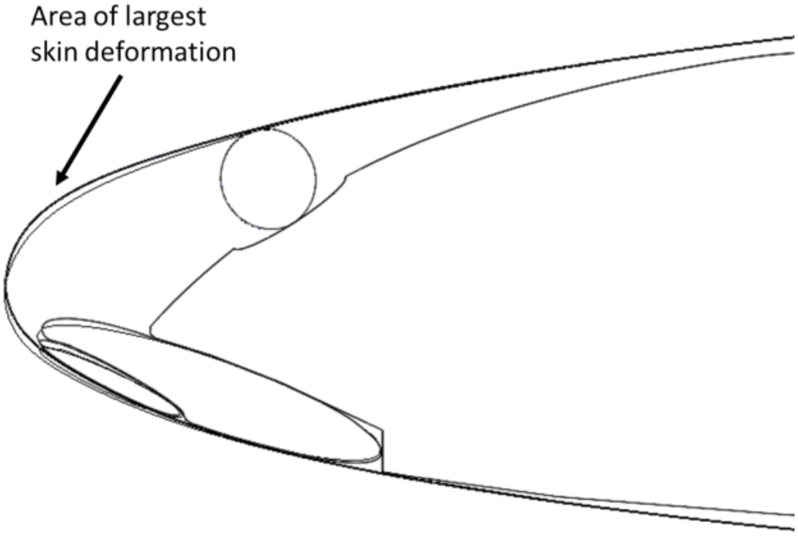

Figure 90: Pneumatic Stringer in cruise configuration, actuators at 0,004 N/mm²

8.2.4 Single actuator concept

In this variant the deployment of the nose is to be achieved by a single actuator positioned at the front of the nose, see Figure 91. Two different simulations were performed at different Δp values for the actuator. The first simulation was performed with $\Delta p = 0{,}22 \ \frac{N}{mm^2}$ and the second with $\Delta p = 0{,}4 \ \frac{N}{mm^2}.$, as the results at lower pressure were not reaching the targeted deflection. In Figure 92 and Figure 93 the results of the simulation can be seen. The dashed line symbolizes the target shape. Neither simulation achieved a close match to the target shape. They demonstrate however that the general principle of such an actuation system works and that the actuator and the rigid structure are generally correctly positioned. It is also demonstrated that for this target shape one single actuator cannot suffice, as the needed stroke is larger than the target shape front radius. Additionally it can be noticed that the actuator moves considerably when comparing the two different results. This type of behavior can lead to problems after repeated deployments, as it is possible that the actuator moves out of position over time. To eliminite this a connection between the actuator and the rigid structure is nescessary, which in itself can become a problem (as demonstrated in the actuator tests in chapter 7.2).

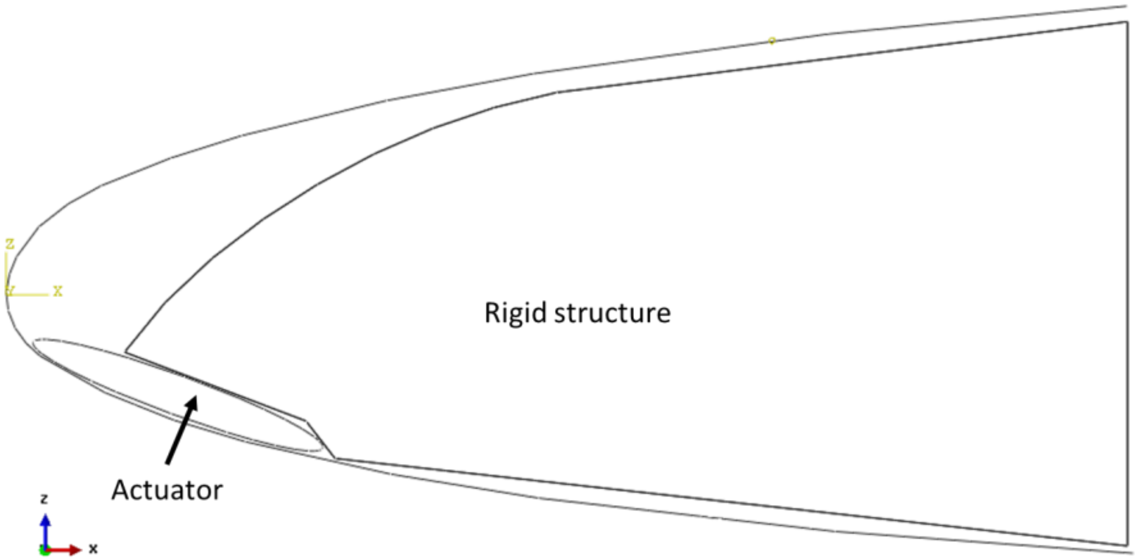

Figure 91: Design Variant: Single Actuator

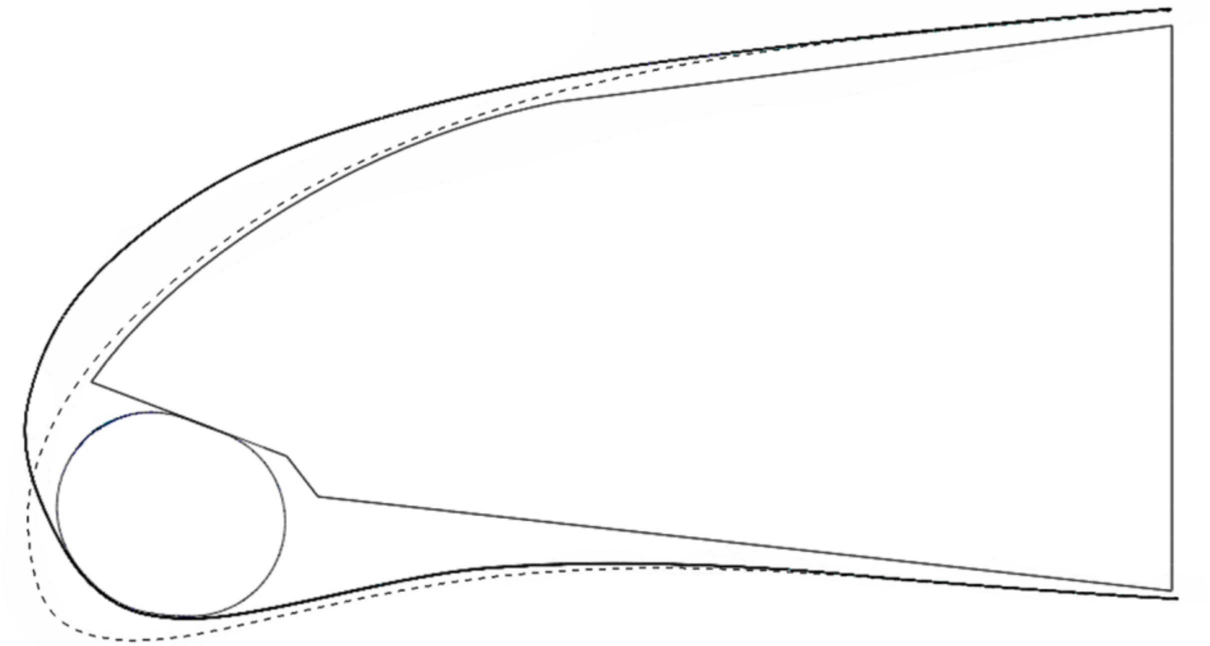

Figure 92: Single Actuator with 0,22 N/mm² internal pressure under landing loads

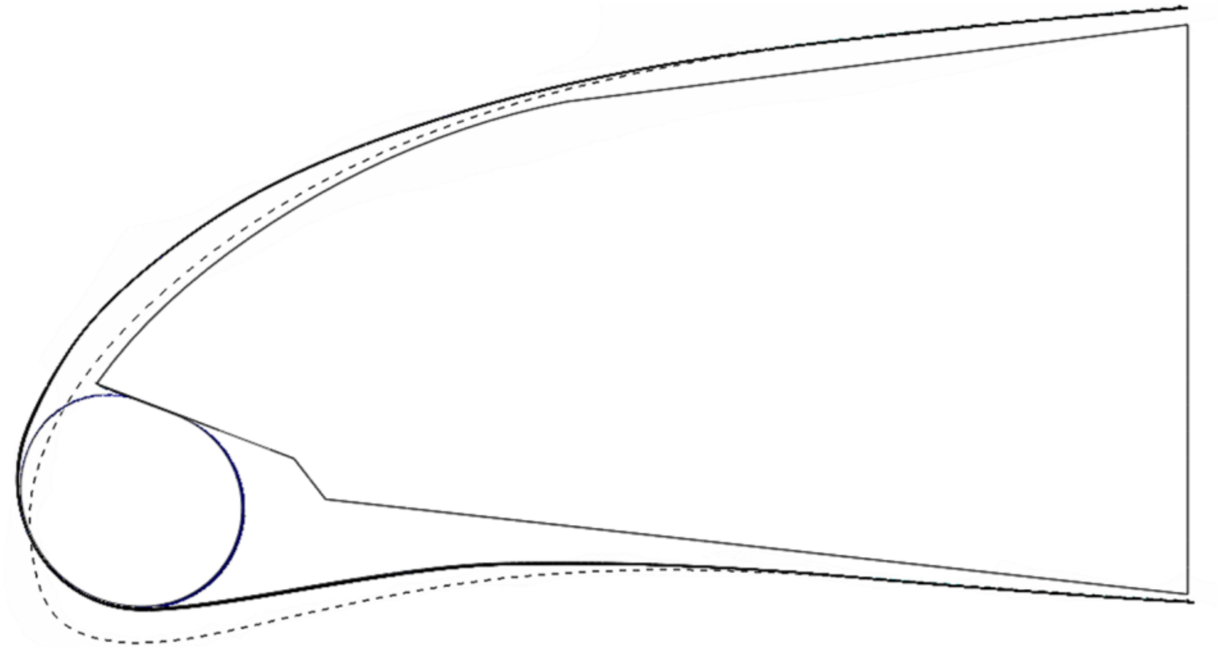

Figure 93: Single Actuator with 0,4 N/mm² internal pressure under landing loads

8.2.5 Single actuator with rubber support concept

For this variant the actuator is supported by a rubber strip positioned directly at the point of maximum deformation. The strip is fixed to the skin. Adding this rubber strip was decided based on the results from the simulation of the single actuator. The goal was to increase the stroke of the single actuator and change the overall deformation radius. The rubber is simulated as a solid with C3D8R elements (Hexahedron, 8-node linear brick, reduced integration, hourglass control). It is simulated as a very soft linear material, for its properties see Table 25. The first simulation was performed with $\Delta p = 0{,}22 \ \frac{N}{mm^2}$ and the second with $\Delta p = 0{,}4 \ \frac{N}{mm^2}$. In Figure 95 and Figure 96 the results of the simulation can be seen.

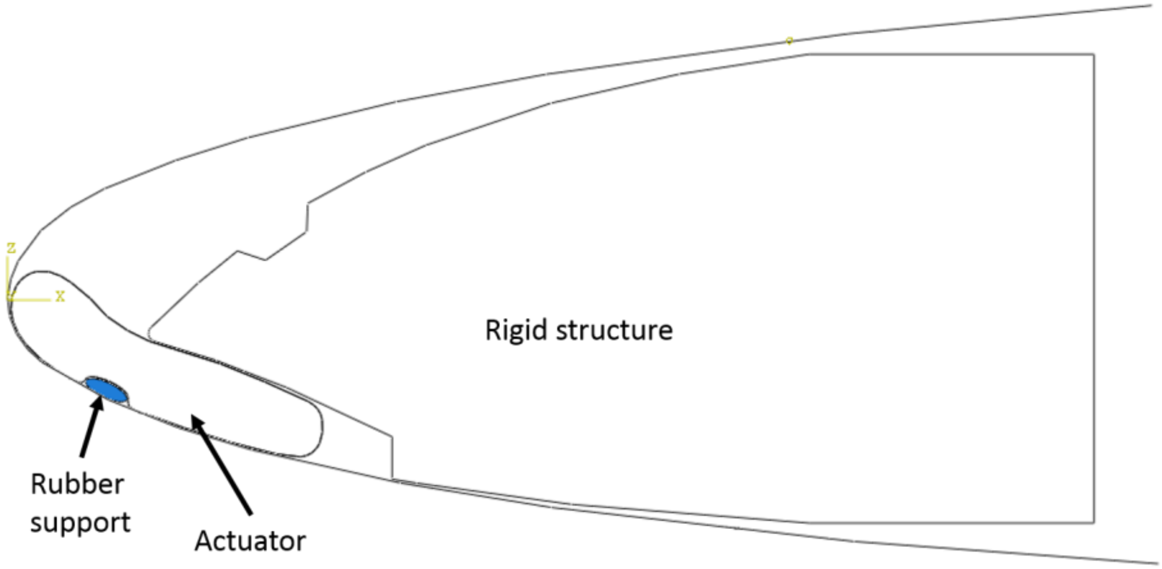

Figure 94: Design variant: Single Actuator with rubber support

Table 25: Mechanical properties: Rubber in the Simulation

E [N/mm²]	v
2	0,45

In both cases the rubber strip does not have the desired effect. As the actuator and the rubber are not rigidly connected the actuator can move in relation to the rubber strip. This results in a misalignment of the actuator and as a result in an incorrect deployment off the droop nose. Increasing the size and changing the shape of the rubber strip could help against this kind of behavior, but it would also have an impact on the stiffness of the skin. As the effect in these simulations was not beneficial further work in this direction was stopped.

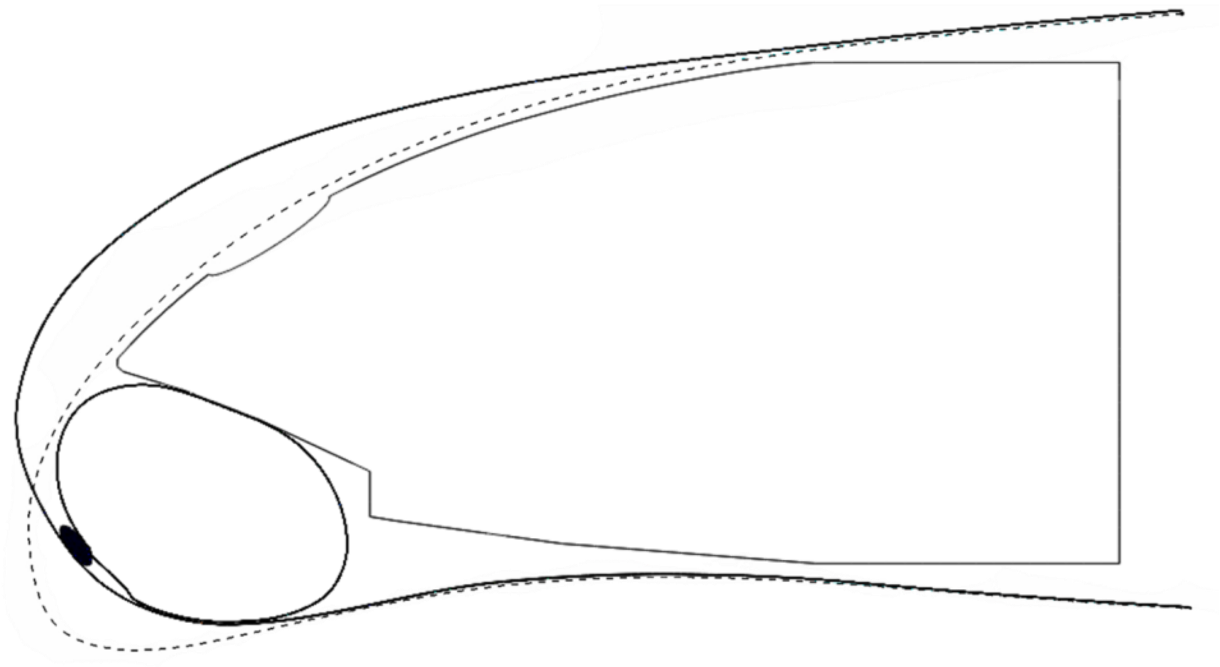

Figure 95: Single Actuator with rubber support at 0,22 N/mm² under landing loads

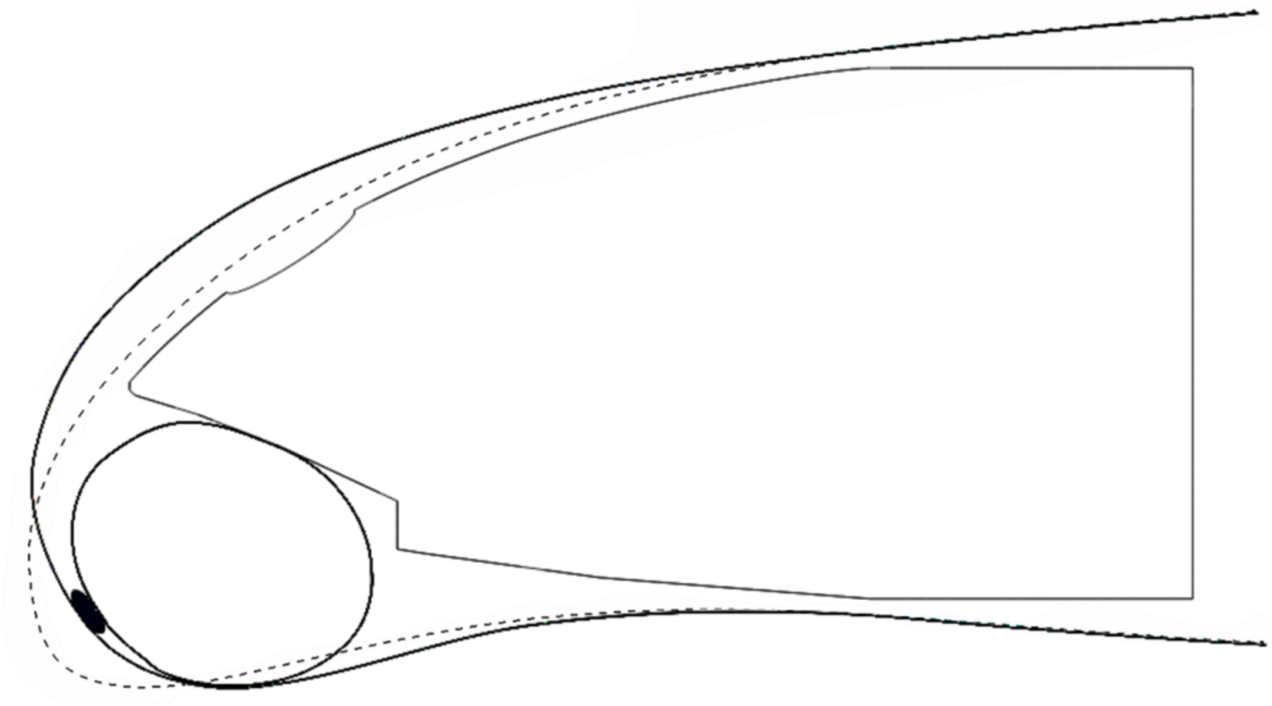

Figure 96: Single Actuator with rubber support at 0,4 N/mm² under landing loads

8.2.6 Two actuators concept

In this variant the actuation concept uses two dissimilar sized actuators. The larger actuator overlaps the smaller one. The whole setup can be seen in Figure 97.

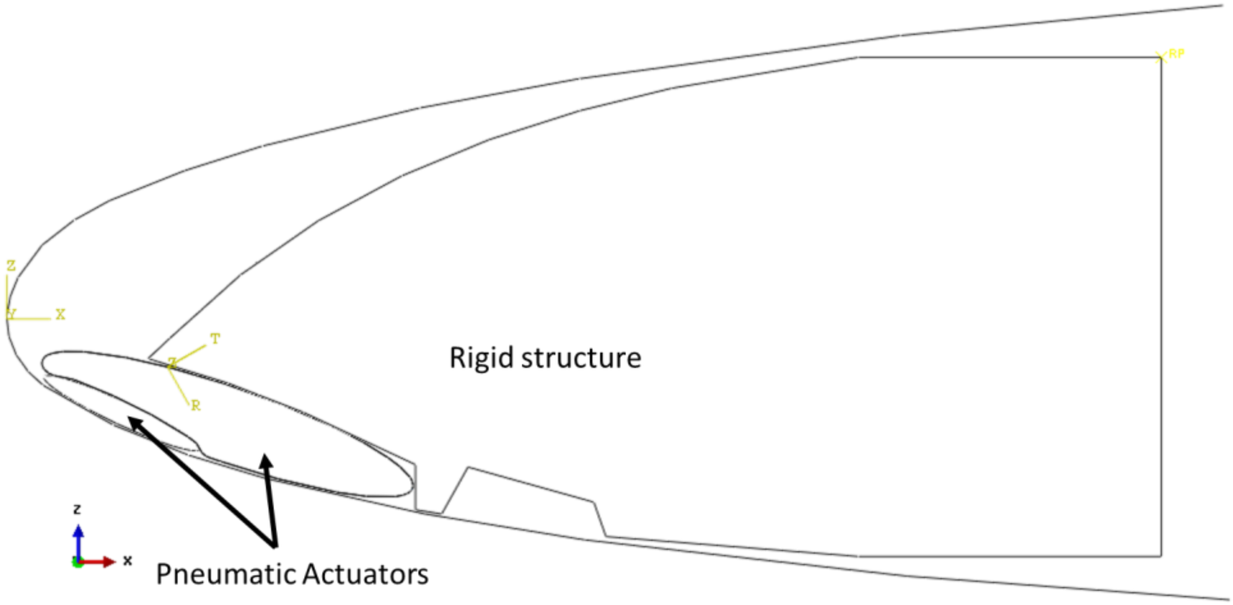

Figure 97: Design variant: Two Actuators

As can be seen in Figure 98 the actuators are able to deploy the nose skin very close to the correct position. In three areas a divergence from the target shape can be observed. The maximum deviation from the target shape is 2,1mm. The overall circumferential deviation can be seen in Figure 100 (green).

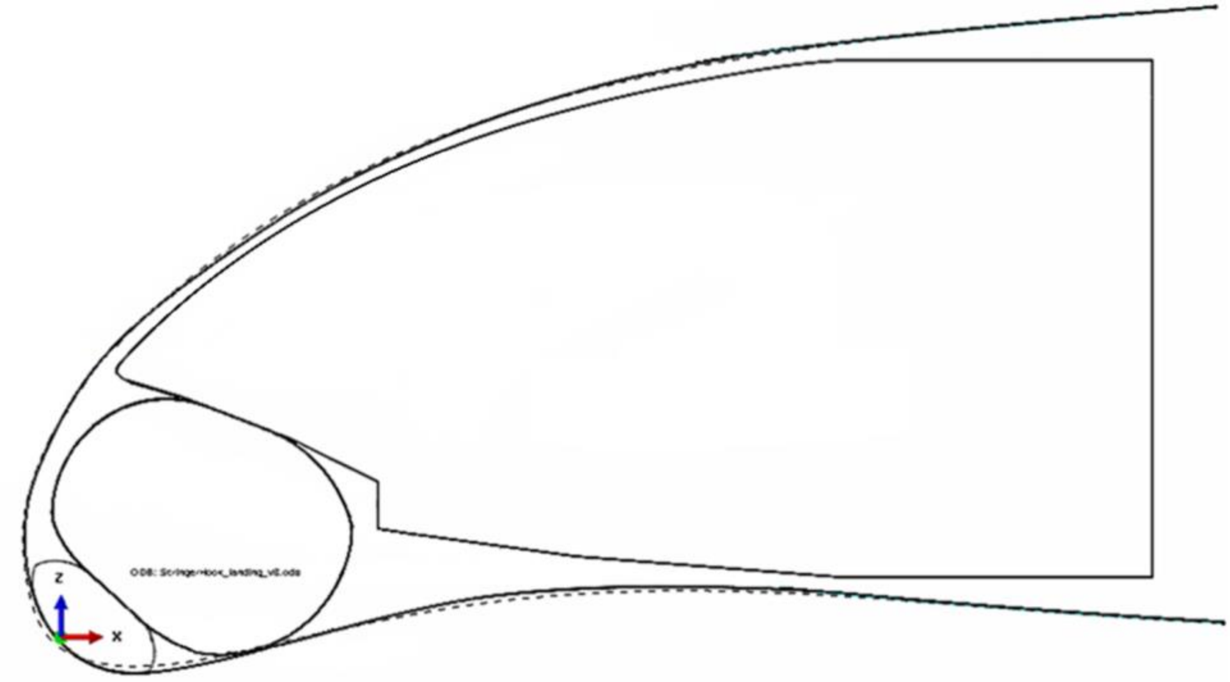

Figure 98: Two Actuators at 0,22 N/mm² under landing loads

8.3 Comparison and evaluation of the different actuation concepts

In chapter 3.1 the different concepts were first presented and afterwards a preliminary comparison was made. With the results of the simulations it is now possible to perform a final selection of the most promising concept. While the simulation themselves are accurate they still are the result of idealized modelling. As such they are very useful to compare the concepts with each other, but a certain caution must be taken with absolute values. As such no performance evaluation of the concepts “aerodynamically speaking” will be performed. With the natural laminar flow criteria provided in chapter 2, the “cruise variant”-concepts could be partially evaluated. Nonetheless a real aerodynamic assessment would need CFD analysis of every simulation result. As this was outside the scope of this work no aerodynamic assessment was performed. As a benchmark for each concept the target shapes of the cruise or drooped position of the nose were chosen. For this the location and the amount of divergence of each concept was considered.

Of the three different tensile concepts presented the design variant “stringer hook” shows the best match with the target shape. Second best is the “tensile belt” concept, whereas the “pneumatic stringer” fails to keep the skin its position. It certainly would be possible to optimize the pneumatic stringer to perform better than it did, but in a direct comparison it did not perform favorably.

Comparing the three actuation concepts with each other the “single actuator” and the “two actuator” concept show the best results. Adding the rubber support to one actuator does not lead to a better overall performance, it rather seems to hinder the correct deployment of the actuator. For this study and the provided geometry the two actuator system worked best. Table 26 shows a summary of the performance of each concept; see also Figure 99 and Figure 100 (the position of the measurement points along the skin can be seen in Appendix K).

Table 26: Summary of concept performance

Concept	Purpose	Result	Deviation
Stringer Hook	Maintain cruise shape	Good overall match	max. 1,3mm
Tensile Belt	Maintain cruise shape	Good match at front, larger deformation rearwards	0,3mm front 3,1mm rear
Pneumatic Stringer	Maintain cruise shape	Good match rearwards, larger deformation in the front	4,8mm tip
One actuator	Droop deployment	Large deviation at 0,22 N/mm²; better at 0,4 N/mm²	Large overall deviation, actuator stroke to small
One actuator with rubber support	Droop deployment	Large deviation at 0,22 N/mm²; better at 0,4 N/mm²	Large overall deviation, direction of actuator stroke not correct
Two actuators	Droop deployment	Good match at 0,22 N/mm²	Three areas of deviation, max. 3,6mm

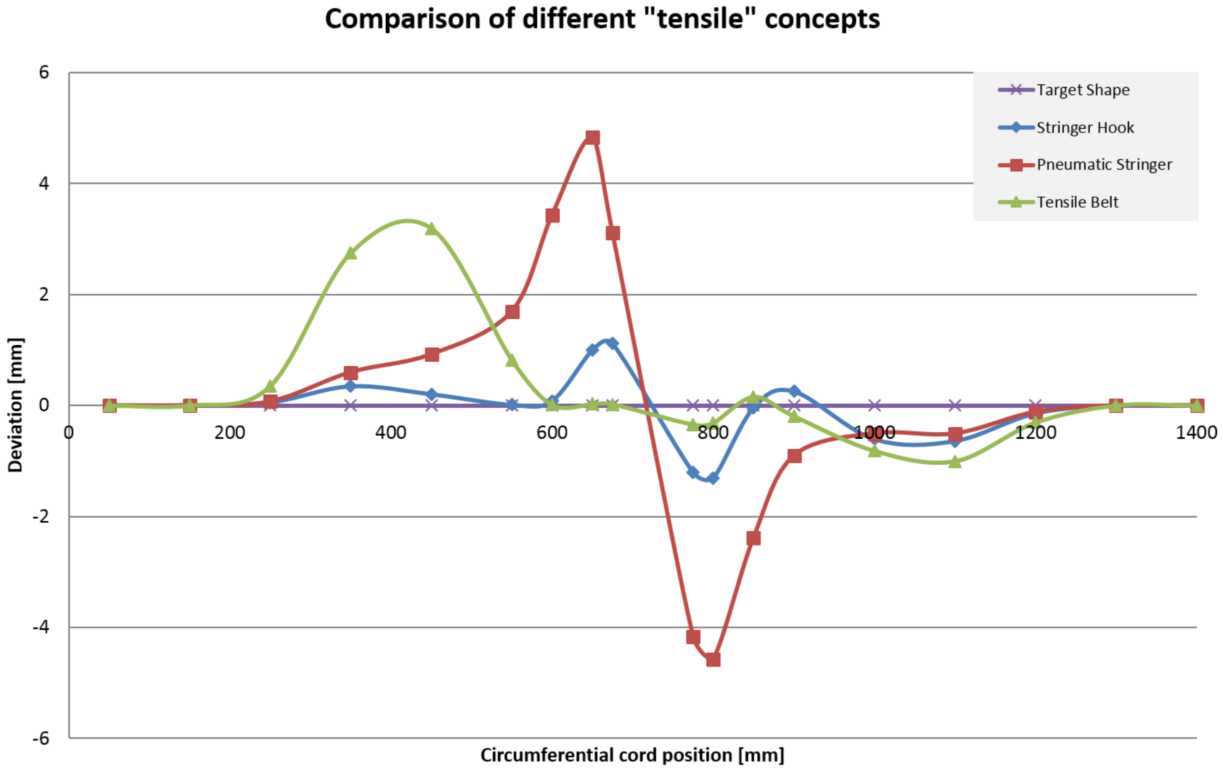

Figure 99: Comparison of different "tensile" concepts

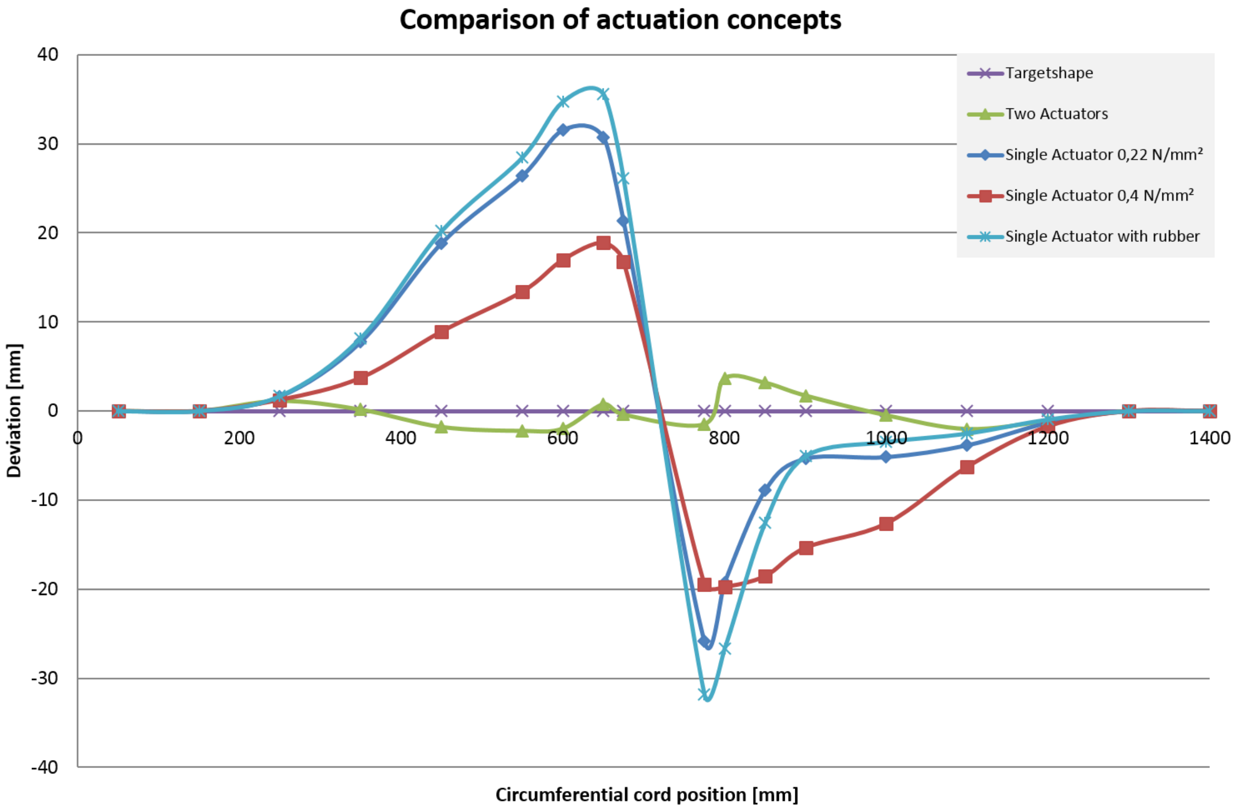

Figure 100: Comparison of actuation concepts

8.3.1 Final design: Stringer hook with two actuators

Based on the preliminary assessment of the different concepts in chapter 3.1 and the comparison of the simulation results a complete simulation model of the best concepts for each task was made, this included the stringer hook concept for the tensile function and the two actuators for the actuation function. As the assessment of the tensile function already included the two actuator concept as a baseline, the missing simulation was now a drooped configuration featuring both simultaneously. The result of this simulation can be seen in Figure 101.

The cut-out in the rigid structure was designed to not impede the movement of the stringer hook, during its downward movement during drooping of the nose. The cut-out was nonetheless kept as small as possible, to ensure the load-carrying capability of the rigid structure. As this combination of the different designs showed the best performance at the two target positions, the sensitivity study was performed with this design as a baseline.

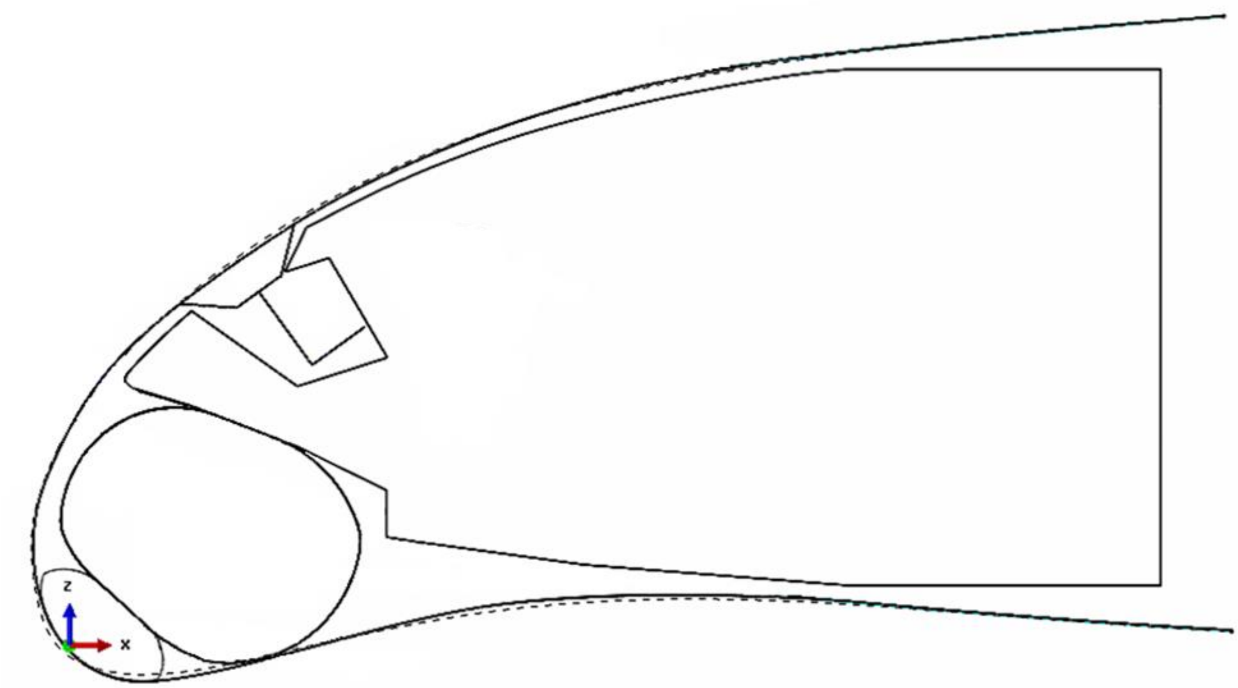

Figure 101: Stringer Hook with deployed actuators at 0,22 N/mm² under landing loads

8.4 Sensitivity study based on final design

Figure 102 shows the overall setup for the sensitivity study. The simulation parameters defined above remain the same unless otherwise stated. To understand the sensitivity of the system geometrical changes, loads changes and stiffness changes were simulated.

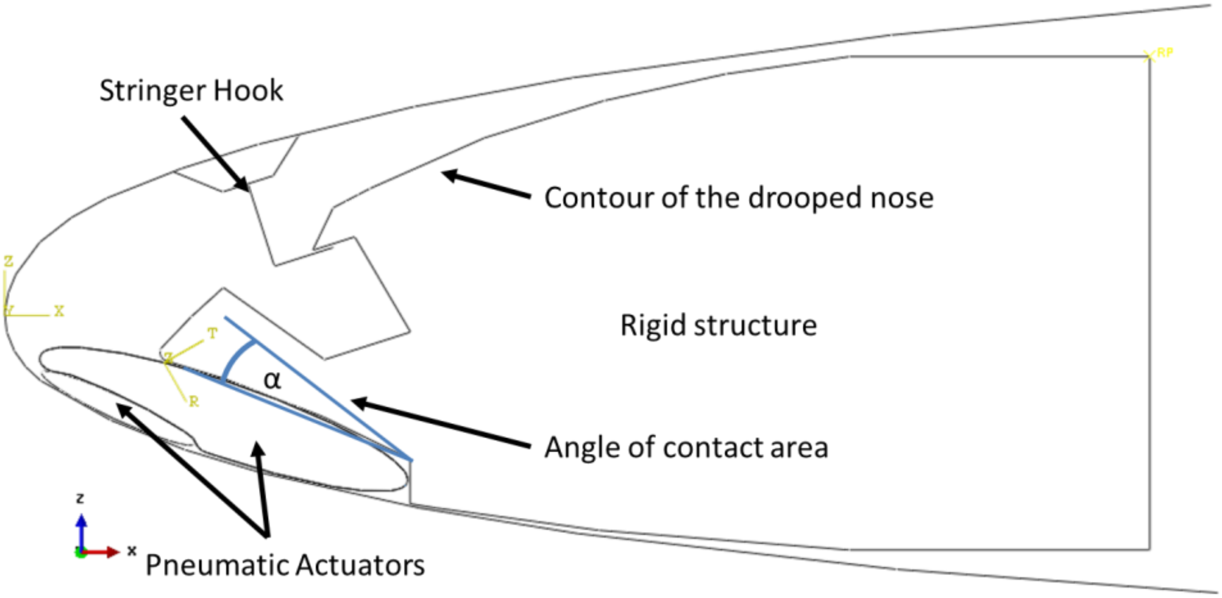

Figure 102: Setup of actuation system sensitivity study: Angle of contact area

8.4.1 Influence of angle of contact area on performance

As a first parameter the angle of the contact surface of the rigid structure was looked at. This is something that has been left out of the design description so far. The indicated angle is to be understood to be in positive direction. To understand the influence three simulations at different angles were performed, at 1°, 2° and 5°. For all these simulations the actuation pressure of the actuators was initially kept at 0,22 N/mm² and the droop nose skin was loaded with the landing pressure distribution. The general parameters described above for the simulation model remain the same. In Figure 103 and Figure 104a the results of these three simulations can be seen. While at 1° the result still looks very good and the overall deviation from the target shape is with 2,5mm only slightly higher than at 0° angle, the deviation grows with each degree. Additionally a clear trend can be seen. The point of maximum deflection moves upwards away from the target.

Based on the knowledge gained during the previous simulations, additional actuation pressure could compensate for the bad angle of the contact area. To prove this a simulation was made at the 5° setting with $\Delta p = 0{,}25\ N/mm^2$.

Figure 104b shows that the additional actuation pressure could partly compensate for the increase angle of the contact area; compare also Figure 105.

This fact in itself is again an indicator to the sensitivity of the design. A change in pressure has a direct influence on the shape. This is not an unexpected result but it makes clear that the actuation pressure must be monitored precisely and actively.

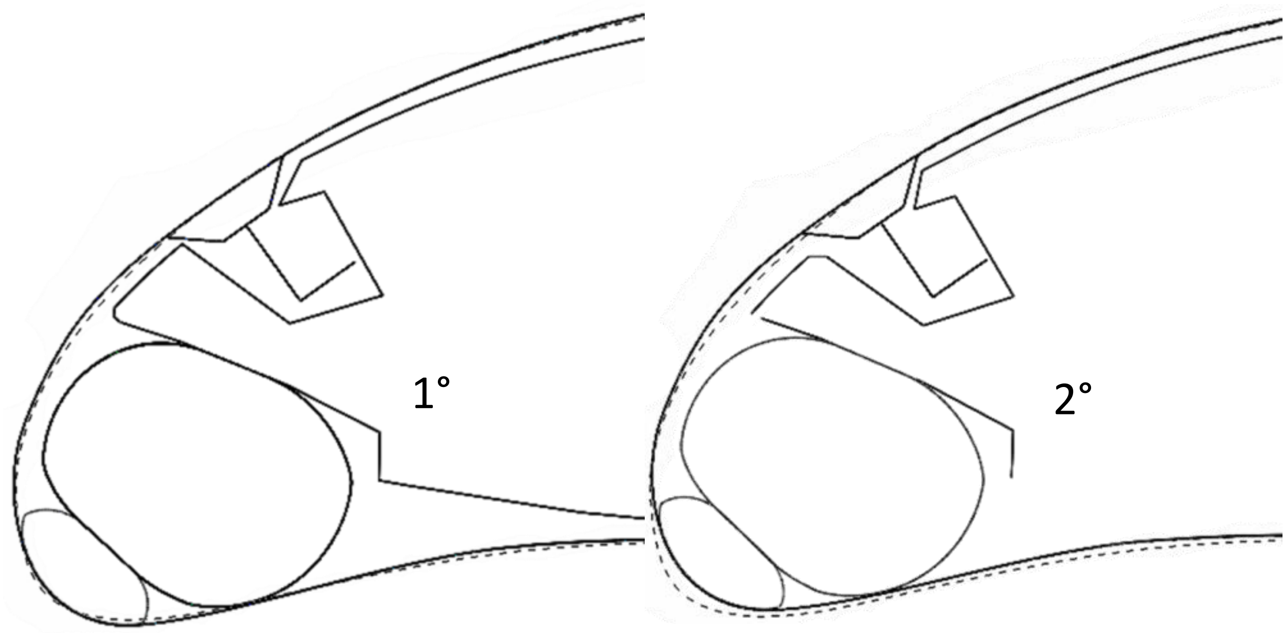

Figure 103: Rotation of contact area of 1° (left) and 2° (right)

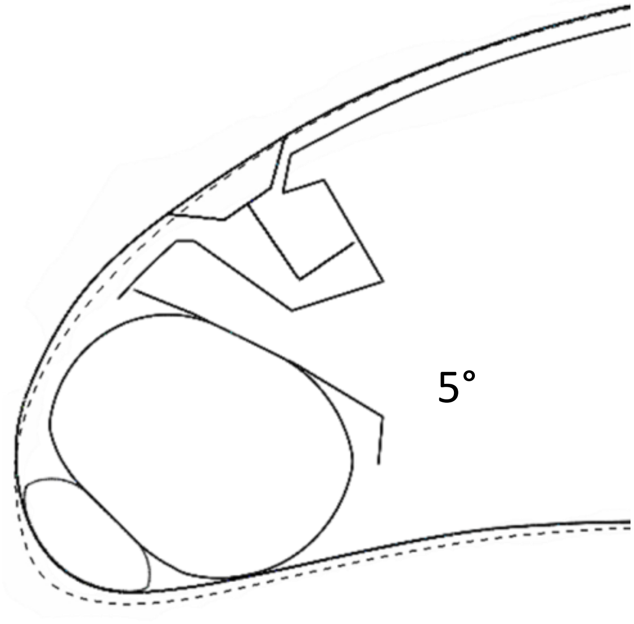

Figure 104a: Rotation of contact area of 5°

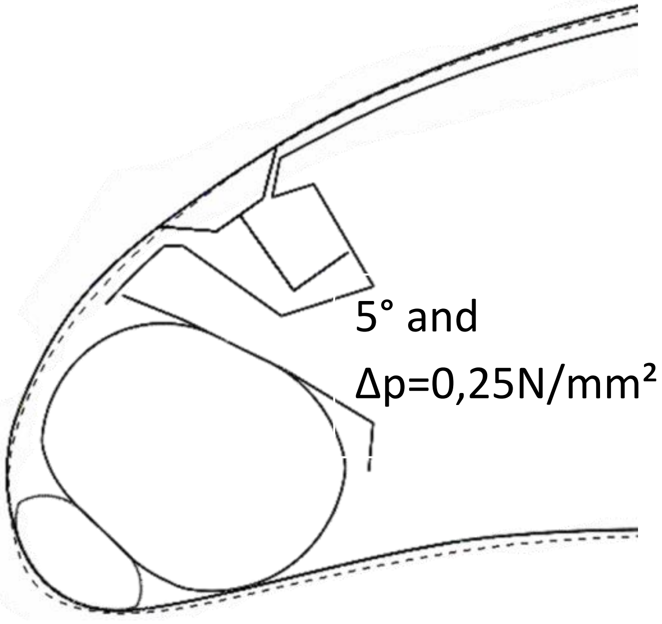

Figure 104b: Rotation of contact area of 5° and $\Delta p = 0,25\ N/mm^2$

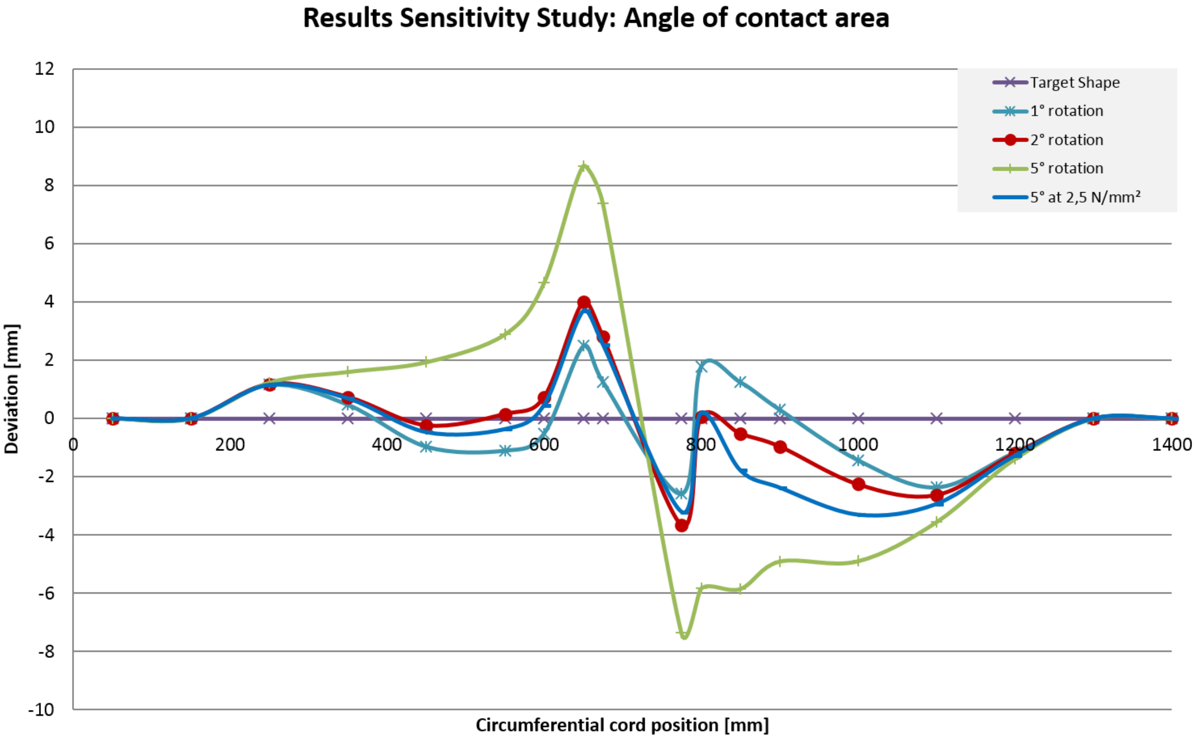

Figure 105: Results of sensitivity study angle of contact area

8.4.2 Influence of varying air loads on deformation performance

It is important to understand, that the deformed shape is a result of the actuation pressure, the position of the actuator, the shape of the rigid structure, the stiffness of the skin and the aerodynamic pressure distribution. Fortunately the c_p distribution remains more or less constant for a distinct shape, but the amplitude of the pressure distribution changes with airspeed and air-density. To have a better understanding of this effect, three simulations with an increased air-load were made. One simulation was made with a 5% increase of the external pressure. For the second and third simulation the air-load was increased for the landing and cruise case by 50%, additionally the actuation pressure was also increased by 50%.

The 50% load increase for the cruise case increases the deformation of the nose slightly from 1,4mm to 1,8mm, compare Appendix L Figure 122, Figure 123 and Figure 106. Interestingly the 50% load increase for the landing case resulted in an overall better performance, suggesting that the proposed solution still has room for improvement, as mentioned earlier.

In the Appendix L Figure 124 result of a 5% increase of air-loads at constant internal pressure can be seen. The blue dots are measurement markers. In a direct comparison with the previously presented results for the cruise case (see Figure 86 and Figure 99) the 5% increase results in a local increase of discrepancy with the target shape of up to 10%. It has to be mentioned that in some regions the load increase even improved the shape.

In Figure 106 a comparison of the different results of the airload sensitivity study is shown. It can be noticed that while the deviation increases (or decreases) locally, the overall behavior does not change. The maximum deviation of 1,7mm observed is located roughly in the tip of the leading edge.

The simulation results prove the design to be relatively robust against certain types of external changes. The biggest influence on the deformation shape is the geometry of the rigid structure and the stiffness distribution of the skin, both parameters that do not change during flight operation. A change in airloads does have an effect on the deformation of the leading edge, as expected. This suggests that active control of the actuation system has to be included in the overall system design. Comparing Figure 105 and Figure 106 shows quiet well the much more pronounced effect of geometrical changes with regard to overall sensitivity.

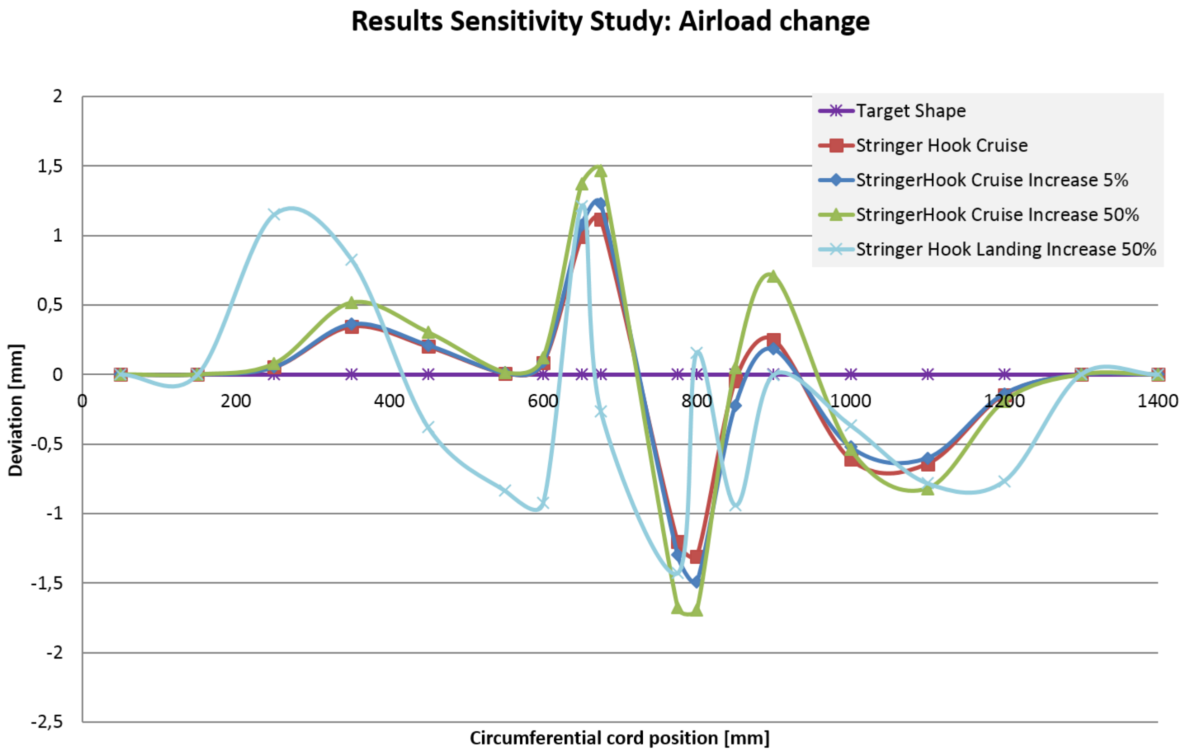

Figure 106: Comparison of air load changes in the sensitivity study (5% only external increase/ 50% increase overall loads)

The simulation case shown in Figure 107, a droop nose skin made from aluminum is not included in the comparison as the divergence is so large and easily recognizable in the figure. This simulation was simply added to draw a complete picture and show the behavior with a non-tailored skin, underlining the importance of an accurate stiffness tailoring of the skin.

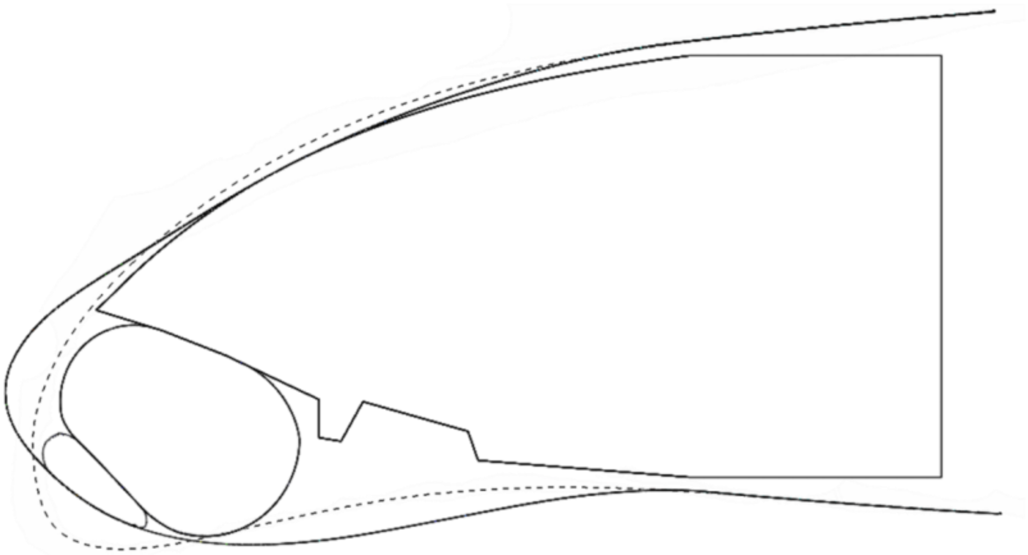

Figure 107: Droop nose with Aluminum skin (2mm constant) with actuation pressure 0,22 N/mm²

8.5 Generalized design guidelines for a pneumatically actuated droop nose

Over the course of this work a feasible design for a pneumatically actuated droop nose was presented. The robustness of the system against various changes was demonstrated. Based on the gained knowledge the following paragraphs aim to be a design guideline for similar systems.

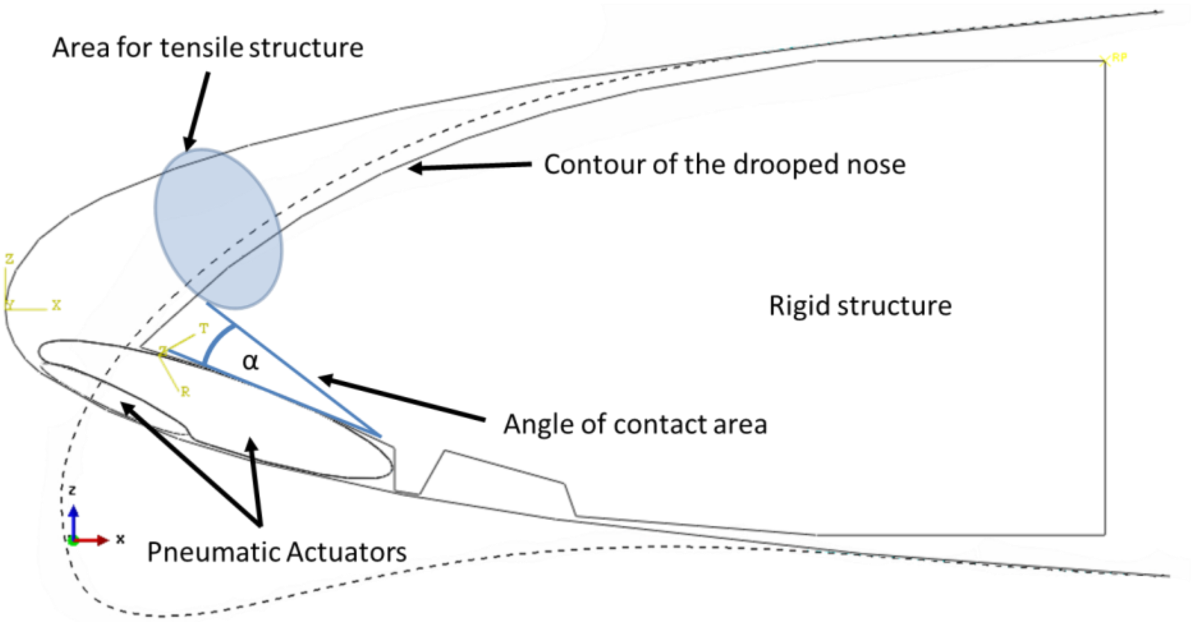

Figure 108: Design of the rigid structure

8.5.1 Influence of geometry

The geometry of the structure has to be separated into the geometry (shape) of the actuators, the shape of the tensile structure and the shape of the rigid structure. The shape of the rigid structure is predominantly driven by the required target shape of the system.

The biggest focus during the design of the rigid structure has to be made on the area of contact with the actuators. The size and shape of this has a direct impact on the direction of the stroke. The contact area has to be more or less perpendicular to the desired direction of stroke. The size/length is determined by the available space in undeformed position and required size (diameter) of the actuator(s)/required stroke. The stiffness distribution of the skin also influences the design of this area.

The shape and position of the tensile structure relies heavily on the available space in the deformed shape, as the tensile structure is always a compromise between its core function and the deformation of the skin.

As already stated in previous chapters the shape of the actuators in inflated position without external loading will always be circular. For the design of the system the deflated size is equally important as the inflated diameter. The size is of course directly related to the required stroke and the available space. It can be further influenced by geometrical criteria like maximum/minimum bending radius of the deformed structure (in this case the skin).

8.5.2 Influence of the number of actuators

The number of actuators is determined by the available space, the required stroke but also, as in this case, the target shape. If the deformation radius of the target shape is dominantly smaller than the required stroke, more than one actuator is necessary.

8.5.3 Influence of (air)-loads

The design developed in this work was heavily influenced by the mechanical actuation system. The actuation pressure for the tubes was calculated by using the lever loads of the mechanical system. If such a comparison is not available (as in most cases), it is possible to estimate the actuation pressure by creating a rough analytical model based on beam theory. For this the upper and lower surface of the nose can be seen as separate beams. The air-loads have to be regarded separately (upper and lower surface) and can each be combined into a singular force. With this two beam-bending problems have been created. It is now necessary to calculate the force for each beam to achieve the required deformation. Afterwards these two forces are combined and create the required actuator force. With this force and the approximated size of the actuator, the actuation pressure can be calculated. Special care has to be taken with regard to the large deformation. Classical beam theory has certain limitations and for large deformations certain presumptions are no longer met. It might therefore be necessary to use continuums mechanics or simple FE-modeling of the beams.

8.5.4 Modeling methods

To analytically or numerically model such a system it is important to note, that due to the large deformations non-linear mechanics have to be used. If flexible and stretchable materials need to be used for the actuators non-linear material models are necessary as well. Due to the large contact-areas between the different sub-structures quasi-static, dynamic, explicit modeling proved to be a good choice. To achieve a quasi-static response of the simulation smooth-step load introduction and small viscous pressure damping showed good result. Mass-scaling did not improve the simulation speed in this case.

Table 27 is a summary of the above described design criteria.

Table 27: Design guideline criteria: Pneumatic droop nose

Design parameter	Details
Geometry	Rigid structure needed for support Contact area of actuators perpendicular to deflection direction
Number of Actuator	Depended on available space vs maximum deflection Deflection shape can have influence
Loads	External forces + bending stiffness of structure
Modeling	Non-linear mechanics / in special cases non-linear material models Highly complex contact problems - Quasi-static dynamic, explicit models - Smooth step load introduction - Viscous pressure damping

8.6 True scale demonstration of actuation principle

A lab demonstrator was built to verify the principal functionality of the concept. For the demonstrator a section of flexible skin (provided by DLR) was fixed to a very stiff rack. Into this skin section a support structure was designed based on the simulation results shown in chapter 8.3. Also additional FE simulation of the rigid structure were performed. The rigid structure was in this cases adapted to the size of the actuator prototypes presented in chapter 7.

Figure 109: Completed demonstrator without actuators

The completed demonstrator was then used to a) prove the concept and b) to verify the deformation behavior of the pneumatic actuators under load. The demonstrator is a 1:1 scale section of the skin, which was tested in the FP7 project SADE, making it a good representation in terms of system weight, for comparison.

Figure 110: Demonstrator with actuators at 0,03 N/mm²

The rigid structure was manufactured as a sandwich structure. The outer shell was constructed out of CFRP and the inside with foam ribs. For stability the foam was segmented and intersected by CFRP plates. The CFRP was 2,5mm or respectively 2mm thick and stacked as quasi-isotropic. In the rear of the rigid structure screw inserts were added to connect it to the “front spar”. The actuators used for the demonstrator were equipped with elliptical, metal endcaps and longer than the demonstrator skin section. Therefore any negative impact of the end-caps on the deformation behavior was minimized. To achieve the maximum possible deflection three actuators were stacked in the front of the demonstrator and inflated at 0,03 N/mm². The achieved deflection is not the target shape as the used actuators are too small, but it shows the feasibility of such a system. It can also be seen that the general interaction between skin and actuators is similar to the simulation results.

8.7 Comparison between mechanical and pneumatic actuation concept

To evaluate and compare a pneumatic actuated droop nose with a mechanical droop nose and a conventional LE system (slats) it is important to understand the differences between the two different approaches of droop nose and slat. In literature several key differences are listed, such as take-off and landing performance, noise generation, drag performance as well as weight. The project LEISA performed by the DLR *[Wild et al., 2006; Kreth et al., 2007; Pott-Pollenske et al., 2007]* showed a significant potential for weight reduction when using a droop nose instead of a conventional slat. Studies performed during the project identified the slat gaps at the leading edge as a dominant source of airframe noise during approach and suggest a potential of noise reduction of up to 10dB(A) for a droop nose. The same studies also show an effect off the varying LE-configurations on the high-lift performance (take-off and landing). Here the droop nose is less effective than a conventional slat. To be able to compare the two different concepts with each other a detailed study based on the same airfoil has to be performed. The data available only allows for an estimation of the effects and differences with regard to weight and complexity.

8.7.1 Weight comparison

With the finalized design, presented in chapter 8.3.1, it was possible to compare the weight of the pneumatic actuation system with an A320 leading edge and the SADE kinematic actuation system. In Table 28 the weight of each design is listed. The A320 is considered as the baseline for the comparison, as it is a proven, flying system. The values for the A320-200 are from measured data from the slat system *[Becker, 2000]*.

Table 28: Weight comparison of different leading edge actuation systems (scaled to 1m span)

	A 320 - 200	Kinematic	Pneumatic
Leading Edge skin [kg]	10,20	10,7	10,1
Actuation [kg]	18,63	35	4
Other [kg]	-	-	9
Total [kg]	**28,83**	**45,7**	**23,72**
Total [%]	100	156	96

For this comparison it was assumed, that the skin for the kinematic system and the pneumatic system are identical, expect for the number of stringer used for each concept. The kinematic system uses 4 stringers, while the pneumatic system uses only one. The weight difference over one meter is roughly 0,7 kg. In Figure 111 a DMU of a SADE kinematic in drooped position can be seen, included in the figure are values for the weight of the most prominent components. The overall weight of one station including fasteners and cables is about 17,5kg. As for one meter span two stations are needed, the actuation weight of the kinematic system is 35kg/m. The data for the pneumatic actuation system comes mostly from the demonstrator (see chapter 8.6). As the design of the demonstrator used the same load cases as the kinematic system, the values are comparable. It is important to note, that both the kinematic system and the pneumatic system do not fulfill all requirements demanded of a leading edge. Neither system was designed with bird-strike or lightning strike protection or an anti-ice system. Therefore the comparison to the A320-200 system cannot be seen as absolute. The static structure necessary for the pneumatic system could be designed as a bird strike protection system. Therefore a certain degree of synergy can be expected with this design, resulting in a further weight benefit for the pneumatic structure in comparison to the kinematic system. Overall neither for the pneumatic nor for the mechanical system is a full weight analyses possible as no information exist on cables, feed-pipes, sensors, electronic equipment, power consumption etc.

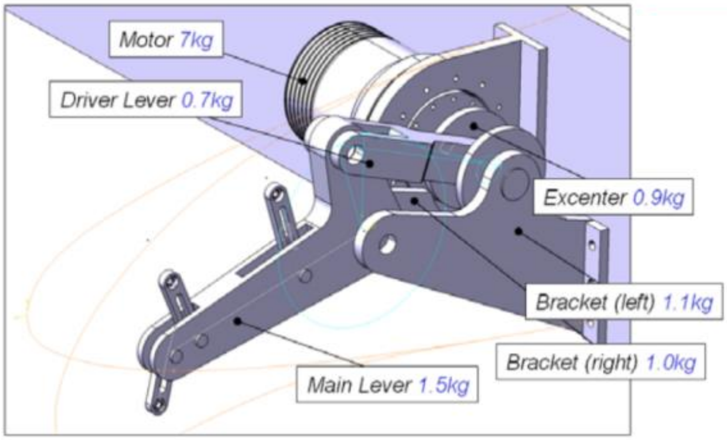

Figure 111: SADE Kinematic system (DMU with mass)

8.7.2 Comparison of the deformation performance

Based on the results published in *[Kintscher et al., 2011]* a comparison of the two concepts was possible, based on FE-modelling, see Figure 112. In direct comparison the pneumatic system achieves a better performance with regard to the drooped target shape. A similar comparison was not possible for the cruise shape as the data for the kinematic system for one cross-section was not available. But data for a 2m long segment of the kinematic system under cruise loads was available.

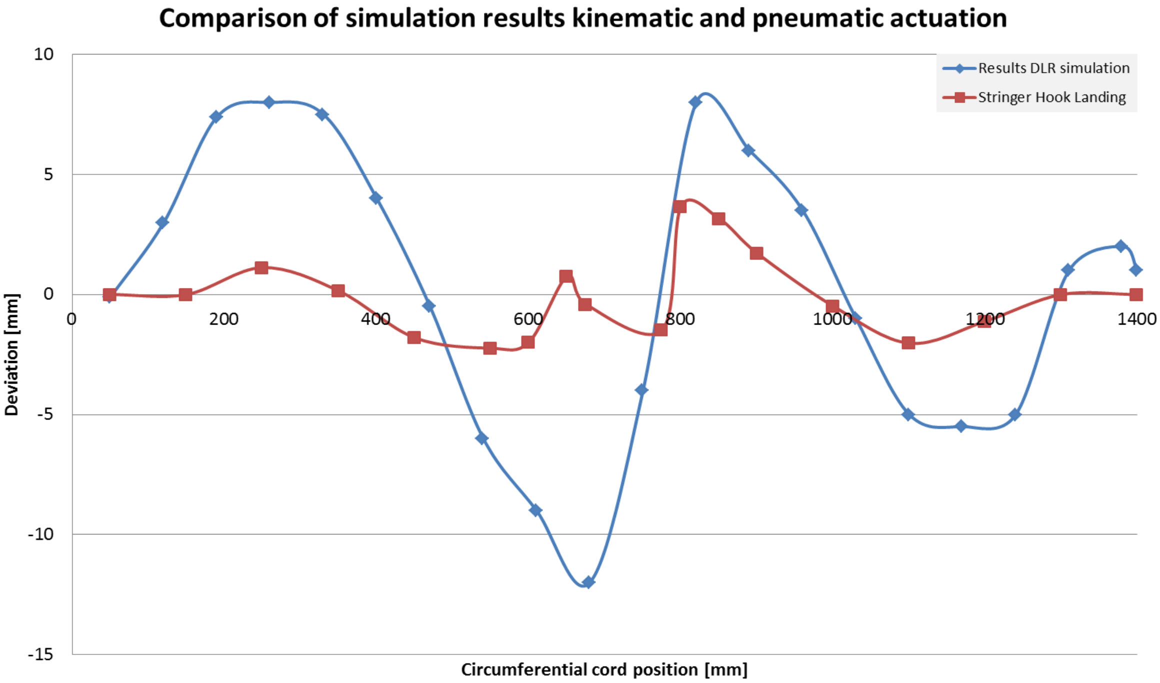

Figure 112: Comparison of kinematic vs pneumatic actuation simulation results for drooped configuration under air loads

The maximum deviation of about 1,1-1,3mm for the kinematical system during cruise was observed at the tip of the nose, see Figure 113. In the same area the pneumatic system shows a deviation of 1,2-1,4mm.

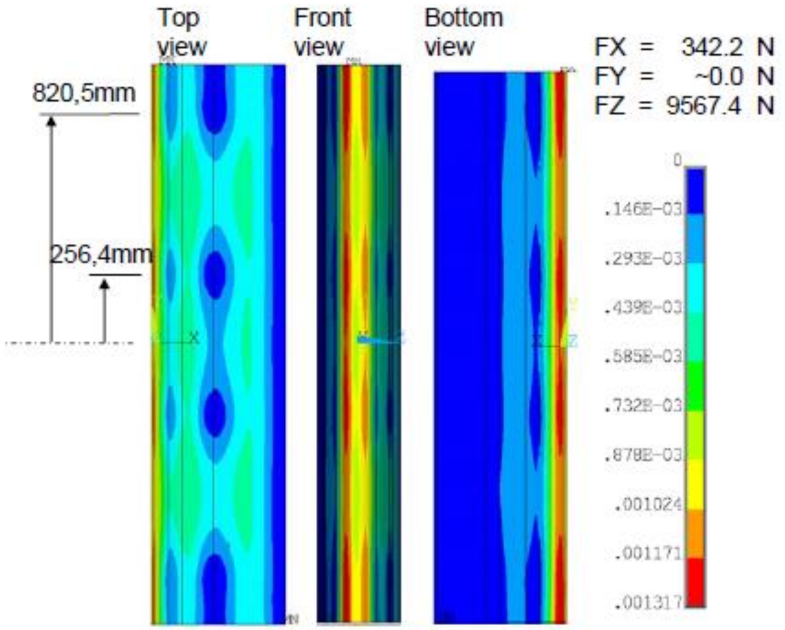

Figure 113: Deformation in meters in cruise configuration with limit stop position *[Kintscher et al., 2011]*

In a comparison only focused on the values of deviation from the target shape the pneumatic system is the better system, but as the deformation has a direct impact on the aerodynamic performance the slightly higher deviation during cruise of the pneumatic system might change this result.

Using the in chapter 2.1 stated requirements for natural laminar flow as a benchmark both concepts have a slightly too high deviation from the target-shape. When creating the b/a ratio for the deviations of the pneumatic system at the tip of the nose the result is a ratio of 0,003, which is three times as high as the stated allowable. This appears to be a bad result but as the deformation at the tip of the nose is deformed as a whole and does not really create a “bump” it is very difficult to judge whether this really is a to high deformation or not. As stated above an aerodynamic performance evaluation of the concepts has not been performed.

8.8 Complexity and scale-ability of the pneumatic system concept

Based on the best design (chapter 8.3.1) and the demonstrator (see chapter 8.6) a preliminary system setup for the pneumatic actuators was described, based on this it is possible to compare the complexity of the two systems with each other. As the development for both systems is not at an aircraft level, a first good indicator of complexity is the part count. In Table 29 the number of parts over a meter span for both systems is compared to the number of parts used on an A320 *[Becker, 2000]*. In this comparison the pneumatic system can really show its strength, without the need for any levers or similar the part count is drastically reduced.

Table 29: Comparison of part counts (scaled to 1m span)

	A 320 - 200	Kinematic	Pneumatic
Fixed LE [pt]	35	1	2-3
Kinematic [pt]	27	82	0
Actuator + Connectors [pt]	8	2	20-30 (estimate)
Total [pt]	**70**	**85**	**23-33**
Total [%]	100	121	33-47

Apart from the part count the complexity of both systems is difficult to evaluate at this stage. The mechanical system is most likely easier to adapt to a full scale A/C system as similar systems are in use today and the principals involved are very well known. Such a switch from today's mechanical system to the pneumatic system would involve a bigger change in A/C system design, than from the flap kinematic to the droop nose kinematic. Therefore it has to be said, that for the kinematic system the development complexity is lower. Disregarding the higher TRL of the kinematic system the scale-ability of both systems is likely similar, but requires a more in depth analysis.

In terms of weight and complexity the pneumatic systems shows to be better than the kinematic system at this stage of development. With regard to performance the deformation behavior of both systems is almost equally good during cruise while the pneumatic system shows a better performance for the deployed condition. An assessment on system failure probabilities cannot be performed at this stage.

The main objective of this work was to perform a feasibility analyses for a pneumatic actuated leading edge of an A/C and for this develop the required tools (simulation model) and components (actuators). As such during the design for the pneumatic system certain issues were deliberately omitted from the design and assessment process. While A/C certification requirements were considered they were not fully applied. For example the temperature range for the material used on the actuators does not fit the requirements stated in the CS25. This issue was not pursued as a full system design was not completed and the list of requirements not fixed. As such the temperature requirement stated in CS25 cannot be automatically assumed to be applicable to the actuators, as e.g. a heating of the actuators is easily possible by using heated air to inflate. The stiffness-increase at lower temperatures could even be beneficial for the system. Additionally for a complete assessment material tests with regard to hot-wet and fatigue behavior have to be performed and a mock-up of the system should be tested under varying conditions. Maintenance issues were also not considered however it is possible to repair the membrane of the actuators.

8.9 Adaptation and impact on A/C-level of the pneumatic concept

Most work in this thesis was focused on the detailed solution of a pneumatic actuation system for a 2D-cut extruded section of an A320 like wing. In the previous chapters it was shown, that a pneumatic actuation system can provide the required deformation for the selected 2D geometry, but on a real A/C the leading edge is rarely an extruded 2D- part. A wing can be geometrically very complex with doubly curved surfaces and constantly changing shape (span-wise). The geometry of the leading edge on an A/C usually decreases in size with increasing span-position. This means the design space for the pneumatic actuation system decreases in size the further away from the fuselage.

Considering the space-allocation for the actuators in this 2D study, an adaptation to a larger or smaller geometry should not pose a problem, as long as the maximum deformation scales with the change in geometry. If a full 3D geometry should be equipped with such a pneumatic system the actuators would be conically shaped, to accommodate the geometrical change. Important to note is that in parallel to the changing geometry the pressure distribution changes as well. Again for a 2D profile without any sweep a constant pressure distribution can be assumed in span wise direction. On a 3D profile not only does the cross-section change shape, but due to the usually occurring sweep angle additional cross flow is introduced which also influences the pressure distribution in the relevant area (leading edge).This has a direct impact on the design of the actuation system. The constantly changing pressure distribution in span wise direction makes it necessary to change the pressure inside the actuator accordingly. As the pressure inside one actuator is always the same everywhere this is not directly possible. Therefore the pressure inside the actuator has to be chosen to fit either the maximum load or a mean value in between.

If the highest air load determines the internal pressure the actuator walls cannot be stretchable. This also reduces the possibility and necessity to tailor the actuator in its deformation-behavior. Therefore for the application of the droop nose a non-stretchable but at the same time bending-flexible actuator is mandatory for a 3D application. If a non-stretchable actuator with a constant pressure-level has to be used this means realistically more than one actuator is necessary per wing. The actual number of actuators strongly depends on the wing-geometry (as this directly impacts design space and pressure distribution).

To go from a 2D design to a 3D design can be summarized into three main points/issues:

- Skin waviness of the outer skin
- Changing pressure distribution in span
- Changing design space along span

Each of these points lead to in part interconnected design requirements that have to be considered additionally to the 2D design.

Having multiple discrete actuators along the span of a leading edge of a wing will have to be analyzed in terms of skin waviness and interactions between the actuators. As shown in chapter 7.2 the actuators have a constant stroke in the middle part with a decrease of stroke towards the ends of the actuators until the height of the endcaps is reached. This leads to unsupported segments of skin at least during the drooping of the skin. The endcaps could be designed in such a way to support the skin in cruise mode. These two aspects have to be considered during the layout and design of the overall system. As the two parameters are partially contradictory to each other they should be considered in an optimization loop during the design.

8.9.1 From 2D simulation to 3D system design

To design a 3D system the simulation has to be adapted to a representative 3D simulation. For such a simulation the part count increases which automatically increases the modeling complexity, which also increases the simulation complexity as well. In a full 3D simulation the actuators can no longer be modelled as tubes with a constant diameter. They would have to be geometrically divers and be represented with endcaps, or at least boundary conditions acting as endcaps. As mentioned above the required deformation along the span is changing continuously. Therefore either the actuators reflect this change by a continuous change in maximum diameter or a multitude of small identical actuators is used creating a stair like rigid structure.

Creating a representative 3D simulation of such a system would drastically increase the DOF of the simulation (the extruded 2D models in this work have around 250k DOF). A good approach would be to create multiple 2D simulations at various locations along the span of the wing as a first design step. If a common solution for different locations is found, these results can then be used to interpolate between the positions and create first multiple short 3D models and finally an overall model. The intermediate step of creating short 3D models (double the simulation-size shown in this study) can help to identify and evaluate possible scale-ability or potential 3D related issues (e.g. airload distribution, double curved surfaces). The suggested process can be seen in Figure 114.

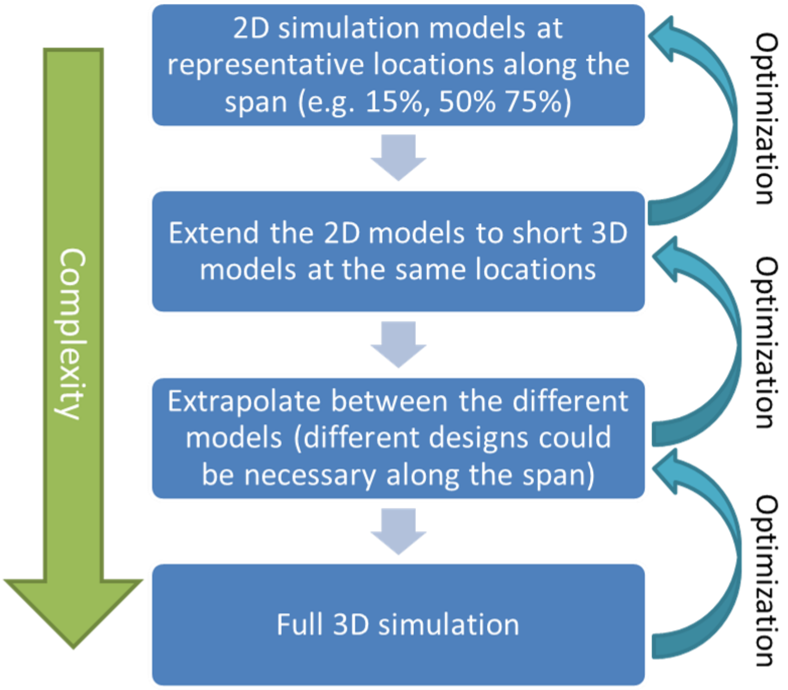

Figure 114: From 2D to 3D simulation process

Besides scaling the 2D model creating a complete 3D model would make further simplification necessary to reduce the simulation time and DOF. One option could be to use adaptive mesh-sizing (using a coarse mesh in areas of small deformation, or low interest) or to use superelemets. Another could be to remove the actuators from the simulation and use pressure loading inside the skin as a simplified representation of the actuators for the full 3D simulation during the design process. For a final full-scale simulation this is not recommended. Which approach is chosen depends completely on the overall simulation target.

8.9.2 Actuation pressure distribution on A/C level

For the operation of the pneumatic actuators on an aircraft a reliable source of pressurized air is needed. On an aircraft the main source of pressurized air are the engines. The APU can also supply pressurized air to aircraft systems. Usually each source can be deactivated by an isolation valve. Figure 115 shows a very simplified concept for a redundant pressure supply for the pneumatic leading edge actuators. Both engines and the APU feed pressure to a centralized location, from where the pressure is distributed back to the actuators. This way an unsymmetrical failure of the actuation system is prevented in case of one engine loss (for a two engine A/C). This centralized location is also equipped with a dump valve, in case of over-pressure or emergency. The pressurized air taken as bleed air from the engines is (a.t.m.) at about 0,25 N/mm² and 200°C *[Scholz, 1998]*. As a result it will be necessary to first cool the air down to acceptable levels for the actuators (≈20°C), secondly pressure control valves will be necessary as the actuation pressure will change over the span. As show in chapter 8.2 the pressure needed for the 2D geometry is 0,22 N/mm² the output of 0,25 N/mm² from the engines will not be enough for the actuation system, as pressure loses will occur along the way. Additionally the 2D case study presented here is taken from the middle of the wing, the pressure requirement for the more inboard sections of the actuation system are likely to be higher. The conclusion is therefore an additional pressure generator is needed, or the bleed air has to be taken from another point of the engine. Which option is more preferable requires a more detailed analysis than can be provided here, and will therefore not be answered in this work. For more information on weight penalty and aircraft systems please see e.g. *[Scholz, 1998]* and *[Raymer, 1992]*.

In Figure 115 alternating colored actuators are drawn, these symbolize that for each wing more than one actuation combo (meaning one small and one large actuator as presented e.g. in Figure 101) will be needed. The alternating color symbolizes also, that neighboring actuators should not be directly connected, to avoid a cascading failure scenario. If such a setup (only half the actuators active) can still provide reliable or useful deformation remains unanswered at this point.

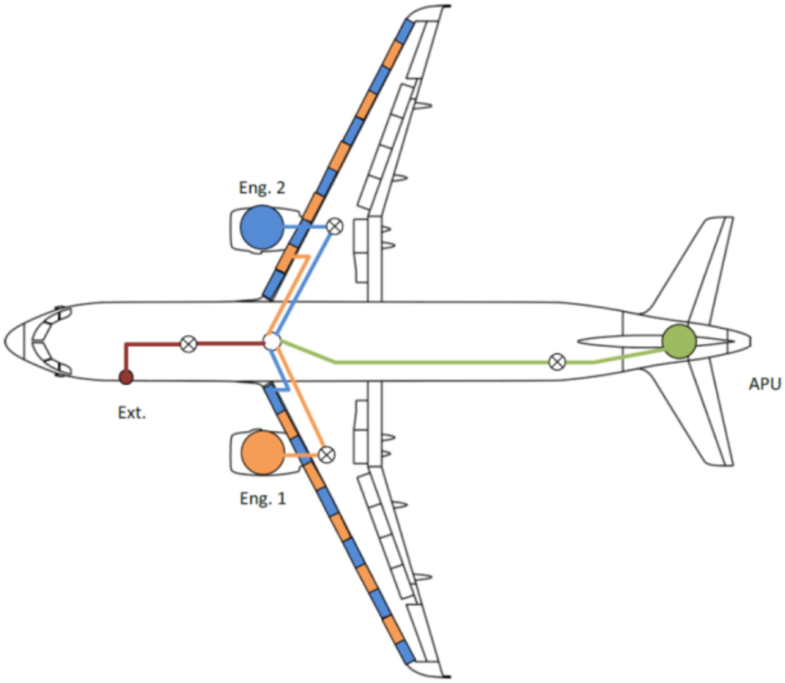

Figure 115: Source of pneumatic pressure on A/C (with redundancy)

8.9.3 Actuator control on aircraft level

A possible actuator control system is shown in Figure 116. The FCS (flight control system) commandeers a pressure differential between p_{ref} actuator and the current atmospheric pressure p_0 based on the required position of the actuator. The inflow and outflow valves have then to match this reference value. The actuator is permanently monitored for leakage. A certain amount of leakage can be tolerated by the system, if the pressure loss $-\dot{p}_{akt}$ exceeds $-\dot{p}_{akt,max}$ the control unit will close the inflow valve to this particular actuator permanently (if the outflow valve is closed). This prevents a pressure drop in the supply duct. If the pressure inside the actuator is too high, a relief valve is installed to protect the actuator from being damaged. The check valve between the waste duct and the actuator prevents unwanted inflation of the actuator in case of a pressure increase in the waste duct (e.g. deflation of an actuator further down the line, etc.). To achieve a balanced and quick actuation response, it could be beneficial to operate with a high pressure difference between the supply duct and the actuator. The response-time of the droop nose does not need to be very fast (actuation time between 20s - 30s). A very rapid pressure increase in the actuators might lead to damage and failure of the actuators, therefore a throttle valve is installed in front of the inflow valve. Using a buffer tank in a pressurized system reduces the risk of abrupt pressure jumps in the system and it can also provide pressure when/if the generators fail. The buffer tank should contain enough pressurized air to achieve a full droop of the nose even in case of complete power loss.

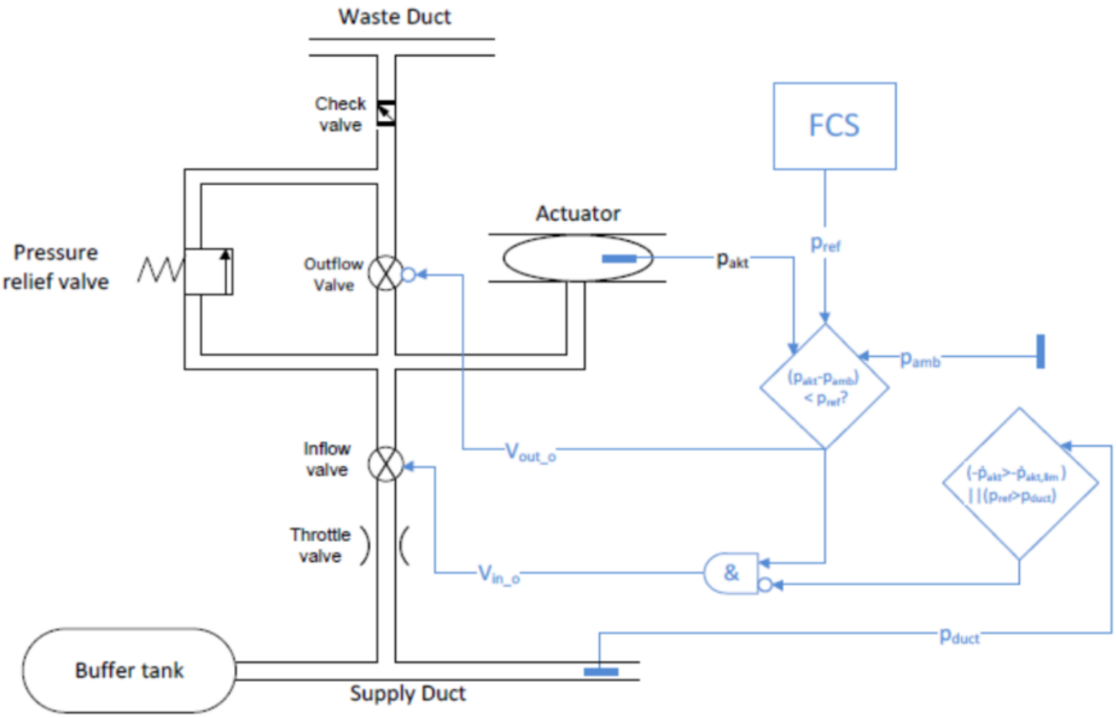

Figure 116: Actuator control logic (pneumatic black, electric blue)

9. Summary and conclusion

9.1 Summary

In this work a pneumatic actuation system for an adaptive leading edge droop nose of an aircraft was developed and its potential benefits and drawbacks were shown. The global design parameters like geometry and loads were taken from the EU FP7 project SADE and (partially) the EASA CS25. Based on the therein contained requirements several potential actuation concepts were presented. For this the characteristics of pneumatic systems had to be taken into account. Based on the conceptual designs of the system material and structural requirements were identified. Flexible matrix composites (FMC) were recognized as a potential type of material. As such a material was not commercially available (at the time), research in the production and testing of such type of material was performed. The production trials resulted in a feasible material combination and end-product. This prepreg like FMC was then used to create tensile and bending test-specimen to create an analytical and numerical model of the developed material. The material was also used to design and test pneumatic actuators. The conceptual designs, the tensile tests and the pneumatic actuator prototypes were used to derive, evaluate and prepare a simulation model for a pneumatic actuation system. This was then used to perform FE simulations of the different pneumatic actuation systems for the droop nose at different external load conditions. The results were compared to the two distinct target shapes from the project SADE. The best design (best shape-fit) was afterwards evaluated with a sensitivity study. The same design was then used to extrapolate a 3D system design for an A320 like airplane. A comparison between the developed system and the SADE kinematic was performed and the weight and the accuracy were compared.

9.2 Conclusion and outlook

The herein developed pneumatic actuators are comparable to inflatable seals and show a high energy density. The actuators consist of a flexible but non-stretchable skin which is made of a composite material and is therefore adaptable to the required loads. Variation in the skin stiffness on one actuator did not show a usable directional inflation behavior, it rather let to a failure of the actuator. As the failure always occurred in the softer regions of the actuator a more gradual transition between the stiffener and the rest of actuator does not solve this issue. This behavior has a direct influence on the system design as it impacts the overall deformation capability of the system and therefore has to be included in the design process. The actuators in this work were designed for a very specific use-case but they could be also used for different applications. The actuators themselves are very simple, light weight components. In any case the directionality of theses actuators has to be kept in mind.

For the evaluation of the different possible system designs a simulation model was created partly based on material test results. Even though the material showed non-linear behavior during testing it was decided to use a simplified, linear material model. This was due to the overall complexity of the system, and an acceptable simplification (as shown in chapter 6.6). With this model it is now possible to simulate the deformation behavior of the actuators as well as the overall system behavior under external loading at the same time.

While the finalized design shows good results with regard to the target shapes it was not optimized with the help of optimization tools. Doing so would most likely result in an even better solution. The sensitivity analyses in chapter 8.4 proved a robustness of the design against certain influences but also showed that slight changes in design can have an impact on the performance. Not included in the analyses were weight and complexity assessment, which could also benefit from an optimization loop. Here it again became apparent that for such an integrated system a structural and system design have to be performed simultaneously. The sensitivity analyses showed that a small structural (geometrical) change leads to a measurable change in the systems performance.

As mentioned above in chapter 8.7/8.8 several issues were not fully considered during the selection of the most promising pneumatic system. As such it is suggested to perform a complete system design assessment and to build a system demonstrator in future work. With this a complete A/C level evaluation of a pneumatically actuated droop nose should be possible. The pneumatic system showed a good robustness of the design against external influences but revealed also the large impact of geometrical or stiffness change on the surrounding structure. It is important to note, that the design was performed for a single geometry and therefore all solutions and design guidelines are based on this one geometry. The author could not identify specific reasons why the systematic approach demonstrated should not work on other geometries but has not proven this assumption.

In this work it was shown that a pneumatic actuation system has the capability to be used as a leading edge actuation system for high-lift operation on an A/C. In a direct comparison with a mechanical solution for the same application the pneumatic system shows an overall better performance. During the cruise phase the kinematic system and the pneumatic system show almost identical deviation from the target shape, for the drooped configuration the pneumatic system shows better results. Also in terms of weight the pneumatic system shows a clear potential to be lighter.

Bibliography

Amiryants, G.;
Adaptive selectively-deformable structures; new concept in engineering
21st Congress of the International Council of the Aeronautical Sciences, Melbourne, AUS, 13.- 18.09.1998; ICAS-98-6,8,3; A98-31695; 1998

Andreou, C., Graham, W., & Shin, H.;
Aeroacoustic Comparison of Airfoil Leading Edge High-Lift Geometries and Supports
Proceedings of the 45th AIAA Aerospace Sciences Meeting and Exhibit, AIAA Paper 2007-230, 1-20; 2007

Babu, R.R.; Naskar, K.;
Recent Developments on Thermoplastic Elastomers by Dynamic Vulcanization
Springer, Advanced Rubber Composites, Advances in Polymer Science Volume 239, 2011, pp 219-247

Bae, J-S.; Seigler, T.M.; Inman, D.J.; Lee, I.;
Aerodynamic and Aeroelastic Considerations of A Variable-Span Morphing Wing
45th AIAA/ASME/ASCE/AHS/ASC Structures, Structural Dynamics & Materials Conference 19-22 April 2004, Palm Springs, California, USA, 2004, AIAA-2004-1726

Baier, H.; Datashvili, L.; Müller, U.;
Optimization and Exp. Characterization of Functional Hybrid Material Space Structures
ESA`s Antenna Conference, June 2005

Barbarino, S.; Bilgen, O.; Ajaj, R.F.; Friswell, M.I.; Inman, D.J.;
A Review of Morphing Aircraft
Journal of Intelligent Material Systems and Structure, Vol. 22 – June 2011

Barbarino, S.; Pecora, R.; Lecce, L.; Concilio, A.; Ameduri, S.; De Rosa, L.;
Airfoil Structural Morphing Based on S.M.A. Actuator Series: Numerical and Experimental Studies
Journal of Intelligent Material Systems and Structure, Vol. 22; No. 10 –July 2011

Bathe, K.-J.:
Finite Elemente Methoden
Springer Verlag, Berlin. 2002 (2. Aufl.)

Batra, R.C.;
Elements of Continuum Mechanics
AIAA Education Series, Blacksburg, VA, USA; 2006

Becker, H.;
CFK-Tragflügel - Verifikation eines CFK- Demonstrator- Flügelkastens durch statische / dynamische Versuche
Hamburg: DaimlerChrysler Aerospace Airbus GmbH; 2000..

Benedix, R.:
Bauchemie: Chemie für Bauingenieure
Vieweg+Teubner Verlag, 2te Auflage; Stuttgart, Leipzig. 2003

Betten, J.;
Kontinuumsmechanik
Springer, Berlin, 1993

Bonet, J.; Wood, R.;
Nonlinear Continuu Mechanics for FEA
First Edition, Cambridge University Press, 1997

Bowman, J.; Sanders, B.; Weisshaar,T.;
Evaluating the Impact of Morphing Technologies on Aircraft Performance
43rd AIAA/ASME/ASCE/AHS/ASC Structures, Structural Dynamics, and Materials Conference
22-25 April 2002, Denver, Colorado; AIAA 2002-1631

Braslow, A.L.;
A History of Suction-Type Laminar-Flow Control with Emphasis on Flight Research
NASA History Division; Monographs in Aerospace History, No. 13; 1999

Brown, L.; Smith, L;
A simple transversely isotropic hyperelastic constitutive model suitable for finite element analysis of fiber reinforced elastomers
Journal of Engineering Materials and Technology, 2011

Carmichael, B. H.;
Summary of past experience in natural laminar flow and experimental program for resilient leading edge
NASA, 1979

Cadogan, D.; Smith, T.; Uhelsky, F.; MacKusick, M.;
Morphing Inflatable Wing Development for Compact Package Unmanned Aerial Vehicles
45th AIAA/ASME/ASCE/AHS/ASC Structures, Structural Dynamics & Materials Conference
19-22 April 2004, Palm Springs, California; AIAA 2004-1807

Cesnik, C.E.S; Last, H.R.; Martin, C.A.;
A Framework for morphing capability assessment
45th AIAA/ASME/ASCE/AHS/ASC Structures, Structural Dynamics & Materials Conference 19-22 April 2004, Palm Springs, California, USA; 2004, AIAA-2004-1654

Chen, Y.; Scarpa, F.; Remillat, C.; Farrow, I.; Liu,Y.; Leng, J.;
Curved Kirigami SILICOMB cellular structures with zero Poisson's ratio for large deformations and morphing
Journal of intelligent Material Systems and Structures 2014, Vol.25(6) 731-743

Chow, L. C., Mau, K.,; Remy, H.;
Landing Gears and High Lift Devices Airframe Noise Research
AIAA 2002-2408. Colorado: American Institute of Aeronautics and Astronautics, 2002

Croom, C. C.; Holmes, B. J.;
Insect contamination protection for laminar flow surfaces
Langley Symposium on Aerodynamics, Volume 1, pp. 539-556; 1988

Coffey, A.B.; O'Bradaigh, C.M.; Young, R.J.;
Interfacial stress transfer in aramid reinforced thermoplastic elastomer
Journal of Materials Science; No.: 19/2007; 8053-8061, 2007

Collier, F.;
NASA Sponsored Activities in Laminar Flow – Technologies for Advanced Transport Aircraft
2nd UTIAS-MITAS International Workshop on Aviation and Climate Change; May 27-28, 2010; Toronto, Canada

Datashvili, L.; Baier, H.; Schimitschek, J.; Lang, M.; Huber, M.;
High Precision Large Deployable Space Reflector Based on Pillow-Effect-Free Technology
48th AIAA/ASME/ASCE/AHS/ASC Structures, Structural Dynamics, and Materials Conference
23-26 April 2007, Honolulu, Hawaii; AIAA 2007-2186

Datashvili, L.; Baier, H.; Lang, M.; Sixt, T.;
Membranes for Large and Precision Deployable Reflectors
European Conference on Spacecraft Structures, Materials & Mechanical Testing 2005, Noordwijk, The Netherlands, 10 – 12 May 2005

Daynes, S.; Weaver, P.M.; Trevarthen, J.A.;
A Morphing Composite Air Inlet with Multiple Stable Shapes
Journal of Intelligent Material Systems and Structure, Vol. 22 – June 2011

DeBreuker, R.; Abdalla, M.M.; Gürdal, Z.;
A Generic Morphing Wing Analysis and Design Framework
Journal of Intelligent Material Systems and Structure, Vol. 22; No. 10 –July 2011

Domininghaus, H.;
Kunststoffe – Eigenschaften und Anwendungen
Springer Verlag, 2008 (Hrsg. Elsner, P.; Eyerer, P.; Hirth, T.)

Drechsler, *K.:*
Skript zu "Werkstoffe und Fertigungsverfahren"
IFB, Universität Stuttgart, 2007

Drechsler, K.:
Leichtbauskript
IFB, Universität Stuttgart, 2007

Dreßler, U.; Szodruch, J.;
Flugversuche mit dem Laminarhandschuh am VFW 614 - ATTAS
MBB- Jahrbuch 1988 (S. 133-140)

Fink, D.A.; Reinhardt, N.; Severance, R.; Phillips, R.; Gaudreau, M.P.J.;
Deformable Leading Edge Electromechanical Airfoil
Annual Forum Proceedings; American Helicopter Society; 63; 785-805; 2007

European Aviation Safety Agency,
Certification Specification for Large Aeroplanes (CS-25)
European Aviation Safety Agency, Amendment 3, 2007

Fung, Y.C.;
Biomechanics: Mechanical Properties of Living Tissue
Springer, Berlin, Second Edition, 1993

Gasser, T.C.; Ogden, R.W.; Holzapfel, G.A.:
Hyperelastic modelling of arterial layers with distributed collagen fiber orientations
Journal of the Royal Society, 3(6), pp15-35, 2006

Gautschi, G.;
Piezoelectirc Sensorics
Springer, Berlin, 1st edition, 2002

Gomis-Bellmunt, O.; Campanile, L.F.;
Design Rules for Actuators in Active Mechanical Systems
Springer, London, UK; 2010

Grambow, A.:
FEM und die Beschreibung des mechanischen Werkstoffverhaltens II: Elastomere. In: CAE in der Kunststoffverarbeitung –Grundlagen, Anwendungen, Perspektiven
Institut für Kunststoffverarbeitung RWTH Aachen, 2001, Umdruck zum gleichnamigen Seminar

Gramüller, B.;
Druckaktuierte zelluläre Strukturen – Dimensionierung und experimentell Evaluierung
VDI- Fachtagung: Industrielle Anwendung der Bionik 2015, Esslingen

Grohmann, B.A.; Storm, S.; Jaenker, P.; Maucher, C.K.; Dietrich, O.;
Active Trailing Edge for Morphing Helicopter Blades
AVT-168 Symposium on “Morphing Vehicles”, Evora, Portugal;2009

Grohmann, B.A.; Müller, F.; Ahci, E.; Pfaller, R.; Bauer, M.; Maucher, C.; Dietrich, O.; Storm, S.; Jaenker, P.;
Design, Evaluation and Test of Active Trailing Edge
67th American Helicopter Society International Annual Forum, Virginia Beach, USA, 2011

Harris, J.W.; Witmer, D.B.;
Variable Geometry Airfoils Using Inflatable Surfaces
AIAA 22nd Aerospace Sciences meeting; Reno, Nevada, January 9-12, 1984; AIAA-84-0072

Holmes, B. J., Croom, C. C., Hastings, E. C., Obara, C. J.; Vandam, C. P.;
Flight research on natural laminar flow
Langley Research Center: NASA, 1986

Holmes, B.J.; Obara, C.J.;
Flight Research on Natural Laminar Flow Applications
Natural Laminar Flow and Laminar Flow Control; ICASE/NASA LaRC Series 1992, pp 73-142

Holzapfel, G.A.;
Determination of material models for arterial walls from uniaxial extension tests and histological structure
Journal of Theoretical Biology 238; 290-302; 2006

Holzapfel, G.A.; Gasser, T.C.; Ogden, R.W.:
Comparison of structural model with a Fung-type model using a carotid artery: issues of material stability
1st GAMM Seminar on Continuum Biomechanics, Report No.: II-14, Institute of Applied Mechanics (CE), University of Stuttgart, 2005, 79-89

Holzapfel, G.A.; Ogden, R.W.:
On planar biaxial tests for anisotropic nonlinearly elastic solids. A continuum mechanical framework
Mathematics and Mechanics of Solids 2009 14: 474

Hutchings, A.L.; Braun, R.; Masuyama, K.; Welch, J.;
Experimental Determination of Material Properties for Inflatable Aeroshell Structures
AIAA 2009-2949, 20th AIAA Aerodynamic Decelerator Systems Technology Conference and Seminar, Seattle, WA, May 2009.

Ishikaia, S.; Tokuda, A.; Kotera, H.;
Numerical Simulation for Fiber Reinforced Rubber
Journal of Computational Science and Technology, Vol.2, No.4, 2008

Jenkins, C.H.M;
Gossamer Spacecraft: Membrane and Inflatable Structures Technology for Space Applications
AIAA, Vol. 191 Progress in Astronautics and Aeronautics, Cambridge, MA, USA; 2001

Jiang, Y.; Ye, Z.; Zhan, Z.;
A Method of Inflatable Leading Edge for High Lift, Deicing and Noise Reduction
47th AIAA Aerospace Sciences Meeting Including The New Horizons Forum and Aerospace Exposition; 5 - 8 January 2009, Orlando, Florida

Keun, C.-A.; Schulte, K.;
Novel design of semi-flexible composites by warp-knit reinforced thermoplastic elastomers (Development of a novel handrail for escalators)
SAMPE '06. Creating New Opportunities for the World Economy. Long Beach, USA, 30.04.2006 - 04.05.2006

Kintscher, M.; Monner, H.P.; Kühn, T.; Wiedemann, M.;
Low Speed Wind Tunnel Test of a Morphing Leading Edge
AIDAA XXII Conference Napoli, 9-12th September 2013

Kintscher, M.; Wiedemann, M.; Monner, H.P.; Heintze, O.; Kühn, T.;
Design of a Smart Leading Edge Device for Low Speed Wind Tunnel Tests in the European Project SADE
International Journal of Structural Integrity, Vol. 2 (Iss: 4), Page 383-405, 2011

Kirn, J., Lorkowski, T.; Baier, H.;
Development of Flexible Matrix Composites (FMC) for Fluidic Actuators in Morphing Systems
International Journal of Structural Integrity, Vol. 2, Issue 4 , pp. 458 – 473; 2011

Kirn, J., Lorkowski, T.; Baier, H.;
Pneumatic Actuation Tubes Using Flexible Matrix Composites for Morphing Aero-Structures
SAMPE-SETEC 11, 14.-16.09.2011 Leiden, Netherlands; 2011

Kreth, S.; König, R.; Wild, J.;
Aircraft noise determination of novel wing configurations
INTER-NOISE 2007, Istanbul, Turkey, 2007

Kress, G.; Ermanni, P.;
Mechanik der Faserverbundwerkstoffe
ETH Zurich, Zentrum für Strukturtechnologie, 2006

Kudva, J. N.;
Overview of the DARPA Smart Wing Project
Journal of Intelligent Material Systems and Structures , pp. 261-267; 2004

Kyriacou, S.K.; Schwab, C.; Humphrey, J.D.;
Finite element analysis of nonlinear orthotropic hyperelastic membranes
Computational Mechanics 18 (1996), 296-278, 1996

Lammering, T.; Anton, E.; Henke, R.;
Technology Assessment on Aircraft-Level: Modeling of Innovative Aircraft Systems in Conceptual Aircraft Design
Fort Worth, Texas: American Institute of Aeronautics and Astronautics; 2010

Lan, X.; Liu, Y.; Lv, H.; Wang, X.; Leng, J.; Du, S.;
Fiber reinforced shape-memory polymer composite and its application in a deployable hinge
Smart Materials and Structures 18, Issue 2, 2009

Larsen, J.J.; Jenkins, C.H.; Denowh, C.; Woo, K.;
A Bio-Inspired Lightweight MRF-Foam Actuator
50th AIAA/ASME/ASCE/AHS/ASC Structures, Structural Dynamics, and Materials Conference
4 - 7 May 2009, Palm Springs, California; AIAA 2009-2143

Laulusa, A.; Bauchau, O.A.; Choi, J-Y.; Tan, V.B.C.; Li, L.;
Evaluation of some shear deformable shell elements
International Journal of Solids and Structures 43, P. 5033-5054, 2006 (available since Oct. 2005)

Long, A.C.;
Design and Manufacture of textile composites
Woodhead Publishing Limited, 2005

Luo, S.-Y.; Chou, T.-W.;
Finite deformation of flexible composites
Proc. Royal Society London, 429, 569-86; 1990

Mathiak, F.U.;
Die Methode der finite Elemente (FEM) – Einführung und Grundlagen
Hochschule Neubrandenburg, Bauingenieur-und Vermessungswesen, Neubrandenburg 2010

McKnight, G.; Doty, R.; Keefe, A.; Herrera, G.; Henry, C.;
Segmented Reinforcement Variable Stiffness Materials for Reconfigurable Surfaces
Journal of Intelligent Material Systems and Structure, Vol. 21; No. 17 – November 2010

Meschke, G.; Helnwein, P.;
Large-strain 3D-anlysis of fibre-reinforced composites using rebar elements: hyperelastic formulations for cords
Computational Mechanics 13, 241-254, 1994

Monner, H.P.
“Classic” and Emerging Smart Materials and their Applications
RTO-AVT-141 - Specialists' Meetings on Multifunctional Structures / Integration of Sensors and Antennas, 2-6 October 2006, Vilnius, Lithuania

Monner, H.P.; Kintscher, M.; Lorkowski, T.; Storm, S.:
Design of a Smart Droop Nose as Leading Edge High Lift System for Transportation Aircrafts
50th AIAA/ASME/ASCE/AHS/ASC Structures, Structural Dynamics & Materials Conference, Palm Springs, California, USA, 2009; AIAA-2009-2128

Müller, I.; Struchtrup, H.;
Inflating a Rubber Balloon
Journal of Mathematics and Mechanics of Solids, October 2002, vol. 7 no. 5 569-577

Murray, G.; Gandhi, F. B. C.;
Flexible Matrix Composite Skins for One-Dimensional Wing Morphing
48th AIAA/ASME/ASCE/AHS/ASC Structures, Structural Dynamics, and Materials Conference 23-26 April 2007, Honolulu, Hawaii, USA, 2007 AIAA-2007-1737

Nagdi, K.;
Gummi Werkstoffe – Ein Ratgeber für Anwender
Würzburg: Vogel-Verlag, 1981

Nasdala, L.;
FEM-Formelsammlung Statik und Dynamik
Vieweg+Teubner, Wiesbaden, Germany, 2010

Ogden, R. W.:
Large Deformation Isotropic Elasticity - On the Correlation of Theory and Experiment for Incompressible Rubberlike Solids
Proceedings of the Royal Society of London. Series A, Mathematical and Physical Sciences, Vol. 326, No. 1567, pp. 565-584., 1972

Olympio, K.R.; Gandhi, F.;
Flexible Skins for Morphing Aircraft Using Cellular Honeycomb Cores
Journal of Intelligent Material Systems and Structure, Vol. 21; No. 17 – November 2010

Olympio, K.R.; Gandhi, F.; Asheghian, L.; Kudva, J.;
Design of a Flexible Skin for a Shear Morphing Wing
Journal of Intelligent Material Systems and Structure, Vol. 21; No. 17 – November 2010

Parr, A.;
Hydraulics and Pneumatics: A technican‘s and engineer‘s guide
Butterworth & Heinemann, Oxford, UK, 2nd Edition, 2006

Pecora, R.; Barbarino, S.; Concilio, A.; Lecce, L.; Russo, S.;
Design and Functional Test of a Morphing High-Lift Device for a Regional Aircraft
Journal of Intelligent Material Systems and Structure, Vol. 22; No. 10 –July 2011

Peel, L.;
Fabrication and Mechanics of Fiber-Reinforced Elastomers
Dissertation, Brigham Young University, USA, 1998

Pennycuick, C;
The Flight Environment (Chapter 2)
Theoretical Ecology Series, Vol. 5, Academic Press, 2008

Perkins, D.A.; Reed, J., Jr.; Havens, E.;
Morphing wing structures for loitering air vehicles
45th AIAA/ASME/ASCE/AHS/ASC Structures, Structural Dynamics & Materials Conference 19-22 April 2004, Palm Springs, California, USA, 2004, AIAA-2004-1888

Philen, M.; Shan, Y.; Wang, K.W.; Bakis, C.E.; Rhan, C.D.;
Fluidic Flexible Matrix Composites for the Tailoring of Variable Stiffness Adaptive Structures
48th AIAA/ASME/ASCE/AHS/ASC Structures, Structural Dynamics, and Materials Conference 23-26 April 2007, Honolulu, Hawaii, USA, 2007, AIAA-2007-1703

Philen, M.; Shan, Y.; Wang, K.W.; Bakis, C.E.; Rhan, C.D.;
Variable Stiffness Adaptive Structures utilizing Hydraulically Pressurized Flexible Matrix Composites with Valve Control
47th AIAA/ASME/ASCE/AHS/ASC Structures, Structural Dynamics, and Materials Conference 1-4 May 2006, Newport, Rhode Island, USA, 2006 AIAA-2006-2134

Pott-Pollenske, M.; Wild, J.;
Entwicklung und Validierung eines Verfahrens zur Beurteilung der Schallabstrahlung von Hochauftriebssystemen
DAGA 2007, Stuttgart, 2007

RameshGupta, B.; Harursampath, D.;
Asymptotically Accurate Non-linear Analysis of Inflatable Structures
48th AIAA/ASME/ASCE/AHS/ASC Structures, Structural Dynamics, and Materials Conference; 23-26 April 2007, Honolulu, Hawaii; AIAA 2007-1823

Raymer, D.P.;
Aircraft design: A conceptual approach
AIAA Education Series, 2nd Edition, Washington, 1992

Reinhard, A.; To, F.E.; Ramseier, O.; Res, K.;
Adaptive pneumatic wing for fixed wing aircraft
United States Patent; US 6,199,796 B1; 2001

Rudolph, P. K.;
High- Lift Systems on Commercial Subsonic Airliners
Ames Research Center: NASA, 1996

Ruggiero, E.; Park, G.; Inman, D.J.; Main, J.A.;
Smart Materials in Inflatable Structure Applications
43rd AIAA/ASME/ASCE/AHS/ASC Structures, Structural Dynamics, and Materials Conference
22-25 April 2002, Denver, Colorado; AIAA 2002-1563

Sanders, K. L.;
High-lift devices, a weight and performance trade-off methodology
SAWE Technical Paper No. 761. San Francisco, California: The Society of Aeronautical Weight Engineers, Inc; 1996

Saeed, T.I.; Grahamy; W.R., Babinsky H.; Eastwood, J.P.; Hall, C.A.; Jarrett, J.P.; Lone, M.M.; Seffen, K.A.;
Conceptual Design for a Laminar Flying Wing Aircraft
27th AIAA Applied Aerodynamics Conference 22 - 25 June 2009, San Antonio, Texas, USA, AIAA-2009-3616

Salama, M.; Kuo, C.P.; Lou, M.;
Simulation of Deployment Dynamics of Inflatable Structures
AIAA Journal, Vol. 38, No. 12, pp. 2277-2283; 2000

Scholz, Dieter;
DOC_{SYS} – A Method to Evaluate Aircraft Systems
In: Schmitt, D.; Bewertung von Flugzeugen / Workshop: DGLR Fachausschuß S2 – Luftfahrtsysteme, München, 26./27. October 1998

Shan, Y.; Bakis, C.E.;
Flexible Matrix Composite Actuators
20th Technical Conference of the American Society for Composites, Drexel University, Philadelphia, USA, 07.09.2005 - 09.09.2005

Suhey, J.D.; Kim, N.H.; Niezrecki, C.;
Numerical modeling and design of inflatable structures – application to open-ocean-aquaculture cages
Aquacultural Engineering 33: 285-303; 2005

Stojek, M., Stommel, M, Korte, W.;
FEM zur mechanischen Auslegung von Kunststoff- und Elastomerbauteilen.
Düsseldorf. 1998

Thill, C.; Etches, J.; Bond, I.; Potter, K.; Weaver, P.;
Morphing skins
The Aeronautical Journal, Vol. 1129 , pp117-129, 2008

To, F.E.; Kammer, R.;
Adaptive pneumatic wings for flying devices with fixed wings
United States Patent; US 6,347,769 B1; 2002

Tobolsky, A.;
Mechanische Eigenschaften und Struktur von Polymeren
Stuttgart. 1967

Vocke III, R.D.; Kothera, C.S.; Woods, B.K.S.; Wereley, N.M.;
Development and Testing of a Span-Extending Morphing Wing
Journal of Intelligent Material Systems and Structure, Vol. 22 – June 2011

Voit-Nitschmann, R.;
Skript zu „Einführung in die Luftfahrttechnik“
IFB, University of Stuttgart, 2006

Vos, R.; Barrett, R.; Romkes, A.;
Mechanics of Pressure-Adaptive Honeycomb
Journal of Intelligent Material Systems and Structure, Vol. 22; No. 10 –July 2011

Wagg, D.; Bond, I.; Weaver, P.; Friswell, M.;
Adaptive Structures – Engineering Applications
Wiley, Chichester, UK; 2007

Wereley, N.; Kothera, C.; Bubert, E.; Woods, B.; Gentry, M.; Vocke, R.
Pneumatic Artificial Muscles for Aerospace Application
50th AIAA/ASME/ASCE/AHS/ASC Structures, Structural Dynamics, and Materials Conference 4 - 7 May 2009, Palm Springs, California, AIAA 2009-2140

Wernicke, K.G.;
Inflatable Wing Leading Edges for High Lift and Deicing
NASA Glenn Research Center; NASA Tech Briefs LEW-16660; 1996

Westphal-Kay, B.;
Festigkeits- und Verformunsgverhalten von Fugendichtstoffen im Kreuzfugenbereich
Technical University Berlin, 2005

Wild, J.; Pott-Pollenske, M.; Nagel, B.;
An integrated design approach for low noise exposing high-lift devices
3rd AIAA Flow control Conference, San Francisco, California, 2006; AIAA 2006-2843

Wittmann, J; Steiner, H.-J.; Sizmann, A.;
Framework for Quantitative Morphing Assessment on Aircraft System Level
50th AIAA/ASME/ASCE/AHS/ASC Structures, Structural Dynamics, and Materials Conference 17th
4 - 7 May 2009, Palm Springs, California, USA, AIAA-2009-2129

Wlezien, R.W.; Horner, G.C.; McGowan, A.R.; Padula, S.L.; Scott, M.A.; Silcox, R.J.; Simspon, J.O.;
The Aircraft Morphing Program
39th *AIAA/ASME/ASCE/AHS/ASC Structures, Structural Dynamics, and Materials Conference*
20-23 April 1998, Long Beach, California; AIAA 98-1927

Woods, B. K. S.; Choi, Y.-T.; Kothera, C.S.; Wereley, N.M.;
Control System Development for Pneumatic Artificial Muscle Driven Active Rotor Systems
AIAA J. Guidance, Control, and Dynamics. 36(4):1177-1185; 2013

Yerkes, N.; Wereley, N.
Pneumatic Artificial Muscle Activation for Trailing Edge Flaps
46th AIAA Aerospace Science Meeting and Exhibit 7 - 10 January 2008, Reno, Nevada, AIAA 2008-1418

Yokozeki, T.; Takeda, S.; Ogasawara, T.; Ishikawa, T.;
Corrugated Composite as a Candidate for Flexible Wing Elements
20th Technical Conference of the American Society for Composites, Drexel University, 07- 09 September 2005, Philadelphia, USA, 2005

Zupan, M.; Ashby, M.F.; Fleck, N.A.;
Actuator Classification and Selection – The Development of a Database
Advanced Engineering Materials 2002, 4, No. 12, 933-939, 2002

Appendix

Appendix A: Material parameters Hexply 913

HexPly® 913

257°F (125°C) Curing Epoxy Matrix

Product Data

Description

HexPly® 913 is a proven modified epoxy matrix with a low temperature cure cycle which exhibits outstanding environmental resistance, whilst retaining good hot/wet mechanical performance. This versatile matrix system can be processed using a wide range of techniques according to the application and is capable of co-cure with epoxy film adhesives.

Benefits and Features

- Exceptional environmental resistance
- Controlled minimum viscosity giving easy processing
- Capable of being processed by various techniques
- Good tack and drape characteristics
- Long shelf life and out life at room temperature
- Compatible with Redux 312 adhesive film

Applications

HexPly® 913 is a highly successful matrix used extensively in the aerospace industry for primary aircraft structures and helicopter blades. In addition 913 prepregs are used in various industrial and recreational products, which include medical equipment and bikes.

Neat Resin Properties

Property, Units US (SI)	Value	Test Method
Specific Gravity	1.02	ASTM D792
Tg, °F (°C)	314 (157)	DMA
Gel Time at 250F, mins	11.5	BSS7276
Density, lbs/in^3 (g/cc)	0.0444 (1.23)	ASTM D792
G1C, in-lbs/in^2	6.10	ASTM D6671

Rheology

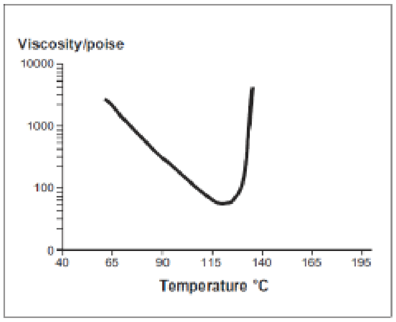

Gel Time

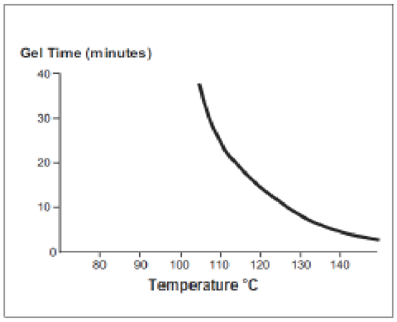

HexPly® 913

Product Data

Availability

Available on a wide variety of products:

Form	Hexcel Designation	Fiber	Fiber Areal Wt. g/m²	Weave	Count Warp x Fill	Widths Available, In (cm)	Resin Content, %
Glass Fabric	120GL/R913 120GL/F913S	EDC 450 - 1/2	105	4H Satin	60 x 58	38 (96.5)	35 45
	7781GL/R913 7781GL/F913S	ECDE 75 - 1/0	300	8H Satin	57 x 54	38 (96.5)	35 39-40
Glass Tape	S2GL/R913	S2GL	111, 222, 284, 295, 2556	Tape: UD; ±45°, ±60° X-ply	n/a	16, 24, 36, 40, 48, 48.5 (41-123)	32.5 - 33
Carbon Fabric	AGP193/R913	AS4 GP 3K	193	Plain	11.5 x 11.5	60 (152)	37
	AGP195CSW/ R913	AS4 GP 3K	195	4H Satin	11.5 x 11.5	60 (152)	38
	XAGP195/ R913	AS4 GP 3K	195	±45° 4H Satin	11.5 x 11.5	50 (127)	36
	XSGP196/ R913	IM7 GP 6K	196	±45° Plain	11 x 11	50 (127)	37
	W3X 286/ R913S	3K 33MSI	197	4H Satin	12 x 12	24 (61)	36
Carbon Tape	AS4GP 12K/ R913	AS4GP 12K	272, 195	Tape	n/a	12, 48 (30.5-122)	34 - 35
	IM2CGS 12K/ R913	IM2CGS-12K	110, 140	Tape	n/a	12, 24 (30.5, 61)	31 - 38
	IM7G 12K/R913	IM7G 12K	148, 296	Tape, ±45° X-ply	n/a	12, 24, 36, 48 (30.5-122)	33
	IM8-GS 12K/ R913	IM8-GS 12K	70	Tape	n/a	24 (61)	38

HexPly® 913 *Product Data*

Physical & Mechanical Properties

Form:			Carbon Fabric		Carbon Tape	
Category	**Property**	**Parameter, Units US (SI)**	**AGP195CSW/ R913;38%; 195AW**	**XSGP196/ R913LM;37; 196AW**	**IM7G/R913 ; 33%; 148AW**	**AS4GP 12K/R913; 35%; 272AW**
Physical Properties:	Prepreg:	Resin Content (dry), %	38	37	33	35
		Area Weight, g/m^2	195	196	148	272
		Volatile Content, %	< 0.5	< 0.4	-	< 0.2
	Laminate:	Cured Thickness per ply, inch (cm)	0.0070 (0.0178)	0.0084 (0.0214)	0.0056 (0.0142)	0.0101 (0.0257)
		Fiber Volume, %	62	-	-	60
		Density, g/cc	1.58	-	-	1.61
Mechanical Properties:	0° Tensile	Strength, ksi (MPa)	141 (970)	-	216 (1490)	331 (2280)
		Modulus, Msi (GPa)	10.1 (69.8)	-	12.2 (83.9)	19.5 (134)
		Strain,%	1.40	-	1.68	1.51
	90° Tensile	Strength, ksi (MPa)	145 (998)	152 (1048)	-	-
		Modulus, Msi (GPa)	10.3 (71.0)	10.9 (75.5)	-	-
		Strain, %	1.38	1.34	-	-
	0° Compression	Strength, ksi (MPa)	121 (832)	-	-	224 (1540)
		Modulus, Msi (GPa)	9.5 (65.2)	-	-	17.9 (123)
	90° Compression	Strength, ksi (MPa)	116 (799)	-	-	-
		Modulus, Msi (GPa)	9.7 (66.5)	-	-	-
	0° Short Beam Shear	Strength, ksi (MPa)	10.6 (73.3)	10.4 (71.8)	-	15.3 (105)
	0° Flexure	Strength, ksi (MPa)	-	131 (902)	-	-
		Modulus, Msi (GPa)	-	10.2 (70.2)	-	-

*Dry/Room Temperature Average Values

HexPly® 913 *Product Data*

Form			Glass Fabric		Glass Tape
Category	**Property**	**Parameter, Units US (SI)**	**120GL/R913; 37%;105AW**	**7781GL/R913; 37%;300AW**	**S2GL/R913;33%; 280AW**
Physical Properties:	Prepreg:	Resin Content (dry), %	37	37	33
		Area Weight, g/m^2	105	300	280
	Laminate:	Density, g/cc	1.83	1.83	1.80
Mechanical Properties:	0° Tensile	Strength, ksi (MPa)	70.9 (489)	65.3 (450)	203 (1400)
		Modulus, Msi (GPa)	3.1 (21.0)	3.2 (22.0)	6.4 (44.0)
	0° Compression	Strength, ksi (MPa)	85.3 (588)	66.7 (460)	160 (1100)
		Modulus, Msi (GPa)	-	4.1 (28.0)	6.7 (46.0)
	0° Short Beam Shear	Strength, ksi (MPa)	10.7 (74.0)	9.4 (65.0)	11.9 (82)
	0° Flexure	Strength, ksi (MPa)	104 (714)	88.5 (610)	-
		Modulus, Msi (GPa)	-	3.3 (23.0)	-

*Dry/Room Temperature Average Values

Cure Cycle

Recommended Cure:

60 minutes at 257°F (125°C) and 102 psi (700kPa) pressure. Heat up rate 3.6°F (2°C) to 14.4°F (8°C) per minute.

Alternative Cures:

Temperature °F (°C)	Time (Min)
284°F (140°C)	40
302°F (150°C)	20
320°F (160°C)	10

Components up to 0.118 inches (3 mm) thick can be cured without a dwell in the schedule provided that the heat-up rate is not more than 9°F (5°C)/minute. For thicker parts a dwell period is necessary in the heat-up to avoid the occurrence of a resin exotherm, but the dwell period will depend on the mass and type of tool. The standard dwell period is 30 minutes at 195°F during heat-up.

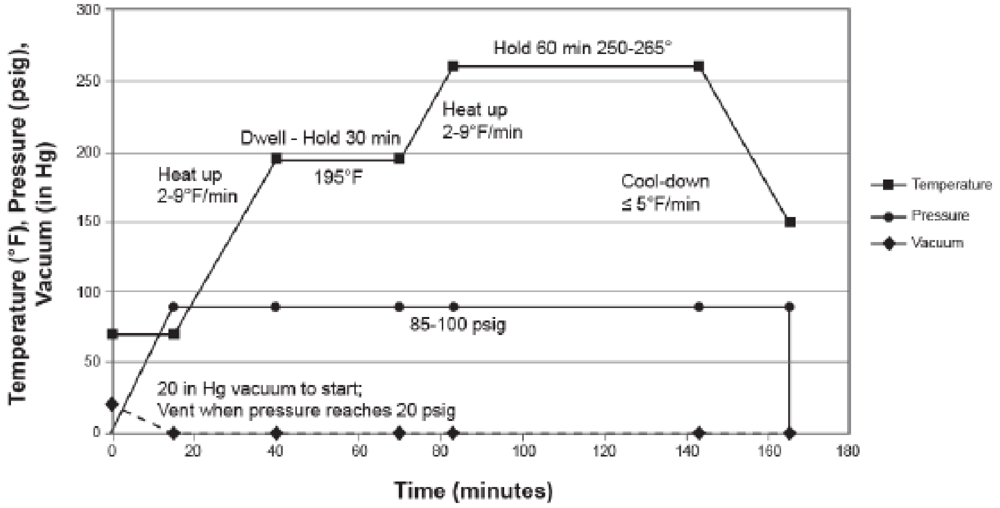

HexPly® 913

Product Data

Storage

Out Life: 30 days @ 73°F (23°C)
Guaranteed Shelf Life: 12 months @ 0°F (-18°C)

Storage Conditions

HexPly® 913 prepregs should be stored as received in a cool dry place or in a refrigerator. After removal from refrigerator storage, prepreg should be allowed to reach room temperature before opening the polythene bag, thus preventing condensation. (A full creel in its packaging can take up to 48 hours).

Precautions for Use

The usual precautions when handling uncured synthetic resins and fine fibrous materials should be observed, and a Safety Data Sheet is available for this product. The use of clean disposable inert gloves provides protection for the operator and avoids contamination of material and components.

Shipping

Prepreg is generally shipped in a sealed polyethylene bag in refrigerated transportation or in containers with dry ice.

Disposal of Scrap

Disposal of this material should be in a secure landfill in accordance with state and federal regulations.

Important

Hexcel Corporation believes, in good faith, that the technical data and other information provided herein is materially accurate as of the date this document is prepared. Hexcel reserves the right to modify such information at any time. The performance values in this data sheet are considered representative but do not and should not constitute specification minima. The only obligations of Hexcel, including warranties, if any, will be set forth in a contract signed by Hexcel or in Hexcel's then current standard Terms and Conditions of Sale as set forth on the back of Hexcel's Order Acknowledgement.

For more information

Hexcel is a leading worldwide supplier of composite materials to aerospace and other demanding industries.
Our comprehensive product range includes:

- Carbon Fiber
- Reinforced Fabrics
- Carbon, Glass, Aramid and Hybrid Prepregs
- RTM Materials
- Engineered Core
- HexTOOL® composite tooling material
- Structural Film Adhesives
- Honeycomb Cores

For US quotes, orders and product information call toll-free 1-800-688-7734. For other worldwide sales office telephone numbers and a full address list, please click here: http://www.hexcel.com/contact/salesoffices.

June 2014

Appendix B: Material parameters Torayca T700S

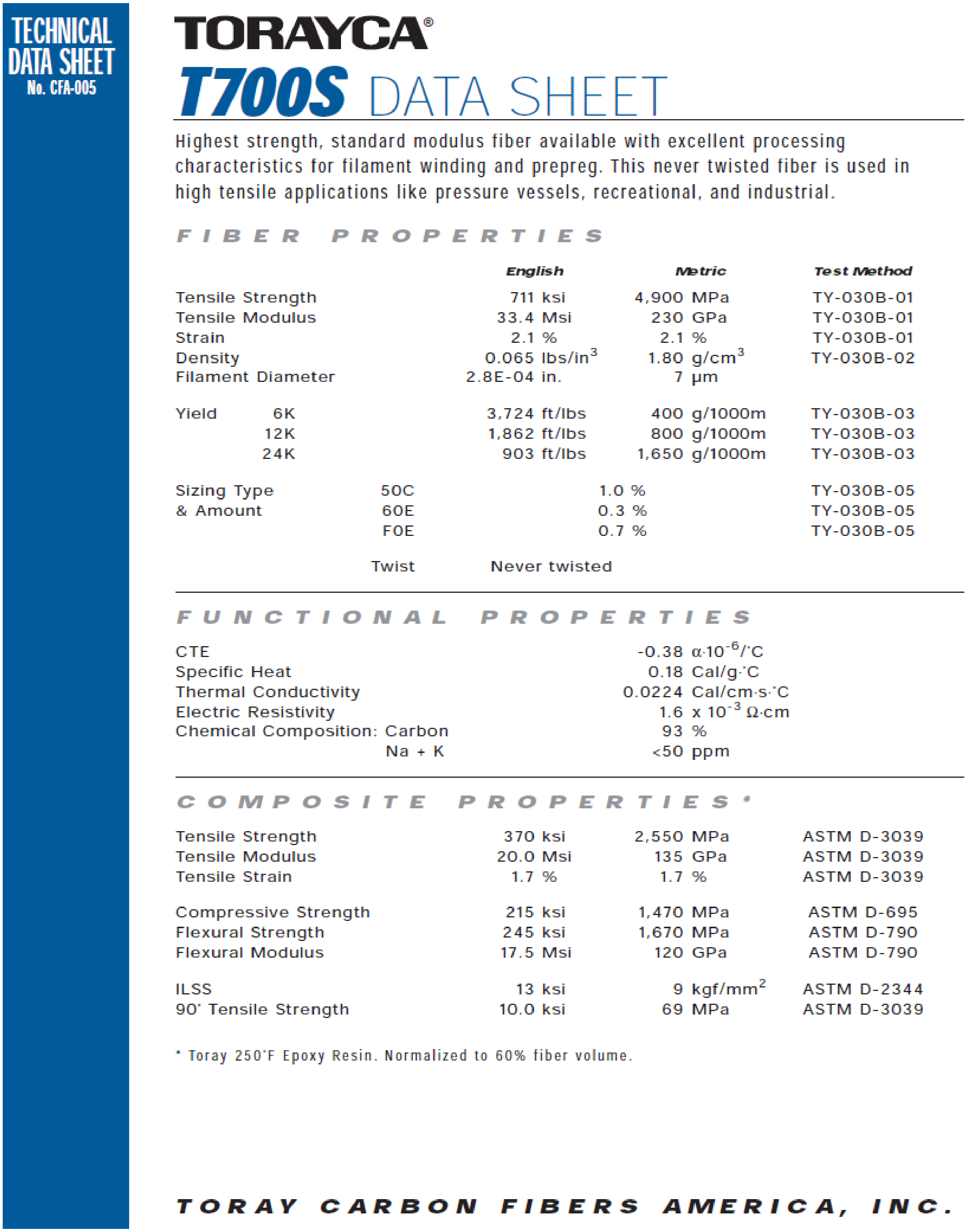

TECHNICAL DATA SHEET
No. CFA-005

TORAYCA®

T700S DATA SHEET

Highest strength, standard modulus fiber available with excellent processing characteristics for filament winding and prepreg. This never twisted fiber is used in high tensile applications like pressure vessels, recreational, and industrial.

FIBER PROPERTIES

		English	Metric	Test Method
Tensile Strength		711 ksi	4,900 MPa	TY-030B-01
Tensile Modulus		33.4 Msi	230 GPa	TY-030B-01
Strain		2.1 %	2.1 %	TY-030B-01
Density		0.065 lbs/in^3	1.80 g/cm^3	TY-030B-02
Filament Diameter		2.8E-04 in.	7 μm	
Yield	6K	3,724 ft/lbs	400 g/1000m	TY-030B-03
	12K	1,862 ft/lbs	800 g/1000m	TY-030B-03
	24K	903 ft/lbs	1,650 g/1000m	TY-030B-03
Sizing Type & Amount	50C	1.0 %		TY-030B-05
	60E	0.3 %		TY-030B-05
	FOE	0.7 %		TY-030B-05
	Twist	Never twisted		

FUNCTIONAL PROPERTIES

CTE	-0.38 $\alpha \cdot 10^{-6}/^\circ C$
Specific Heat	0.18 Cal/g·°C
Thermal Conductivity	0.0224 Cal/cm·s·°C
Electric Resistivity	1.6 x 10^{-3} Ω·cm
Chemical Composition: Carbon	93 %
Na + K	<50 ppm

COMPOSITE PROPERTIES*

	English	Metric	Test Method
Tensile Strength	370 ksi	2,550 MPa	ASTM D-3039
Tensile Modulus	20.0 Msi	135 GPa	ASTM D-3039
Tensile Strain	1.7 %	1.7 %	ASTM D-3039
Compressive Strength	215 ksi	1,470 MPa	ASTM D-695
Flexural Strength	245 ksi	1,670 MPa	ASTM D-790
Flexural Modulus	17.5 Msi	120 GPa	ASTM D-790
ILSS	13 ksi	9 kgf/mm^2	ASTM D-2344
90° Tensile Strength	10.0 ksi	69 MPa	ASTM D-3039

* Toray 250°F Epoxy Resin. Normalized to 60% fiber volume.

TORAY CARBON FIBERS AMERICA, INC.

T700S

COMPOSITE PROPERTIES**

Tensile Strength	355 ksi	2,450 MPa	ASTM D-3039
Tensile Modulus	18.0 Msi	125 GPa	ASTM D-3039
Tensile Strain	1.7 %	1.7 %	ASTM D-3039
Compressive Strength	230 ksi	1,570 MPa	ASTM D-695
Compressive Modulus	--- Msi	--- GPa	ASTM D-695
In-Plane Shear Strength	14 ksi	98 MPa	ASTM D-3518
ILSS	15.5 ksi	11 kgf/mm^2	ASTM D-2344
90° Tensile Strength	10.0 ksi	70 MPa	ASTM D-3039

** Toray Semi-Toughened 350°F Epoxy Resin. Normalized to 60% fiber volume.

See Section 4 for Safety & Handling information. The above properties do not constitute any warranty or guarantee of values. These values are for material selection purposes only. For applications requiring guaranteed values, contact our sales and technical team to establish a material specification document.

PACKAGING

The table below summarizes the tow sizes, twists, sizing types, and packaging available for standard material. Other bobbin sizes may be available on a limited basis.

Tow Sizes	Twist[1]	Sizing	Bobbin Net Weight (kg)	Bobbin Type[2]	Bobbin Size (mm)					Spools per Case	Case Net Weight (kg)
					a	b	c	d	e		
6K	C	50C	2.0	III	76.5	82.5	280	140	252	12	24
12K	C	50C	6.0	III	76.5	82.5	280	200	252	4	24
	C	60E	6.0	III	76.5	82.5	280	200	252	4	24
	C	F0E	6.0	III	76.5	82.5	280	200	252	4	24
24K	C	50C	6.0	III	76.5	82.5	280	200	252	4	24
	C	60E	6.0	III	76.5	82.5	280	200	252	4	24
	C	F0E	6.0	III	76.5	82.5	280	200	252	4	24

[1] **Twist** A: Twisted yarn B: Untwisted yarn made from a twisted yarn through an untwisting process C: Never twisted yarn

[2] **Bobbin Type** See Diagram below

TYPE I

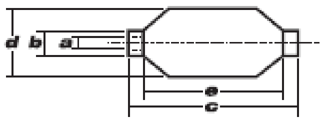

TYPE II

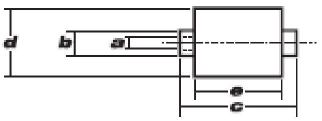

TYPE III

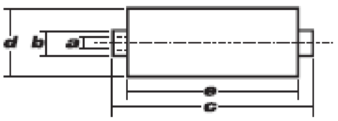

Appendix C: Material parameters Rubber SAA1052/70

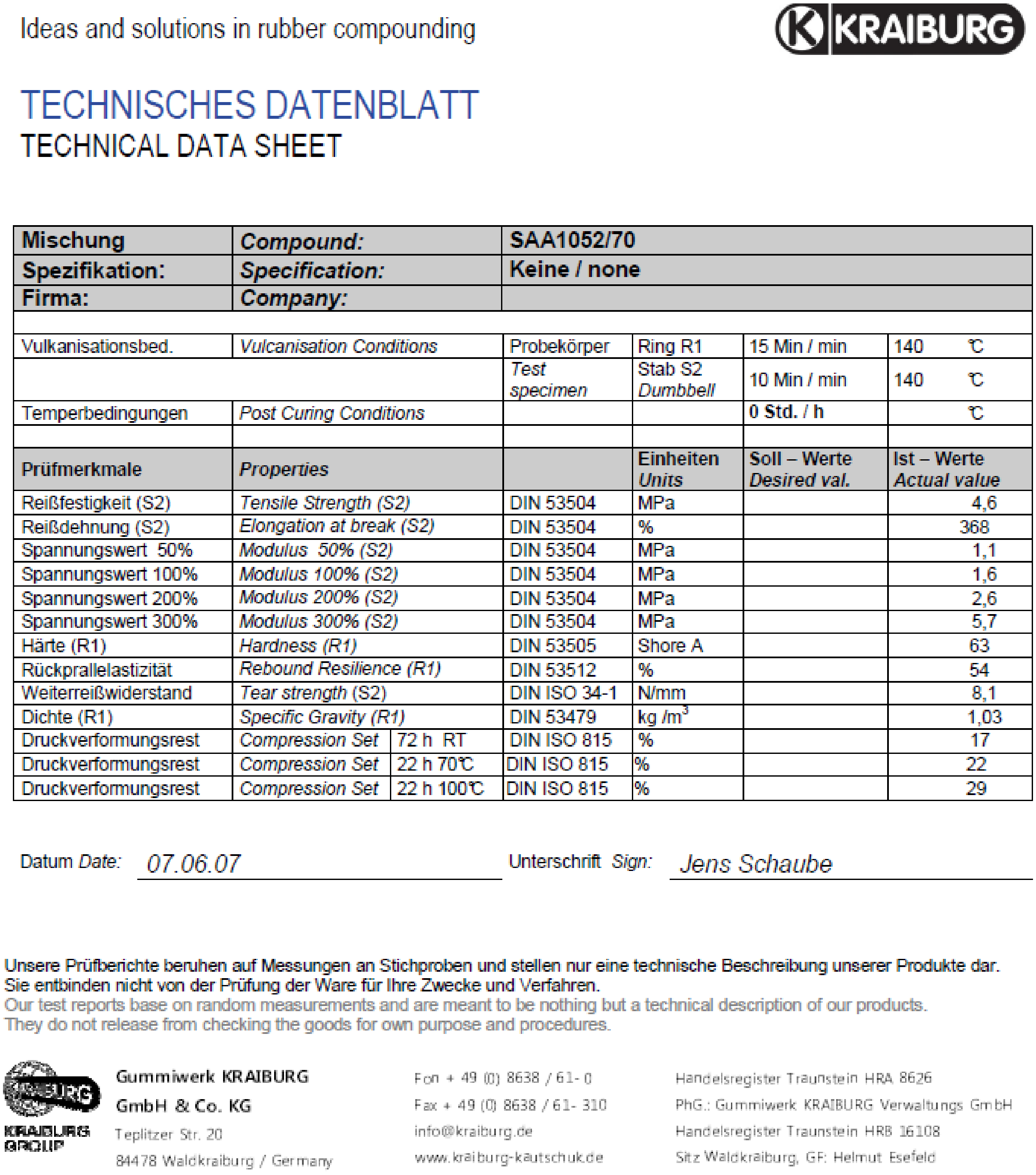

Ideas and solutions in rubber compounding

KRAIBURG

TECHNISCHES DATENBLATT

TECHNICAL DATA SHEET

Mischung	***Compound:***	**SAA1052/70**
Spezifikation:	***Specification:***	**Keine / none**
Firma:	***Company:***	

Vulkanisationsbed.	*Vulcanisation Conditions*	Probekörper	Ring R1	15 Min / min	140 °C
		Test specimen	Stab S2 *Dumbbell*	10 Min / min	140 °C
Temperbedingungen	*Post Curing Conditions*			**0 Std. / h**	°C

Prüfmerkmale	***Properties***			**Einheiten** *Units*	**Soll – Werte** *Desired val.*	**Ist – Werte** *Actual value*
Reißfestigkeit (S2)	*Tensile Strength (S2)*		DIN 53504	MPa		4,6
Reißdehnung (S2)	*Elongation at break (S2)*		DIN 53504	%		368
Spannungswert 50%	*Modulus 50% (S2)*		DIN 53504	MPa		1,1
Spannungswert 100%	*Modulus 100% (S2)*		DIN 53504	MPa		1,6
Spannungswert 200%	*Modulus 200% (S2)*		DIN 53504	MPa		2,6
Spannungswert 300%	*Modulus 300% (S2)*		DIN 53504	MPa		5,7
Härte (R1)	*Hardness (R1)*		DIN 53505	Shore A		63
Rückprallelastizität	*Rebound Resilience (R1)*		DIN 53512	%		54
Weiterreißwiderstand	*Tear strength* (S2)		DIN ISO 34-1	N/mm		8,1
Dichte (R1)	*Specific Gravity (R1)*		DIN 53479	kg /m^3		1,03
Druckverformungsrest	*Compression Set*	72 h RT	DIN ISO 815	%		17
Druckverformungsrest	*Compression Set*	22 h 70°C	DIN ISO 815	%		22
Druckverformungsrest	*Compression Set*	22 h 100°C	DIN ISO 815	%		29

Datum *Date:* *07.06.07*

Unterschrift *Sign:* *Jens Schaube*

Unsere Prüfberichte beruhen auf Messungen an Stichproben und stellen nur eine technische Beschreibung unserer Produkte dar. Sie entbinden nicht von der Prüfung der Ware für Ihre Zwecke und Verfahren.

Our test reports base on random measurements and are meant to be nothing but a technical description of our products. They do not release from checking the goods for own purpose and procedures.

KRAIBURG GROUP

Gummiwerk KRAIBURG
GmbH & Co. KG
Teplitzer Str. 20
84478 Waldkraiburg / Germany

Fon + 49 (0) 8638 / 61- 0
Fax + 49 (0) 8638 / 61- 310
info@kraiburg.de
www.kraiburg-kautschuk.de

Handelsregister Traunstein HRA 8626
PhG.: Gummiwerk KRAIBURG Verwaltungs GmbH
Handelsregister Traunstein HRB 16108
Sitz Waldkraiburg, GF: Helmut Esefeld

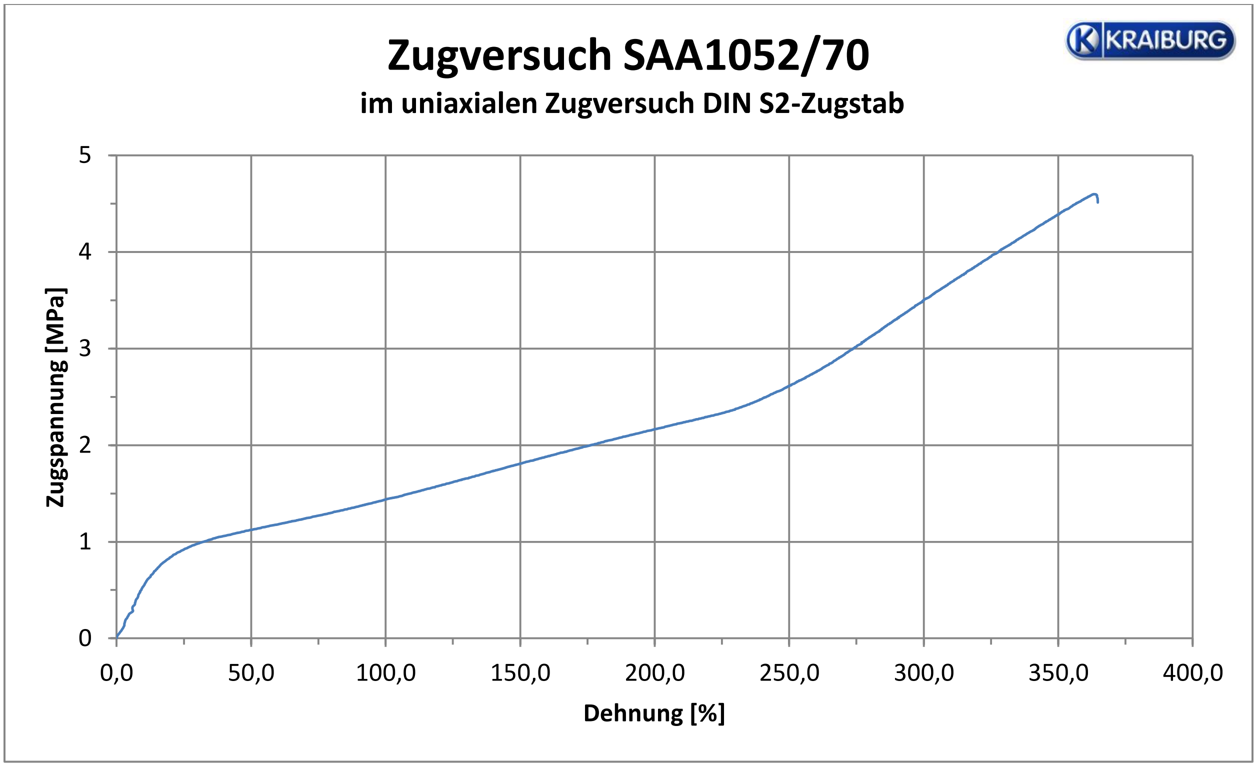
Zugversuch SAA1052/70
im uniaxialen Zugversuch DIN S2-Zugstab
KRAIBURG
Zugspannung [MPa]
0
1
2
3
4
5
Dehnung [%]
0,0
50,0
100,0
150,0
200,0
250,0
300,0
350,0
400,0

Appendix D: Material parameters TPE HTF9471/16

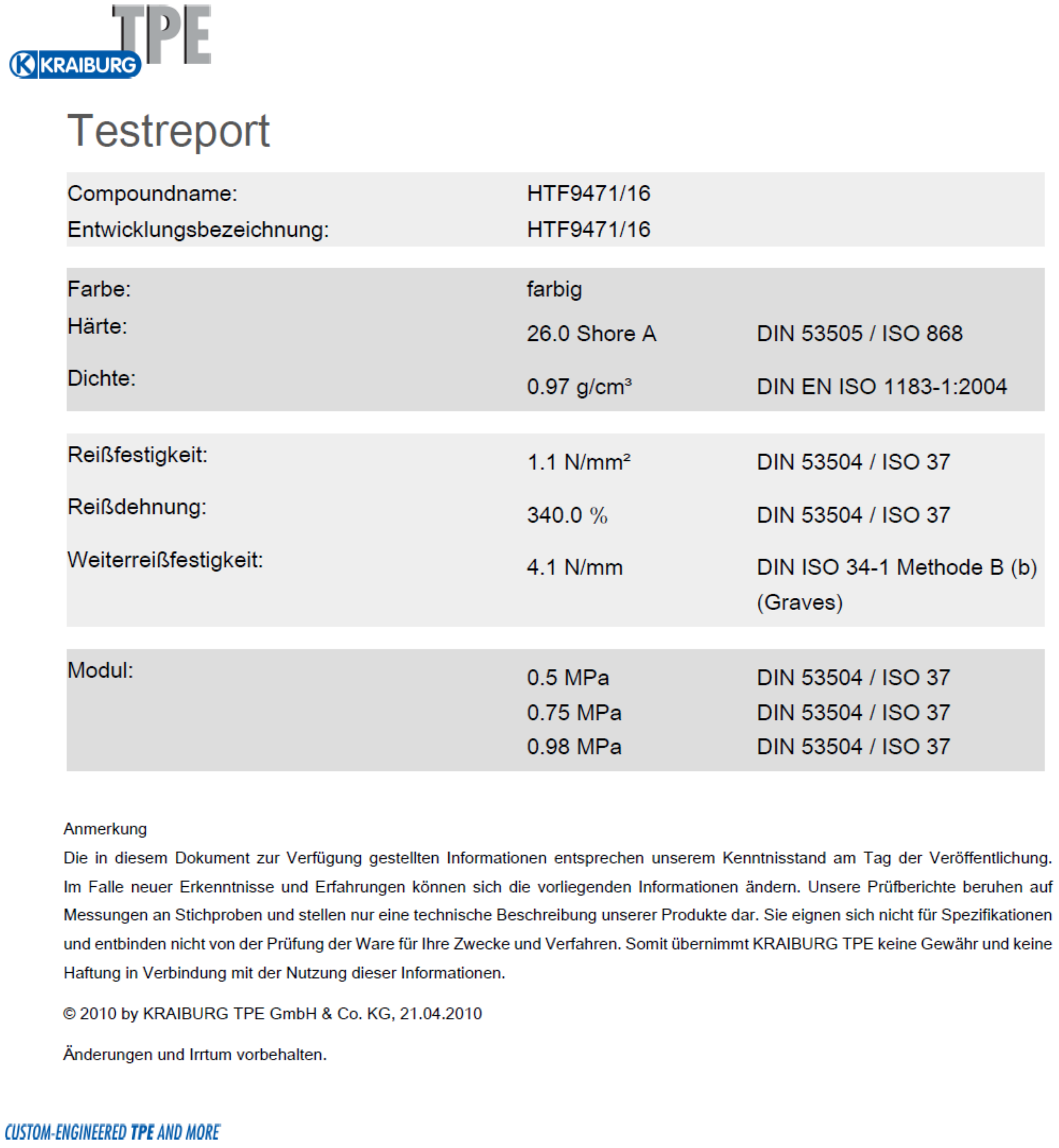

KRAIBURG TPE

Testreport

Compoundname:	HTF9471/16	
Entwicklungsbezeichnung:	HTF9471/16	
Farbe:	farbig	
Härte:	26.0 Shore A	DIN 53505 / ISO 868
Dichte:	0.97 g/cm^3	DIN EN ISO 1183-1:2004
Reißfestigkeit:	1.1 N/mm^2	DIN 53504 / ISO 37
Reißdehnung:	340.0 %	DIN 53504 / ISO 37
Weiterreißfestigkeit:	4.1 N/mm	DIN ISO 34-1 Methode B (b) (Graves)
Modul:	0.5 MPa	DIN 53504 / ISO 37
	0.75 MPa	DIN 53504 / ISO 37
	0.98 MPa	DIN 53504 / ISO 37

CUSTOM-ENGINEERED TPE AND MORE

TPE Material properties used for calculations (based on Test Data)		
E=0,9 N/mm^2	v=0.48	G=0,3 N/mm^2

Appendix E: Material parameters Silicone LR 7665 A/B

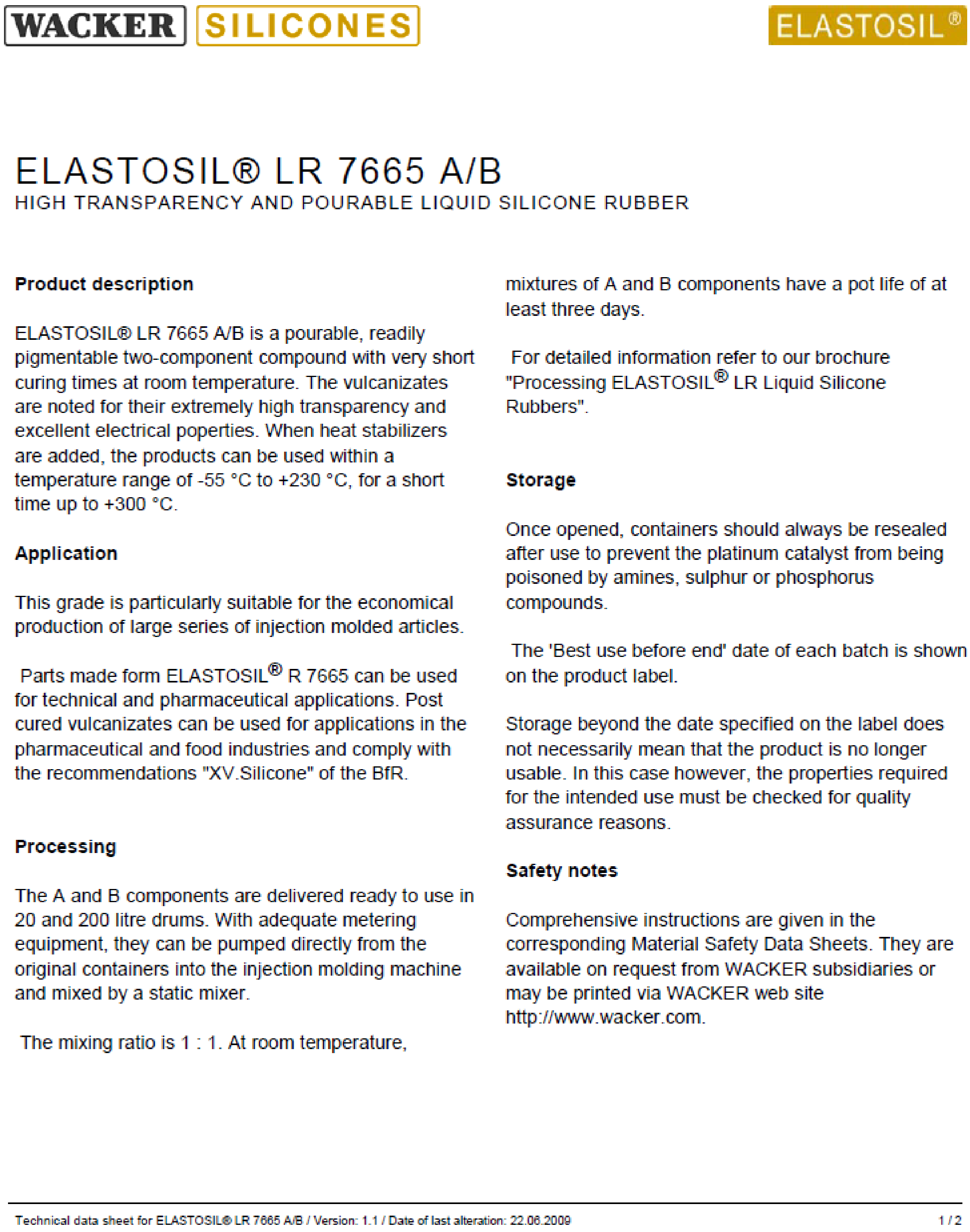

WACKER SILICONES ELASTOSIL®

ELASTOSIL® LR 7665 A/B

HIGH TRANSPARENCY AND POURABLE LIQUID SILICONE RUBBER

Product description

ELASTOSIL® LR 7665 A/B is a pourable, readily pigmentable two-component compound with very short curing times at room temperature. The vulcanizates are noted for their extremely high transparency and excellent electrical poperties. When heat stabilizers are added, the products can be used within a temperature range of -55 °C to +230 °C, for a short time up to +300 °C.

Application

This grade is particularly suitable for the economical production of large series of injection molded articles.

Parts made form ELASTOSIL® R 7665 can be used for technical and pharmaceutical applications. Post cured vulcanizates can be used for applications in the pharmaceutical and food industries and comply with the recommendations "XV.Silicone" of the BfR.

Processing

The A and B components are delivered ready to use in 20 and 200 litre drums. With adequate metering equipment, they can be pumped directly from the original containers into the injection molding machine and mixed by a static mixer.

The mixing ratio is 1 : 1. At room temperature, mixtures of A and B components have a pot life of at least three days.

For detailed information refer to our brochure "Processing ELASTOSIL® LR Liquid Silicone Rubbers".

Storage

Once opened, containers should always be resealed after use to prevent the platinum catalyst from being poisoned by amines, sulphur or phosphorus compounds.

The 'Best use before end' date of each batch is shown on the product label.

Storage beyond the date specified on the label does not necessarily mean that the product is no longer usable. In this case however, the properties required for the intended use must be checked for quality assurance reasons.

Safety notes

Comprehensive instructions are given in the corresponding Material Safety Data Sheets. They are available on request from WACKER subsidiaries or may be printed via WACKER web site http://www.wacker.com.

Product data

Typical general characteristics	Inspection Method	Value
Product data (single components)		
Appearance		transparent
Component A		
Density	ISO 1183-1 A	1,02 g/cm^3
Viscosity (Brookfield viscometer)		20000 mPa s
Component B		
Density	ISO 1183-1 A	1,01 g/cm^3
Viscosity (Brookfield viscometer)		19000 mPa s
Product data (non-postcured)		
Hardness Shore A	DIN 53505	54
Tensile strength	DIN 53504 S 1	7,5 N/mm^2
Elongation at break	DIN 53504 S 1	180 %
Tear strength	ASTM D 624 B	8,3 N/mm
Rebound resilience	DIN 53512	56 %
Dielectric strength , 1 mm sheet	DIN IEC 243-2	27 kV/mm
Volume resistivity	DIN IEC 93	4 x 10^{15} Ω cm
Dielectric Constant (50 Hz) εr	DIN VDE 0303	2,8
Dissipation Factor (50 Hz) tan δ	DIN VDE 0303	2 x 10^{-4}
Tracking resistance	DIN 53 480	KA 3 c

Cure conditions: 5 min / 165 °C, postcuring: 2 h / 200 °C
These figures are only intended as a guide and should not be used in preparing specifications.

For technical, quality, or product safety questions, please contact:

Wacker Chemie AG
Hanns-Seidel-Platz 4
81737 München, Germany
info.silicones@wacker.com

www.wacker.com

Appendix F: Introduction to continuums mechanics

To properly describe the stress/strain relationship in non-linear elastic deformations various different definitions and descriptions need to be made. To begin with there is the definition of a reference system based either on a Lagrangian or an Euler system. The Lagrangian system is used for material description and is moving with the deformed body. Here the observer is connected to–the moving particle and measures the changes over time. As for most solids the reference configuration is known, and the deformed configuration is of interest, Lagrange definition is usually used for solid body mechanics. The Euler system uses a fixed frame of reference and observes a fixed point in space over time from the outside; it is therefore often used to study fluid mechanic. It is always possible to transform from one system to the other if the equation of motion of the relevant point/body is known.

In Figure 117 a body at time=0 can be described as a sum of material points, that occupy a region of space. The movement of each point, e.g. Q can be described. The vector x_o denotes the position of point Q at time 0 and the vector x_t the position at time t. With this the deformation-gradient **F** can be described.

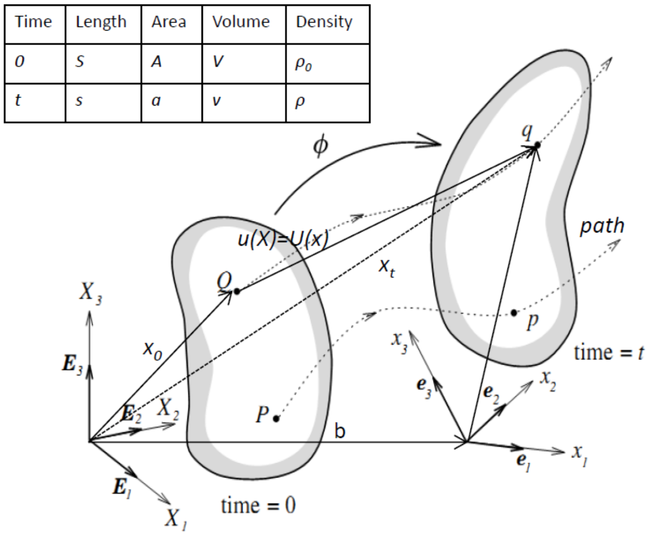

Time	Length	Area	Volume	Density
0	*S*	*A*	*V*	ρ_0
t	*s*	*a*	*v*	ρ

Figure 117: General Motion of a Deformable body
[Bonet et al., 1997]

The deformation-gradient is usually an unsymmetrical tensor.

$$\boldsymbol{F} = \frac{\delta \boldsymbol{x}_t}{\delta \boldsymbol{x}_o} \tag{37}$$

with: F: Deformation gradient

x_0: position vector of a point at time=0

x_t: position vector of a point at time=t

The determinant of $\boldsymbol{F}$ is also called Jacobian-(determinant) J and must fulfill the following requirements:

$$J = det\boldsymbol{F} \; \neq 0 \; and \; J > 0 \tag{38}$$

It is also possible to transform volume elements from the reference volume dV_0 to the current volume dV_t, for this applies:

$$J = \frac{dV_t}{dV_0} \tag{39}$$

with: J: Jacobian(-determinant); $[J] = 1$

V_t: volume of the actual configuration; $[V_t] = m^3$

V_0: volume of the initial configuration; $[V_0] = m^3$

For ideally incompressible materials the Jacobean becomes 1, meaning that the volume does not change during a deformation. This assumption is usually made when working with elastomers e.g. rubber. The complete motion of a body consists of a rigid body movement (this can be a translation, rotation or a combination) and a distortion due to a change of position of the individual particles. The deformation gradient $\boldsymbol{F}$ describes the complete motion and does not differentiate between rigid body motion and distortion. With polar decomposition of $\boldsymbol{F}$ it is possible to differentiate between rotation $\boldsymbol{R}$ and dilation $\boldsymbol{U}$ dilation or compression $\boldsymbol{V}$.

$$\boldsymbol{F} = \boldsymbol{RU} = \boldsymbol{UV} \tag{40}$$

The Tensors U and V are symmetrical and positive.

The polar decomposition of the deformation gradient leads to the Cauchy-Green – deformation tensors $\boldsymbol{C}$ and $\boldsymbol{B}$.

$$\boldsymbol{C} = \boldsymbol{U}^2 = \boldsymbol{F}^T\boldsymbol{F} \tag{41}$$

$$\boldsymbol{B} = \boldsymbol{V}^2 = \boldsymbol{F}\boldsymbol{F}^T \tag{42}$$

with $\boldsymbol{C}$: right Cauchy-Green-deformation tensor; $[\boldsymbol{C}] = 1$

$\boldsymbol{B}$: left Chauchy-Green-deformation tensor; $[\boldsymbol{B}] = 1$

For a rigid body motion (no deformation) the deformation tensor $\boldsymbol{F}$ for the reference-configuration becomes equal to the unit vector $\boldsymbol{I}$. Therefore the deformation-tensors $\boldsymbol{C}$ and $\boldsymbol{B}$ are also equal to $\boldsymbol{I}$. As $\boldsymbol{U}$ and $\boldsymbol{V}$ respectively $\boldsymbol{C}$ and $\boldsymbol{V}$ are similar tensors, they have the same eigenvalue. It is defined as:

$$C_{ii} = \lambda_i^2 \tag{43}$$

with: $C_{ii}; i = 1{,}2{,}3$: Eigenvalue of the Cauchy-Green-deformation tensor; $[C_{ii}] = 1$

$\lambda_i; i = 1{,}2{,}3$: aspect ratio along the principal axis; $[\lambda_i] = 1$

$$\lambda_i = \frac{I_i}{I_{0i}} = \varepsilon_i + 1 \tag{44}$$

I_i: actual length; $[I_i] = m$

I_0: initial length; $[I_0] = m$

ε_i: technical strain; $[\varepsilon_i] = 1$

With the invariants I_1, I_2 and I_3 of the Cauchy-green-deformation tensor $\boldsymbol{C}$ it is possible to describe the (deformation-)behavior of some materials; e.g. hyperelastic materials. Following the calculation of the invariants is shown:

$$I_1 = tr(C) = C_{11} + C_{22} + C_{33} = \lambda_1^2 + \lambda_2^2 + \lambda_3^2 \tag{45}$$

$$\begin{aligned} I_2 = \frac{1}{2}[I_1^2(\boldsymbol{C}) - I_1(\boldsymbol{C}^2)] &= C_{11}C_{22} + C_{22}C_{33} + C_{11}C_{33} - C_{12}C_{21} - C_{23}C_{32} - C_{31}C_{13} \\ &= \lambda_1^2\lambda_2^2 + \lambda_2^2\lambda_3^2 + \lambda_3^2\lambda_1^2 \end{aligned} \tag{46}$$

$$I_3 = \det(\boldsymbol{C}) = C_{11}C_{22}C_{33} + 2C_{12}C_{23}C_{31} - C_{11}C_{23}C_{32} - C_{22}C_{31}C_{13} - C_{33}C_{12}C_{21} = \lambda_1^2\lambda_2^2\lambda_3^2 \tag{47}$$

For the development of material models it can be helpful to introduce a deformation (strain)-measure, as the deformation-measure is zero for the reference configuration as well as for a rigid body motion and it is not 1 like the deformation tensor for these cases. For large deformations the Green-Lagrange deformation tensor $\boldsymbol{G}$ has been established as a good choice.

$$\boldsymbol{G} = \frac{1}{2}(\boldsymbol{C} - \boldsymbol{I}) = \frac{1}{2}(\boldsymbol{F}^T\boldsymbol{F} - \boldsymbol{I}) = \frac{1}{2}(\boldsymbol{U}^2 - \boldsymbol{I}) \tag{48}$$

with: $\boldsymbol{G}$: Green-Lagrange deformation tensor; $[\boldsymbol{G}] = \boldsymbol{1}$

The Green-Lagrange deformation tensor $\boldsymbol{G}$ is symmetrical and the diagonal entries of the tensor represent the “normal” deformations, change in length, while the non-diagonal entries represent the shear-deformation.

As a result of the deformation of a material stress occurs in the body. Stress is the response of a material body to external forces (mechanical, thermal, environmental). Usually a difference is made between true and technical stress. For internal stress analyses a sectional view is used, see Figure 118.

Taking the actual resulting force on the area-segment of the reference configuration, it is now possible to determine the stress-vector $\boldsymbol{s}$. The related stress-tensor is called 1st Piola-Kirchhoff stress-tensor. This tensor is also called technical stress. This is especially relevant during e.g. testing, as it can be measured directly.

$$\boldsymbol{s}(\boldsymbol{x}_0, \boldsymbol{n}_o, t) = \frac{\boldsymbol{df}}{d\boldsymbol{A}_0} = \boldsymbol{n}_0 \boldsymbol{\sigma}(\boldsymbol{x}_0, t) \tag{49}$$

with: $\boldsymbol{s}$: stress-vector; $[\boldsymbol{s}] = \frac{N}{m^2}$

$\boldsymbol{n}_0$: normal unit-vector of the reference configuration

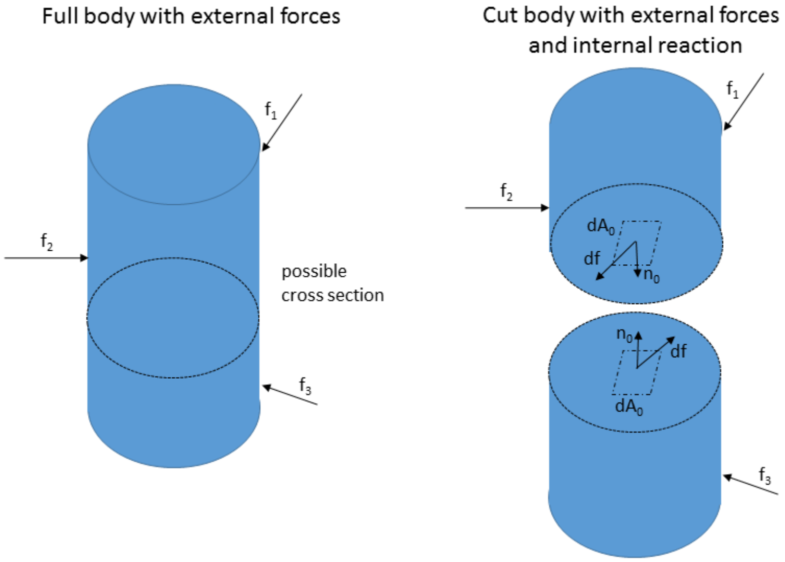

Figure 118: Full body with external forces and cut body with area-segment dA$_0$ for the reference configuration

t: time

$\boldsymbol{f}$:resulting current force-vector; $[\boldsymbol{f}] = N$

$\boldsymbol{A}_0$: area element of the reference configuration; $[\boldsymbol{A}_0] = m^2$

$\boldsymbol{\sigma}$: 1st Piola-Kirchhoff stress-tensor; $[\boldsymbol{\sigma}] = Pa$

The 1st Piola-Kirchhoff stress-tensor is an unsymmetrical tensor, which not always suited as a link between stress- and deformation-tensors. For this a modification is necessary that leads to the 2nd Piola-Kirchhoff stress tensor $\boldsymbol{S}$. This tensor is symmetric but has no physical relevance.

$$\boldsymbol{S} = \boldsymbol{\sigma}(\boldsymbol{F}^{-1})^T \tag{50}$$

with: $\boldsymbol{S}$: 2nd Piola-Kirchhoff stress tensor; $[\boldsymbol{S}] = \frac{N}{m^2}$

To obtain the true stress the resulting force-vector on the area-segment of the current reference configuration has to be used. This is also called the Cauchy-stress tensor.

$$\boldsymbol{k}(\boldsymbol{x}_t, \boldsymbol{n}_t, t) = \frac{\boldsymbol{df}}{d\boldsymbol{A}_t} = \boldsymbol{n}_t \boldsymbol{t}(\boldsymbol{x}_t, t) \tag{51}$$

with: $\boldsymbol{k}$: stress-vector; $[\boldsymbol{k}] = \frac{N}{m^2}$

$\boldsymbol{n}_t$: normal unit-vector of the reference configuration

t: time

$\boldsymbol{f}$: resulting actual force-vector; $[\boldsymbol{f}] = N$

$\boldsymbol{A}_t$: area element of the reference configuration; $[\boldsymbol{A}_t] = m^2$

$\boldsymbol{t}$: Cauchy stress-tensor; $[\boldsymbol{t}] = Pa$

The Cauchy stress-tensor always refers to the current geometry of the deformed body. It is possible to transform the Cauchy stress tensor $\boldsymbol{t}$, the 1st Piola-Kirchhoff stress tensor $\boldsymbol{\sigma}$ and the 2nd Piola-Kirchhoff stress tensor $\boldsymbol{S}$ into each other when going from the reference area section to the current deformed area section.

$$d\boldsymbol{A_t} = (\det \boldsymbol{F})(\boldsymbol{F}^{-1})^T d\boldsymbol{A}_0 \tag{52}$$

$$\boldsymbol{t} = (\det \boldsymbol{F})^{-1} \boldsymbol{F}\boldsymbol{\sigma} \tag{53}$$

$$\boldsymbol{\sigma} = (\det \boldsymbol{F})\boldsymbol{F}^{-1} \boldsymbol{t} \tag{54}$$

$$\boldsymbol{S} = (\det \boldsymbol{F})\boldsymbol{F}^{-1} \boldsymbol{t}(\boldsymbol{F}^{-1})^T \tag{55}$$

The entities of stress vectors at one point describe the current stress at this point.

In Figure 119 the stress vectors $\boldsymbol{s}_k$ for the technical stress and the stress components of the stress tensors $\boldsymbol{\sigma}$ are shown on an infinitesimal small element of a body. The arrows in Figure 119 named $\boldsymbol{\sigma_{ii}}$ are the normal stresses, which are perpendicular to the plane and $\boldsymbol{\sigma_{ij}}$ are the shear stresses, which are parallel to the plane.

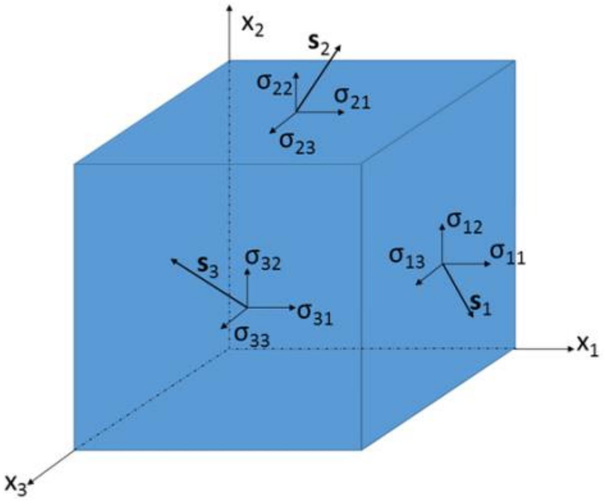

Figure 119: Stress vectors S_k and all components of the stress tensor σ_{ij} exemplary on a body

As a result to the equilibrium of forces on the body the stress tensor, which describes the current stress at any point of the body, can be written as:

$$\boldsymbol{\sigma} = \begin{pmatrix} \sigma_{11} & \sigma_{12} & \sigma_{13} \\ \sigma_{21} & \sigma_{22} & \sigma_{23} \\ \sigma_{31} & \sigma_{32} & \sigma_{33} \end{pmatrix} \tag{56}$$

All shear stresses pointing at the same edge of the body, e.g. σ_{12} and $\sigma_{21}$are identical due to the moment equilibrium acting on the body. It is therefore possible to describe the stress in the body with six components of the stress tensor:

$$\boldsymbol{\sigma} = \begin{pmatrix} \sigma_{11} & \sigma_{12} & \sigma_{13} \\ \sigma_{12} & \sigma_{22} & \sigma_{23} \\ \sigma_{13} & \sigma_{23} & \sigma_{33} \end{pmatrix} \tag{57}$$

As depicted in Figure 119 the components of the stress-tensor are dependent on the chosen coordinate system, but always describe the same stress condition independently of the coordinate system. For the principal coordinate system the shear stresses become zero, and only the normal stresses remain and are now called principal stresses.

$$\boldsymbol{\sigma} = \begin{pmatrix} \sigma_{11} & 0 & 0 \\ 0 & \sigma_{22} & 0 \\ 0 & 0 & \sigma_{33} \end{pmatrix} \tag{58}$$

Every stress tensor can be transformed into the principal coordinate system through mathematical operations.

Appendix G: Classical laminate theory

With E_{11}, E_{22} and G_{12} known for each ply it is possible to calculate the reduced stiffness matrix $[Q]$ for each single ply. If, as very often is the case, all plies consist of the same material, there will only be one stiffness matrix. Q describes the elastic behavior of the ply in plane loading:

$$[Q] = \begin{bmatrix} Q_{11} & Q_{12} & 0 \\ Q_{12} & Q_{22} & 0 \\ 0 & 0 & Q_{66} \end{bmatrix}, \tag{59}$$

where: $$Q_{11} = \frac{E_{11}}{1 - \nu_{12}\nu_{21}},\ Q_{12} = \frac{\nu_{21}E_{11}}{1 - \nu_{12}\nu_{21}},\ Q_{22} = \frac{E_{22}}{1 - \nu_{12}\nu_{21}} \text{ and } Q_{66} = G_{12} \tag{60-63}$$

Based on $[Q]$ and the individual ply angle, $[Q]$ can be transformed using transformation matrices $[T_\sigma]\ and\ [T_\epsilon]$ to$[\bar{Q}]$, which is the stiffness matrix of the ply in the global coordinate system.

$$[\bar{Q}] = [T_\sigma][Q][T_\epsilon]^{-1} \tag{64}$$

$$[T_\sigma] = \begin{bmatrix} m^2 & n^2 & 2mn \\ n^2 & m^2 & -2mn \\ -mn & mn & m^2 - n^2 \end{bmatrix} \tag{65}$$

$$[T_\epsilon]^{-1} = \begin{bmatrix} m^2 & n^2 & -mn \\ n^2 & m^2 & mn \\ 2mn & -2mn & m^2 - n^2 \end{bmatrix} \tag{66}$$

With $m = \cos\alpha$ and $n = \sin\alpha$

With the transformed stiffness-matrix $[\bar{Q}]$ it is now possible to calculate the overall stiffness matrix of the laminate using the following equations:

$$A_{ij} = \sum_{k=1}^{n} (\overline{Q})_k\,(z_k - z_{k-1}) \tag{67}$$

$$B_{ij} = \frac{1}{2}\sum_{k=1}^{n} (\overline{Q})_k\,(z_k^2 - z_{k-1}^2) \tag{68}$$

$$C_{ij} = \frac{1}{3}\sum_{k=1}^{n} (\overline{Q})_k\,(z_k^3 - z_{k-1}^3) \tag{69}$$

with z_k describing the distance of ply k from the center plane of the laminate and n is the number of plies in the laminate.

$$\begin{bmatrix} N_x \\ N_y \\ N_{xy} \\ M_x \\ M_y \\ M_{xy} \end{bmatrix} = \begin{vmatrix} \begin{pmatrix} A_{11} & A_{12} & A_{13} \\ A_{21} & A_{22} & A_{23} \\ A_{31} & A_{31} & A_{33} \end{pmatrix} & \begin{pmatrix} B_{11} & B_{12} & B_{13} \\ B_{21} & B_{22} & B_{23} \\ B_{31} & B_{32} & B_{33} \end{pmatrix} \\ \begin{pmatrix} B_{11} & B_{12} & B_{13} \\ B_{21} & B_{22} & B_{23} \\ B_{31} & B_{32} & B_{33} \end{pmatrix} & \begin{pmatrix} C_{11} & C_{12} & C_{13} \\ C_{21} & C_{22} & C_{23} \\ C_{31} & C_{32} & C_{33} \end{pmatrix} \end{vmatrix} * \begin{bmatrix} \varepsilon_{x0} \\ \varepsilon_{y0} \\ \varepsilon_{xy0} \\ \kappa_{x0} \\ \kappa_{y0} \\ \kappa_{xy0} \end{bmatrix} \tag{70}$$

with: $[A]$: Matrix of strain- or plane stiffness

$[B]$: Coupling- matrix

$[C]$: Matrix of bending- or plate stiffness

$\varepsilon_{x0}, \varepsilon_{y0}$ and ε_{xy0}: describe strains

κ_{x0}, κ_{y0} and κ_{xy0}: describe curvature

Appendix H: Stacking sequence GFRP of the droop nose

	Segment												
Ply number	**1**	**2**	**3**	**4**	**5**	**6**	**7**	**8**	**9**	**10**	**11**	**12**	**13**
1	0	0	0	0	0	0	0	0	0	0	0	0	0
2	-45	-45	-45	0	0	0	0	0	0	0	-45	-45	-45
3	90	45	45	-45	-45	-45	-45	-45	-45	-45	45	45	90
4	45	0	0	45	45	45	45	45	45	45	0	0	45
5	0	-45	-45	45	0	-45	45	0	-45	-45	-45	-45	0
6	-45	45	45	0	-45	45	-45	-45	45	45	45	90	-45
7	90	0	-45	-45	90	45	0	90	0	0	0	45	90
8	45	-45	45	45	45	-45	0	45	-45	-45	-45	0	45
9	0	90	0	0	45	45		45	90	90	90	-45	0
10	-45	45	-45	-45	90	-45		90	45	45	45	90	-45
11	90	0	45	90	-45	0		-45	45	0	0	45	90
12	45	-45	0	45	0	0		0	90	-45	-45	0	45
13	0	90	-45	45	45			45	-45	90	90	-45	0
14	-45	45	90	90	-45			-45	0	45	45	90	-45
15	90	0	45	-45	0			0	45	45	0	45	90
16	45	-45	45	0	0			0	-45	90	-45	0	45
17	0	90	90	45					45	-45	90	-45	0
18	-45	45	-45	-45					-45	0	45	90	-45
19	90	45	0	0					0	45	45	45	90
20	45	90	45	45					0	90	90	45	45
21	45	-45	-45	45						-45	-45	90	45
22	90	0	0	-45						0	0	-45	90
23	-45	45	45	0	Ply angle					45	45	0	-45
24	0	90	-45	0						-45	90	45	0
25	45	-45	45							45	-45	90	45
26	90	0	-45							-45	0	-45	90
27	-45	45	0							0	45	0	-45
28	0	90	45							0	90	45	0
29	45	-45	-45								-45	90	45
30	90	0	0								0	-45	90
31	-45	45									45	0	-45
32	0	-45									-45	45	0
33	45	0									0	90	45
34	90	45									45	-45	90
35	-45	-45									-45	0	-45
36	0	0									0	45	0
37	45											-45	45
38	90											0	90
39	-45												-45
40	0												0
Circumferencial position %	0,176	0,19	0,218	0,25	0,362	0,398	0,54	0,575	0,653	0,685	0,755	0,8	1

Figure 120: Stacking sequence of the GFRP droop nose (segment one starts on the bottom of the skin at the front spar) (Source: DLR; M.Kintscher)

Appendix I: Excerpt input-file tube in contact with two plates

Node numbers and positioning information not included.

```
…
480, 519, 520, 533, 532
*Node
    534,         -60.,          40.,         400.
*Nset, nset=Part-3-RefPt_, internal
534,
*Nset, nset=_PickedSet3, internal, generate
   1,  533,    1
*Elset, elset=_PickedSet3, internal, generate
   1,  480,    1
*Nset, nset=Set-5
 534,
*Nset, nset=Set-6, generate
   1,  533,    1
*Elset, elset=Set-6, generate
   1,  480,    1
** Section: Section-2
*Shell Section, elset=Set-6, material=alu, offset=SPOS
1., 5
*End Part
**
**
** ASSEMBLY
**
*Assembly, name=Assembly
**
*Instance, name=Part-1-1, part=Part-1
*End Instance
**
*Instance, name=Part-2-1, part=Part-2
*End Instance
**
*Instance, name=Part-3-1, part=Part-3
*End Instance
**
*Nset, nset=Set-4, instance=Part-2-1, generate
   1,  533,    1
*Elset, elset=Set-4, instance=Part-2-1, generate
   1,  480,    1
*Nset, nset=Set-5, instance=Part-3-1, generate
   1,  533,    1
*Elset, elset=Set-5, instance=Part-3-1, generate
   1,  480,    1
*Nset, nset=Set-6, instance=Part-3-1, generate
   1,  533,    1
*Elset, elset=Set-6, instance=Part-3-1, generate
   1,  480,    1
*Nset, nset=Set-7, instance=Part-3-1, generate
   1,  533,    1
*Elset, elset=Set-7, instance=Part-3-1, generate
```

```
  1,  480,    1
*Nset, nset=Set-8, instance=Part-3-1, generate
  1,  533,    1
*Elset, elset=Set-8, instance=Part-3-1, generate
  1,  480,    1
*Nset, nset=Set-9, instance=Part-1-1, generate
   1,  4050,     1
*Elset, elset=Set-9, instance=Part-1-1, generate
   1,  4000,     1
*Nset, nset=Set-10, instance=Part-2-1
 534,
*Nset, nset=Set-11, instance=Part-3-1
 534,
*Nset, nset=Set-12, instance=Part-3-1
 534,
*Nset, nset=m_Set-10, instance=Part-3-1
 534,
*Elset, elset=_Surf-3_SNEG, internal, instance=Part-3-1, generate
  1,  480,    1
*Surface, type=ELEMENT, name=Surf-3
_Surf-3_SNEG, SNEG
*Elset, elset=_Surf-4_SNEG, internal, instance=Part-1-1, generate
   1,  4000,     1
*Surface, type=ELEMENT, name=Surf-4
_Surf-4_SNEG, SNEG
*Elset, elset=_Surf-5_SNEG, internal, instance=Part-1-1, generate
   1,  4000,     1
*Surface, type=ELEMENT, name=Surf-5
_Surf-5_SNEG, SNEG
*Elset, elset=_Surf-6_SPOS, internal, instance=Part-1-1, generate
   1,  4000,     1
*Elset, elset=_Surf-6_SNEG, internal, instance=Part-3-1, generate
  1,  480,    1
*Surface, type=ELEMENT, name=Surf-6
_Surf-6_SPOS, SPOS
_Surf-6_SNEG, SNEG
*Elset, elset=_Surf-7_SNEG, internal, instance=Part-1-1, generate
   1,  4000,     1
*Surface, type=ELEMENT, name=Surf-7
_Surf-7_SNEG, SNEG
*Elset, elset=_Surf-8_SNEG, internal, instance=Part-3-1, generate
  1,  480,    1
*Surface, type=ELEMENT, name=Surf-8
_Surf-8_SNEG, SNEG
*Elset, elset=_Surf-9_SPOS, internal, instance=Part-1-1, generate
   1,  4000,     1
*Surface, type=ELEMENT, name=Surf-9
_Surf-9_SPOS, SPOS
*Elset, elset=_Surf-10_SPOS, internal, instance=Part-3-1, generate
  1,  480,    1
*Surface, type=ELEMENT, name=Surf-10
_Surf-10_SPOS, SPOS
*Elset, elset=_Surf-11_SNEG, internal, instance=Part-3-1, generate
```

```
  1,  480,    1
*Surface, type=ELEMENT, name=Surf-11
_Surf-11_SNEG, SNEG
*Elset, elset=_s_Surf-9_SNEG, internal, instance=Part-3-1, generate
  1,  480,    1
*Surface, type=ELEMENT, name=s_Surf-9
_s_Surf-9_SNEG, SNEG
*Rigid Body, ref node=Part-2-1.Part-2-RefPt_, elset=Part-2-1.Part-2
** Constraint: Constraint-1
*Coupling, constraint name=Constraint-1, ref node=m_Set-10, surface=s_Surf-9
*Kinematic
*End Assembly
*Amplitude, name=Amp-1, definition=SMOOTH STEP
             0.,              0.,            0.08,              1.
**
** MATERIALS
**
*Material, name=FMC_Lin_approx
*Density
 1e-09,
*Elastic, type=ENGINEERING CONSTANTS
40000.,5.,5.,0.,0.,0.,5.,5.
5.,
*Material, name=alu
*Density
 2.7e-09,
*Elastic
70000., 0.3
**
** INTERACTION PROPERTIES
**
*Surface Interaction, name=IntProp-1
*Friction
 0.8,
*Surface Behavior, pressure-overclosure=HARD
** ----------------------------------------------------------------
**
** STEP: Dynamic
**
*Step, name=Dynamic, nlgeom=YES
*Dynamic, Explicit
, 0.1
*Bulk Viscosity
0.06, 1.2
**
** BOUNDARY CONDITIONS
**
** Name: BC-1 Type: Displacement/Rotation
*Boundary
Set-10, 1, 1
Set-10, 2, 2
Set-10, 3, 3
Set-10, 4, 4
```

```
Set-10, 5, 5
Set-10, 6, 6
** Name: BC-2 Type: Displacement/Rotation
*Boundary, amplitude=Amp-1
Set-11, 1, 1
Set-11, 3, 3
Set-11, 4, 4
Set-11, 5, 5
Set-11, 6, 6
** Name: BC-3 Type: Displacement/Rotation
*Boundary
Set-9, 3, 3
Set-9, 5, 5
**
** LOADS
**
** Name: Load-2   Type: Pressure
*Dsload, amplitude=Amp-1
Surf-4, P, 0.03
** Name: Load-3   Type: Pressure
*Dsload
Surf-9, VP, 1e-06
** Name: Load-4   Type: Pressure
*Dsload
Surf-10, VP, 1e-06
** Name: Load-6   Type: Pressure
*Dsload, amplitude=Amp-1
Surf-11, P, 0.01
**
** INTERACTIONS
**
** Interaction: Int-1
*Contact, op=NEW
*Contact Inclusions, ALL EXTERIOR
*Contact Property Assignment
 ,  , IntProp-1
**
** OUTPUT REQUESTS
**
*Restart, write, number interval=1, time marks=NO
**
** FIELD OUTPUT: F-Output-1
**
*Output, field, variable=PRESELECT
**
** HISTORY OUTPUT: H-Output-1
**
*Output, history, variable=PRESELECT
*End Step
```

Appendix J: Excerpt input-file actuation variant: Two actuators

Node numbers and positioning information not included, also left out is the skin setup with ply orientation!

```
.
.
.
20876,   88.9311218,   98.5074615,   -26.479208
*Element, type=S4R
   1,    1,    5,   747,   492
.
. *End Assembly
*Amplitude, name=Amp-1, definition=SMOOTH STEP
          0.,             0.,           0.08,            1.
**
** MATERIALS
**
*Material, name=FMC-Lin
*Density*** [t/mm³]
1e-9,
*Elastic, type=ENGINEERING CONSTANTS
47000.,47000.,   4.5,    0.,    0.,    0.,   3.5,   3.5
   3.5,
*Material, name=GFK
*Density *** [t/mm³]
 1.8e-9,
*Elastic, type=ENGINEERING CONSTANTS
42000.,15000.,15000.,  0.26,  0.26,  0.26, 5600., 5600.
 5600.,
**
** INTERACTION PROPERTIES
**
*Surface Interaction, name=IntProp-1
*Friction
0.5,
*Surface Behavior, pressure-overclosure=HARD
** ----------------------------------------------------------------
**
** STEP: Step-1
**
*Step, name=Step-1, nlgeom=YES
*Dynamic, Explicit
, 0.1
*Bulk Viscosity
0.06, 1.2
**
** BOUNDARY CONDITIONS
**
** Name: BC- Actuators Y constrain Type: Displacement/Rotation
*Boundary
_PickedSet84, 2, 2
** Name: BC-Rigid Structure Type: Displacement/Rotation
```

```
*Boundary
Set-5, 1, 1
Set-5, 2, 2
Set-5, 3, 3
Set-5, 4, 4
Set-5, 5, 5
Set-5, 6, 6
** Name: BC-SKIN Lower Type: Displacement/Rotation
*Boundary
"Final Skin contour undeformed-1".Constraint_Unten, 1, 1
"Final Skin contour undeformed-1".Constraint_Unten, 2, 2
"Final Skin contour undeformed-1".Constraint_Unten, 3, 3
"Final Skin contour undeformed-1".Constraint_Unten, 4, 4
"Final Skin contour undeformed-1".Constraint_Unten, 5, 5
"Final Skin contour undeformed-1".Constraint_Unten, 6, 6
** Name: BC-SKIN Upper Type: Displacement/Rotation
*Boundary
"Final Skin contour undeformed-1".Contraint_oben, 1, 1
"Final Skin contour undeformed-1".Contraint_oben, 2, 2
"Final Skin contour undeformed-1".Contraint_oben, 3, 3
"Final Skin contour undeformed-1".Contraint_oben, 4, 4
"Final Skin contour undeformed-1".Contraint_oben, 5, 5
"Final Skin contour undeformed-1".Contraint_oben, 6, 6
**
** LOADS
**
** Name: AeroLoad Land   Type: Pressure Using Field: AnalyticalField-1
*Dload, amplitude=Amp-1
"Final Skin contour undeformed-1".1, P, -0.00150412
.
.[Air load distribution not included]
.
"Final Skin contour undeformed-1".9100, P, 0.00495768
** Name: Load Large Akt   Type: Pressure
*Dsload, amplitude=Amp-1
_PickedSurf86, P, 0.22
** Name: Load Small Akt   Type: Pressure
*Dsload, amplitude=Amp-1
_PickedSurf88, P, 0.22
** Name: ViscousSkin   Type: Pressure
*Dsload
_PickedSurf85, VP, 1e-06
**
** INTERACTIONS
**
** Interaction: Int-1
*Contact, op=NEW
*Contact Inclusions, ALL EXTERIOR
*Contact Property Assignment
 ,  , IntProp-1
**
** OUTPUT REQUESTS
**
```

```
*Restart, write, number interval=1, time marks=NO
**
** FIELD OUTPUT: F-Output-1
**
*Output, field, variable=PRESELECT
**
** HISTORY OUTPUT: H-Output-1
**
*Output, history, variable=PRESELECT
*End Step
```

Appendix K: Measurement points to evaluate the divergence from the target-shape

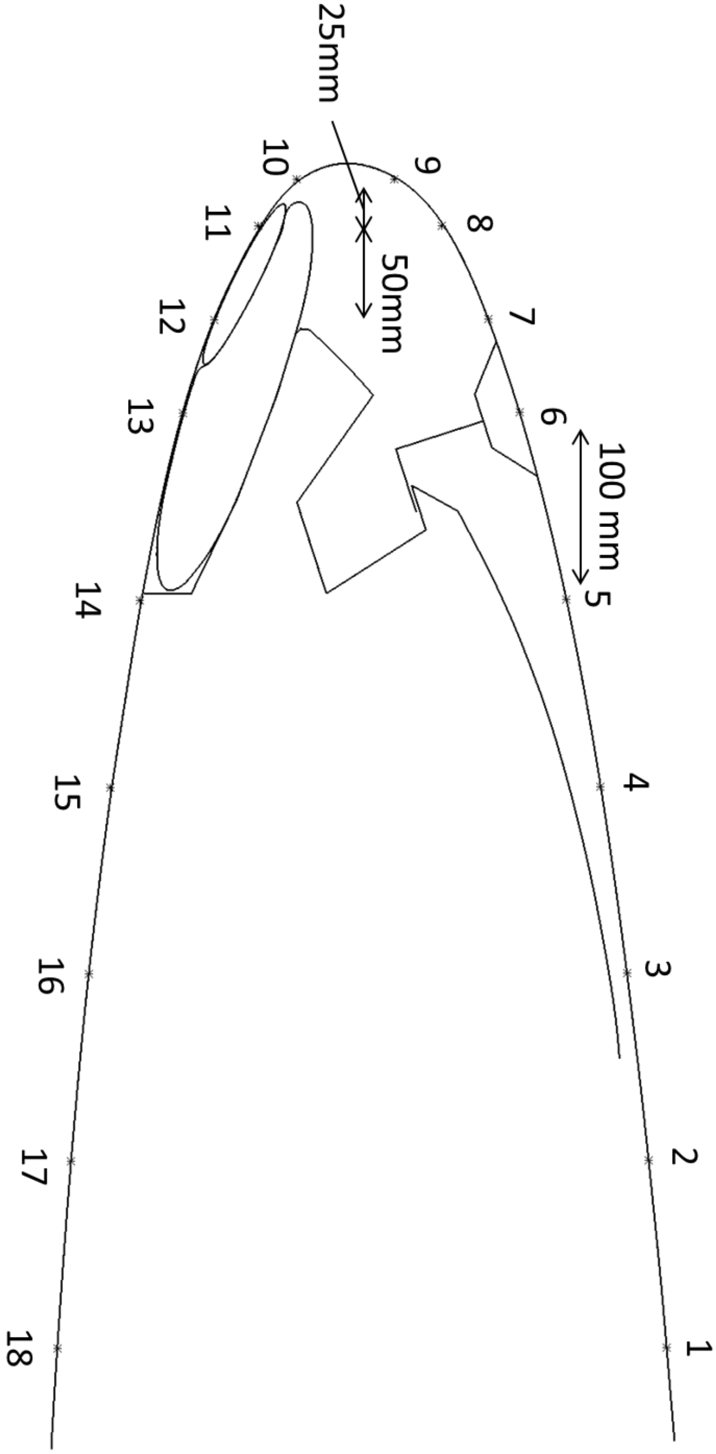

Figure 121: Measurement points along the skin

Appendix L: Results from sensitivity study (Pictures)

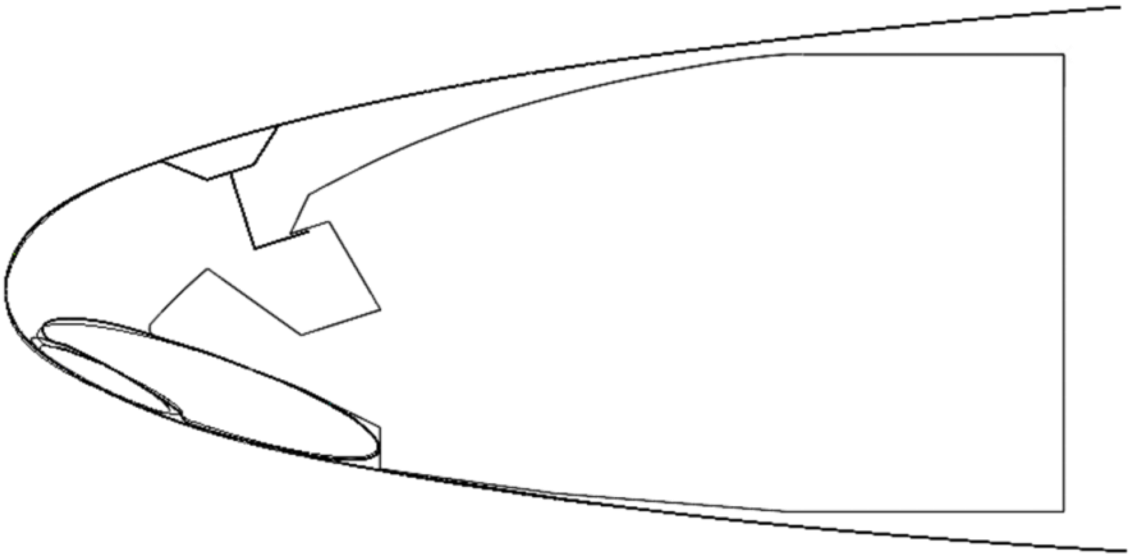

Figure 122: Cruise and actuation loads increased by 50%

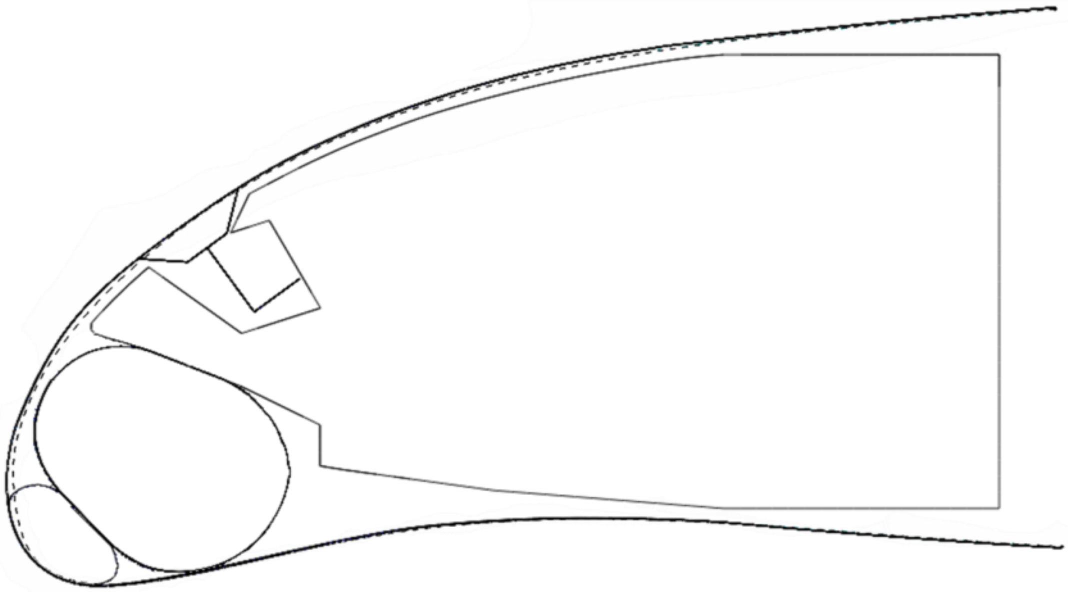

Figure 123: Landing and actuation loads increased by 50%

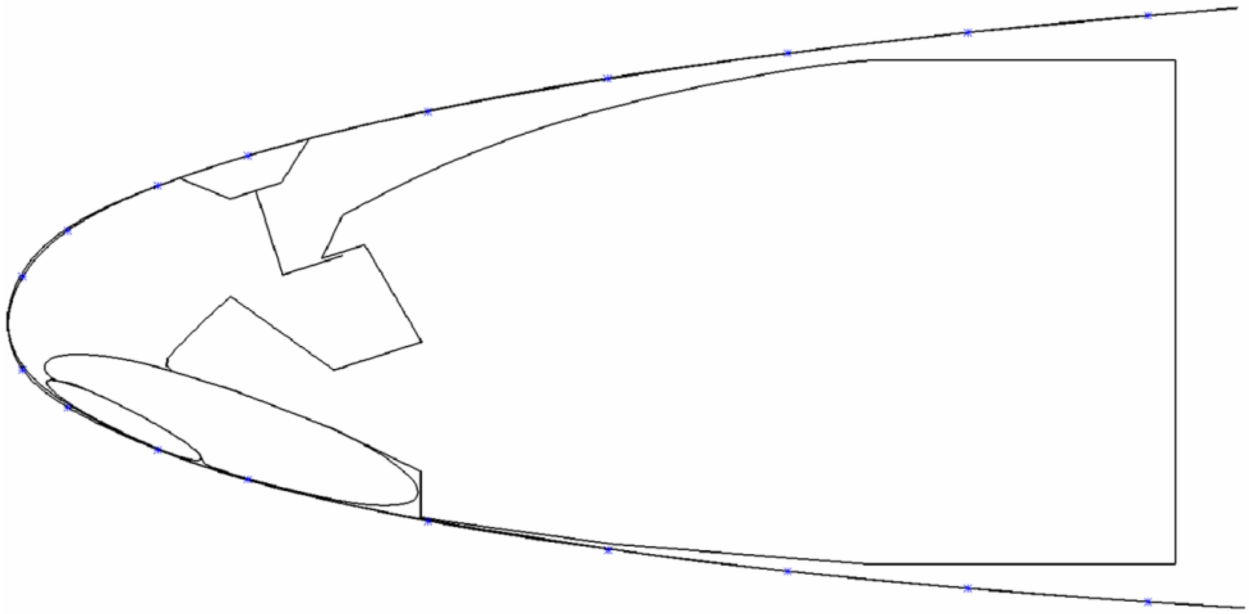

Figure 124: Cruise loads increased by 5%